NORTHWESTERN UNIVERSITY

# Synchrotron X-ray Studies of Epitaxial Ferroelectric Thin Films and Nanostructures

A DISSERTATION

SUBMITTED TO THE GRADUATE SCHOOL

IN PARTIAL FULFILLMENT OF THE REQUIREMENTS

for the degree

DOCTOR OF PHILOSOPHY

Field of Physics and Astronomy

By

Jeffrey A. Klug

EVANSTON, ILLINOIS

June 2010

# ABSTRACT

Synchrotron X-ray Studies of Epitaxial Ferroelectric Thin Films and Nanostructures

Jeffrey A. Klug

The study of ferroelectric thin films is a field of considerable scientific and technological interest. In this dissertation synchrotron x-ray techniques were applied to examine the effects of lateral confinement and epitaxial strain in ferroelectric thin films and nanostructures. Three materials systems were investigated: laterally confined epitaxial $BiFeO_3$ nanostructures on $SrTiO_3$ (001), ultra-thin commensurate $SrTiO_3$ films on Si (001), and coherently strained films of $BaTiO_3$ on $DyScO_3$ (110). Epitaxial films of $BiFeO_3$ were deposited by radio frequency magnetron sputtering on $SrRuO_3$ coated $SrTiO_3$ (001) substrates. Laterally confined nanostructures were fabricated using focused ion-beam processing and subsequently characterized with focused beam x-ray nanodiffraction measurements with unprecedented spatial resolution. Results from a series of rectangular nanostructures with lateral dimensions between 500 nm and 1 $\mu$m and a comparably-sized region of the unpatterned $BiFeO_3$ film revealed qualitatively similar distributions of local strain and lattice rotation with a 2-3 times larger magnitude of variation observed in those of the nanostructures compared to the unpatterned film. This indicates that lateral

confinement leads to enhanced variation in the local strain and lattice rotation fields in epitaxial $BiFeO_3$ nanostructures. A commensurate 2 nm thick film of $SrTiO_3$ on Si was characterized by the x-ray standing wave (XSW) technique to determine the Sr and Ti cation positions in the strained unit cell in order to verify strain-induced ferroelectricity in $SrTiO_3$ / Si. A Si (004) XSW measurement at 10 °C indicated that the average Ti displacement from the midpoint between Sr planes was consistent in magnitude to that predicted by a density functional theory (DFT) calculated ferroelectric structure. The Ti displacement determined from a 35 °C measurement better matched a DFT-predicted nonpolar structure. The thin film extension of the XSW technique was employed to measure the polar displacement of the Ba cations in a 50 nm thick coherently strained $BaTiO_3$ film on $DyScO_3$ (110). An analysis assuming a bulk-like ratio between the Ti and Ba displacements found that the polar shift of Ba cations was larger than in bulk $BaTiO_3$, which was consistent with strain-induced enhancement of ferroelectric polarization in $BaTiO_3$ / $DyScO_3$ (110).

Approved

---

Professor Michael J. Bedzyk
Department of Materials Science and Engineering and
Department of Physics and Astronomy
Northwestern University
Evanston, Illinois

Final Examination Committee
Prof. Michael J. Bedzyk, Chair
Prof. William P. Halperin
Prof. John B. Ketterson

## Acknowledgements

First I would like to thank my advisors, Professor Michael Bedzyk and Dr. Orlando Auciello. I have learned a great deal from working with each of them, and I am grateful for their support throughout my time at Northwestern. I thank Professor Bedzyk for impressing upon me the importance of conducting research with an acute attention to detail. Dr. Auciello I thank for sharing his passion and enthusiasm for science. I am grateful for the opportunity I have been given to work in the Materials Science Division (MSD) and at the Advanced Photon Source (APS) and Center for Nanoscale Materials (CNM) at Argonne National Laboratory. I have benefited not only from access to these facilities, but also from working with the scientists and postdocs who inhabit them.

I thank Professors Bill Halperin and John Ketterson for serving on my doctoral committee. I especially thank Professor Halperin for filling out numerous faculty appraisal forms on my behalf for my various graduate positions at Argonne over the years.

I also thank my collaborators at Argonne and Penn State. I especially thank Ramesh Premnath (MSD) for his tireless and invaluable work on the $BiFeO_3$ project. Seungbum Hong (MSD) I thank for sharing his expertise in Piezoresponse Force Microscopy as well as his willingness to discuss many aspects of scientific reseach. I thank Alexandra Imre for her work as the CNM scientific contact for the nanofabrication portion of the $BiFeO_3$ project. Beamline scientist Martin Holt (CNM) deserves many thanks for his role as scientific contact in the $BiFeO_3$ Hard X-ray Nanoprobe experiments. I thank Michael Biegalski,

Maitri Warusawithana, and Professor Darrell Schlom (Penn State) for providing samples for the $BaTiO_3$ and $SrTiO_3$ x-ray standing wave measurements, and I thank Denis Keane (DND-CAT) for his countless hours of help during beamtime at 5ID-C.

I am grateful to have had the opportunity to work along side many talented scientists at Northwestern and at Argonne. Among my colleagues in the Bedzyk Group, I thank Steve Christensen for his friendship and many insightful discussions as well as for humoring me as my go-to reference for "materials science" questions. I thank Jon Emery for his humor, his thoughful questions, appreciation for good music, and discerning taste in beer. I have also appreciated my interaction with and the various help I have received from Phillip Lin, Yuan-Chieh Tseng, Chang-Yong Kim, Zhenxing Feng, Duane Goodner, Anthony Escuadro, Vaibhav Kohli, Curtis Leung, and Martin McBriarty. Among my friends and classmates in the Northwestern Physics department, I am especially glad to have known Jon Andreasen, Johannes Pollanen, and Meghan Anzelc. At Argonne, I have enjoyed my interaction with Guoren Bai, Wei Li, Bing Shi, Matt Highland, Stephan Hruszkewycz, Volker Rose, Moonkyu Park, and Mengchun Pan.

Finally, I wish to thank my family for their love, support and encouragement: My mom, Jane, who has always supported me; My brothers Bill and Andrew, fellow scientists and two guys I would hang out with even if we weren't brothers; My father Ken and my daughter Leah, both of whom I love and deeply miss. I wish you were here, today and everyday; My son Tommy, who is my most favorite distraction. The sound of your laughter gives me perspective when I need it.

Above all I thank my wife Amy who is my best friend and partner in this endeavor and many more to come. I could not have done this without you. Nor would I wish to.

For Amy

# Table of Contents

# List of Tables

# List of Figures

CHAPTER 1

# Introduction

The science and technology of ferroelectric thin films has been a highly active and growing field of research over the last two decades, largely due to applications in a broad range of advanced microelectronic devices such as nonvolatile ferroelectric random access memorys (FeRAMs), piezoelectrically actuate microelectromechanical systems (MEMS) and nanoelectromechanical systems (NEMS) devices, and integrated optics devices. While the ferroelectric properties of thin films are routinely characterized via electrical and atomic force microscopy (AFM)-based piezoresponse measurements, these methods do not relate the measured ferroelectric performance directly to the underlying atomic-scale processes responsible for ferroelectric domain formation and switching, i.e., ion displacement in the ferroelectric layer. In contrast, advanced x-ray characterization methods directly probe structure and structural deformations which are strongly coupled to ferroelectric properties. Such methods are particularly well suited to the study of strain effects in epitaxial films and nanostructures. In this respect, the work presented in this dissertation has employed synchrotron x-ray techniques to study the effects of lateral confinement in epitaxial $BiFeO_3$ (BFO) nanostructures, strain-induced ferroelectricity in commensurate $SrTiO_3$ (STO) on Si, and enhanced ferroelectric polarization in strained $BaTiO_3$ (BTO).

An overview of ferroelectric thin films and nanostructures is presented in Chapter 2 with particular attention paid to previous studies related to the work presented in this dissertation. Section 2.1 introduces ferroelectrics, describes some of the applications of

ferroelectric thin films, and discusses the motivation for studying the particular materials characterized in this work, i.e. the search for a robust Pb-free ferroelectric material. Section 2.2 briefly discusses strain effects in ferroelectric thin films, and Section 2.3 provides motivation for studying lateral size effects in epitaxial nanostructures.

The primary x-ray characterization methods used in this dissertation are introduced in Chapter 3. Section 3.1 discusses the focused beam nanodiffraction technique which was used in the $BiFeO_3$ nanostructure study found in Chapter 5. The single crystal x-ray standing wave (XSW) technique is described in Section 3.2. This atomic-scale structural probe was employed in the $SrTiO_3$ / Si measurements discussed in Chapter 6. The thin film extension of the XSW technique is introduced in Section 3.3. Such measurements were used in the $BaTiO_3$ study found in Chapter 7. Section 3.4 details the analysis of crystal truncation rod (CTR) measurements, which were used in both the $SrTiO_3$ and $BaTiO_3$ studies.

Chapter 4 describes the growth and fabrication of $BiFeO_3$ thin film nanostructures which were subsequently characterized in the nanodiffraction study presented in Chapter 5. The structure of the ferroelectric antiferromagnet $BiFeO_3$ is discussed in Section 4.1. Section 4.2 describes the thin film growth process and optimization of deposition parameters for the samples studied for this dissertation. Single-phase, epitaxial $BiFeO_3$ films were grown by off-axis radio frequency (RF) magnetron sputter deposition on $SrRuO_3$ (SRO) coated $SrTiO_3$ (001) substrates. The fabrication strategies employed to produce isolated $BiFeO_3$ nanostructures from the sputter-grown films are discussed in Section 4.3. Nanostructures were fabricated via focused ion-beam (FIB) processing with either a protective platinum film or an electron-beam patterned tungsten mask.

Chapter 5 presents the results of focused beam x-ray nanodiffraction measurements of local strain in epitaxial $BiFeO_3$ nanostructures. Measurements made at the new Hard X-ray Nanoprobe beam line at sector 26ID-C of the Advanced Photon Source (APS) enabled structural characterization of this novel system with unprecedented spatial resolution. Section 5.1 describes the experimental setup and measurement procedure for the nanodiffraction study. The nanodiffraction results from the Pt-protected nanostructures are presented in Section 5.2, while those from the W-protected structures are presented in Section 5.3. The previous two sections are summarized in Section 5.4. Measurements of an as-fabricated Pt-protected sample revealed virtually no diffraction from the nanostructures, while characterization of an annealed sample found a significant recovery of the diffracting volume. However, the observed diffraction from the annealed sample was weak, and therefore provided limited information about the strain state of the nanostructures. In contrast, the as-fabricated W-protected nanostructures were found to be strongly diffracting. Comparison of the results from the nanostructures and the unpatterned film indicated enhanced variation in the local strain and lattice rotation distributions in the nanostructures. These results represent the first measurements of local strain in laterally confined heteroepitaxial structures using the world's most advanced hard x-ray microscope.

Chapter 6 covers synchrotron measurements of ultra thin commensurate films of $SrTiO_3$ grown on Si (001). Background on the $SrTiO_3$ / Si system is presented in Section 6.1, and the structure and growth of commensurate films are discussed in Section 6.2. The samples characterized in this work were grown by a molecular beam epitaxy (MBE)

based deposition process by collaborators at the Pennsylvania State University. Section 6.3 describes the experimental setup for the $SrTiO_3$ measurements. Experiments were carried out at APS beam line 5ID-C. The results of single crystal XSW and specular CTR measurements are presented in Section 6.4 and Section 6.5, respectively. Section 6.6 summarizes the $SrTiO_3$ results. Analysis of the XSW results for a 5 monolayer (ML) $SrTiO_3$ film at 10 °C and 35 °C indicated that average noncentrosymmetric displacement of the Ti cations at 10 °C was opposite in direction but consistent in magnitude with that from a density functional theory (DFT)-predicted ferroelectric structure, whereas at 35 °C the Ti displacement was similar to that of a DFT-predicted nonpolar structure. The results of a 30 °C $(00l)$ CTR measurement indicated that the mean Ti displacement was in the same direction but significantly smaller than that of the polar DFT model. The inconsistency of the XSW and CTR results may be due to lateral inhomogeneity of the sample and a significantly larger beam footprint during the CTR measurement.

Chapter 7 discusses the x-ray studies of a strained 50 nm thick $BaTiO_3$ film on $DyScO_3$ (DSO). Section 7.1 describes the structure of $BaTiO_3$ and $DyScO_3$ and briefly details the film growth performed by our collaborators at Pennsylvania State University. Results of thin film XSW measurements are presented in Section 7.2, and a specular CTR measurement is discussed in Section 7.3. The XSW experiments were conducted at APS beam line 12ID-D, while the CTR measurement was made in the x-ray laboratory at Northwestern. Section 7.4 summarizes the x-ray results. The Ti cation position could not be experimentally determined due to limited resolution of the x-ray fluorescence detector used in the XSW measurement. However, analysis of the Ba XSW data with an assumed bulk-like ratio between the the Ba and Ti displacements indicated that the film was polarized

up, and that the magnitude of the Ba displacement was larger than for bulk, unstrained $BaTiO_3$. This was qualitatively consistent with a strain-enhanced polarization. Analysis of the CTR measurement also found that the film was polarized up, with an interfacial layer thickness appropriately contracted in response to the downward shift of the oxygen anions in the film.

Chapter 8 briefly summarizes this dissertation and comments on future work.

CHAPTER 2

# Overview of Ferroelectric Thin Films and Nanostructures

## 2.1. Ferroelectric Thin Films Introduction

Ferroelectrics are a class of materials which possess a spontaneous and switchable electric polarization [1]. Application of an external electric field results in a hysteretic response of the ferroelectric polarization, as illustrated in Figure 2.1. Ferroelectric materials are necessarily both pyroelectric and piezoelectric, and they exhibit various technologically relevant dielectric and electro-optical properties. As a result, ferroelectric thin films are of interest for use in a broad range of advanced microelectronic devices such as non-volatile FeRAMs [2–4], piezoelectrically actuate MEMS and NEMS devices [5, 6], and integrated optics devices [7]. To date, $Pb(Zr_xTi_{1-x})O_3$ (PZT) is the most extensively used ferroelectric material. However, the microelectronics industry is on schedule to phase Pb out of future micro- and nanoelectronic devices due to environmental concerns related to the toxicity of Pb. Finding a suitable Pb-free ferroelectric material with properties comparable to $Pb(Zr_xTi_{1-x})O_3$ is of great concern for the current and future development of high-density ferroelectric memories, piezoelectrically driven MEMS/glsnems, and other devices. Two potential paths to the realization of a robust Pb-free ferroelectric are the use of epitaxial strain to tailor the properties of known materials such as $BaTiO_3$ or $SrTiO_3$, and the use of a new or previously overlooked material, such as multiferroic $BiFeO_3$.

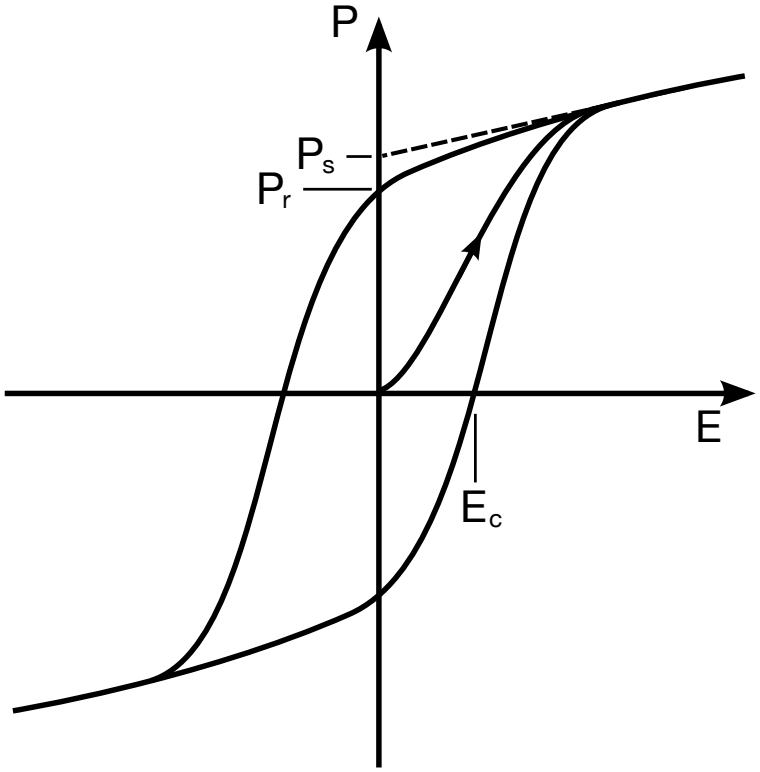


Figure 2.1. Ideal ferroelectric hysteresis loop. Under an applied electric field, ferroelectric domains align with the field to lower the net dipole energy. Saturation occurs when all domains are aligned. When the external field is removed, some relaxation of the domain alignment occurs leaving a net "remnant" polarization, $P_{\mathrm{r}}$ at zero field. The spontaneous polarization, $P_{\mathrm{s}}$ is defined as the value extrapolated from saturation polarization (dashed line). The coercive field, $E_{\mathrm{c}}$ is the applied field required to return the polarization to zero.

Recently, so-called multiferroic materials, which may exhibit multiple ferroic properties (e.g. ferroelectricity, ferromagnetism, or ferroelasticity) in a single phase, have attracted much interest [8–10]. Specifically, intense study has focused on magnetoelectric multiferroic materials, which are simultaneously (anti-) ferroelectric and (anti-) ferromagnetic with coupling between the electric and magnetic order parameters. Materials in which the electric field from the ferroelectric behavior can affect the magnetic performance and

vice versa provide a rich platform for exciting research on new fundamental materials science and device physics. In addition, multiferroic thin films have a great potential for application to new advanced devices using the coupling of electric and magnetic order parameters in a single material.

Among the known single-phase multiferroics, $BiFeO_3$ is the most widely studied due to its robust ferroelectric and antiferromagnetic order parameters. However, $BiFeO_3$ is also an important material for purely ferroelectric applications in addition to potential devices exploiting its magnetoelectric properties. While early bulk studies showed a small polarization ($P_r \sim 6.1\mu C/cm^2$), recent measurements revealed that $BiFeO_3$ thin films exhibit much higher polarization ($P_r \sim 90\mu C/cm^2$) [11–14] than $Pb(Zr_xTi_{1-x})O_3$ ($P_r \sim 60 - 70\mu C/cm^2$). This dramatic increase was first viewed as an effect of epitaxial strain [11], similar to strain-induced enhancements observed in titanate (e.g. $SrTiO_3$, $BaTiO_3$) films. However, subsequent experimental and theoretical studies have led to the conclusion that a large polarization is an intrinsic property of bulk $BiFeO_3$, and that the early bulk measurements were influenced by high leakage [10, 13]. A large polarization and a high Curie temperature ($T_C \sim 1100$ K) make $BiFeO_3$ a very robust ferroelectric material, which provides a new platform for the development of advanced technologies based on a Pb-free material.

## 2.2. Strain Effects in Ferroelectric Thin Films

Epitaxial strain can significantly alter the structure and physical properties of a material, and even stabilize a phase not present in bulk [15–18]. For example, Choi and coworkers reported enhanced ferroelectricity in coherently strained $BaTiO_3$ films [18], and

Haeni *et al.* reported room temperature ferroelectricity in strained $SrTiO_3$ [16], which in bulk remains paraelectric down to zero kelvin. Choi found an increase in ferroelectric transition temperature from $T_C = 393$ K for bulk single crystals to $\sim 673$ K and $\sim 813$ K for films grown on orthorhombic substrates $GdScO_3$ (110) and $DyScO_3$ (110), with in-plane biaxial compressive strain $\epsilon_s = -1.0$ and $\epsilon_s = -1.7$, respectively. The elevated Curie temperatures were identified by high resolution x-ray diffraction measurements which observed an anomaly in the temperature dependence of the out-of-plane lattice constant. The anomalous lattice expansion was consistent with a polar-to-nonpolar phase transition as calculated by a Landau-Devonshire phenomenological thermodynamic analysis [18–20]. Furthermore, the measured transition temperatures were consistent with those predicted for each value of biaxial strain, as shown in Figure 2.2.

Polarization hysteresis measurements by Choi *et al.* of a 200 nm thick coherent $BaTiO_3$ film on $GdScO_3$ and a 200 nm thick partially relaxed film ($\epsilon_s = -1.3$) on $DyScO_3$ (with conductive $SrRuO_3$ electrodes) showed a remnant polarization of $P_r \sim 50$ $\mu C/cm^2$ and $P_r \sim 70$ $\mu C/cm^2$, respectively. These polarizations are significantly larger than the bulk value $P_r = 26$ $\mu C/cm^2$, and comparable to $Pb(Zr_xTi_{1-x})O_3$ for the film on $DyScO_3$. A thinner, coherently strained film on $DyScO_3$ may have an even larger polarization (due to the greater strain of $\epsilon_s = -1.7$ compared to $\epsilon_s = -1.3$ for the relaxed film). However, hysteresis measurements of the thinner samples suffered from excessive dielectric leakage.

In the study by Haeni and coworkers, a ferroelectric transition at $T_C \sim 293$ K was observed for a $SrTiO_3$ film with in-plane biaxial tensile strain $\epsilon_s = +0.8$ grown on $DyScO_3$ (110) [16]. The tensile strain gave rise to an in-plane ferroelectric polarization in the strained film. Measurements of the temperature dependence of the complex dielectric

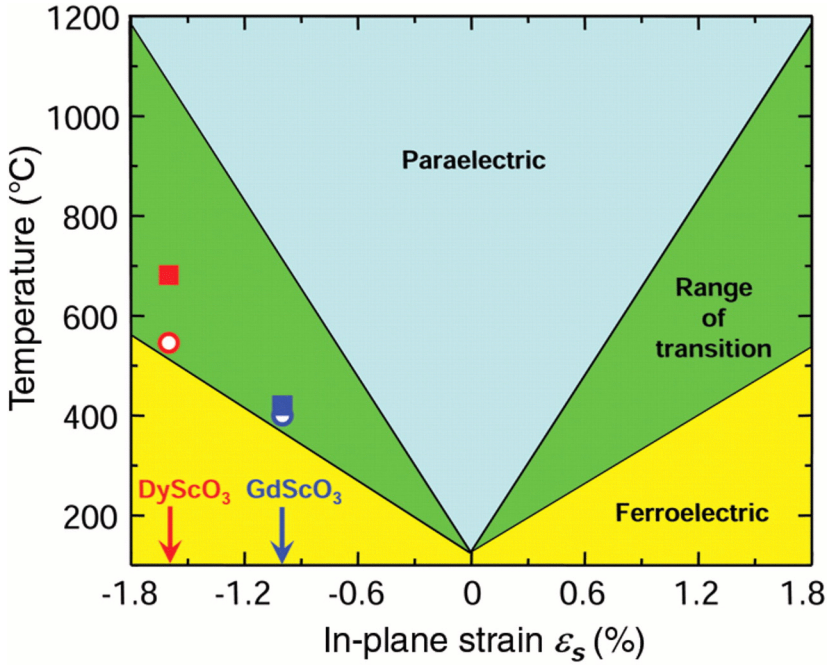


Figure 2.2. Predicted and measured dependence of the ferroelectric Curie temperature of $BaTiO_3$ on biaxial in-plane epitaxial strain. From Choi *et al.* [18].

permittivity were performed to demonstrate the presence of a ferroelectric phase and to determine $T_C$. The in-plane dielectric constant $\epsilon_r$ and the loss tangent $\tan\delta$ were measured at 10 GHz using interdigitated electrodes. Haeni observed a peak in both quantities at $T_C \sim 293$ K in agreement with expected Curie-Weiss behavior. Furthermore, the overall magnitude of the in-plane dielectric constant was larger than that measured for a strained $SrTiO_3$ film grown on a compressive $(LaAlO_3)_{0.29} \times (SrAl_{0.5}Ta_{0.5}O_3)_{0.71}$ (LSAT) substrate with $\epsilon_s = -0.9\%$. This was consistent with a in-plane ferroelectric polarization in the film on $DyScO_3$.

More recently, Warusawithana *et al.* reported room temperature ferroelectricity in commensurate ultra-thin films of $SrTiO_3$ grown directly on Si (001) under a compressive strain of $\epsilon_s = -1.66\%$ [17]. The $SrTiO_3$ / Si (001) system is discussed further in Chapter 6.

As discussed previously, while the 2003 study by Wang *et al.* reported a strain enhanced polarization in epitaxial $BiFeO_3$ films [11], it is now known that a large polarization is an intrinsic property of bulk $BiFeO_3$. Furthermore, theoretical studies by both phenomenological [21] and first principles [22, 23] methods have since shown that ferroelectric polarization in $BiFeO_3$ is actually quite insensitive to epitaxial strain. However, as predicted by Zhang *et al.* [21] and demonstrated by Jang and coworkers [24], epitaxial strain can lead to a rotation of the nominally [111] oriented polarization in pseudocubic (001) oriented $BiFeO_3$ films. Jang studied $BiFeO_3$ films with varying degrees of in-plane compressive and tensile strain using high resolution x-ray diffraction, transmission electron microscopy (TEM), and polarization hysteresis measurements. An approximately linear dependence of the out-of-plane polarization on in-plane strain was observed, with a $\sim 25\%$ change in $P_\mathrm{r}$ for $\epsilon_\mathrm{s} = 1.0\%$. Jang found the measured $P_\mathrm{r}$ values to be in excellent aggreement with the strain dependence predicted from the Landau-type thermodynamic analysis of Zhang which found that while the absolute magnitude of the polarization was nearly invariant, the relative amplitudes of the in-plane and out-of-plane components were modified such that the polarization rotates toward the [001] direction for biaxial compressive strain, and toward the [110] direction for tensile strain. Interestingly, the rotation of the polarization vector was determined to be larger than that expected due only to the strain-induced change in $c/a$ ratio.

## 2.3. Epitaxial Ferroelectric Nanostructures

Like like the coupling between polarization and epitaxial strain, finite size effects in ferroelectric materials are of both fundamental and technological interest. Numerous

studies of ultra-thin films have been performed to understand how film thickness can affect ferroelectric properties and to determine a critical thickness at which ferroelectricity becomes unstable [25]. Fong and coworkers observed synchrotron x-ray scattering evidence of ferroelectricity in $PbTiO_3$ films as thin as three unit cells [26]. Béa *et al.* observed by piezoresponse force microscopy (PFM) [27] that ferroelectricity in $BiFeO_3$ is preserved in films at least as thin as 2 nm [28]. However, in addition to the influence of finite thickness effects on ferroelectric properties, lateral size effects in ferroelectric nanostructures are also of interest.

A study by Nagarajan *et al.* examined the effects of lateral confinement in epitaxial $PbZr_{0.2}Ti_{08}O_3$ thin film capacitors fabricated by focused ion-beam milling [29]. PFM measurements of an isolated 1 $\mu m^2$ capacitor observed clear evidence of 90° domain wall motion under applied electric field, and polarization hysteresis loops measured as a function of maximum applied field found a factor of two increase in remnant polarization (from $\sim 40\mu C/cm^2$ to $\sim 80\mu C/cm^2$) for applied fields above $\sim$ 15 MV/m. Similar measurements on a region of the continuous film found no enhancement. Furthermore, Nagarajan observed a significantly enhanced ($\sim 300\%$) $d_{33}$ piezoelectric coefficient in a 1 $\mu m^2$ capacitor. These results were attributed to contributions from 90° ferroelastic switching which was enabled by a reduction of substrate clamping as a result of decreased lateral size. The dependence of the clamping effect of the substrate on lateral island size was modeled for PZT with a continuum mechanics analysis. The analysis found that the degree of clamping was significantly reduced for islands with lateral dimensions less than 10× the film thickness. The ability to increase the mobility of ferroelastic domain wall with lateral confinement may have significant implications for lateral size effects in $BiFeO_3$ for which

pseudocubic (001) oriented films have been experimentally observed to contain exclusively ferroelastic (71° and 109°) domain walls [14, 30]. In particular, the results of Nagarajan may be relevant in light of two significant barriers to the use of $BiFeO_3$ as a viable Pb-free ferroelectric in high-density FeRAMs: a large coercive field and high leakage current [10, 14].

$BiFeO_3$ films typically have a coercive field ∼250 kV/cm, which is considerably larger than the typical value necessary for FeRAM applications (∼50-70 kV/cm). The mechanism(s) responsible for such a high coercivity are largely unexplored [14]. However, a recent study [31] by Jang and coworkers found a substantial reduction in the coercive field (∼80 kV/cm) for $BiFeO_3$ membranes which were produced by using a dry etch process to remove the underlying Si substrate on which they were grown. A coercive field $25\% - 30\%$ higher was measured for the same films prior to removal of the substrate. The $BiFeO_3$ membranes also exhibited reduced leakage and no polarization fatigue up to $2.4\times10^{10}$ cycles. Based on these findings, Jang suggested that the high coercivity of $BiFeO_3$ films was the result of a substrate clamping effect and that the removal of epitaxial constraint enabled increased domain wall motion. The reduced coercive field seems consistent with the work of Nagarajan. The physical basis for the observed reduction in leakage is less obvious. However, a recent study by Seidel and Martin *et al.* provides a possible explanation.

Seidel, Martin and coworkers reported the observation of room temperature conduction at 109° and 180° domain walls in $BiFeO_3$ thin films [32]. Conductive atomic force microscopy (c-AFM) measurements observed localized electrical conductivity at 109° and

180° domain walls in 100 nm thick epitaxial films grown on (001), (110), and (111) oriented $SrTiO_3$. No conduction was observed at 71° walls. A combined high resolution TEM and DFT study found evidence of a small displacement of the Fe cations in the direction normal to a 109° domain wall. DFT calculations determined that this structrual modification results in a 0.15 eV step in the electrostatic potential across the wall. A 0.1 eV reduction in the bandgap was calculated near the 109° wall relative to domain centers (1.3 eV). Similar results were calculated for 180° domain walls whereas no such perpendicular Fe displacement was observed via TEM or DFT for 71° walls. In light of these results, the reduced leakage observed by Jang *et al.* in $BiFeO_3$ membranes may also be related to increased domain wall mobility resulting from the removal of substrate clamping. If 109° domain walls provide conduction paths, then pinning of these ferroelastic domain walls in the clamped films may explain the higher leakage measured relative to the unclamped membranes.

From the work of Jang *et al.* it appears that substrate clamping may have a significant effect on the ferroelectric properties of $BiFeO_3$ films. However, the use of lateral confinement as a means to control the degree of clamping has been thus far almost entirely unexplored. In this respect, work was begun to study laterally confined $BiFeO_3$ nanostructures in the Interfacial Materials Group of the Materials Science Division at Argonne National Laboratory. Focused ion-beam lithography was used to fabricate $BiFeO_3$ nanostructures from epitaxial films grown by RF magnetron sputter deposition on $SrRuO_3$ coated (001) $SrTiO_3$ substrates. An initial PFM study led by Seungbum Hong examined 120 nm thick square and circular shaped nanostructures with lateral dimensions of 500 nm [33]. The measured ferroelectric domain configurations of the two different shaped

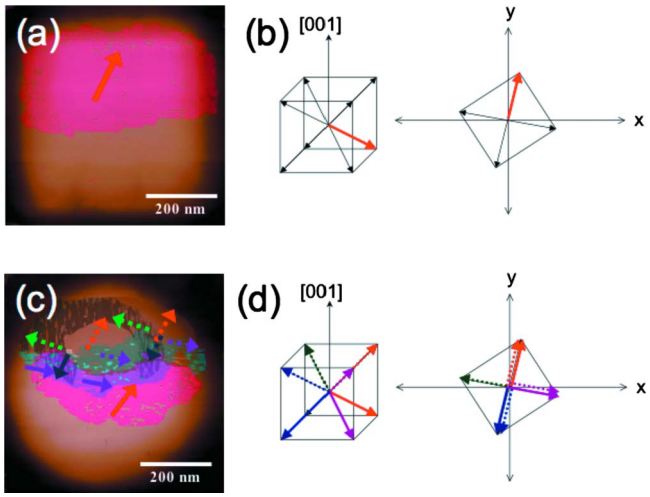


Figure 2.3. Ferroelectric domain configuration of 500 nm square and circular $BiFeO_3$ nanostructures as measured by PFM, from [33]. The PFM domain maps are shown overlayed on top of AFM topography in (a) and (c), and the observed polarization directions (relative to the crystallographic orientations) are illustrated schematically in (b) and (d).

structures are shown in Figure 2.3. The PFM domain maps are shown overlayed on top of AFM topography in (a) and (c), and the observed polarization directions are illustrated schematically in (b) and (d) relative to the crystallographic orientations. For the square nanostructure the observed domain configuration consisted of a single polarization variant aligned along the $[\bar{1}1\bar{1}]$ direction. In contrast, the circular nanostructure exhibited seven polarization variants along the $[\bar{1}1\bar{1}]$, $[1\bar{1}\bar{1}]$, $[11\bar{1}]$, $[111]$, $[\bar{1}11]$, $[1\bar{1}1]$, and $[\bar{1}\bar{1}1]$ directions. Additionally, hysteresis measurements of the local $d_{33}$ piezoelectric coefficient showed that the square nanostructure could not be switched with the application of up to $\pm$10 V (DC), whereas the circular structure could be poled up or down with less than 10 V (5 V for positive domains and -8 V for negative domains). The differences in switching behavior were understood in relation to the as fabricated domain configurations. The

multi-variant domain structure of the circular nanostructure better facilitated the nucleation and growth of domains which resulted in easier switching in either direction. In contrast, the single variant domain configuration of the square nanostructure suggested the presence of a self-poling effect resulting in a highly imprinted polarization state.

These results suggest that in addition to affecting the degree of substrate clamping (as demonstrated by Nagarajan for PZT), lateral confinement may enable shape dependent control of the ferroelectric domain configuration in $BiFeO_3$ nanostructures. However, the physical origin of the observed shape dependence of the domain structure was not clear. The shape dependence may have resulted from differences in electrostatic boundary conditions, symmetry in strain field, or spatial distribution of FIB-induced damage. Significant damage was observed in both the square and circular nanostructures. The portions of the nanostructures in the AFM topography images in Figure 2.3 where no PFM signal is overlayed showed minimal piezoelectric activity. Steps that were taken to recover the damaged areas are discussed in Section 4.3.1.

As a next step, fabrication strategies utilizing protective coatings were explored to limited ion damage in order to separate intrinsic lateral size effects from fabrication related effects. This work is detailed in Section 4.3. The subsequent synchrotron x-ray experiments which are discussed in Chapter 5 were conducted to better understand the effects of lateral confinement on local strain in $BiFeO_3$ nanostructures.

CHAPTER 3

# X-Ray Methods

## 3.1. Focused Beam X-Ray Diffraction Microscopy

X-ray microscopy is a powerful tool for micro- and nanoscale imaging with the unique strengths of x-ray scattering and spectroscopy methods. This enables the imaging of buried layers and interfaces as well as materials under extreme conditions (e.g. high pressure, large magnetic or electric fields, high or low temperature). There are three basic types of x-ray microscopy, including full-field, scanning probe, and lensless coherent diffraction imaging [34]. Full-field x-ray microscopy uses an objective lens to measure the spatial dependence of the intensity of transmitted or reflected x-rays directly with a 2D imaging detector. In scanning x-ray probe measurements, images are acquired one small region at a time. When x-ray diffraction is used as a contrast-producing interaction, the scanning probe method is generally termed "microdiffraction." This is the x-ray microscopy technique employed in the present work. The remaining approach, coherent diffraction imaging produces real space images with high spatial resolution through analysis of the "speckle" patterns arising when the transverse coherence length of the x-ray beam exceeds the size of the sample. While the x-ray source utilized in the microscopy measurements in this dissertation was fully coherent, this aspect was not exploited.

The fundamental limit to spatial resolution in x-ray microdiffraction measurements is the size of the x-ray spot, which is itself limited by the x-ray wavelength, $\lambda$ and the

numerical aperture (NA) of the focusing optic used. The NA is a dimensionless measure of the angular acceptance or emittance of an optical system. In general, it is defined as NA $= n \sin\theta$ where$n$ is the index of refraction of the optical element and $2\theta$ is the angular acceptance/emittance width. The focused spot full width-at-half maximum is $0.61\lambda$/NA. Hard x-rays are most commonly focused by either Kirkpatrick-Baez (KB) mirrors [35] or Fresnel zone plate (FZP) optics [36–41]. With KB mirrors, focusing is achieved with a crossed pair of curved total external reflection (TER) x-ray mirrors. NA is limited by the critical angle for TER, $\theta_c = \lambda\sqrt{r_e\rho/\pi}$, where $\lambda$ is the x-ray wavelength in air, $r_e$ is the classical electron radius, and $\rho$ is the electron number density of the mirror material. Kirkpatrick and Baez showed that for elliptically bent x-ray mirror, the maximum aperture angle is equal to $2\theta_c$, which leads to NA $\propto \lambda$ such that the resolution is energy independent [35]. Furthermore, for elliptical mirrors, the focal length depends on the size and curvature of the mirror, and is therefore inherently independent of wavelength. Thus KB mirrors are particularly useful for measurements requiring x-rays with a wide range of photon energies. For the monochromatic x-ray microdiffraction measurements discussed in this dissertation, FZP focusing optics were used to produce a sub-50 nm 10 keV x-ray beam spot.

A Fresnel zone plate and the commonly fabricated binary approximation [36, 37] are shown in Figure 3.1. The zone plate is a parabolic focusing x-ray lens which is condensed into zones of height $\Lambda$, which the is length the x-ray must travel in the lens material such that the transmitted wave and a wave traveling through air are in phase [42] given by

$$\Lambda = \frac{2\pi}{\lambda r_e \rho}. \tag{3.1}$$

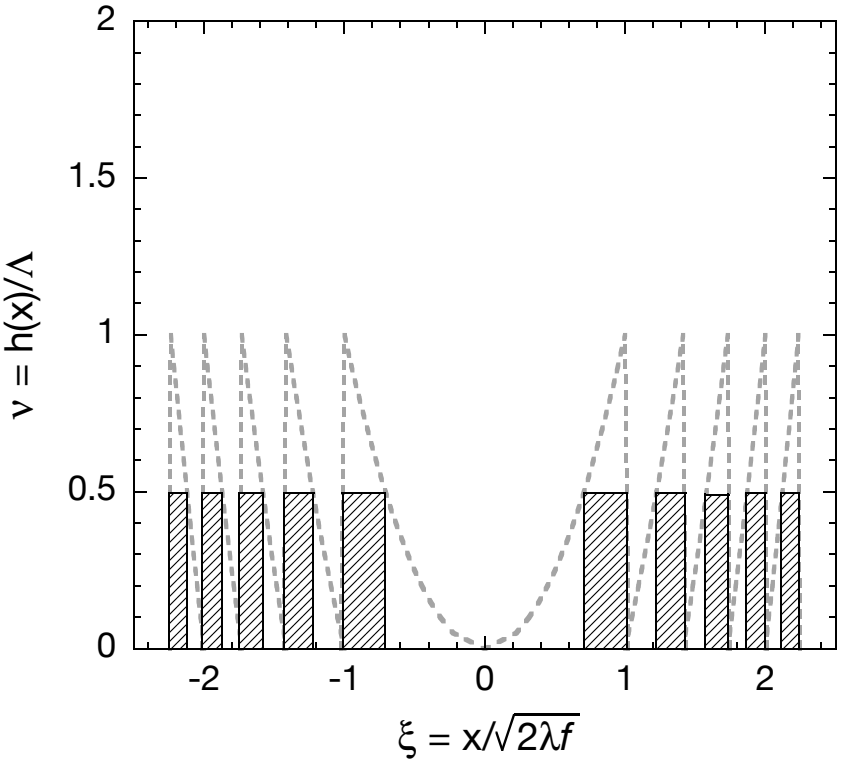


Figure 3.1. Fresnel zone plate (dotted grey) and the commonly fabricated binary approximation (black).

Collapsing the parabolic structure into zones results in a lens with the same optical properties, but with greatly reduced size and absorption since material which only contributes a phase shift of $2n\pi$ is removed.

The spot size resolution of a zone plate optic is largely determined by the width of the outermost zone , $\Delta r$. The numerical aperture is NA $= \lambda/2\Delta r$ which gives a spot size of $1.22\Delta r$. The focal length is $f = 4N\left(\Delta r\right)^2/\lambda$, where $N$ is the number of zones, and the depth of focus is $\pm\lambda/2\left(\mathrm{NA}\right)^2$. Zone plates are typically fabricated by electron beam lithography and use a binary approximation to a true Fresnel zone plate. In the approximation, zones of height $\Lambda/2$ ideally result in a phase shift of $\pi$ relative to x-rays

passing through the empty zones. However, maintaining an ideal height for smaller and smaller zone widths poses a significant nanolithography challenge [43], and high-resolution zone plates tend to have greatly reduced focusing efficiency. Nevertheless, current hard x-ray zone plates have demonstrated focused spot sizes smaller than 40 nm [41].

X-ray microdiffraction using a Fresnel zone plate optic is shown schematically in Figure 3.2. A central stop is mounted on the optic to block the zeroth order beam. A circular order-sorting aperture (OSA) (not shown) is used to reduce background by selecting the first order focused beam and blocking higher orders. The zone plate optic produces a well defined cone of monochromatic x-rays with an angular width $2\theta$ related to the numerical aperture by NA $= \sin\theta$. For 10 keV x-rays focused to a 40 nm spot size, $2\theta = 0.22°$. This sizable beam divergence introduces significant differences in focused-beam diffraction measurements compared to conventional parallel-beam experiments.

A schematic depiction of scattering with a highly focused x-ray beam is shown in 3.3. The focused beam is effectively a circular image of the zone plate with a dark spot in the center due to the central beam stop, although the intensity profile is Gaussian at the focus. This is depicted in the outgoing cone of elastically scattered intensity in Figure 3.3 (a). The case of Bragg diffraction from a perfect crystal is shown in Figure 3.3 (b). The expected intensity distribution is a narrow slice of intensity with a width in the $\theta/2\theta$ direction corresponding to the "acceptance" or Darwin width. For a well ordered thin film, shown in Figure 3.3 (c), the intensity distribution will be broadened due to finite thickness effects. The case of a disordered thin film is depicted in Figure 3.3 (d). Since the incident radiation from the zone plate is highly monochromatic, each ray within the intensity cone has a well defined scattering angle [34]. Thus, for a disordered film, x-rays

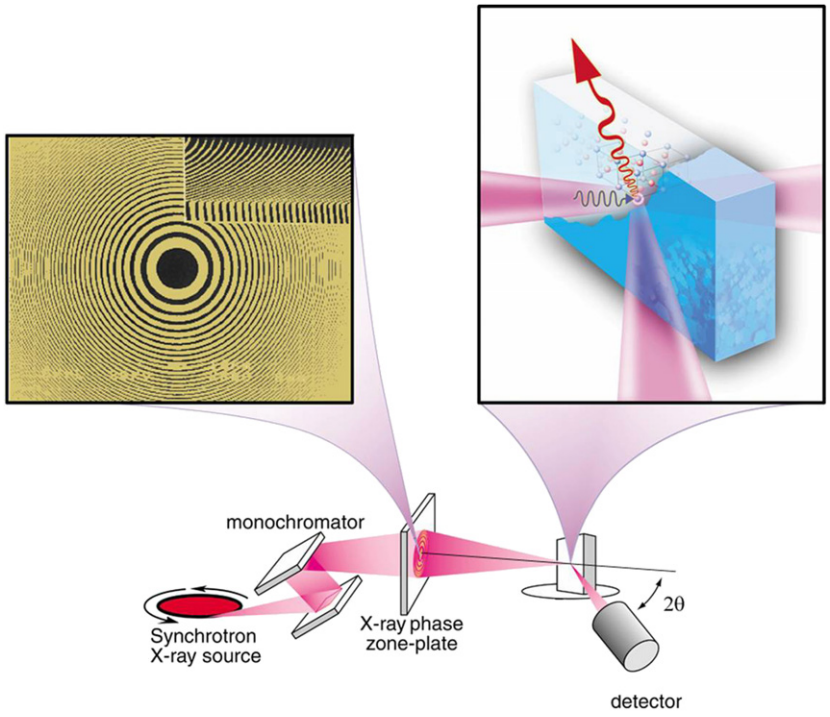


Figure 3.2. X-ray microdiffraction with a Fresnel zone plate focusing optic, from [34].

which satisfy the Bragg condition for individual crystalline domains within the beam spot will be diffracted to different $\chi$ and $\theta/2\theta$ positions. Furthermore, since the incident beam must be fully coherent to achieve optimal focus, interference between x-rays diffracted from different crystallites can reveal further structural information.

If the diffracted x-rays are collected using a charge coupled device (CCD) area detector [40, 44], the distribution in $2\theta$ and $\chi$ of the diffracted intensity can be observed and analyzed to extract information about local strain and lattice rotation as well as substructure within the diffracting volume. Xiao *et al.* performed x-ray nanodiffraction measurements of tin oxide nanobelts using a hard x-ray microprobe with a 190 nm spot size at the 2ID-D station of the Advanced Photon Source (APS). Diffraction from the

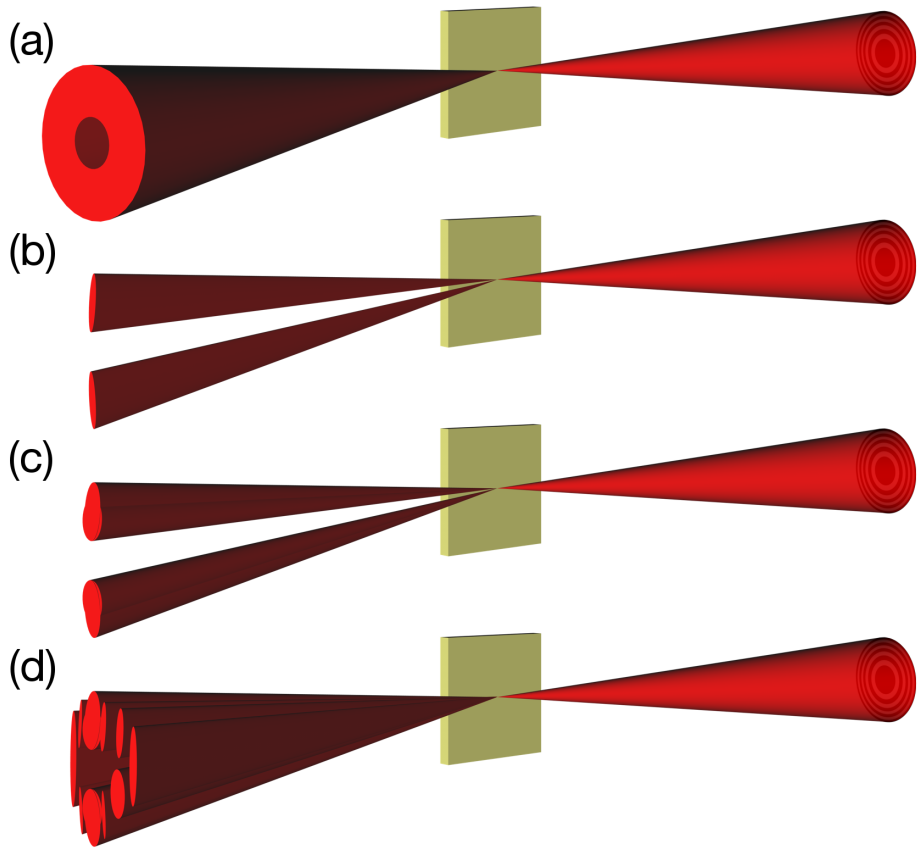


Figure 3.3. Schematic diagram illustrating scattering with a focused x-ray beam. Shown are cases of (a) elastic scattering, and Bragg diffraction from (b) a perfect crystal, (c) a well-ordered thin film, and (d) a disordered thin film. In all cases, the dark spot in the center of the outgoing beam is a result of a central beam stop mounted on the focusing optic.

$Sn_2O_3$ (030) reflection was collected with a CCD detector. The collected images revealed diffraction patterns composed of several subspots which were split along the $\chi$ direction with a three to five times smaller splitting in $\theta/2\theta$. This indicated that the nanobelts contained highly textured subgrains with relatively small strain variation between grains [40].

Holt and coworkers used x-ray microdiffraction to study the microstucture of 90° (**a-c**) ferroelectric domains in a $BaTiO_3$ single crystal [44]. Measurements were performed at APS station 8ID-E using a focused x-ray spot of 0.3 $\mu$m × 3 $\mu$m and a CCD diffraction detector. Diffraction from the (002) and (200) (**c** and **a**) reflections was measured as a function of position across a periodic **a-c-a** stripe domain structure where the domain widths were approximately 10 $\mu$m. The periodic domain structure was observed clearly in the the integrated diffraction intensity maps. A detailed analysis of the integrated intensity and the $2\theta$, $\theta$, and $\chi$ locations of the (002) reflection across a single 90° domain wall revealed a deviation of the nominal 45° walls to $\sim$ 20° within 1 $\mu$m of the surface. Further, in addition to the symmetric strain profile expected due to lattice mismatch, the strain was observed to become asymmetric as the domain boundary approached the surface. This was attributed to differences in elastic stress between a 45° wedge and a 135° corner.

The unparalleled spatial resolution of the Hard X-Ray Nanoprobe instrument operated by the Center for Nanoscale Materials (CNM) and located at APS beam line 26ID-C enables x-ray diffraction experiments similar to that by Holt *et al.* but which examine local ferroelectric domain structure in epitaxial thin films and nanostructures where the domain size is significantly smaller than in bulk crystals. Similar analysis of integrated intensity and $\theta/2\theta$ and $\chi$ positions extracted from CCD diffraction data can yield structural information such as local strain and lattice rotation with sub-50 nm spatial resolution.

## 3.2. The X-Ray Standing Wave Technique

The x-ray standing wave (XSW) technique is an element-specific, atomic-resolution structural probe [45–47], that can enable measurement of the cation positions within a ferroelectric unit cell, which provides a direct measurement of domain polarity. The traditional single crystal Bragg diffraction XSW measurement exploits the interference of the incident and diffracted x-ray beams as a crystal is rocked through a Bragg reflection. The resulting standing wave field, which is illustrated in Figure 3.4, has a period given by

$$D = \frac{\lambda}{2\sin\theta} = \frac{2\pi}{Q} \tag{3.2}$$

where $\lambda$ is the x-ray wavelength, $2\theta$ is the angle between the incident and reflected wave vectors $\mathbf{K}$ and $\mathbf{K}'$, and $Q$ is the amplitude of the scattering vector defined by $\mathbf{Q} = \mathbf{K}' - \mathbf{K}$.

The XSW period is equivalent to the d-spacing of the Bragg reflection generating the standing wave. As $\theta$ is rocked through the Bragg condition, the XSW node/antinode position shifts by $D/2$ due to a shift in the phase of the reflected wave relative to the incident wave. By monitoring a secondary process such as x-ray fluorescence (XRF), the resulting site-specific intensity modulation can be measured for each atomic species of interest. The technique is shown schematically in Figure 3.5.

The E-field of the incident and diffracted plane waves can be expressed as

$$\mathcal{E}_0(\mathbf{r}, t) = \mathbf{E}_0 \mathrm{e}^{i(\omega t - \mathbf{K}_0 \cdot \mathbf{r})}, \tag{3.3}$$

and

$$\mathcal{E}_\mathrm{H}(\mathbf{r}, t) = \mathbf{E}_\mathrm{H} \mathrm{e}^{i(\omega t - \mathbf{K}_\mathrm{H} \cdot \mathbf{r})}, \tag{3.4}$$

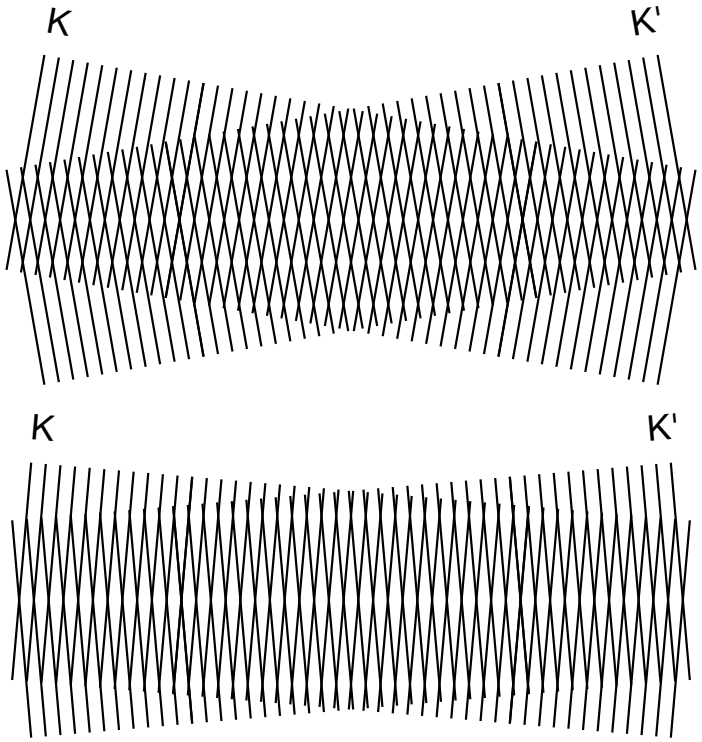


Figure 3.4. The standing wave field resulting from the interference between two plane waves with wavevectors $\mathbf{K}$ and $\mathbf{K}'$, corresponding to the incoming and outgoing x-ray beams, respectively. The standing wave period is smaller for a larger $2\theta$ (above) and larger for a smaller $2\theta$ (below).

where $\omega$ is the x-ray frequency and $\mathbf{K}_0$ and $\mathbf{K}_\mathrm{H}$ are the complex incident and diffracted wavevectors inside the crystal, respectively. The total E-field inside the crystal is then given by

$$\mathcal{E}_\mathrm{Total} = \mathcal{E}_0 + \mathcal{E}_\mathrm{H} = \left[\mathbf{E}_0 \mathrm{e}^{-i\mathbf{K}_0\cdot\mathbf{r}} + \mathbf{E}_\mathrm{H}\mathrm{e}^{-i\mathbf{K}_\mathrm{H}\cdot\mathbf{r}}\right] \mathrm{e}^{i\omega t}, \tag{3.5}$$

and the normalized intensity of the total E-field is

$$I\left(\theta, \mathbf{r}\right) = \frac{\left|\mathcal{E}_\mathrm{Total}\right|^2}{\left|E_0\right|^2}. \tag{3.6}$$

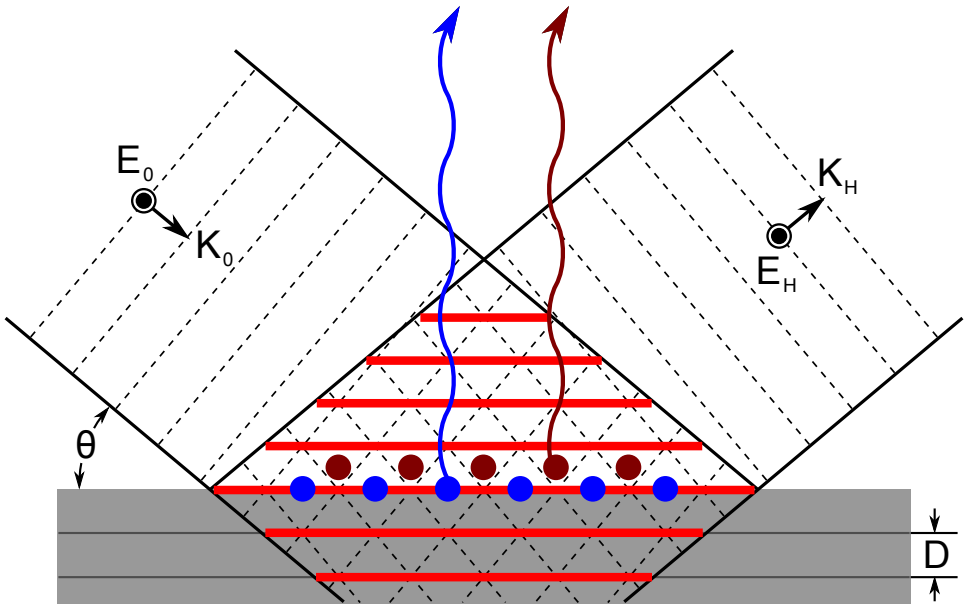


Figure 3.5. The x-ray standing wave technique.

The complex E-field amplitudes $\mathbf{E}_0$ and $\mathbf{E}_\mathrm{H}$ are vector quantities with directions $\hat{\mathbf{e}}_0$ and $\hat{\mathbf{e}}_\mathrm{H}$, respectively. In the case of $\sigma$-polarization where $\hat{\mathbf{e}}_0$ and $\hat{\mathbf{e}}_\mathrm{H}$ point perpendicular to the scattering plane defined by $\mathbf{K}_0$ and $\mathbf{K}_\mathrm{H}$, as is true for the experiments in this dissertation, $\hat{\mathbf{e}}_0 \cdot \hat{\mathbf{e}}_\mathrm{H} = 1$ and the complex E-field amplitude ratio can be expressed in scaler form as:

$$\frac{E_\mathrm{H}}{E_0} = \left|\frac{E_\mathrm{H}}{E_0}\right| \mathrm{e}^{i\nu}, \tag{3.7}$$

where $\nu$ is the phase difference between $\mathbf{E}_\mathrm{H}$ and $\mathbf{E}_0$.

In the Bragg case, the incident and diffracted wavevectors are related by the Laue condition

$$\mathbf{K}_\mathrm{H} = \mathbf{H} + \mathbf{K}_0, \tag{3.8}$$

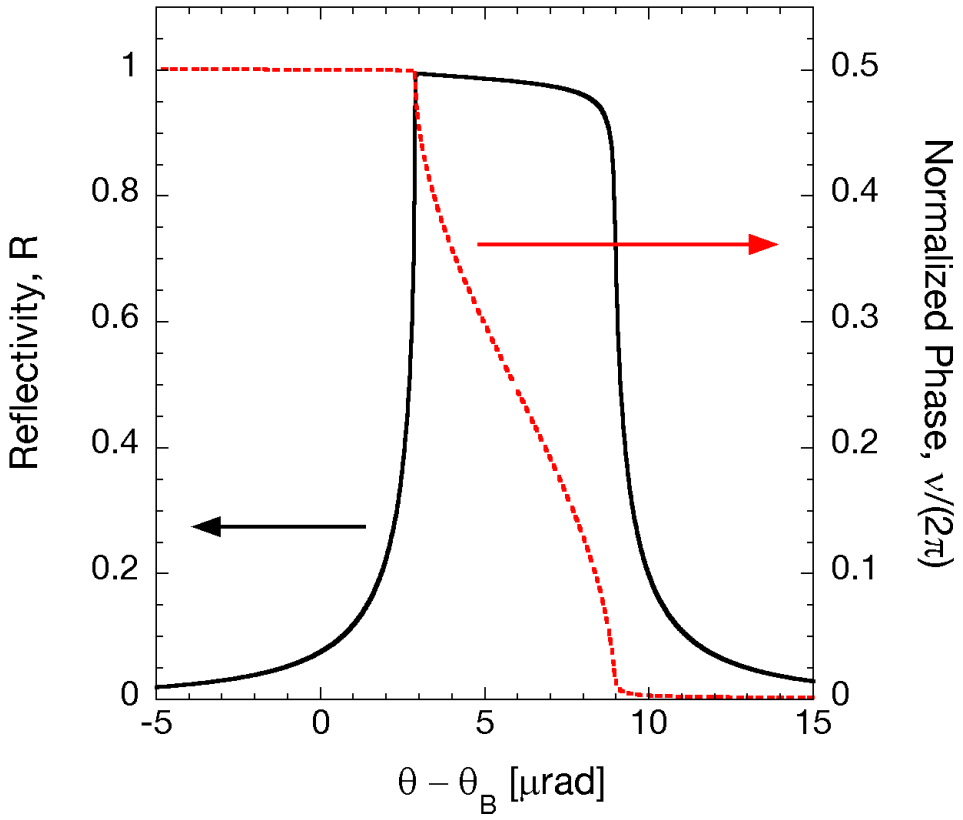


Figure 3.6. Simulated rocking curve and normalized XSW phase for Si (004) at an incident photon energy of 18.5 keV.

where $\mathbf{H} = h\mathbf{a}_1^* + k\mathbf{a}_2^* + l\mathbf{a}_3^*$ is a reciprocal lattice vector. Combining Equations (3.5)–(3.8), the normalized E-field intensity near the surface of the crystal is

$$I(\theta, \mathbf{r}) = 1 + \left|\frac{E_\mathrm{H}}{E_0}\right|^2 + \left|\frac{E_\mathrm{H}}{E_0}\right| \cos\left[\nu(\theta) - \mathbf{H}\cdot\mathbf{r}\right]. \tag{3.9}$$

At a depth $z$ below the surface, Equation (3.9) is modified by a factor of $\mathrm{e}^{-\mu_z(\theta)z}$, where $\mu_z$ is the effective absorption coefficient of the incident wave.

In the dipole approximation, the photoelectric cross section is proportional to the E-field intensity at an atom's center. Therefore, neglecting higher-order multi-pole terms

(which is appropriate in most XSW measurements) the probability of a photoelectric transition for an atom within the XSW field will depend linearly on the standing wave intensity at the atom's position. The intensity of consequently emitted fluorescent x-rays and Auger electrons will therefore be sensitive to the position of the atom relative to the d-spacing of the XSW-generating Bragg reflection. In the case of XRF, the normalized fluorescence yield is defined

$$Y(\theta) = \int I(\theta, \mathbf{r})\, \rho(\mathbf{r})\, \mathrm{e}^{-\mu_f(\alpha) z} d\mathbf{r}. \tag{3.10}$$

Here, $\rho(\mathbf{r})$ is the normalized atomic distribution of the fluorescent species and $\mu_f(\alpha)$ is the effective absorption coefficient of the fluorescent x-rays given by

$$\mu_f(\alpha) = \frac{2\sqrt{2}\pi}{\lambda_f} \left[ \sqrt{(2\delta - \alpha^2)^2 + 4\beta^2} + 2\delta - \alpha^2 \right]^{\frac{1}{2}}, \tag{3.11}$$

where $\alpha$ is the takeoff angle between the direction of travel of an emitted fluorescent photon and the crystal surface, $\lambda_f$ is the wavelength of the fluorescence, and $\delta$ and $\beta$ are related to the index of refraction calculated at $\lambda_f$

$$n = 1 - \delta - i\beta. \tag{3.12}$$

Combining Equations (3.9) and (3.10) and integrating gives the normalized XSW yield

$$Y(\theta) = \left[ 1 + R(\theta) + 2\sqrt{R(\theta)} f_{\mathrm{H}} \cos\left(\nu(\theta) - 2\pi P_{\mathrm{H}}\right) \right] Z(\theta), \tag{3.13}$$

where $R(\theta)$ is the normalized reflectivity which is defined as the absolute square of the E-field amplitude ratio

$$R = \left| \frac{E_H}{E_0} \right|^2, \tag{3.14}$$

and $\nu(\theta)$ is the XSW phase which is identical to the relative phase in Equation (3.7) [48]. Figure 3.6 shows the reflectivity and normalized XSW phase calculated for Si (004). As $\theta$ is rocked through the Bragg condition, the phase shifts by $\pi$ radians and the XSW nodes and antinodes shift by $D/2$. The parameters $f_{\mathrm{H}}$ and $P_{\mathrm{H}}$ are the amplitude and phase of the $\mathbf{H}^{\mathrm{th}}$ Fourier component of $\rho(\mathbf{r})$

$$\mathcal{F}_{\mathrm{H}} = \int_{uc} \rho(\mathbf{r})\, \mathrm{e}^{i\mathbf{H}\cdot\mathbf{r}} d\mathbf{r} = f_{\mathrm{H}} \mathrm{e}^{2\pi i P_{\mathrm{H}}} \tag{3.15}$$

and are termed the coherent fraction and the coherent position, respectively. The coherent position represents the location of the fluorescing atoms relative to the origin of the diffraction planes, measured in units of $d$ along the $\mathbf{H}$ direction. The coherent fraction is typically separated into three factors

$$f_{\mathrm{H}} = C a_{\mathrm{H}} D_{\mathrm{H}} \tag{3.16}$$

with each ranging from zero to one. The parameter $C$ is the ordered fraction and represents the fraction of fluorescing atoms coherently located with respect to the XSW field. The remaining quantities, $a_{\mathrm{H}}$ and $D_{\mathrm{H}}$, are the geometrical and Debye-Waller factors which account for the possibility of multiple lattice sites and thermal vibrations respectively.

From dynamical diffraction theory [49], an expression can be derived for the complex E-field ratio defined in Equation (3.7) which is used to calculate $R(\theta)$ and $\nu(\theta)$. This treatment is detailed elsewhere [48] and covered in a review by Zegenhagen [50].

The remaining term in Equation (3.13), $Z(\theta)$, is an effective-thickness factor which accounts for the angular dependence of absorption and extinction of the incident x-rays as well as absorption of the outgoing fluorescence. For atoms on or above the surface, $Z(\theta) = 1$, and for atoms at a depth much less than the extinction length, $Z(\theta) \approx 1$. For a uniform distribution of atoms throughout the crystal,

$$Z(\theta) = \frac{\mu_0 \left(\sin\theta_{\mathrm{B}}\right)^{-1} + \mu_f\left(\alpha\right)}{\mu_z\left(\theta\right) + \mu_f\left(\alpha\right)} \tag{3.17}$$

where $\mu_0$ is the linear absorption coefficient.

By collecting both the reflectivity and fluorescence yield, the structure of an atomic distribution within or absorbed on the surface of the crystal can be characterized with atomic-resolution. $R(\theta)$ and $\nu(\theta)$ are determined by fitting the substrate reflectivity or "rocking curve" with dynamical diffraction theory and $f_{\mathrm{H}}$ and $P_{\mathrm{H}}$ are extracted by fitting the normalized fluorescence yield described by Equation (3.13). Since the coherent fraction and position are the amplitude and phase of the element specific normalized **H** geometrical structure factor for the fluorescent atomic species, summing these Fourier components from multiple reflections can produce a model independent direct space map of the individual atomic distributions relative to the substrate diffraction planes.

### 3.3. Thin Film X-Ray Standing Waves

In general, the single crystal XSW technique is not suitable for characterizing epitaxial thin films of more than a few monolayers (MLs) in thickness since in most cases the film and substrate will have different lattice constants. That is, the fundamental periodicity of the film is incommensurate with that of the single crystal substrate. As depicted schematically in Figure 3.7 (a), at different heights in the film, the nodes and antinodes of the XSW field generated by a substrate reflection will pass through the atomic planes at different values of $\theta$, which would result in a measured coherent fraction of zero. The solution to this problem is to use the weak kinematical reflection from the thin film itself to generate the XSW as shown in Figure 3.7 (b). The thin-film XSW technique [47] was first demonstrated by Kazimirov and coworkers in the case of a $SmBa_2Cu_3O_{7-d}$ film on $SrTiO_3$ (001) [51]. The Bedzyk research group has previously demonstrated that the thin film XSW technique can be used to probe the polarity of as-grown $PbTiO_3$ (PTO) [52] and electrically poled $Pb(Zr_xTi_{1-x})O_3$ / electrode heterostructures [53]. The thin film XSW method has also been applied by Kazimirov *et al.* to determine the polarity of GaN thin films grown by plasma induced molecular beam epitaxy (PIMBE) on $\alpha$-$Al_2O_3$ (0001) [54], and by hydride vapor phase epitaxy (HVPE) on the Si-face SiC [55].

While diffraction from a film is weak when the thickness is less than the x-ray extinction length, an XSW field is still present due to interference of the incident and diffracted x-ray beams. Furthermore, the amplitude of the XSW fluorescence modulation in Equation (3.13) scales with $\sqrt{R}$. Thus, a thin film Bragg reflection with 0.01% reflectivity will lead to a modulation of order 1% in the fluorescence yield. In order to measure such

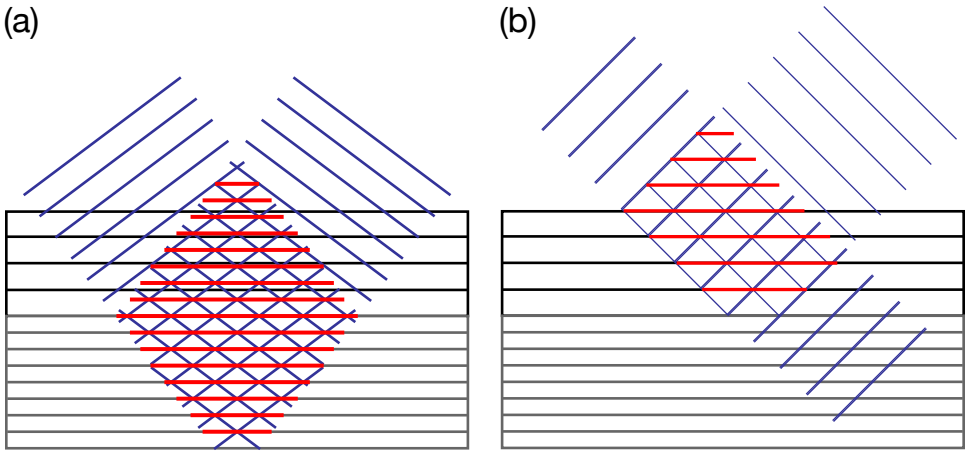


Figure 3.7. Diagram illustrating the use of the XSW field generated by a Bragg reflection from (a) the substrate and (b) the film to probe the structure of a thin film.

a modulation with 10% counting statistics, $\sim 1 \times 10^6$ counts must be collected at each angular step. This can be achieved with a high-brilliance undulator source.

In a thin film XSW measurement, since the fluorescing atoms being probed are part of the crystalline structure generating the standing wave field, the coherent fraction in Equation (3.13) has a different physical meaning than previously described by Equation (3.16). In particular, a structure with an ordered fraction significantly less than one would lack sufficient ordering for diffraction of x-rays. Therefore, for a structure with a single lattice site, a single Debye-Waller-type factor can be used in place of the coherent fraction. This static Debye-Waller factor represents a Gaussian distribution about the ideal lattice positions due to a combination of structural disorder and thermal fluctuations.

As in the case of single crystal XSW, both x-ray fluorescence and reflectivity are measured simultaneously in the thin film XSW technique. However, as the fluorescing atoms are located throughout the thickness of the film, the XSW field must be calculated as a function of depth throughout the film. This can be achieved with an analysis based

on Takagi-Taupin dynamical diffraction theory. In the 1960s, Takagi [56, 57] and Taupin [58] independently developed a generalized theory of diffraction from crystals deformed by strain perpendicular to the surface. The Takagi-Taupin theory was extended by Bartels for crystals with reflecting properties which vary with depth [59]. Bartels developed a recursion formula for calculating the D-field amplitude ratio at a given depth and applied the theory to multilayers and superlattices.

An analysis based on Bartels' recursion formulae was applied by Lee, Marasco and Bedzyk to calculate the reflectivity, $R(\theta)$, of an epitaxial thin film / single crystal substrate heterostructure. This treatment is detailed elsewhere [60–62] and is not reproduced here.

### 3.4. Crystal Truncation Rod Measurements

Due to the interference of the waves scattered from the different layers in a thin film / substrate heterostructure [63], the scattering profile can be strongly dependent on both the polarity and interface morphology of an epitaxial ferroelectric film. This sensitivity was demonstrated by C. Thompson and coworkers for both $PbTiO_3$ films on $SrTiO_3$ (001) [64] and $Pb(Zr_xTi_{1-x})O_3$ / $SrRuO_3$ capacitors on $SrTiO_3$ (001) [65]. The $Pb(Zr_xTi_{1-x})O_3$ study showed that, in addition to allowing direct determination of domain polarity, analysis of the crystal truncation rod (CTR) also revealed a structural signature related to ferroelectric fatigue. Similar measurements were also made by former Bedzyk group member D. L. Marasco [62].

In the kinematical, or weak scattering limit, which neglects multiple scattering effects, it can be shown that for an infinite periodic lattice, diffraction peaks occur at singular points which satisfy the Laue condition, $\mathbf{Q} = \mathbf{H}$, in a 3D reciprocal space [42]. That is,

peaks in the scattering intensity are given by $I(Q) \propto \delta(\mathbf{Q}-\mathbf{H})$, where $\mathbf{H} = h\mathbf{a}_1^* + k\mathbf{a}_2^* + l\mathbf{a}_3^*$ is a reciprocal lattice vector. However, the scattering from any real crystal is necessarily more complicated due to the termination of the periodic array at the interface.

Following the treatment by Als-Nielsen and McMorrow, the electron density profile of such a semi-infinite crystal can be represented as the product of the bulk crystal density and a step function.

(3.18a) $$\rho_{\mathrm{CTR}}(\mathrm{z}) = \rho(\mathrm{z}) \cdot \mathrm{h}(\mathrm{z})$$

where

(3.18b) $$\rho(\mathrm{z}) = \rho(\mathrm{z} + \mathrm{lc})$$

and

(3.18c) $$h(\mathrm{z}) = \begin{cases} 1 & \text{if } z > 0 \\ 0 & \text{if } z < 0 \end{cases}$$

The scattering intensity, $I_{\mathrm{CTR}}(\mathrm{q})$ is proportional to the square of the modulus of the Fourier transform of the electron density, $\mathrm{P}_{\mathrm{CTR}}(\mathrm{q})$, which is given by the convolution of $\mathrm{P}(\mathrm{q})$ and $H(\mathrm{q})$, where

(3.19)
$$\mathrm{P}(\mathrm{q}) = \int_{-\infty}^{\infty} \rho(\mathrm{z}) \mathrm{e}^{i\mathrm{qz}} d\mathrm{z} = \sum_{l=-\infty}^{\infty} \left( \frac{1}{c} \int_0^c \rho(\mathrm{z}) \mathrm{e}^{i\mathrm{qz}} d\mathrm{z} \right) \delta \left( \mathrm{q} - \frac{2\pi l}{c} \right) = \sum_{l=-\infty}^{\infty} \hat{\rho}_l \delta \left( \mathrm{q} - \frac{2\pi l}{c} \right)$$

(3.20) $$H(\mathrm{q}) = \int_{-\infty}^{\infty} h(\mathrm{z}) \mathrm{e}^{i\mathrm{qz}} d\mathrm{z} = \int_0^{\infty} \mathrm{e}^{i\mathrm{qz}} d\mathrm{z} = \frac{i}{\mathrm{q}}$$

Thus, near a Bragg peak (i.e. close to each of the infinite array of delta functions in Equation (3.19)),

$$\mathrm{P_{CTR}(q)} \propto \int_{-\infty}^{\infty} \frac{i}{\mathrm{q'}} \delta\left(\mathrm{q'} - \mathrm{q}\right) d\mathrm{q'} = \frac{i}{\mathrm{q}} \tag{3.21}$$

and the scattering intensity is $I_{\mathrm{CTR}}(q) \propto q^{-2}$. The diffraction peaks from a truncated crystal are therefore smeared out in reciprocal space in the direction normal to the surface forming crystal truncation rods.

A formal expression for the CTR intensity can be derived by considering a semi-infinite stack of identical atomic layers with scattering amplitude $A(\mathrm{q})$. The scattering amplitude of the stack is

$$R_{\mathrm{CTR}} = A(\mathrm{q}) \sum_{j=0}^{\infty} \mathrm{e}^{iqcj} = \frac{A(\mathrm{q})}{1 - \mathrm{e}^{-iqc}}, \tag{3.22}$$

where $c$ is the out-of-plane lattice constant of the crystal. The scattering intensity will then be given by

$$I_{\mathrm{CTR}} = |R_{\mathrm{CTR}}|^2 = \frac{|A(\mathrm{q})|^2}{4\sin^2(\mathrm{q}c)}. \tag{3.23}$$

Note that close to a Bragg peak, where $\mathrm{q} - 2n/\pi c << 1$, the denominator can be expanded $\sin^2(\mathrm{q}c) \approx \mathrm{q}^2c^2$ so that Equation (3.23) reduces to $I_{\mathrm{CTR}}(\mathrm{q}) \propto \mathrm{q}^{-2}$ as in the simplified step function model discussed previously. A factor $\mathrm{e}^{-\epsilon_j c \mathrm{q}^{-1}}$ can be included to correct for absorption so that Equation (3.22) is modified to become

$$R_{\mathrm{CTR}} = A(\mathrm{q}) \sum_{j=0}^{\infty} \mathrm{e}^{iqcj} \mathrm{e}^{-\epsilon_j c \mathrm{q}^{-1}} = \frac{A(\mathrm{q})}{1 - \mathrm{e}^{-c(i\mathrm{q} + \epsilon \mathrm{q}^{-1})}}, \tag{3.24}$$

where $\epsilon = 4\pi\mu_0/\lambda$ is related to the linear absorption coefficient, $\mu_0$.

To analyze the interference between the scattering from an epitaxial film and the CTR of the single crystal substrate, the reflected amplitude from each layer can be calculated separately and added at the level of fields. From Equation (3.24), the reflected amplitude for a single crystal substrate is given by

$$R_{\mathrm{CTR}} = \frac{i4\pi r_e}{a_{\mathrm{sub}} b_{\mathrm{sub}}} F_{\mathrm{sub}}(\mathrm{q}) \frac{1}{1 - \mathrm{e}^{-c_{\mathrm{sub}}(i\mathrm{q} + \epsilon_{\mathrm{sub}}\mathrm{q}^{-1})}} \tag{3.25}$$

where $r_e$ is the classical electron radius, $a_{\mathrm{sub}}$, $b_{\mathrm{sub}}$, and $c_{\mathrm{sub}}$ are the lattice constants of the substrate, and $F_{\mathrm{sub}}(\mathrm{q})$ is the substrate structure factor. This expression, however, ignores the attenuation of the primary beam as it penetrates deeper into the crystal. The reflected amplitude can be corrected for this extinction effect by the expression [64]

$$R_{\mathrm{sub}} = \frac{2R_{\mathrm{CTR}}}{1 + \left[1 + (2R_{\mathrm{CTR}})^2\right]^{1/2}}. \tag{3.26}$$

The scattered field amplitude of a finite film of N layers is given by

$$R_{\mathrm{film}} = A(\mathrm{q}) \sum_{j=0}^{N-1} \mathrm{e}^{iqcj} \mathrm{e}^{-\epsilon_j c \mathrm{q}^{-1}} = A(\mathrm{q}) \frac{1 - \mathrm{e}^{-cN\left(i\mathrm{q} + \epsilon\mathrm{q}^{-1}\right)}}{1 - \mathrm{e}^{-c(i\mathrm{q} + \epsilon\mathrm{q}^{-1})}} \tag{3.27}$$

$$R_{\mathrm{film}} = \frac{i4\pi r_e}{a_{\mathrm{film}} b_{\mathrm{film}}} F_{\mathrm{film}}(\mathrm{q}) \frac{1 - \mathrm{e}^{-c_{\mathrm{film}} N\left(i\mathrm{q} + \epsilon_{\mathrm{film}}\mathrm{q}^{-1}\right)}}{1 - \mathrm{e}^{-c_{\mathrm{film}}(i\mathrm{q} + \epsilon_{\mathrm{film}}\mathrm{q}^{-1})}} \tag{3.28}$$

To combine the film and substrate fields, a phase factor is included to account for the separation between the surface of the film and the surface of the substrate:

$$R_{\mathrm{total}} = R_{\mathrm{film}} + R_{\mathrm{sub}} \mathrm{e}^{-c_{\mathrm{film}}(N + \delta_{\mathrm{film}})\left(i\mathrm{q} + \epsilon_{\mathrm{film}}\mathrm{q}^{-1}\right)} \tag{3.29}$$

where $\delta_{\text{film}}$ is the thickness of an interfacial layer in units of $c_{\text{film}}$. The surface and interface roughness can be included with a Gaussian factor $\mathrm{e}^{-0.5\sigma^2(\mathrm{q}-2\pi/c)^2}$ for both $R_{\text{film}}$ and $R_{\text{sub}}$. Lastly, the scattered intensity is given by

$$I\left(\mathrm{q}\right) = \left|R_{\text{total}}\right|^2 . \tag{3.30}$$

By fitting the measured CTR scattering profile with the extinction-corrected kinematical analysis outlined above as demonstrated by Thompson *et al.*, one can accurately determine the film polarity, lattice constant, and thickness, the interface roughness, and thickness of an interfacial layer.

CHAPTER 4

# Synthesis of $BiFeO_3$ Thin Films and Nanostructures

## 4.1. $BiFeO_3$ Structure

$BiFeO_3$ (BFO) is widely studied as it is currently the only known multiferroic material with ferroelectric and (anti-) ferromagnetic ordering at ambient temperatures. $BiFeO_3$ has a ferroelectric Curie temperature, $T_C \sim 1100$ K, and Néel temperature, $T_N \sim 640$ K, which are both well above room temperature. Furthermore, $BiFeO_3$ is a robust, environmentally benign ferroelectric material, which gives it an additional advantage over Pb-based materials in future device applications. Bulk $BiFeO_3$ has a rhombohedrally distorted perovskite structure, with space group $R3c$ and $a_{rh} = 5.6343$ Å and $\alpha_{rh} = 59.348°$[66]. Ferroelectricity in $BiFeO_3$ is related to counter-rotations of adjacent oxygen octahedra about the [111] axis, which give rise polar displacements of the $Bi^{3+}$, $Fe^{3+}$, and $O^{2-}$ along the [111] direction [67]. The primitive unit cell is shown in Figure 4.1. Within the rhombohedral unit cell there is a pseudocubic structure with $a_c = 3.965(1)$ Å and $\alpha_c = 89.45(5)°$. Unless otherwise noted, $BiFeO_3$ is indexed in the pseudocubic notation in this dissertation.

In bulk, $BiFeO_3$ is a G-type antiferromagnet, meaning that the $Fe^{3+}$ ions in each adjacent $(111)_{rh}$ plane have antiparallel spins such that each $Fe^{3+}$ is surrounded by six nearest neighbors with opposite spin. While the $R3c$ symmetry allows for a slight canting of the $Fe^{3+}$ spins which would result in small net moment, or "weak ferromagnetism," due to the incomplete cancellation of the two antiferromagnetic sublattices, this is not

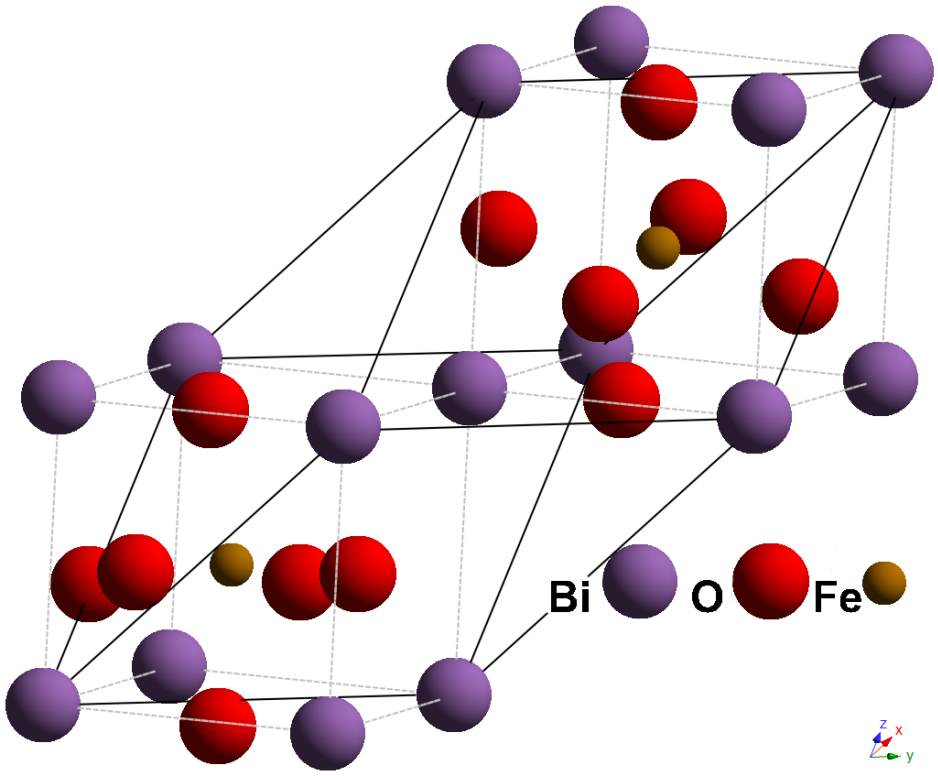


Figure 4.1. The rhombohedrally distorted perovskite crystal structure of $BiFeO_3$: $R3c$, $a_{rh} = 5.6343$ Å, $\alpha_{rh} = 59.348°$. Solid lines outline the rhombohedral unit cell. Dotted lines show the pseudocubic unit cell: $a_c = 3.965(1)$ Å and $\alpha_c = 89.45(5)°$ [66].

observed in bulk $BiFeO_3$. Rather, the G-type ordering is modified by an incommensurate spin cycloid wherein the antiferromagnetic axis rotates throughout the crystal with a wavelength of 620 Å[68]. As a result, the distribution of spins within a single (111) plane is isotropic on the length scale of 620 Åand any local moment due to canting would average to zero.

However, recent first principles calculations by Ederer and Spaldin found that weak ferromagnetism is preferred in $BiFeO_3$ if the spiral spin structure is suppressed [69]. Furthermore, experiments by Ruette and coworkers recently showed that the application of

a large magnetic field (H > 18 T) can destroy the spin cycloid and induce a phase transition to homogeneous spin order [70]. The spin spiral was expected to be absent also in $BiFeO_3$ thin films, based reports of sizable magnetizations measured in $BiFeO_3$ films [11]. Recent neutron scattering measurements by Béa *et al.* confirmed the absence of the cycloid structure in epitaxial films of $BiFeO_3$ grown on $SrTiO_3$ (001) by pulsed laser deposition (PLD), which they attribute to epitaxial strain [71]. Weak ferromagnetism in $BiFeO_3$ thin films may provide a path to electrical control of magnetization and vice versa.

The crystal structure of (001) oriented $BiFeO_3$ thin films can be modified by epitaxial strain. Tetragonal and monoclinic distortions have both been observed and reported for films grown on $SrTiO_3$ (001) and $SrRuO_3$ / $SrTiO_3$ (001). In 2003, Wang *et al.* reported a "tetragonal-like" structure with a monoclinic distortion on the order of 0.5° for a 200 nm thick film grown on $SrRuO_3$ / $SrTiO_3$ (001) by PLD, although the measured in-plane lattice constant was 3.935 Å ($a_{STO}$ = 3.905 Å) indicating the film was not coherently strained [11]. Similarly, Xu and coworkers observed a monoclinic distortion of 0.8 ° for a 200 nm thick film deposited on $SrTiO_3$ (001) by PLD [72]. In contrast, Qi *et al.* reported that a 200 nm thick film grown on $SrRuO_3$ / $SrTiO_3$ (001) by liquid phase epitaxy (LPE) was almost fully relaxed with a bulk-like rhombohedral structure: $a$ = 3.9618 Å and $\alpha = 89.45°$ [73]. Qi found a similar result for a film deposited on bare Nb-doped $SrTiO_3$. Saito [74] and Béa [71] each reported at transition from tetragonal symmetry to monoclinic with increasing film thickness for (001) oriented epitaxial $BiFeO_3$ grown on $SrTiO_3$ (001). Both studies utilized high-resolution x-ray diffraction reciprocal space mapping (RSM). Saito *et al.* studied films with thickness ranging from 15 nm to 500 nm

grown by metalorganic chemical vapor deposition (MOCVD) on $SrRuO_3$ / $SrTiO_3$. Films below a thickness of 50 nm were observed to be tetragonal and fully coherent, whereas thicker films were monoclinic. The magnitude of the monoclinic distortion was found to increase with film thickness from $\sim 0.5^\circ$ for a 100 nm film to $\sim 1^\circ$ for films thicker than 200 nm. Béa and coworkers reported that a 70 nm thick film deposited by PLD on $SrTiO_3$ was fully strained with a tetragonal structure. Béa observed a splitting of the (103) and (202) peaks of a 240 nm thick film, consistent with a monoclinic structure. While diffraction measurements of a 120 nm film showed a relaxation of the in-plane lattice constant, Béa found that the crystal symmetry could not be easily deduced from analysis of the (103) and (202) reflections. Recent experimental work by Béa *et al.* found a strain induced giant axial ratio ($c/a = 1.23$) tetragonal polymorph in $BiFeO_3$ films grown on (001) oriented $LaAlO_3$ substrates [75]. $LaAlO_3$ is a rhombohedrally distorted perovskite with a pseudocubic lattice constant $a = 3.79$ Å, and the resulting $BiFeO_3$ films were observed to have lattice parameters $a \approx 3.79$ Å and $c = 4.67$ Å, in agreement with a $c/a = 1.27$ tetragonal phase previously predicted by Ederer and Spaldin [23]. Zeches and coworkers recently reported a study of the structure of $BiFeO_3$ / $LaAlO_3$ films as a function of film thickness [76]. In films thicker than 50 nm, Zeches observed the coexistence of two $BiFeO_3$ phases: the large ratio tetragonal polymorph and a distorted bulk-like rhombohedral phase. Furthermore, films with a mixture of tetragonal and rhombohedral phases exhibited enhanced piezoelectric behavior similar to that observed in materials such as Pb with a chemically induced morphotropic phase boundary. However the $BiFeO_3$ (001) films grown and studied for this dissertation were deposited with thicknesses below

50 nm on $SrTiO_3$ substrates, and appear from x-ray diffraction to have (low $c/a$ ratio) tetragonal symmetry.

The ferroelectric domain structure for pseudocubic (001) oriented epitaxial $BiFeO_3$ films can be quite complicated as there are eight distinct polarization variants corresponding to $\mathbf{P}^+$ and $\mathbf{P}^-$ variants directed along each of the four (111) family body diagonals. The eight polarizations are given by $\mathbf{P}_1^+ = [P_s\hat{x}, P_s\hat{y}, P_s\hat{z}]$, $\mathbf{P}_2^+ = [-P_s\hat{x}, P_s\hat{y}, P_s\hat{z}]$, $\mathbf{P}_3^+ = [-P_s\hat{x}, -P_s\hat{y}, P_s\hat{z}]$, $\mathbf{P}_4^+ = [P_s\hat{x}, -P_s\hat{y}, P_s\hat{z}]$, and $\mathbf{P}_n^- = -\mathbf{P}_n^+$ where $P_s$ is the magnitude of the spontaneous polarization [77, 78]. The ferroelectric polarization, therefore, has both an in-plane and out-of-plane component. However, the ferroelectric domain structure of (001) oriented films can be engineered using substrate vicinality [30, 79].

Chu *et al.* found that the use of miscut $SrTiO_3$ (001) substrates could effectively tilt and break the symmetry of the otherwise energetically equivalent polarization variants [30]. $BiFeO_3$ films grown on conductive $SrRuO_3$ with no top electrode were observed to have uniform out-of plane polarization, likely due to the asymmetry of the top and bottom interfaces. However, by varying the angle $\alpha$ and direction $\beta$ of the substrate miscut, Chu was able to produce films with four, two and one in-plane polarization variant. Films with a miscut $\alpha < 0.5^\circ$ were found to contain equal numbers of two sets of 71° stripe domains corresponding to all four in-plane variants. However, for larger $\alpha$ and $\beta \approx 0^\circ$ (i.e. close to [010]) the fraction of stripe domains with a long axis perpendicular to the substrate atomic step edges was observed to decrease. A single set of stripe domains oriented parallel to the substrate terrace edges was observed for a miscut of $\alpha \geq 1^\circ$, $\beta \approx 0^\circ$. With a miscut of $\alpha \geq 3^\circ$, $\beta = 45^\circ$ a single in-plane polarization variant was observed. Chu attributed these results to broken symmetry of the in-plane variants due to electrostatic forces and

the elastic energy of local stress at substrate terrace edges. Jang and coworkers studied this phenomenon further and found that growth on an exact ($\alpha = 0.05°$) and a miscut ($\alpha = 4°$) substrate led to 3D island and step-flow growth, respectively [79]. Further, Jang observed by high resolution x-ray diffraction and transmission electron microscopy a preferential distortion of the $BiFeO_3$ unit cell which made two of the four variants mechanically unfavorable in films grown on miscut substrates. For a film growing in a step-flow mode, the rhombohedral distortion toward the substrate step edges would be energetically unfavorable, and thus, the two variants distorted away from the step edges were preferred. In contrast, random nucleation of all four variants could occur in a film growing by a 3D island mode. Jang *et al.* therefore attributed the preferential domain selection in $BiFeO_3$ films on miscut $SrTiO_3$ (001) substrates to a combination of step-flow growth and preferential distortion due to substrate anisotropy.

## 4.2. Thin Film Growth and Standard Characterization

### 4.2.1. Off-Axis RF Magnetron Sputter Deposition

Off-axis radio frequency (RF) magnetron sputtering has been used extensively for the growth of complex oxide thin films and heterostructures (including high temperature superconductors (HTSCs) [80, 81], colossal magnetoresistance (CMR) materials [82], and ferroelectrics [83, 84]. This technique, first developed by Eom *et al.* [80], utilizes a geometry wherein the substrate is placed at a large angle (often 90°) from the axis of a planar magnetron gun and target. While this arrangement decreases the deposition rate, it minimizes damage to the film produced by backsputtered negative oxygen ions as well as energetic heavy atoms from the target impacting on the growing film. A diagram of

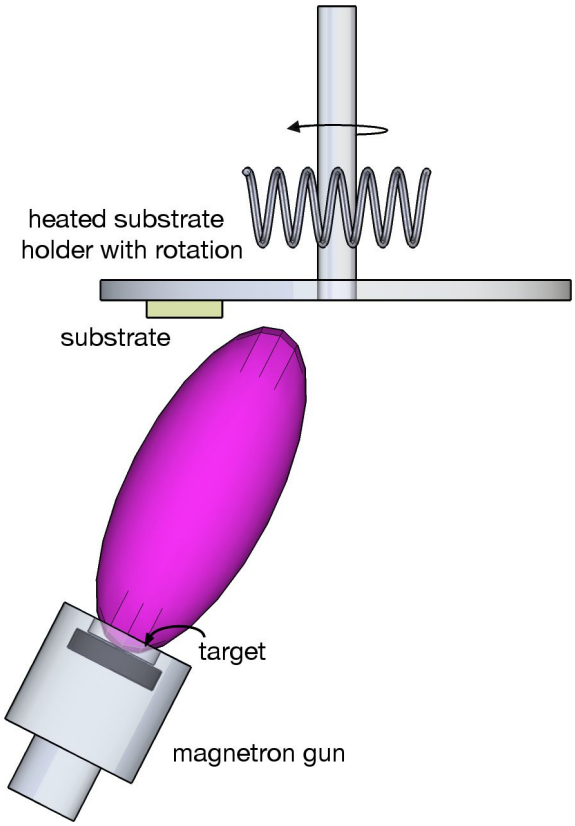


Figure 4.2. Off-axis geometry used in the AJA Rapier Series RF magnetron sputtering system.

the sputtering geometry used in the work presented in this dissertation is shown in Figure 4.2. The off-axis method has been shown to produce high quality films which are uniform over a large area at growth temperatures in the $\sim 500 - 650$ °C range. For example, Kuffer and Fischer recently reported a root mean square (RMS) roughness less than 3 Å over 6 $\mu$m $\times$ 6$\mu$m areas for a 30 nm thick $Pb(Zr_xTi_{1-x})O_3$ film grown on (001) $SrTiO_3$ at $\sim$ 500 °C [83]. Growth of high quality $BiFeO_3$ films by off-axis sputtering has also been demonstrated by Eom and coworkers [79, 84] as well as in the present work.

### 4.2.2. AJA Rapier Series Magnetron System

The sputter-deposited $BiFeO_3$ films discussed in this dissertation were grown in a commercial multi-target magnetron deposition system (Rapier Series, AJA International). The system has three deposition sources (AJA Stiletto Series ST10 unbalanced magnetron) designed to accommodate 0.125 inch thick, 1 inch diameter targets. It is equipped with two RF power supplies (R301, SEREN Industrial Power Systems) and two manual impedance matching networks (SEREN MM3X) which allow independent operation of up to two sources (although the codeposition capability was not utilized in the present work).

The system consists of a high vacuum chamber equipped with a side-mounted turbomolecular pump (Pfeiffer TMU 261) backed by a mechanical roughing pump (Alcatel Pascal 2005 SD). A second mechanical pump is connected directly to the main chamber for use when operating at higher pressure ($> 0.1$ Torr). The typical base pressure of the chamber is $10^{-8} - 10^{-7}$ Torr. A 4 inch Viton® o-ring sealed manual gate valve (MDC) is located between the turbopump and the main chamber. Pressure is controlled during deposition by manually throttling the turbo with the gate valve. A butterfly valve is used to prevent sputtered materials from entering the turbopump. Flowrates of Ar and $O_2$ gas supplies are controlled by MKS Mass-Flo® controllers with Type 167 Flow Readout monitors. Chamber pressure is measured with a dual Pirani / inverted magnetron active wide range gauge (Edwards WRG-S-NW35). A substrate heater assembly and rotation stage are fixed to a 12 inch CF flange mounted on the top of the chamber, and three magnetron guns with variable tilt are fixed to a second 12 inch CF flange mounted on the bottom of the chamber.

The direction of the magnetron guns is controlled by a single linear z-translation manipulator which is mechanically coupled to all three guns. This is shown schematically in Figure 4.3. The three guns are arranged radially equidistant and separated by 120° around the z-manipulator, which is positioned in the center of the chamber. A vacuum bellows and single pivot on each gun allows for coupled rotation toward or away from the center of the chamber. The dependence of the tilt angle in degrees (measured relative to the substrate normal direction) on the dial reading of the linear manipulator (in inches) is plotted in Figure 4.4. The tilt range is approximately $0° - 27.3°$. At a dial reading of 0.05 inches, the guns are directed at the center of the sample platen with a tilt angle of 25.6°.

The substrate heater consists of two halogen lamps positioned behind the back of the 4.5 inch diameter stainless steel sample platen. The system uses two type K thermocouples to monitor and control the substrate temperature and to prevent the system from overheating. The first, which is positioned between the halogen lamps and the platen, is used for feedback control of the substrate temperature setpoint. The second is located on the back of a cooling block which is used to thermally isolate the heater from the rest of the chamber. The second temperature reading is part of a safety interlock system which cuts power to the heater and magnetron guns to protect the system from damage in the case of overheating. The heater supply is a single phase silicon controlled rectifier (SCR) power controller (Phasetronics EP1-2025-F) which is driven by a Eurotherm 2408. The Eurotherm temperature controller enables automated setpoint temperature feedback as well as programmable control of the substrate temperature cycle (ramp rate, dwell time, cooling rate). Substrates can be mounted at an arbitrary position on the platen with

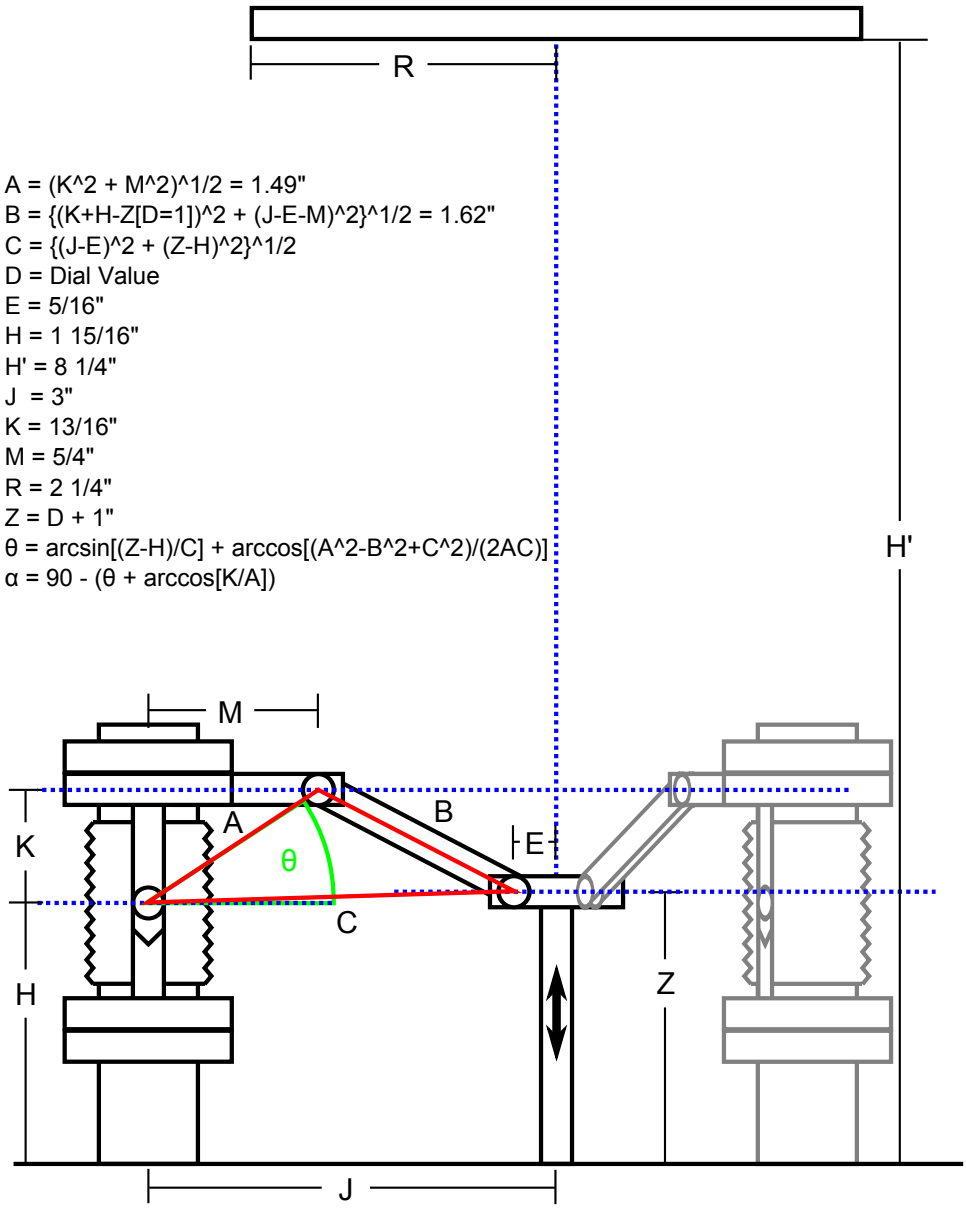


Figure 4.3. Magnetron gun geometry and tilt control in the AJA Rapier system. The dimensions and relation between quantities are contained in the key. Z is the height of the linear manipulator inside the chamber and is related to the dial reading D. The tilt angle, $\alpha$ is measured from substrate normal direction (vertical dotted blue line). In the configuration shown, $\alpha = 0$.

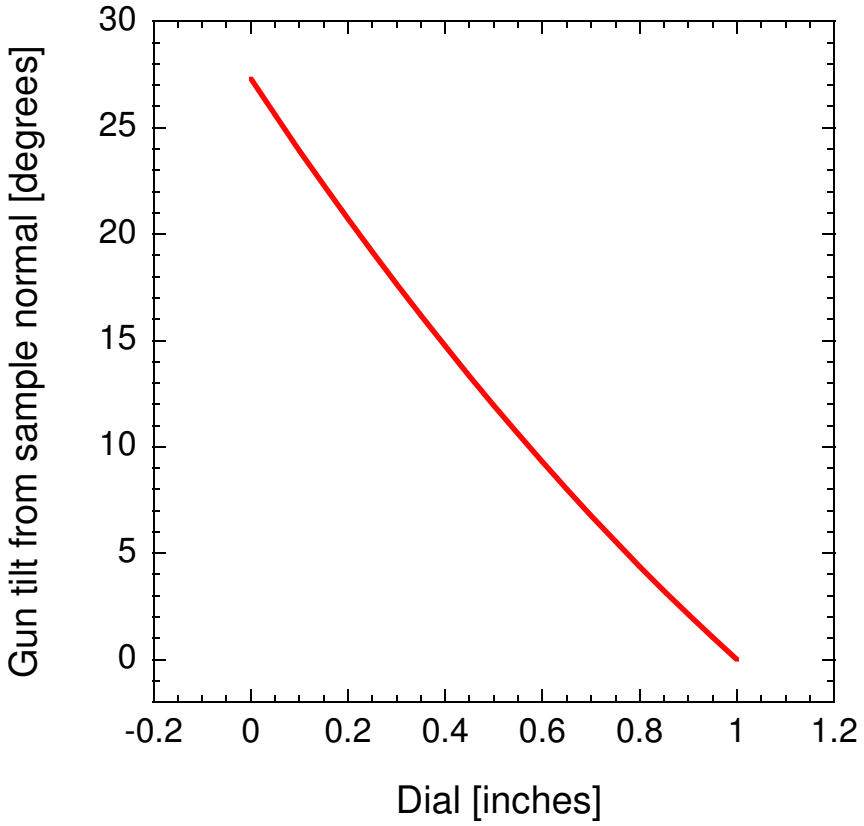


Figure 4.4. Gun tilt angle versus dial reading in the AJA Rapier system.

thermally conductive colloidal silver paint (SPI), or mechanically held at a fixed position using a custom-built low-profile stainless steel clamp. A diagram of the sample platen and low-profile clamp is shown in Figure 4.5. The clamp was designed to hold two 10 mm $\times$ 10 mm substrates at all four corners. A low profile design was used to limit shadowing effects. Substrates smaller than 10 mm $\times$ 10 mm are mounted with silver paint in all cases.

A calibration measurement was performed to determine the relation between the reading of the setpoint feedback thermocouple and the temperature of a single crystal oxide substrate mounted at different locations on the sample platen. Silver paint was used to

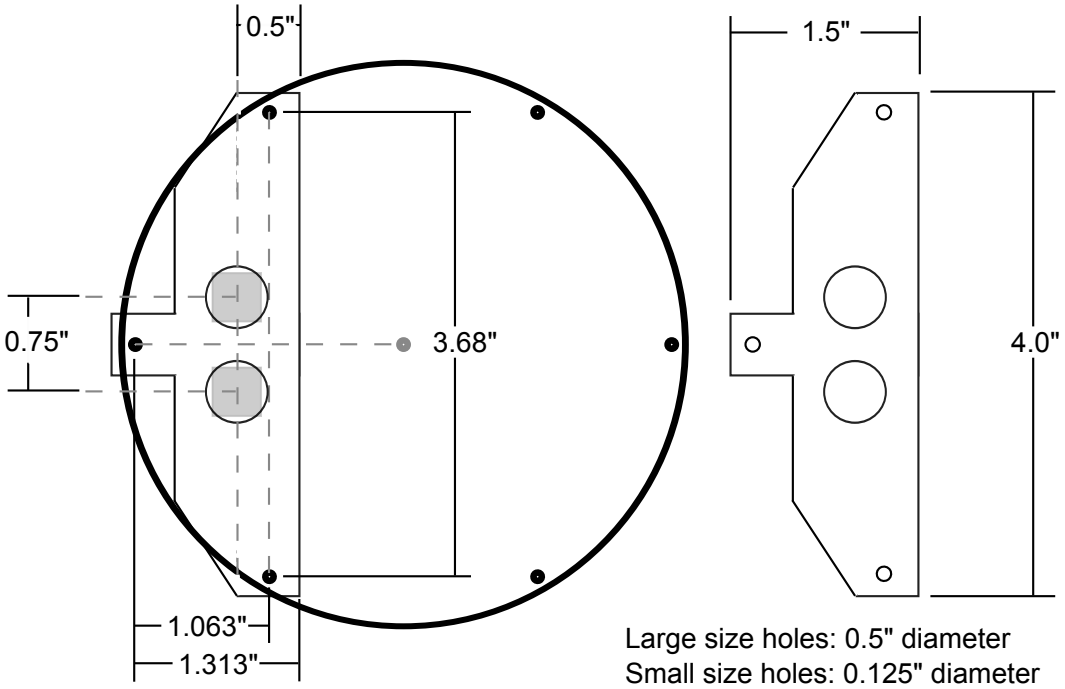


Figure 4.5. Sample platen and custom-built low-profile clamp for AJA magnetron system. The low-profile design reduces shadowing effects during deposition which can affect sample uniformity.

fix a type K thermocouple to the surface of three $SrTiO_3$ single crystal substrates: one 10 mm × 10 mm and two 5 mm × 5 mm. The 10 mm × 10 mm substrate was mounted to the platen using the low-profile clamp and the two 5 mm × 5 mm substrates were mounted with silver paint at two different radial positions on the platen. One was placed at the same radius as the 10 mm × 10 mm and the other was placed closer to the center of the platen, about 1.25 inches from the edge. The substrate at "inner" position was inside the interior region of the platen which was previously observed to glow brighter during heating. The two in the "outer" position were outside the bright region. The recorded temperatures of the three substrates are plotted in Figure 4.6 as a function of the temperature setpoint (feedback thermocouple reading). Temperatures were recorded

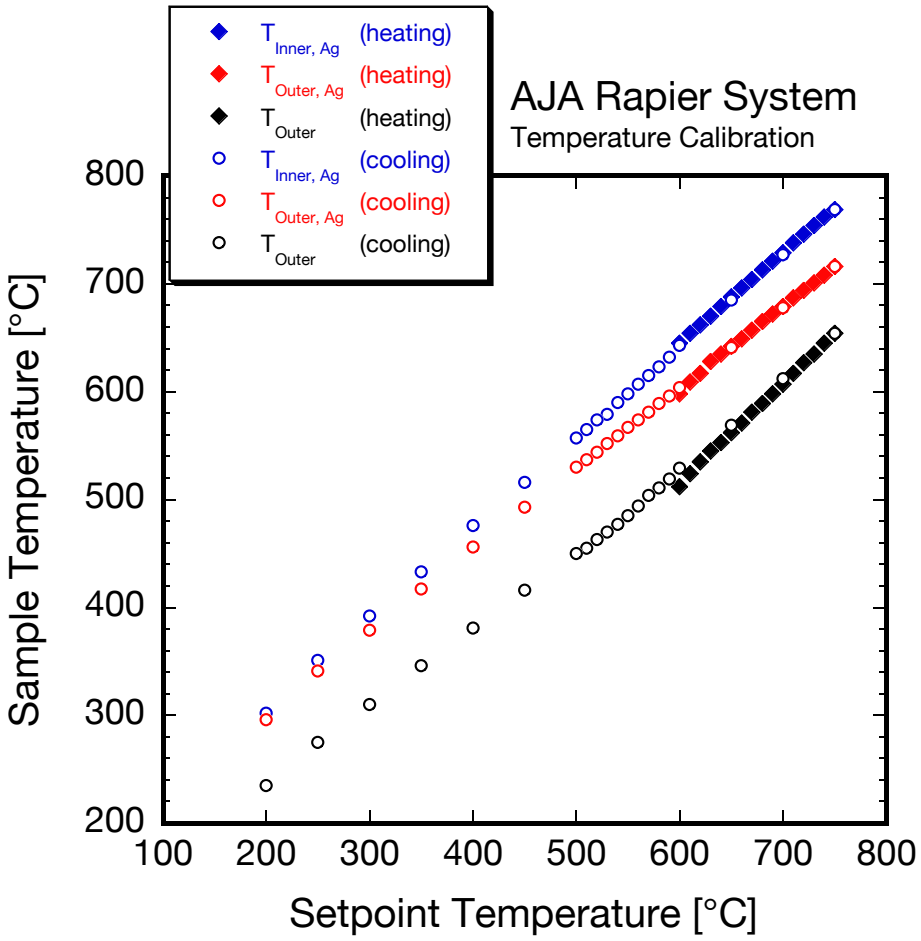


Figure 4.6. Temperature calibration measurement of substrate heater in the AJA Rapier Series sputtering system. The temperature of a $SrTiO_3$ substrate was measured with a type K thermocouple fixed to the crystal surface with silver paint. The recorded temperatures of three substrates at two radial positions on the platen are plotted versus the temperature setpoint (feedback thermocouple). For the outer position, two substrates were measured: one held to the platen with silver paint, and one mechanically held to the platen at all four corners by a custom-built low-profile stainless steel clamp.

10 minutes after stabilization of the feedback thermocouple reading at the setpoint during both heating and cooling. There is some deviation between the heating and cooling values at each position. However, for the films in this dissertation, the value upon cooling is a

more appropriate measure of the true deposition temperature as substrates were heated above the growth temperature for 10 minutes prior to film growth.

The inner region was found to have significantly a higher temperature than the outer region. $T_{\mathrm{Inner,Ag}}$ is as much as 50 °C higher than $T_{\mathrm{Outer,Ag}}$. For the two substrates located at the outer position, the one mounted with silver paint is as much as 80 °C warmer than the one held by the clamp. Unsurprisingly, the silver paint was found to provide a superior thermal contact. Furthermore, the temperature of substrate mounted with silver paint at the outer position, $T_{\mathrm{Outer,Ag}}$ is closest of the three to the setpoint temperature. $T_{\mathrm{Outer,Ag}}$ and $T_{\mathrm{Setpoint}}$ differ by between approximately 5 °C and 25 °C. Due to the better thermal contact provided by the silver paint and for reasons discussed in the next section, the default method of mounting substrates for films grown for this dissertation was with silver paint at the outer position.

The AJA magnetron system provides a large parameter space which can be used to tune the deposition process of complex oxide thin films. The geometry (gun tilt, position of the substrate on the platen), substrate temperature, RF power, process gas mixture, and total pressure can all affect film growth, and therefore can be used to optimize film quality. The $BiFeO_3$ deposition process is particularly sensitive to changes in these parameters due to the significant mass difference between the bismuth and iron cations and the greater volatility of bismuth and bismuth oxide compared to that of iron. The following section discusses the optimization of $BiFeO_3$ film growth in the AJA Rapier sputtering system.

### 4.2.3. Standard Characterization

For all sputter-deposited $BiFeO_3$ films grown for this dissertation, a 1 inch diameter, 0.125 inch thick polycrystalline $Bi_{1.1}FeO_3$ target (Praxair Specialty Ceramics) was used for the deposition source. A 10% Bi-rich target was used to compensate for the greater volatility of bismuth and bismuth oxide compared to that of iron. Optimization of deposition parameters was achieved by applying standard thin film characterization measurements to verify that films were phase-pure and epitaxially (001) oriented with a small mosaic spread and low surface roughness. Standard characterization techniques included x-ray diffraction (XRD), scanning electron microscopy (SEM) and atomic force microscopy (AFM). Unless otherwise noted, measurements were carried out using a Phillips Panalytical X'Pert, a FEI Nova 600 NanoLab dual beam instrument, and an Asylum Research MFP-3D for XRD, SEM, and AFM, respectively.

X-ray diffraction was the principal tool used to detect the presence of secondary phases. Fe-rich films generally showed (012) and (024) diffraction peaks from $\alpha$-$Fe_2O_3$ (rhombohedral, $R\bar{3}c$, $a = 5.112$ Å, $c = 13.82$ Å) and Bi-rich films showed (002) and (220) peaks from $\beta$-$Bi_2O_3$ (tetragonal, $P\bar{4}2_1c$, $a = 7.741$ Å, $c = 5.634$ Å). A comparison of diffraction data from a Bi-rich film and an Fe-rich film is shown in Figure 4.7. Peaks corresponding to $\beta$-$Bi_2O_3$ are marked with a circle (○) and those from $\alpha$-$Fe_2O_3$ are marked with a square (□). Peaks from $BiFeO_3$, $SrRuO_3$, and $SrTiO_3$ are labeled B, R, and S, respectively. Béa and coworkers previously studied the influence of deposition pressure and substrate temperature on the growth of epitaxial $BiFeO_3$ films on $SrTiO_3$ (001) by PLD from a $Bi_{1.15}FeO_3$ target [85]. Béa observed that growth of single-phase $BiFeO_3$ films could be achieved with a substrate temperature and oxygen pressure near $T_{sub} = 580$ °C

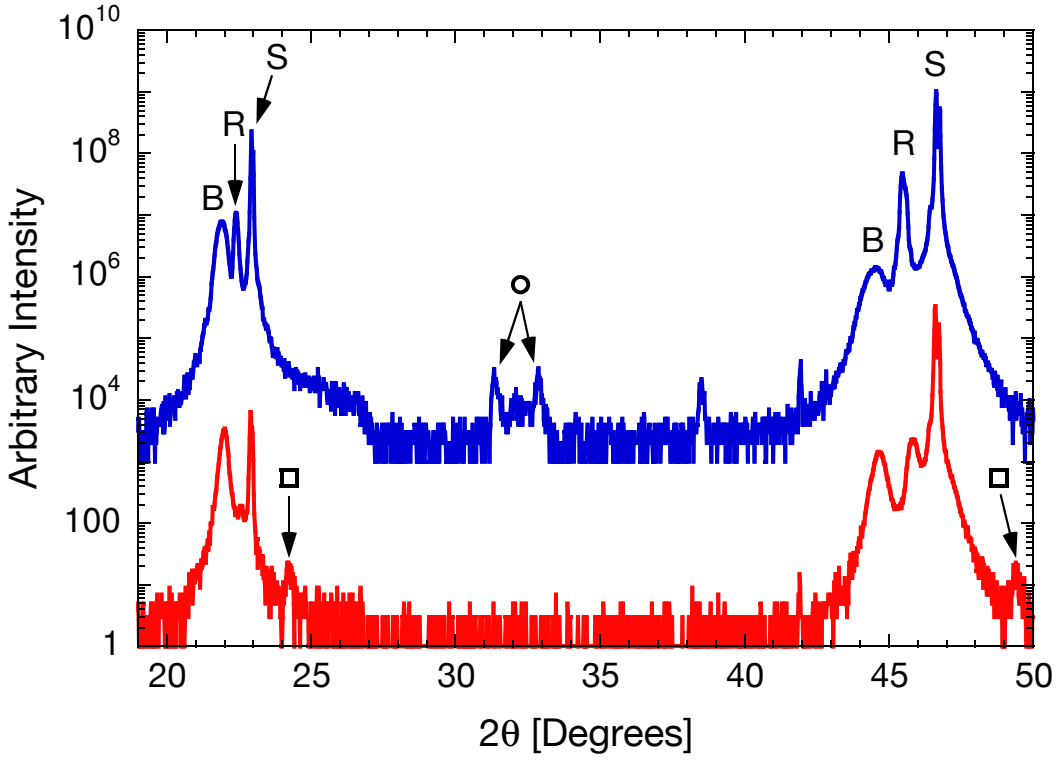


Figure 4.7. Impurity phases in $BiFeO_3$ films observed by x-ray diffraction. Peaks corresponding to $\beta$-$Bi_2O_3$ are marked with a circle (○) and those from $\alpha$-$Fe_2O_3$ are marked with a square (□).Peaks from $BiFeO_3$, $SrRuO_3$, and $SrTiO_3$ are labeled B, R, and S, respectively. The pair of $\beta$-$Bi_2O_3$ peaks are (002) and (220), whereas the two sets of $BiFeO_3$, $SrRuO_3$, and $SrTiO_3$ peaks are (001) and (002). The $\alpha$-$Fe_2O_3$ peaks are (012) and (024). The data from the Bi-rich film (blue) are offset vertically by a factor of $10^3$.

and $P_{O_2}$ = 7.5 mTorr. Deposition at lower temperature or higher pressure led to the formation of $Bi_2O_3$ precipitates while films grown at higher temperature or lower pressure were found to contain $Fe_2O_3$. From analysis of XRD measurements, Béa determined that the PLD-grown Bi-rich films contain (tetragonal) $\beta$- or possibly (cubic) $\delta$-$Bi_2O_3$ (or a mixture of the two phases). The ambiguity is due to the observation of a single peak near $2\theta = 31.7°$ which could correspond to the (002) reflection from either phase. The Fe-rich films grown by Béa *et al.* at low pressure showed diffraction peaks corresponding

to (cubic) $\gamma$-$Fe_2O_3$ whereas films grown at high temperature were found to contain the (rhombohedral) $\alpha$ phase. Furthermore, the high temperature grown films showed only peaks from $\alpha$-$Fe_2O_3$ with no evidence of $BiFeO_3$.

In contrast to the results of Béa, Bi-rich films grown in the AJA magnetron system showed a clear double peak corresponding to the (002) and (220) reflections from tetragonal $\beta$-$Bi_2O_3$, although presence of the $\delta$ phase (cubic, $Fm\bar{3}m$, $a = 5.648$ Å) could not be ruled out as the width of the observed peak exceeds the separation expected between the (002) peaks from the two phases. Further, Fe-rich films were observed to contain both (001) oriented $BiFeO_3$ and (012) oriented $\alpha$-$Fe_2O_3$ with the exception of a single deposition wherein a RF power of 25 W was used rather than the typical 51 W. The film grown at 25 W showed Bragg peaks from (012) oriented $\alpha$-$Fe_2O_3$ and no evidence of $BiFeO_3$. Single phase $BiFeO_3$ films were obtained at substrate temperatures between 590 °C and 650 °C with Ar:$O_2$ gas ratios between 6:4 and 7:3 sccm at total pressure ranging from 4.6 mTorr to 9.0 mTorr. At a given substrate temperature, film stoichiometry was found to depend strongly on the gas ratio and total pressure.

While XRD was the primary tool used to determine phase-purity, it was found to be insufficient to detect impurity phases in some cases. Figure 4.8 shows a comparison of diffraction data measured near the (002) film and substrate peaks for a series of samples grown at varied total pressure. The films were all deposited with an glsrf power $P_{RF}$ = 51 W at a substrate temperature of $T_{sub}$ = 710 °C with a 6:4 sccm Ar:$O_2$ gas mixture. The complete deposition parameters are listed in Table 4.1. Apart from a small peak corresponding to $\alpha$-$Fe_2O_3$ (024) visible in the data from the film grown at $P = 4.6$ mTorr, all films appear to free of secondary phases. However, SEM measurements of the films,

Table 4.1. Deposition parameters for $BiFeO_3$ samples anlbfo08024 and anlbfo09001 through anlbfo09006 grown at varied total pressure. All samples were deposited with an RF power $P_{RF} = 51$ W at a substrate temperature of $T_{sub} = 710$ °C with a 6:4 sccm Ar:$O_2$ gas mixture.

| Sample | DC Bias | Time | Total Pressure | Base Pressure |
|---|---|---|---|---|
| anlbfo08024 | 302 V | 30 min | 4.6 mTorr | $1.0\times10^{-7}$ Torr |
| anlbfo09001 | 294 V | 60 min | 10 mTorr | $1.3\times10^{-7}$ Torr |
| anlbfo09002 | 288 V | 60 min | 15 mTorr | $7.0\times10^{-8}$ Torr |
| anlbfo09003 | 279 V | 45 min | 7.0 mTorr | $9.5\times10^{-8}$ Torr |
| anlbfo09004 | 259 V | 40 min | 6.0 mTorr | $3.8\times10^{-8}$ Torr |
| anlbfo09005 | 254 V | 45 min | 20 mTorr | $9.5\times10^{-8}$ Torr |
| anlbfo09006 | 252 V | 45 min | 16 mTorr | $5.0\times10^{-7}$ Torr |

which are shown in Figures 4.9–4.11 revealed the presence of surface precipitates which appear crystalline based on their regular shape and orientation.

Figure 4.9 shows SEM images of $BiFeO_3$ films grown at 4.6, 6.0, and 7.0 mTorr at 6500× and 25000× magnification. In all three samples the precipitates appear to have a similar triangular shape with 45° and 90° facets. The highest concentration of outgrowths appears in the 4.6 mTorr sample shown in Figure 4.9 (a) and (b). Since this sample showed evidence of $\alpha$-$Fe_2O_3$ in the XRD measurement, it is likely that these precipitates are $Fe_2O_3$ impurities, although no chemical mapping was performed. However, the observed outgrowths were a universal feature of films with an $\alpha$-$Fe_2O_3$ diffraction signature and appeared consistent with $Fe_2O_3$ impurities reported elsewhere in $BiFeO_3$ films [86]. Furthermore, the concentration of precipitates was found to decrease with increasing total pressure as shown in Figure 4.9 (c)-(f). The films grown at 6.0 and 7.0 mTorr contained fewer individual outgrowths, although some appeared to have formed larger dendritic structures. The formation of these larger features may be due to the reduced growth rate resulting from the increased total pressure.

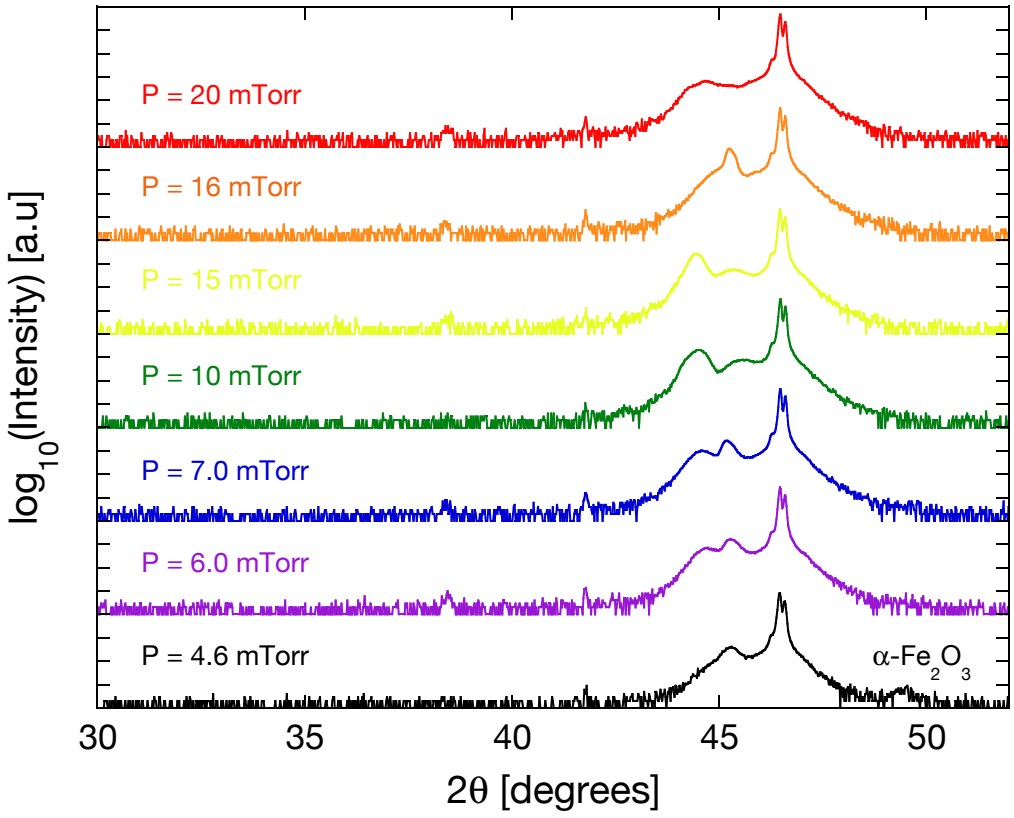


Figure 4.8. X-ray diffraction comparison of $BiFeO_3$ films grown at varied total pressure. All films shown here appear to contain second phases ($\alpha$-$Fe_2O_3$ or $\beta$-$Bi_2O_3$) based on surface precipitates observed in SEM. However, a diffraction peak from an impurity phase is only visible for the 4.6 mTorr film. The small peak located near $2\theta = 41.75°$ in is an artifact of the diffractometer.

SEM images of films grown at total pressures of 10 and 15 mTorr are shown in Figure 4.10. Similar triangular-shaped outgrowths were observed in both films, although in significantly lower concentration compared the films shown in Figure 4.9. The larger dendritic precipitates seen in the Figure 4.9 (c)-(f) images of the 6.0 and 7.0 mTorr films were not observed in the 10 and 15 mTorr samples. The concentration and size of the outgrowths observed in the 10 and 15 mTorr films appeared similar, although the 15 mTorr features were slightly smaller. Similar to the change in concentration observed

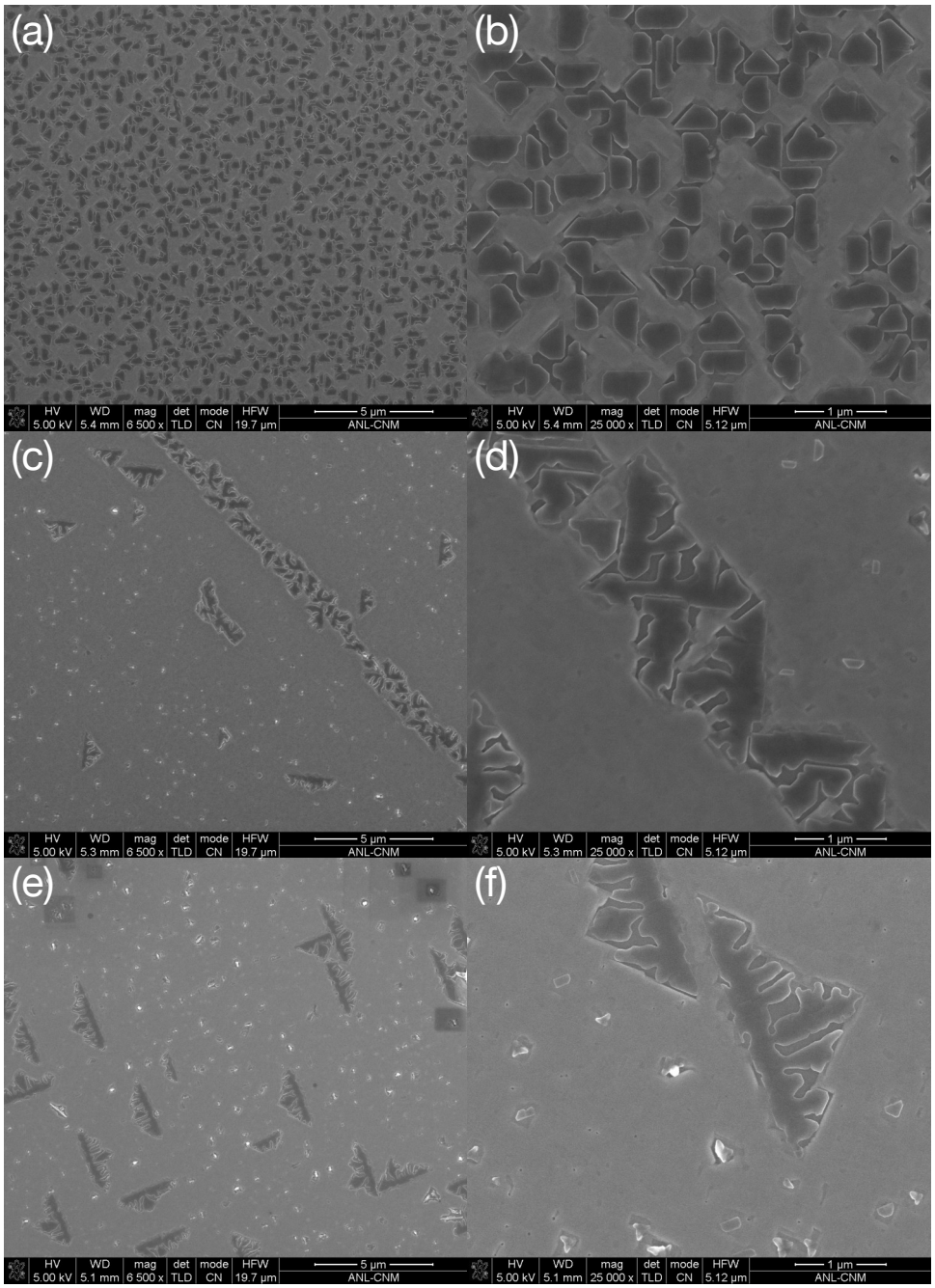


Figure 4.9. SEM images of $BiFeO_3$ films grown at (a)-(b) 4.6, (c)-(d) 6.0, and (e)-(f) 7.0 mTorr. Images are at (a)(c)(e) 6500× and (b)(d)(f) 25000× magnification. Outgrowths are likely due to $\alpha$-$Fe_2O_3$ impurities and appear to decrease in concentration with increasing pressure.

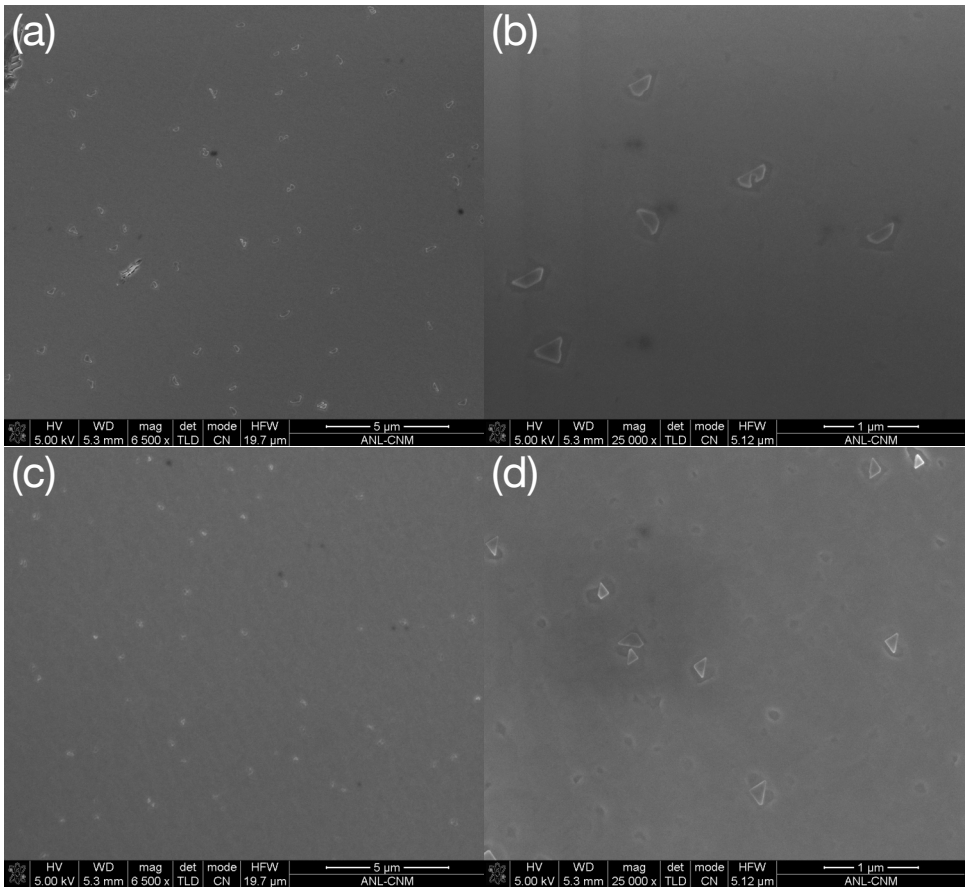


Figure 4.10. SEM images of $BiFeO_3$ films grown at (a)-(b) 10 and (c)-(d) 15 mTorr. Images are at (a)(c) 6500× and (b)(d) 25000× magnification. The concentration of precipitates is similar at 10 and 15 mTorr and significantly less than at $\leq$7.0 mTorr.

between the 4.6 mTorr film and the films grown at 6.0 and 7.0 mTorr, the decrease in the number density of precipitates in the 10 and 15 mTorr films relative to those deposited at a total pressure $\leq$7.0 mTorr suggests that the observed outgrowths were due to $\alpha$-$Fe_2O_3$ impurities in the films.

Figure 4.11 shows SEM images of $BiFeO_3$ films grown with total pressures of 16 and 20 mTorr. The outgrowth concentration was observed to be greater than that of the 15 mTorr film, and significantly larger for the 20 mTorr film compared to the film grown at

16 mTorr. A change in shape from triangular to rectangular and square precipitates was also observed. The reversal of the pressure dependence of the precipitate concentration suggests that the 16 and 20 mTorr films were Bi-rich, rather than Fe-rich like those grown at $\leq$15 mTorr. Furthermore, the square and rectangular shaped outgrowths beginning to appear in the 16 mTorr film and clearly visible in the 20 mTorr film are consistent with $\beta$-$Bi_2O_3$ precipitates observed in several reports [87, 88] including the work of Béa and coworkers [85]. At a substrate temperature of 710 °C there appears to exist a larger pressure window for the formation of small concentrations of $Fe_2O_3$ impurities compared $Bi_2O_3$ impurities. This indicates that $Fe_2O_3$ is more stable at this temperature than $Bi_2O_3$. Moreover, no film grown at $T_{\text{sub}} = 710$ °C was found to be free of surface precipitates as observed in SEM. This suggests that 710 °C is outside the process window for the growth of single-phase $BiFeO_3$ in the AJA magnetron system. Such growth was only achieved at lower substrate temperatures between 590 °C and 650 °C.

These results are qualitatively similar to the findings of Béa *et al.*. Films grown at low pressure or high temperature tended to be Fe-rich and led to the formation of $Fe_2O_3$ precipitates which could be observed by XRD and/or SEM. Alternately, films grown at high pressure or low temperature typically were found to be Bi-rich, containing $Bi_2O_3$ precipitates. In addition, films which showed no detectable diffraction signature from secondary phases were found to contain outgrowths indicative of Bi- and Fe-rich impurities which could be observed by SEM. Differences between the results of Béa and those presented here can be attributed to the fact that it is difficult to compare sputtering directly with PLD due to the differing mechanisms of the two deposition processes, as well as the larger number of process variables in sputter deposition which are related

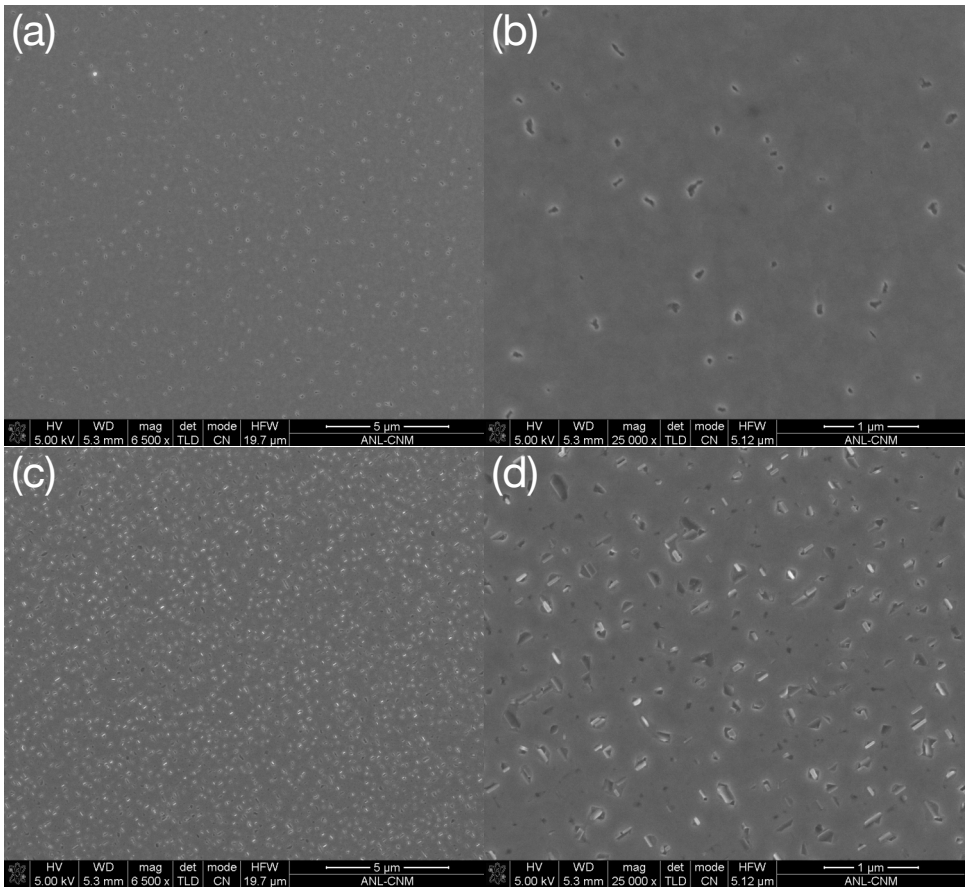


Figure 4.11. SEM images of $BiFeO_3$ films grown at (a)-(b) 16 and (c)-(d) 20 mTorr. Images are at (a)(c) 6500× and (b)(d) 25000× magnification. The outgrowth concentration is greater than that of the 15 mTorr film, and increases further for the 20 mTorr film compared to the film grown at 16 mTorr. A change in shape from triangular to rectangular and square is also observed, which is consistent with $\beta$-$Bi_2O_3$ precipitates.

to the maintenance and control of and interaction with the plasma. Furthermore, it is difficult to compare results even from one magnetron system to another due to the strong dependence on geometry of the deposition process.

The dependence of impurity phase formation on substrate temperature and growth pressure is understood in relation to the greater volatility of Bi and $Bi_2O_3$. At low oxygen pressure, a portion of Bi from the target may be unoxidized and consequently evaporate

from the surface of the growing film due to the high vapor pressure of Bi, which is $\sim 4.3$ mTorr at 650 °C [89]. At high temperature, $Bi_2O_3$ can become unstable and decompose into $O_2$ and Bi which is then evaporated from the surface of the film [85]. Either of these processes will lead to an Fe-rich film which results in the formation $Fe_2O_3$ precipitates. $Bi_2O_3$ precipitates are formed at low temperature or high pressure as excess Bi in the target forms stable $Bi_2O_3$. Total pressure can also lead to changes in film stoichiometry due to the large mass imbalance between Bi and Fe. Changes in total pressure can lead to asymmetric changes in the mean-free-path and sputtering yield of the two cation species. An increase in pressure can preferentially attenuate Fe relative to Bi and lead to a larger relative decrease in the Fe sputtering yield (due to reduced Ar ion energy) [90].

In addition to serving as a tool to detect secondary phases, x-ray diffraction measurements were also used to characterize the film orientation and degree of crystalline alignment. Scans along the specular substrate $(00l)$ direction in reciprocal space ($\theta/2\theta$ scans) revealed only $(00l)$ peaks from $BiFeO_3$ indicating that the films were epitaxially (001) oriented. Furthermore, the width of the film Bragg peaks was used as an indicator as to the strain state and overall crystalline quality. Figure 4.12 shows a scan through the $BiFeO_3$, $SrRuO_3$, and $SrTiO_3$ (001) peaks of a 120 nm thick $BiFeO_3$ film grown on 125 nm $SrRuO_3$ / $SrTiO_3$ (001). Thought the layers are nearly the same thickness, the $BiFeO_3$ peak is significantly broader than that from the $SrRuO_3$. Also, there are no visible thickness fringes from the $BiFeO_3$ film, while there are pronounced oscillations from the $SrRuO_3$ layer, This is due to strain relaxation of the $BiFeO_3$ layer which at 120 nm thick is well beyond the critical thickness of $\sim$ 50 nm - 70 nm for coherent growth on $SrTiO_3$ (001) [71, 74].

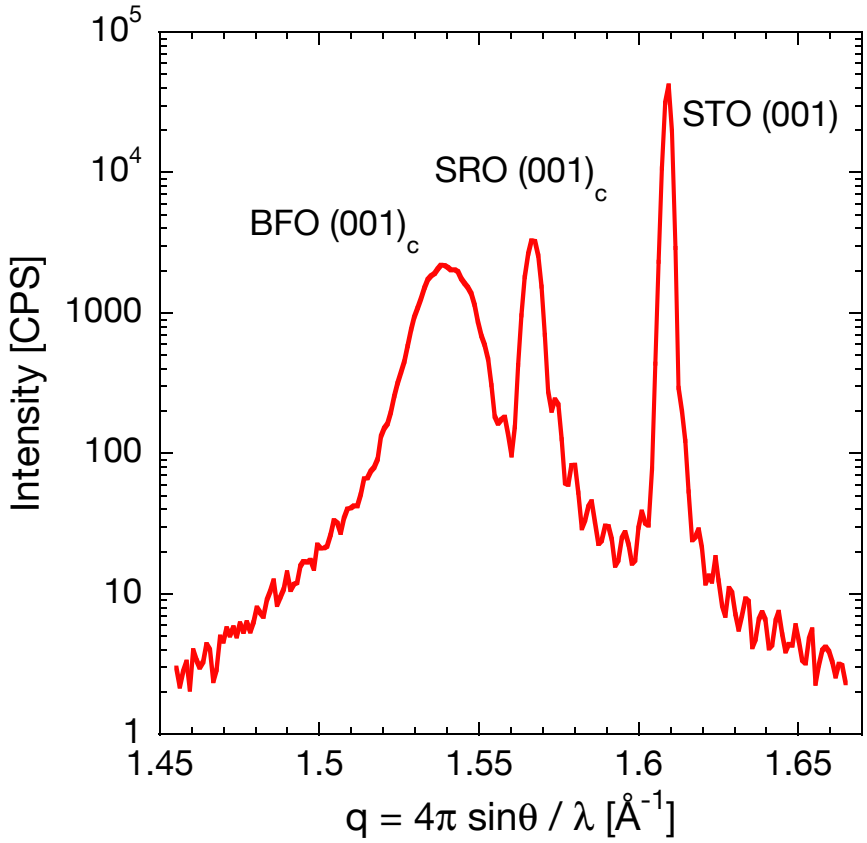


Figure 4.12. X-ray diffraction of a 120 nm $BiFeO_3$ film on (125 nm) $SrRuO_3$ / $SrTiO_3$ (001) near the (001) peaks. The film is beyond the critical thickness for coherent growth on $SrTiO_3$ (001) and the $BiFeO_3$ peak is broadened accordingly due to strain relaxation.

Rocking scans through the (001) and (002) $BiFeO_3$ Bragg peak were used to quantify and compare the degree of crystalline alignment for films grown under various conditions. Films grown at higher substrate temperatures were generally found to have narrower rocking curve widths. Figure 4.13 shows the full width-at-half maximum (FWHM) of the (002) $BiFeO_3$ rocking curve plotted versus substrate growth temperature for a series of films deposited with an RF power $P_{RF}$ = 51 W in a 7:3 sccm Ar:$O_2$ gas mixture at $P_{total}$ = 9.0 mTorr. The FWHM values were determined by a pseudo-Voigt [91] fit to

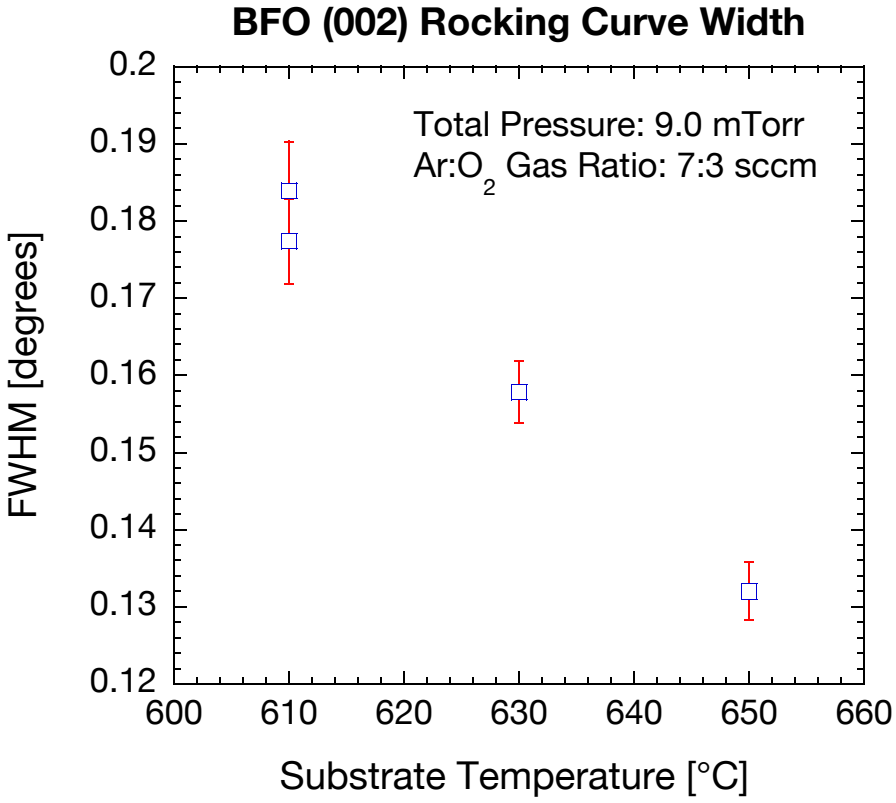


Figure 4.13. $BiFeO_3$ (002) rocking curve width versus of substrate temperature. The full width at half maximum was determined by a pseudo-Voigt fit to each rocking curve scan.

each rocking curve scan. The width of the (002) $BiFeO_3$ rocking curve was found to decrease linearly with increasing substrate temperature, from $0.177(6)^\circ$ at $T_{\text{sub}} = 610$ °C to $0.132(4)^\circ$ at $T_{\text{sub}} = 650$ °C.

A general feature of complex oxide thin films grown in the AJA magnetron system (e.g. $BiFeO_3$, $SrRuO_3$) was a dependence of surface morphology on sputtering geometry. Specifically, the gun tilt and radial position of the sample on the platen were found to affect the surface roughness as measured with AFM. The smoothest films were obtained (with typical RMS roughness $\sim 3 - 5$Å) with the most "off-axis" geometry obtainable in

the Rapier system. Minimizing the interaction of the growing film with the direct plume was found to result in low surface roughness. Samples were mounted at the outer position with silver paint, and a gun tilt of 0.05 inches was used. This tilt value corresponds to a tilt angle of 25.6°. More importantly, in this configuration, the gun is pointed at the center of the platen. Since rotation of the platen was used to produce uniform deposition, a tilt greater or less than this value would bring the sample closer in line with the direct plume. Sample-plasma interactions could also be tuned using gas pressure as increased pressure was observed to lead to a more confined plume and therefore less direct interaction with the sample. Increased pressure also leads to reduced growth rate which can result in smoother films due to increased time for surface diffusion. However, due to the relatively narrow phase-stability window for $BiFeO_3$ growth, pressure was not used as a parameter to control surface morphology.

The optimal deposition parameters for the growth of single-phase (001) oriented epitaxial $BiFeO_3$ on $SrTiO_3$ (001) in the AJA Rapier Series magnetron system are listed in Table 4.2. A 35 minute deposition with these parameters (with a chamber base pressure of $1.2\times10^{-7}$ Torr) produced a 37 nm thick film, indicating a growth rate of $\sim$ 1 nm/min. The film was deposited on a (70 nm) $SrRuO_3$ coated single crystal $SrTiO_3$ (001) substrate. The $SrRuO_3$ layer was grown by RF magnetron sputtering. Prior to deposition, the $SrTiO_3$ substrate (CrysTec GmbH, Germany) was treated with a standard buffered-HF etch followed by an $O_2$ anneal at 950 °C to produce an atomically flat $TiO_2$-terminated surface [92, 93]. Figure 4.14 shows the result of a low resolution XRD measurement. Only (00$l$) peaks from $BiFeO_3$, $SrRuO_3$, and $SrTiO_3$ are observed indicating that the film is (001) oriented and free from secondary phases. Likewise, no precipitates were observed with

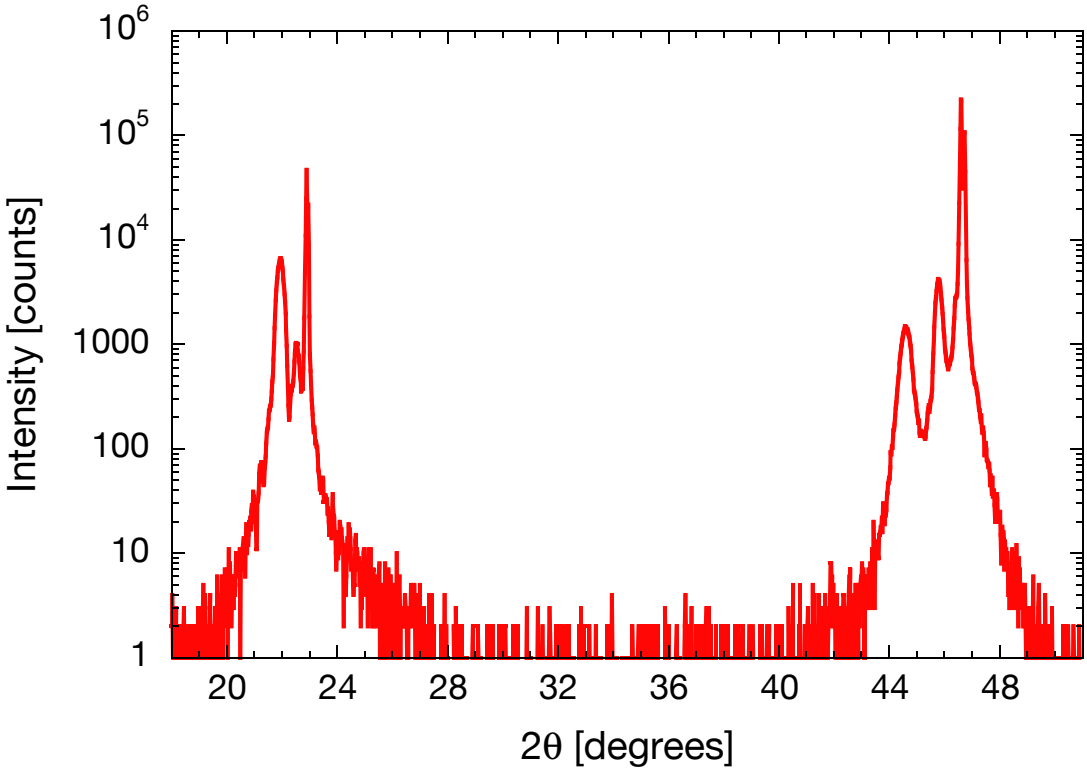


Figure 4.14. Low resolution x-ray diffraction of 37 nm $BiFeO_3$ film. The film is (001) oriented and free from secondary phases.

SEM. A RMS surface roughness of 3Å over 2 $\mu$m × 2 $\mu$m was measured with AFM. The film thickness was calculated from the period of thickness fringes ($t = 2\pi/\Delta q$) observed in a low angle x-ray reflectivity measurement shown in Figure 4.15 (a). Figure 4.15 (b) shows XRD data taken near the (001) peaks. Oscillations with a period consistent with the x-ray reflectivity (XRR)-determined $BiFeO_3$ thickness are visible on both the high and low angle sides of the (001) peaks. This indicates that the film is uniform and highly crystalline. Figure 4.16 shows rocking scans of the (001) Bragg peaks of the $BiFeO_3$ and $SrTiO_3$ layers of the 37 nm sample. The $BiFeO_3$ rocking curve, shown in Figure 4.16 (a) has a FWHM of 0.080(2)° which is on the same order as the 0.0617(1)° FWHM of the

Table 4.2. Optimal deposition parameters for $BiFeO_3$ in the Rapier system. With a gun tilt of 0.05 inches, the guns are directed at the center of the sample platen with a tilt angle of 25.6°

| | |
|---|---|
| RF Power (W) | 51 |
| DC Bias (V) | 230 |
| Gun Tilt (inches) | 0.05 |
| Ar:$O_2$ Gas Flow (sccm) | 7:3 |
| Total Pressure (mTorr) | 9.0 |
| Substrate Temperature (°C) | 650 |

$SrTiO_3$ peak shown in Figure 4.16 (b). The mosaic spread of the film is therefore similar to that of the single crystal substrate.

The 37 nm $BiFeO_3$ film grown with the deposition parameters listed in Table 4.2 was subsequently used to produce epitaxial $BiFeO_3$ nanostructures by a nanopatterning method utilizing focused ion-beam processing with a 100 nm thick patterned W protective mask. A similar 40 nm film grown under slightly different conditions ($T_{sub}$ = 590 °C, $P_{total}$ = 4.6 mTorr, and Ar:$O_2$ = 6:4 sccm) was used to produce nanostructures by a method utilizing a protective 50 nm Pt film. Both fabrication strategies are discussed in the next section.

## 4.3. Fabrication of Epitaxial $BiFeO_3$ Nanostructures

With the exception of the deposition of the protective metal layers (Pt and W) which were grown in the AJA Rapier Series magnetron system, all fabrication steps discussed in the following section took place in the nanofabrication clean room facility at the Argonne Center for Nanoscale Materials.

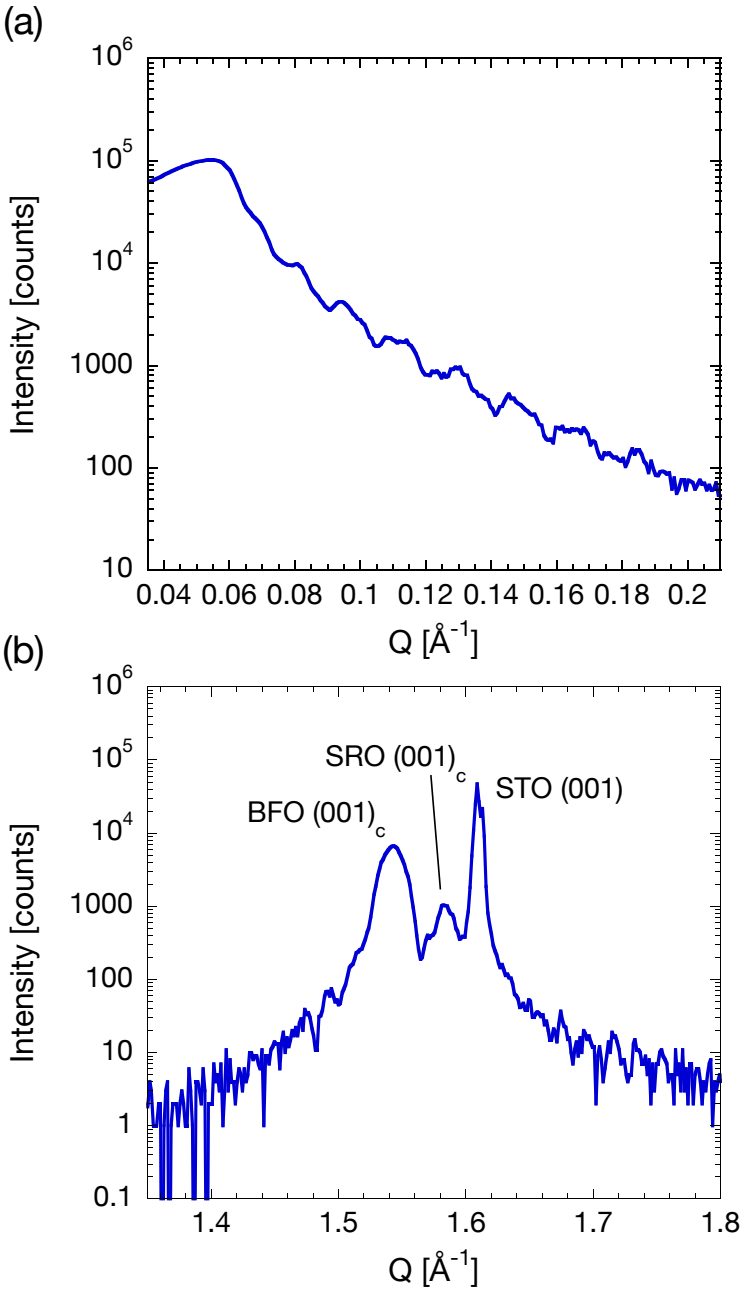


Figure 4.15. X-ray reflectivity (a) and (001) CTR (b) measurement of 37 nm $BiFeO_3$ film on $SrRuO_3$ / $SrTiO_3$ (001). Fringes in the reflectivity (a) and on both the high and low angle sides of the (001) peaks in (b), are due to the finite thickness of the highly crystalline $BiFeO_3$ film. The 70 nm $SrRuO_3$ layer was also deposited by RF magnetron sputtering.

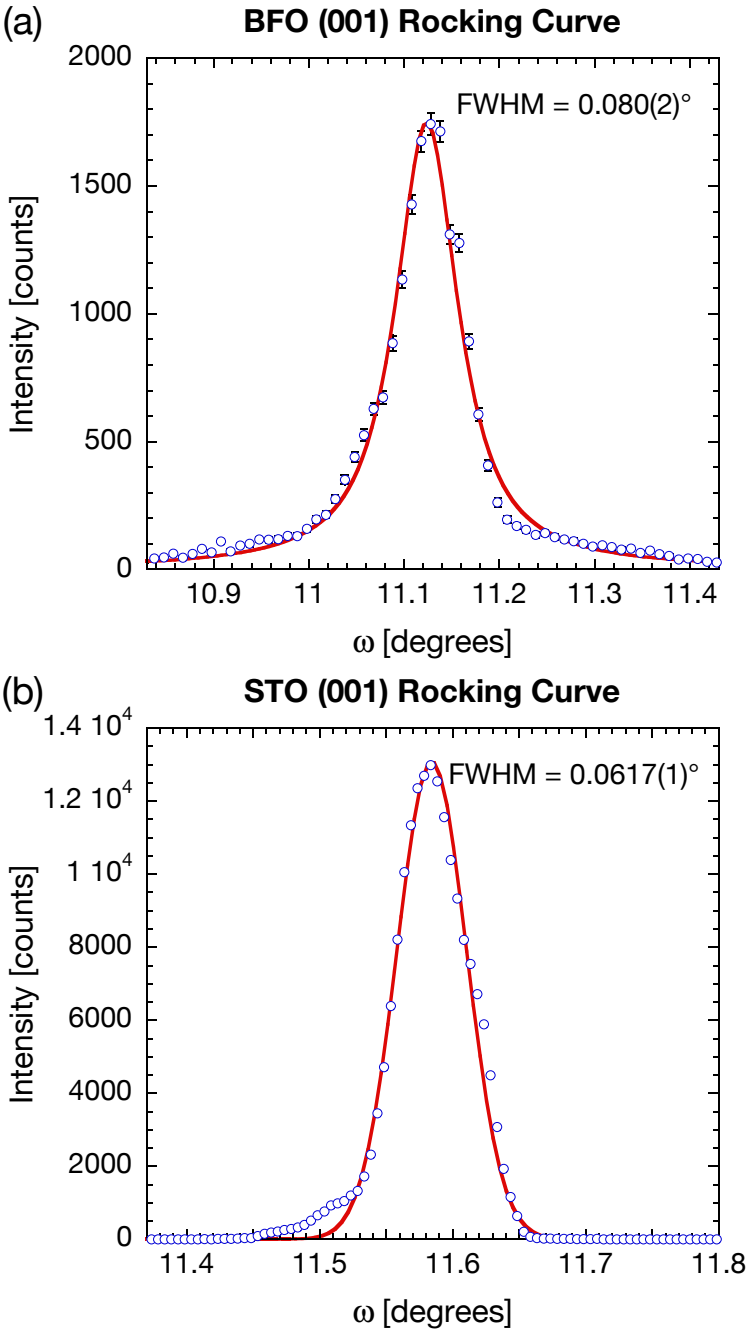


Figure 4.16. Film (a) and substrate (b) (001) rocking curves from a 37 nm $BiFeO_3$ film on $SrTiO_3$ (001).

### 4.3.1. Focused Ion-Beam Lithography

Focused ion-beam (FIB) lithography was used to fabricate nanostructures from the epitaxial (001) oriented $BiFeO_3$ films. The FIB technique was employed as it enables patterning of structures with arbitrary shape with lateral sizes as small as of 10 nm [94]. As a initial study of $BiFeO_3$ nanostructures, FIB processing with a FEI Nova 600 NanoLab, dual beam instrument was used to fabricate square and round nanostructures with 500 nm lateral dimensions from the 120 nm thick partially relaxed $BiFeO_3$ film shown previously in Figure 4.12. The structures were patterned from the bare film without the use of a protective coating. The square and round nanostructures were characterized with piezoresponse force microscopy (PFM) by Argonne collaborator Seungbum Hong using an Asylum Research MFP-3D AFM [33]. Figure 4.17 shows a PFM measurement of a 500 nm $\times$ 500 nm square nanostructure. Shown from left to right are AFM Topography, vertical-PFM (V-PFM) (amplitude and phase), and lateral-PFM (L-PFM) (amplitude and phase) (a) before and (b) after annealing. A significant portion of the as-fabricated structure was piezoelectrically inactive, showing as dark contrast in the V-PFM amplitude image. This was likely due to ion-induced damage incurred by interaction with the tails of the beam. After PFM characterization, the patterned film was annealed for 10 min at 650 °C in 1 Torr of $O_2$. The PFM measurement of the annealed nanostructure, shown in Figure 4.17 (b) shows a clear recovery of piezoelectrically inactive area when compared to the measurement in Figure 4.17 (a) before annealing. The observed recovery of ion-damaged areas by oxygen annealing was consistent with previous reports by Gregg and coworkers [95, 96].

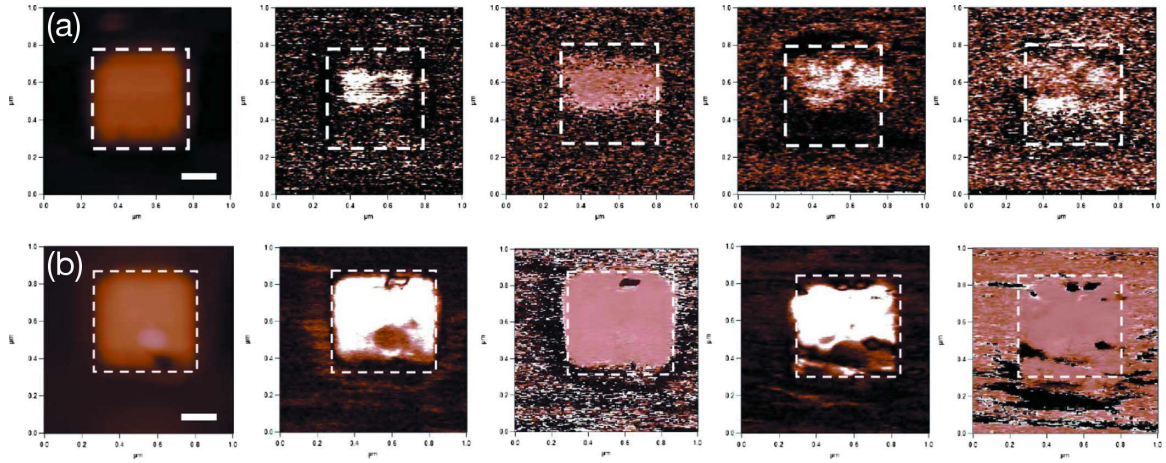


Figure 4.17. AFM Topography, V-PFM (amplitude and phase), and L-PFM (amplitude and phase) (from left to right) of a 120 thick unprotected $BiFeO_3$ nanostructure (a) before and (b) after annealing. The white bar represents the scale bar of 200 nm, and the white dotted lines are drawn only as eye guides to identify the pattern edges, after [33]. The PFM measurement was performed by Seungbum Hong on an Asylum Research MFP-3D AFM (Materials Science Division, Argonne National Laboratory).

While significant recovery of damaged areas was achievable through oxygen annealing, it was still unclear what effects ion damage may have had on the properties of the $BiFeO_3$ nanostructures. Therefore, following discussion describes efforts to fabricate epitaxial $BiFeO_3$ nanostructures by FIB with limited ion damage. Two approaches were explored: the use of a blanket Pt protective film, which is discussed in Section 4.3.2 and the use of a patterned W protective mask, which is discussed in Section 4.3.3.

### 4.3.2. FIB With a Pt Protective Film

In the first patterning strategy explored, a blanket metal film was used as a protective layer to limit damage to the oxide film from the tails of the ion-beam during FIB fabrication. However, for nano-beam x-ray measurements a uniformly coated sample would complicate

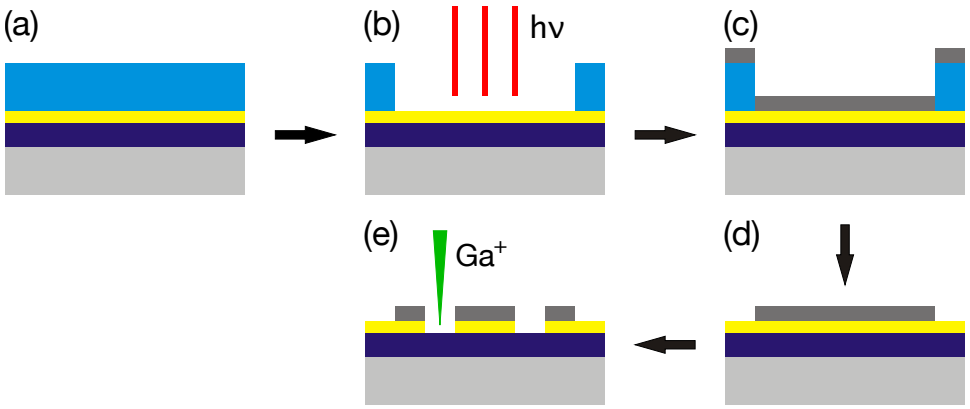


Figure 4.18. Schematic diagram of FIB lithography process utilizing a protective metal film layer. (a) Spin-coated photoresist layer on $BiFeO_3$ / $SrRuO_3$ / $SrTiO_3$, (b) optical lithography, (c) Pt sputter deposition, (d) lift off of photoresist, and (e) focused ion beam lithography.

the process of locating the microscale region of interest. Locating the region of interest typically involves the use of coarse scans across regions with recognizable diffraction or fluorescence contrast. Accordingly, to simplify location of the nanostructures during x-ray experiments, a large (∼50 $\mu$m) Pt pad and alignment grid were fabricated by direct-write optical lithography. A schematic of the full lithography process used is shown in Figure 4.18. To achieve an even photoresist coating, the 5 mm × 5 mm sample was bonded to a 3 inch Si wafer using photoresist A24620 followed by a 1 minute bake on a hotplate at 100 °C. A layer of positive photoresist S1818 was spin-coated onto the sample at 2000 RPM using a SC-400B-6NPP/LITE spin processor (Laurell Technologies, Corp.). The sample was then baked on a hot plate for 1 minute at 110 °C. The pattern for the protective pad and alignment grid were transfered to the photoresist film using a MicroTech LaserWriter LW405A. The pattern contains a central 50 $\mu$m × 40 $\mu$m pad surrounded by an alignment grid consisting of three concentric square frames with side lengths 100 $\mu$m, 500 $\mu$m, and 1 mm plus a crosshair pattern bisecting the sides of the

three frames. The pattern is shown in Figure 4.19 (a) after Pt deposition and lift off. To reduce the symmetry of the alignment grid, segments of the frames and crosshairs above and to the left of the central pad were 4 $\mu$m wide and those below and to the right were 2 $\mu$m wide. The four corners of the 1 mm frame were numbered clockwise from top left with roman numerals.

The exposed photoresist was developed by a 30 second soak in MICROPOSIT$^{TM}$ Developer 351 (20 mL plus 40 mL of deionized water (DIW)) followed by a thorough rinse in DIW. Complete removal of the exposed resist was verified with an optical microscope. The thickness of the resist mask ($\sim$ 2.8 $\mu$m) was measured with a profilometer (Tencor Alpha Step 500). A 50 nm thick Pt film was then deposited on the sample by RF magnetron sputtering at room temperature and normal incidence in the AJA Rapier system. The Pt film was grown with a RF power of 51 W, a DC bias of 250 V, and an Ar flowrate and pressure of 6 sccm and 4.6 mTorr. The growth rate was approximately 2.8 nm/min. Following Pt deposition, lift-off was achieved by soaking the sample overnight in an organic solvent mixture (MICROPOSIT$^{TM}$ Remover 1165) on a 70 °C hotplate. A short ($<$ 1 second) dip in an ultrasonic bath was required to completely lift off the Pt interior to the 1 mm frame. After lift-off was complete, the sample was rinsed in isopropanol (IPA) and DIW.

Pt / $BiFeO_3$ nanostructures were fabricated from the 50 $\mu$m $\times$ 40 $\mu$m pad region of the sample using focused ion-beam processing (FEI Nova 600 NanoLab dual beam FIB/SEM instrument). Objects with lateral sizes ranging from 1$\mu$m to 100 nm were patterned with a 1.8 pA beam of 30 kV $Ga^+$ ions using a multiple-pass circumferential patterning strategy. The beam path was defined by a series of graduated concentric frames with a beam pitch

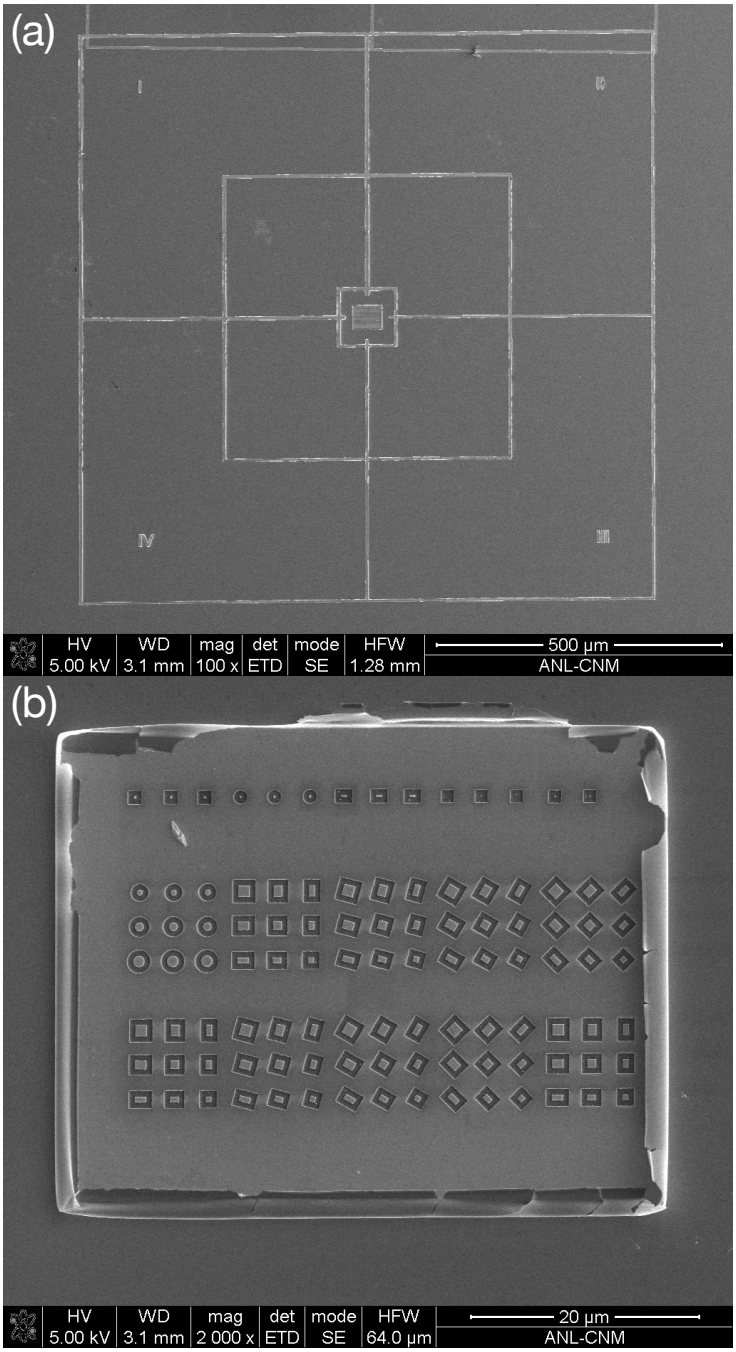


Figure 4.19. SEM images of the Pt / $BiFeO_3$ sample after nanostructure fabrication. The Pt alignment grid and protective pad (a) were fabricated with direct-write optical lithography. The Pt / $BiFeO_3$ nanostructures (b) were produced with by FIB processing.

of 3.5 nm and a spacing of 5 nm between each subsequent frame. Frames were traced from outward to inward to reduce redeposition of sputtered material onto the nanostructures. This patterning method was found to result in sharper feature definition when milling through a polycrystalline metal layer compared to a raster strategy. The patterned array of nanostructures is shown in Figure 4.19 (b). Square and rectangular structures were fabricated with lateral dimensions 1 $\mu$m, 750 nm, and 500 nm and edges aligned at 0°, 15°, 30°, and 45° with respect to the in-plane [010] direction. Circular structures with diameters 1 $\mu$m, 750 nm, and 500 nm were also fabricated.

From calculations using the TRIM software [97], a 50 nm thick Pt layer was determined to be of sufficient thickness to stop 30 keV $Ga^+$ ions within the metal layer in order to prevent implantation of ions from the beam tails in the $BiFeO_3$ nanostructures. The maximum penetration depth was 379.4 Å and the mean depth was 83.3 Å with a standard deviation of 51.0 Å. However, sidewall damage was still expected [98], and a thin cross section containing a 500 nm square nanostructure was prepared from a second unannealed sample for a transmission electron microscopy study. The transmission electron microscopy (TEM) sample was prepared by Jon Hiller in the Argonne Electron Microscopy Center (EMC). Cross-section TEM images of the unannealed 500 nm square Pt / $BiFeO_3$ nanostructure are shown in Figure 4.20. The TEM measurements were performed by Bernd Kabius with a FEI Tecnai F20ST (EMC, Argonne National Laboratory). From the TEM images, only the bottom 12 nm of the $BiFeO_3$ layer was found to be crystalline prior to annealing, while the top 28 nm was amorphous. This indicates that the 50 nm blanket Pt film was not a suitable protective layer. While the Pt film may have been of sufficient thickness to prevent 30 keV $Ga^+$ ions from implanting into

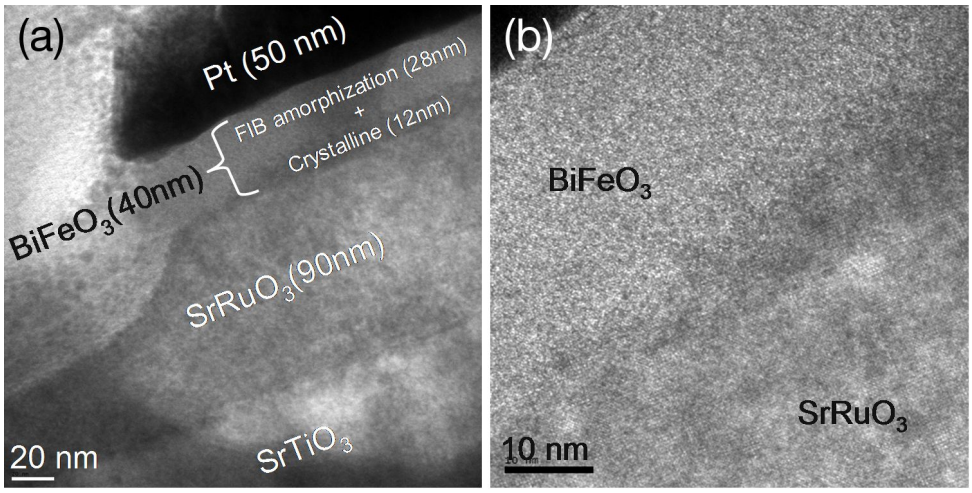


Figure 4.20. Cross-section TEM images of 500 nm square Pt / $BiFeO_3$ nanostructure prior to $O_2$ annealing. Only the bottom 12 nm of the $BiFeO_3$ layer is crystalline, while the top 28 nm is amorphous. The TEM measurements were performed by Bernd Kabius with a FEI Tecnai F20ST (Electron Microscopy Center, Argonne National Laboratory).

the $BiFeO_3$ layer, it did not appear to be effective in insulating the $BiFeO_3$ from damage due to the impacts of the ions on the metal film.

The Pt-protected sample studied by TEM was subsequently annealed for 1 hour in a tube furnace at 650°C in flowing $O_2$. The annealed sample and the as-fabricated sample shown in Figure 4.19 were then characterized with nano-beam x-ray diffraction measurements, which are discussed in Section 5.2.

### 4.3.3. FIB With a Patterned W Protective Film

With the use of a protective blanket metal film, as in the method discussed in the previous section, a significant ion dose was required to mill through the metal layer in order to pattern the oxide beneath. The required ion dose could be substantially reduced if instead a patterned metal layer were used such that the metal acts as a hard mask which

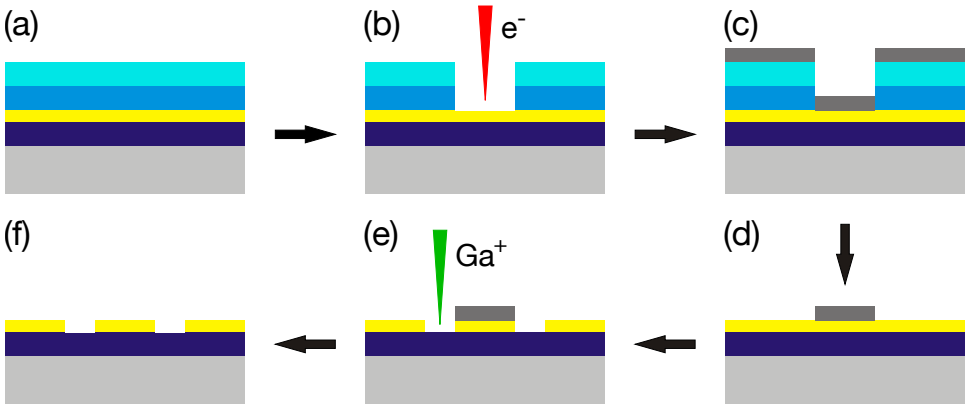


Figure 4.21. Schematic of a two-step eBL / FIB lithography process utilizing a nanopatterned metal film as a protective layer. (a) Spin-coated double layer electron resist on $BiFeO_3$ / $SrRuO_3$ / $SrTiO_3$, (b) electron beam lithography, (c) W sputter deposition, (d) lift off of electron resist, (e) focused ion beam lithography, and (f) chemical removal of W layer.

protects the oxide from the ion-beam tails without increasing the necessary milling depth. Furthermore, in addition to more effectively limiting damage to the oxide features caused by interaction with the ion-beam tails, the use of a patterned metal layer would enable the use of a thicker protective layer as it would not be necessary to mill through the metal film. The following section describes a two-step lithography process involving the use of FIB with an electron-beam patterned protective metal mask developed to produce $BiFeO_3$ nanostructures with limited ion damage.

Epitaxial $BiFeO_3$ nanostructures were fabricated by a combined electron-beam lithography (eBL) and FIB nanopatterning strategy which is depicted schematically in Figure 4.21. In the first step, a patterned metal hard mask was fabricated using electron-beam lithography. As before, to achieve a uniform resist coating, the 5 mm $\times$ 5 mm sample was bonded to a 3 inch Si wafer using photoresist A24620 followed by a 1 minute

bake on a hotplate at 100 °C. A double layer positive electron resist consisting of polymethyl methacrylate (PMMA) (950 PMMA A3) and a copolymer mixture of PMMA and 8.5% methacrylic acid (MMA(8.5)MAA) was spin-coated onto the $BiFeO_3$ film (Laurell WS-400B-6NPP/LITE/SC spin processor). The MMA(8.5)MAA bottom layer is more sensitive than the PMMA to a given electron dose and as a result, the bilayer resist typically enables better control of feature size and shape. The MMA(8.5)MAA layer was coated first at 4000 RPM followed by a 2 minute bake at 180 °C. The PMMA was then coated and baked with the same conditions. A total resist thickness of 730 nm was measured with a profilometer (Tencor Alpha Step 500). The nanopattern was transfered to the resist film by 30 kV eBL (Raith 150) with an aperture of 20 $\mu$m, a working distance (WD) of 7 mm, a dose of 220 $\mu C/cm^2$, and a step size of 6.4 nm. The exposed resist was developed with a 40 second soak in a 1:3 methyl isobutyl ketone (MIBK) / IPA solution followed by a thorough rinse in DIW. A 100 nm tungsten (W) layer was deposited through the resist mask by RF magnetron sputtering at room temperature (AJA Rapier system). Tungsten was used for the protective metal film since it can be removed via etching in hydrogen peroxide ($H_2O_2$) without damaging the oxide layer. This allowed the flexibility of producing heterostructures with or without a top electrode layer. The W film was deposited in a normal incidence geometry to reduce shadowing effects while depositing into the resist mask vias. To minimize the ballistic impact of the target atoms on the oxide surface, the W film was grown at a low RF power of 25 W and DC bias of 113 V with an Ar flowrate and pressure of 6 sccm and 5.0 mTorr.

Lift off was achieved by removal of the electron resist with acetone. Following lift off, two types of $BiFeO_3$ nanostructures were fabricated by FIB lithography (FEI Nova 600)

using a 28 pA beam of 30 kV $Ga^+$ ions. Fully isolated structures, where the $BiFeO_3$ layer surrounding the W islands was completely removed, and supported structures where the surrounding $BiFeO_3$ was imaged with a low ion-dose leading to a crystalline nano-island surrounded by amorphous oxide were produced. After FIB fabrication, the W mask was chemically removed by soaking overnight in a solution of 30% $H_2O_2$ in DIW.

Figure 4.22 shows SEM images of the W-protected $BiFeO_3$ sample after (a) eBL patterning of W layer and (b) FIB fabrication of W / $BiFeO_3$ nanostructures. Structures with square, rectangular, circular, and elliptical shapes and lateral dimensions of 1 $\mu$m, 750 nm, and 500 nm were produced as well as smaller square and rectangular shapes (with lateral sizes 400 nm and 200 nm). Square and rectangular objects were fabricated with sides aligned at 0°, 15°, 30°, and 45° with respect to the in-plane [010] direction. Supported nanostructures were located at the top left and bottom right and left corners of the nanostructure array. Following nanofabrication, a Pt alignment grid for nano-beam x-ray experiments was fabricated by optical lithography following the procedure outlined in Section 4.3.2.

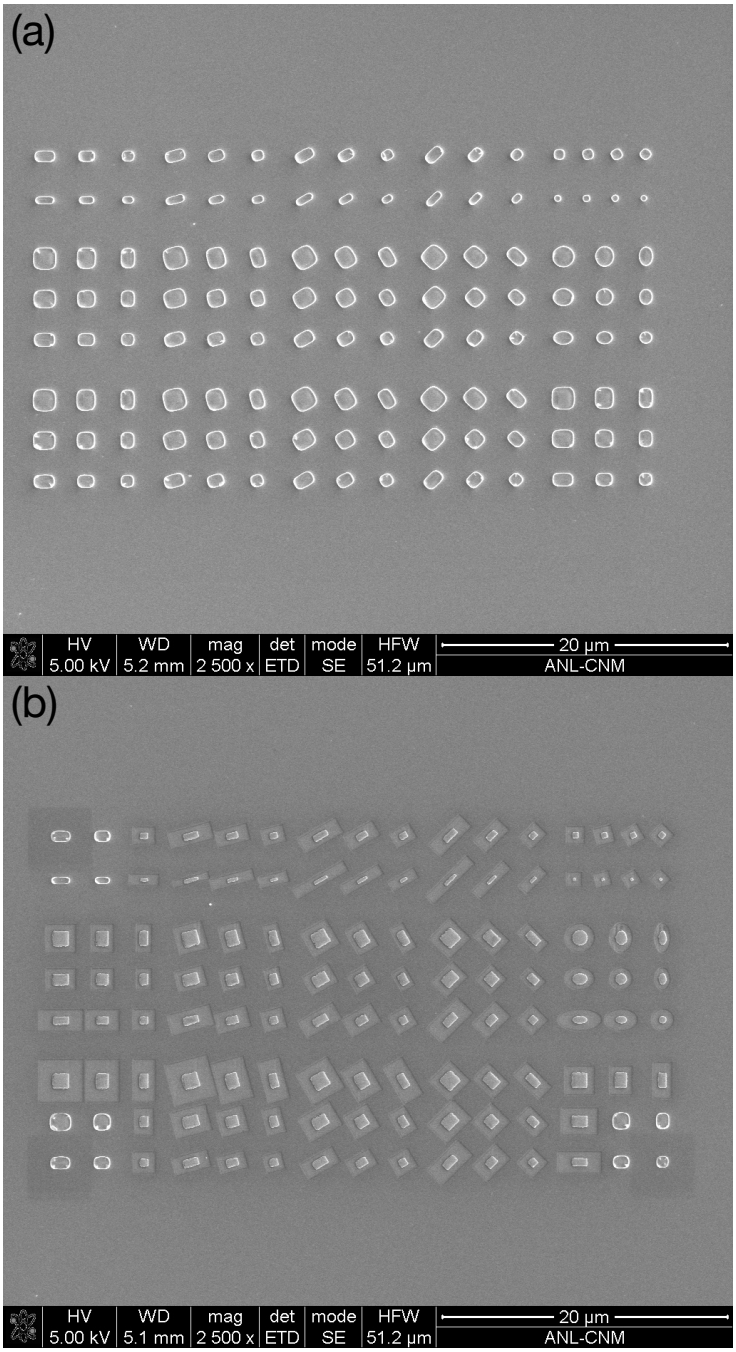


Figure 4.22. SEM images of the W-protected $BiFeO_3$ sample after (a) eBL patterning of W layer and (b) FIB fabrication of W / $BiFeO_3$ nanostructures. The W layer was subsequently removed by soaking in $H_2O_2$.

CHAPTER 5

# Nano-Beam X-Ray Studies of Epitaxial $BiFeO_3$ Nanostructures

Scanning x-ray nanodiffraction measurements of $BiFeO_3$ nanostructures were performed to study the local strain and lattice rotation distributions of epitaxial $BiFeO_3$ nanostructures with varied size, shape and planar orientation. Nanostructures were fabricated by the FIB-based strategies discussed in Section 4.3. Measurements were made of two Pt-protected samples: one unannealed and one annealed. For the W-protected sample, both fully isolated and supported nanostructures were characterized. These unprecedented results represent the first Hard X-ray Nanoprobe beam line diffraction measurements of planar and/or laterally nanostructured strained heteroepitaxial structures.

## 5.1. $BiFeO_3$ Nanodiffraction Experimental

Experiments were carried out at the Hard X-ray Nanoprobe (HXN) beam line operated jointly by the Center for Nanoscale Materials and the X-ray Sciences Division, and located at station 26ID-C of the Advanced Photon Source, Argonne National Laboratory [99]. The HXN is currently the highest resolution hard x-ray microscope in the world, providing an unparalleled nominal focused x-ray spot size of 30 nm at photon energies of $3 - 30$ keV. While soft x-ray based instruments can produce spot sizes of $\sim 15$ nm, the best resolution achieved by other hard x-ray microprobe instruments is $\sim 150$ nm at x-ray energies of $8 - 10$ keV. The Argonne Nanoprobe beamline was first activated (produced its first x-ray beam) on March 15, 2005, and the HXN instrument became operational in October of

2007. Full-scale user operations began in October of 2008. The first and (to-date) only publication to result from measurements at the Nanoprobe was released in July of 2009. Provis *et al.* used the nanoscale x-ray fluorescence mapping capability of the beamline to study the composition of fly ash geopolymers [100].

A schematic of the beam line optics and detectors used in scanning probe experiments at the Nanoprobe is shown in Figure 5.1. Photons were supplied by two collinear undulators (APS "Undulator A", $\lambda_u = 3.3$ cm) which were operated within the first harmonic (2.9 to 13.0 keV energy range). During all measurements, the APS operated in 24 singlet "Top-Up" mode, maintaining a constant storage ring current of 102.4 mA. The horizontal beam size was defined by a pair of water-cooled high heat load (HHL) horizontal focusing mirrors and a beam-defining aperture (BDA). The BDA is positioned at the focus of the mirror system (40 m from the x-ray source) and was typically closed to 0.025 $\mu$m. A liquid nitrogen ($LN_2$) cooled Si (111) double crystal HHL monochromator was used to select a x-ray energy of 10 keV from the white-beam undulator radiation. There was no beam manipulation in the vertical direction in order to preserve the full brilliance and coherence of the undulator source.

A hard x-ray zone plate optic located 75 m from the x-ray source was used to focus the 10 keV photons to a sub-100 nm x-ray beam spot on the sample surface. A circular order-sorting aperture (OSA) located between the zone plate and the sample was used to select the first order focused beam. A focused spot size of approximately 70 nm was achieved during February 2009 for measurements of the Pt-protected $BiFeO_3$ nanostructures. In subsequent measurements of W-protected nanostructures in June 2009, a beam spot of approximately 40 nm was achieved. The typical zone plate efficiency was $\sim$ 5%. In

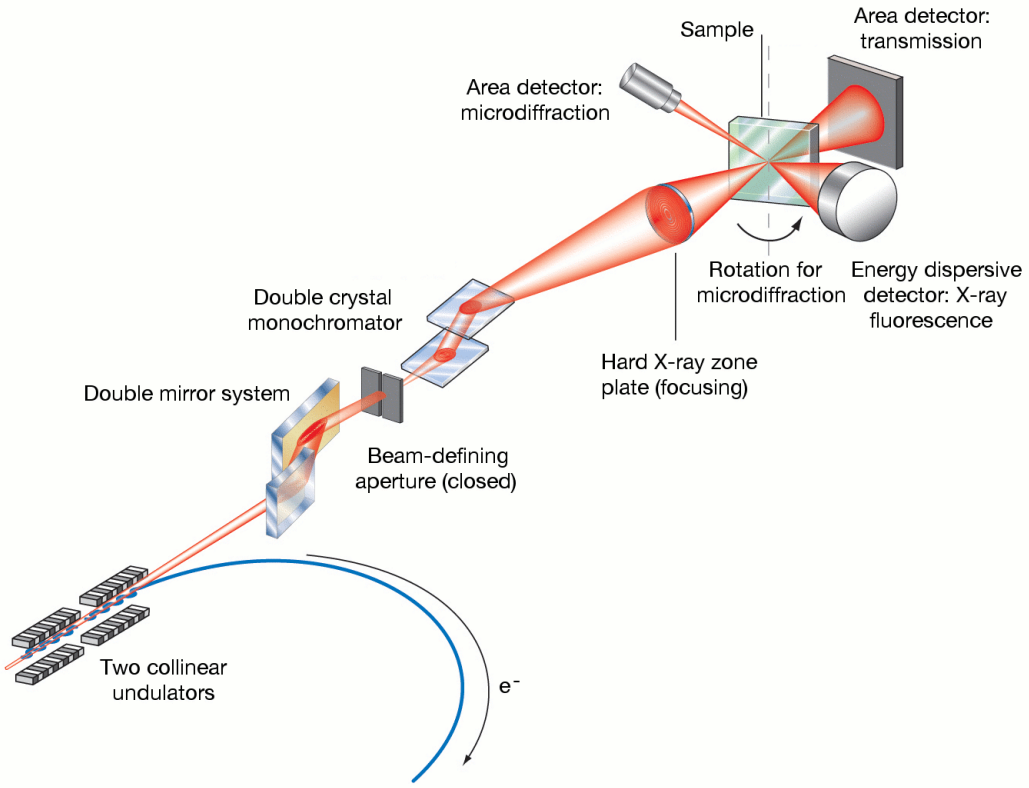


Figure 5.1. Beamline optics and detectors used in scanning probe experiments at the Hard X-ray Nanoprobe at APS/CNM station 26ID-C, after [99]. Note that the sample rotation axis is vertical, which results in a horizontal diffraction geometry. In the diagram, the diffraction detector angle is exaggerated and the sample surface is rotated toward the inboard direction. For diffraction measurements, the sample is rotated toward the outboard direction. In addition to the inboard fluorescence detector (shown), an outboard detector (not shown) can be used to monitor fluorescence in the microdiffraction geometry where the sample faces the outboard direction. The Nanoprobe instrument can also operate in a full-field transmission mode (not shown).

all cases, diffraction measurements were performed at the $BiFeO_3$ (002) Bragg condition where the x-ray footprint on the sample is elongated by a factor of $1/\sin(\theta)$ in the direction parallel to the scattering plane. At an incident x-ray energy of 10 keV, the (002) Bragg peak was located at $\theta = 17.7°$ and the beam footprint was elongated by a factor of about

three. Samples were mounted on a X-Y-Z translation, tilt/rotation stage used to position the sample in the focused beam and to align the sample for diffraction measurements.

Positioning and active vibration control of the Nanoprobe Instrument are provided by a laser Doppler displacement meter (LDDM) based encoder system [101, 102]. The LDDM encoder measures the FZP optic position relative to the absolute sample position to within 1 nm, and provides lock-in differential control of the sample-optic position within 3 - 5 nm up to 100 Hz. Fine-motion of the focusing optics module (FOM), which includes the FZP optic and the OSA, is provided by high resolution vertical and horizontal piezoelectrically driven flexure stages. For further details of the optomechanical design of the HXN instrument, see references [101] and [102].

Spatially resolved diffraction maps were made with 2D lateral X-Y scans of the beam position across the sample. This was achieved by scanning the FOM within the unfocused parallel x-ray beam as the sample positioning module (SM) was only used for coarse translation and alignment. The focusing optic can be scanned approximately $\pm 50\mu$m within the parallel beam without significantly affecting the intensity of the focused beam. The scattering geometry and FOM spatial coordinates are depicted in Figure 5.2. The beam width in FOM X projected a footprint that was $1/\sin(\theta)$ larger on the sample surface. Furthermore, a translation of $\Delta$x in FOM X corresponded to movement of $\Delta \mathrm{x}/\sin(\theta)$ on the sample, whereas there was a one-to-one correspondence between translation in FOM Y and the resulting movement of the bean on the sample. Since FOM Z is along the incident beam direction, translations in FOM Z changed the distance between the sample and the optic and and therefore affected only the focus. However, a translation of $\Delta$x in FOM X also led to a change of $\Delta \mathrm{x}/\tan(\theta)$ in the sample-optic distance. For fine motion

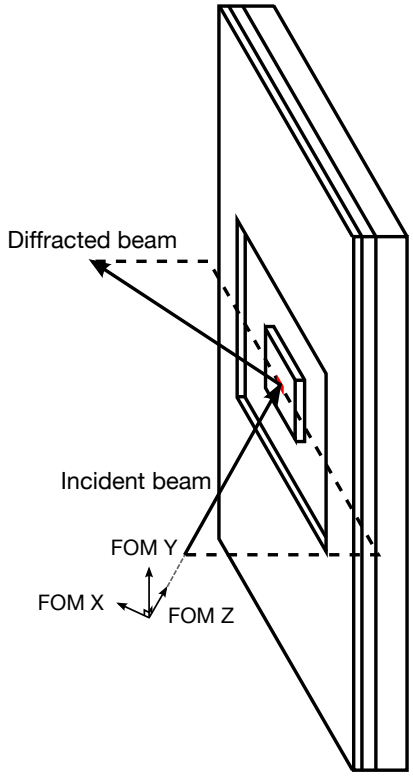


Figure 5.2. Nano-beam scattering geometry and coordinate system of the focusing optics module (FOM). FOM Z moves along the incident beam direction.

during scanning, this change was small compared to the $\sim$ 10 $\mu$m depth of focus of the optic and was therefore ignored. However, for translations of more than a few microns, (e.g. from one nanostructure to another) movements of FOM X were accompanied by translations of FOM Z in order to maintain focus. Diffracted x-rays were collected at each lateral position with a high resolution (1:1 fiberoptic ratio with 38 lp/mm resolution) CCD area detector (Princeton Instruments, PIXIS-XF: 1024F). The PIXIS detector has a 1024 $\times$ 1024 array of 13 $\mu$m $\times$ 13 $\mu$m pixels and was placed at a distance of 70 cm from the sample. Additionally, during the February 2009 measurements of the Pt-protected sample, x-ray fluorescence was measured concurrently using a single element

silicon drift detector (SII Vortex-EM). The XRF detector was not available during the June 2009 measurements of the W-protected nanostructures.

Diffraction data were analyzed with MATLAB code based on routines developed by Martin Holt from the X-Ray Microscopy Group at Argonne's Center for Nanoscale Materials. The raw CCD images (hdf format) were read by MATLAB and corrected for dark counts (i.e. the CCD reading with no x-rays), and zingers (hot pixels due to cosmic rays, $\alpha$ particle decay and other spurious radioactive events). The dark correction was found to be sufficient to flatten the background in the CCD images. The zinger correction was modified from code written by and obtained from Paul Fenter (Argonne). For pixels with a value above a defined threshold, the value was replaced by the mean taken from the eight nearest neighbors. Nearest neighbors above the threshold are excluded from the mean. A region of interest (ROI) was then background corrected by subtracting the per pixel integrated intensity of a background region surrounding the ROI. In all cases the background was calculated from a 100 pixel wide frame around the region of interest. The ROI window was selected to be centered on and include the entire diffracted spot. The smallest ROI possible was selected such that a map of the integrated background intensity showed no variation corresponding to the isolated $BiFeO_3$ object in the integrated ROI intensity. The background corrected ROI image was then used to calculate the integrated diffraction intensity, $2\theta$ center of mass (COM), and $\chi$ COM. The $2\theta$ and $\chi$ COM values were calculated from weighted averages of the x and y pixel indices, respectively, where the indices were weighted by the intensity recorded by each pixel. The COM values were subsequently converted from pixels into degrees.

## 5.2. Pt / $BiFeO_3$ Nanodiffraction Results and Discussion

Two samples with Pt-protected $BiFeO_3$ nanostructures were characterized with x-ray nanodiffraction in February 2009. Both samples were fabricated from the same 10 mm × 10 mm epitaxial 40 nm thick $BiFeO_3$ film on (90 nm) $SrRuO_3$ / $SrTiO_3$ (001). Prior to nanostructure fabrication the thin film sample was diced into four 5 mm × 5 mm pieces. The unannealed sample is the same as that shown in Figure 4.19, while the annealed sample contained a series of rectangular nanostructures 500 nm × 400 nm, 300 nm, 200 nm and 100 nm in size with edges aligned at 15° and 60° relative to the in-plane [010] direction. The sample was annealed for 1 hour in a tube furnace at 650 °C in flowing $O_2$ prior to x-ray experiments. The nanodiffraction measurements were performed in air.

The as-fabricated Pt / $BiFeO_3$ nanostructures were found to be heavily damaged. Figure 5.3 (a) shows a coarse map of the integrated $BiFeO_3$ (002) diffraction intensity from six rectangular nanostructures. From left to right and top to bottom, they are 1 $\mu$m × 1 $\mu$m, 750 nm × 1 $\mu$m, 1 $\mu$m × 750 nm, 750 nm × 750 nm, 1 $\mu$m × 500 nm, and 750 nm × 500 nm. The objects appear as dark regions in the diffracted intensity map, indicating that the nanostructures did not contain any detectable volume of (001) oriented $BiFeO_3$. The structure of the Pt-protected nanostructures, including objects as large as 1 $\mu$m × 1 $\mu$m, was at best markedly altered after FIB fabrication. This was consistent with the TEM result from a 500 nm × 500 nm square discussed in Section 4.3.2 which found that the top 70% of the film was amorphous. Additionally, the spaces between adjacent columns of nanostructures were observed to have reduced diffracted intensity compared to the spaces between rows. The secondary electron contrast was similar in a (b) SEM image of the same nanostructures. The contrast in both images mirrors the ion-beam

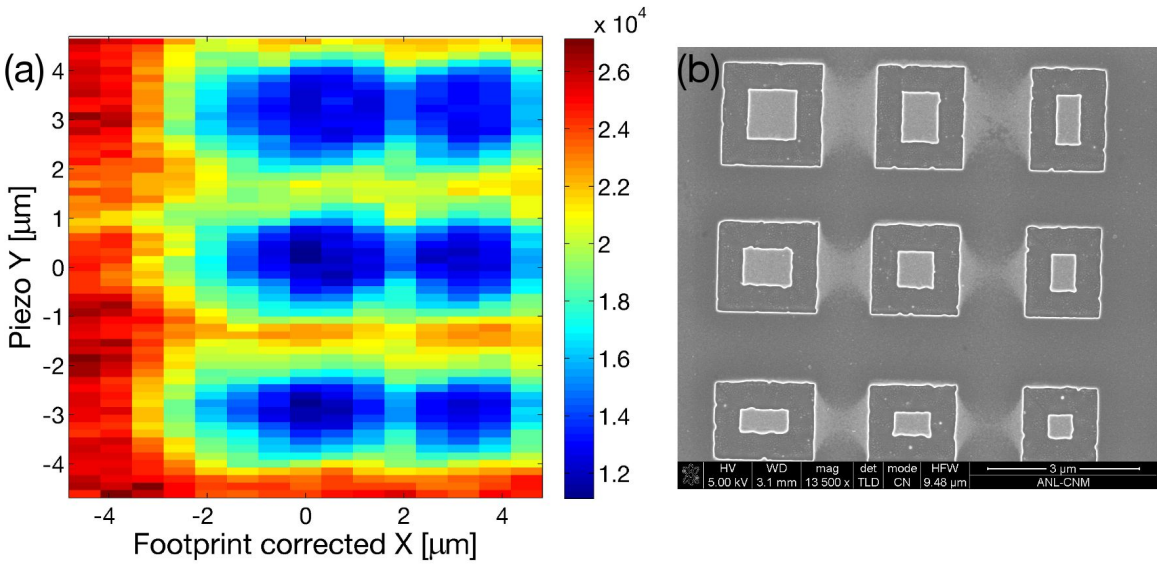


Figure 5.3. Nanodiffraction result for Pt / $BiFeO_3$ nanostructures before annealing. A coarse map of (a) the integrated $BiFeO_3$ (002) diffraction intensity from six rectangular objects shows no diffraction from the nanostructures. Reduced diffracted intensity in the spaces between adjacent columns mirrors the secondary electron contrast in a (b) SEM image of the same nanostructures.

path during fabrication. The structures were fabricated one row of three at a time in a serial fashion with multiple passes, such that the ion-beam moved between structures with a row multiple times during milling. Beam deflection was used to move between objects in a single row, while translations of the sample stage were used to move from one row to the next. The correlation between the beam path and the observed diffraction and SEM contrasts indicates that insufficient blanking of the beam during milling may be responsible for some of the observed damage.

In contrast to the unannealed Pt / $BiFeO_3$ nanostructures, diffraction was observed from annealed objects with lateral dimensions as small as 200 nm. Nanodiffraction results are shown in Figures 5.4 and 5.5 for two 500 nm × 400 nm Pt / $BiFeO_3$ nanostructures

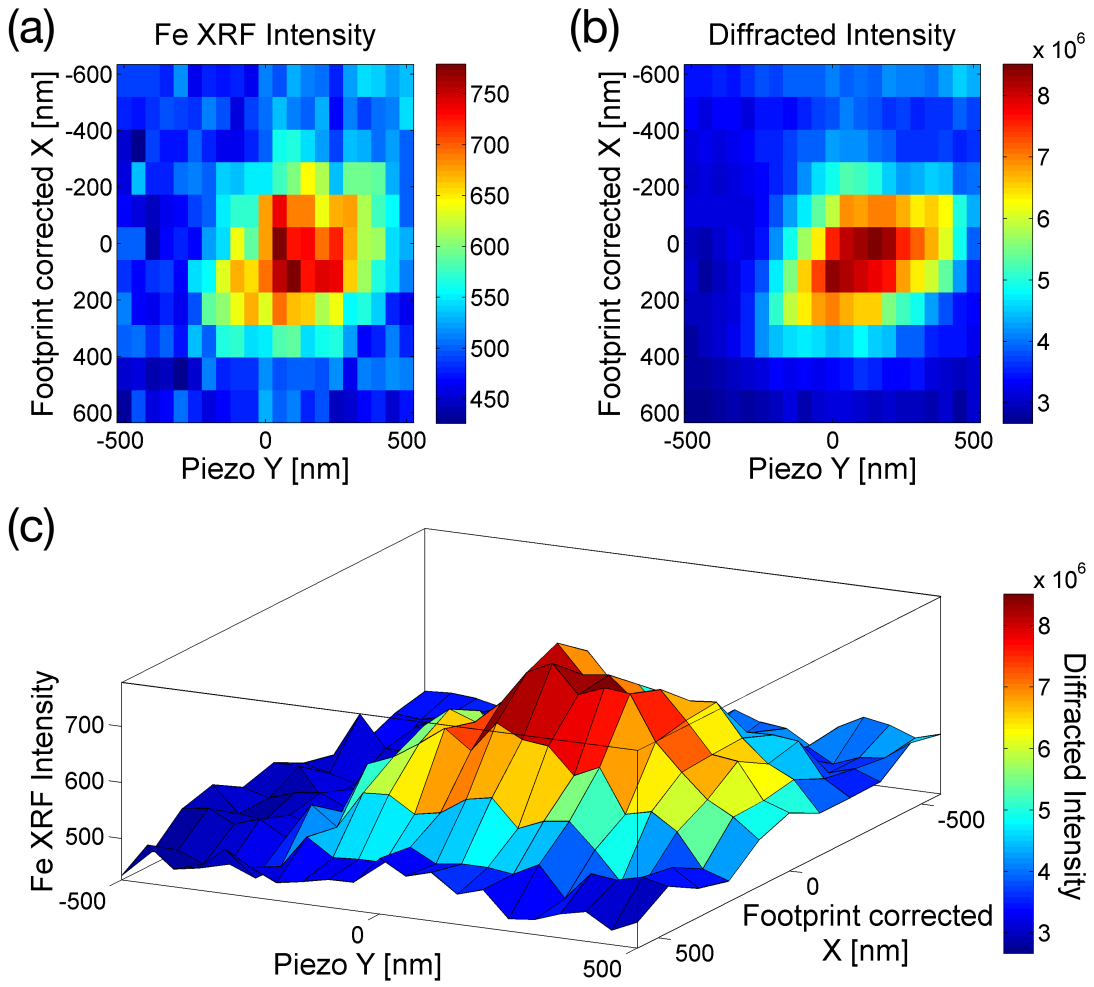


Figure 5.4. Nano-beam x-ray results for annealed a 500 nm × 400 nm Pt / $BiFeO_3$ nanostructure with edges aligned 15° relative to the in-plane [010], [100] directions. Fe K$\alpha$ XRF intensity (a) and integrated $BiFeO_3$ (002) diffracted intensity (b) are superimposed (c) with the height and colormap corresponding to Fe K$\alpha$ and diffraction, respectively.

with edges aligned 15° and 60°, respectively, relative to the in-plane [010] crystallographic direction. In both scans the footprint of the beam on the sample was approximately 70 nm in Y and 230 nm in X. Data were acquired with 2D scans of FOM Y (inner loop) and FOM X (outer loop). The FOM Y step size was 50 nm in the scans of both objects. The

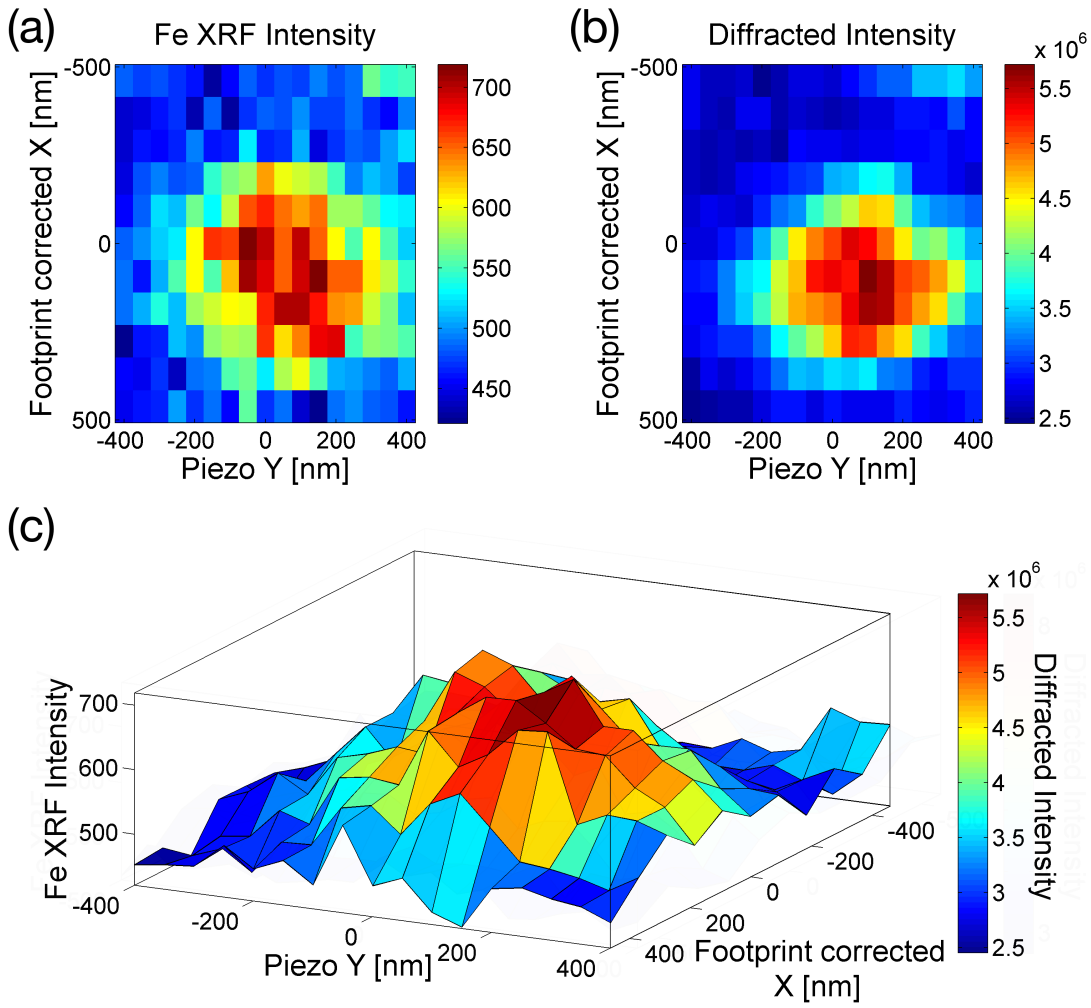


Figure 5.5. Nano-beam x-ray results for annealed a 500 nm × 400 nm Pt / $BiFeO_3$ nanostructure with edges aligned 60° relative to the in-plane [010], [100] directions. Fe K$\alpha$ XRF intensity (a) and integrated $BiFeO_3$ (002) diffracted intensity (b) are superimposed (c) with the height and colormap corresponding to Fe K$\alpha$ and diffraction, respectively.

FOM X step sizes for the 15° and 60° objects were 35 nm and 28 nm respectively, and the corresponding footprint corrected step sizes in X were 115 nm and 92 nm. A 60 second exposure time was used at each point in both sets of scans leading to a total scanning time of 4 hours and 3.5 hours for the 15° and 60°, respectively.

Panels (a) and (b) of Figure 5.4 contain the measured Fe K$\alpha$ XRF and $BiFeO_3$ (002) integrated diffracted intensity maps of the 15° nanostructure. Likewise, the XRF and diffraction maps of the 60° nanostructure are shown in Figure 5.5 (a) and (b). For both nominally 500 nm × 400 nm nanostructures, the Fe K$\alpha$ XRF maps provide a measure of the lateral extent of the $BiFeO_3$ nanostructures. The XRF maps suffer from poor counting statistics and high background as the sample-detector distance and takeoff angle were large (3-4 cm, $\alpha > 20°$) and the detector was not well collimated. However, the observed size and shape of both objects are as expected allowing for some broadening due to the the x-ray beam size. The $BiFeO_3$ (002) diffraction maps of both nanostructures appear similar to the corresponding Fe XRF maps. For each nanostructure, the fluorescence and diffraction maps exhibit higher intensity in the center of the object which falls off over a distance of 2-3 pixels. This indicates that within the resolution of the measurement, there does not appear to be significant variation in the crystalline volume across the lateral span of either object. This is illustrated in Figure 5.4 (c) and Figure 5.5 (c) which show the integrated $BiFeO_3$ (002) diffracted intensity overlayed on top of the Fe K$\alpha$ XRF intensity such that the the height and colormap correspond to Fe K$\alpha$ and diffraction, respectively. Plotted in this way, the intensity distributions appear comparable. In addition, the sets of maps for the different nanostructures appear similar within the resolution of the measurement, although the difference in planar orientation is clear.

The diffraction maps of both objects were observed to have an intensity in the trench regions where the $BiFeO_3$ had been removed by FIB. This persisted in the integrated intensity even though the CCD images were background corrected as described in Section 5.1. While this was surprising, examination of the diffraction CCD detector images

revealed a likely source of this extra intensity. Figure 5.6 shows background corrected CCD images of the $BiFeO_3$ (002) diffraction spot from an (a) unpatterned area where $BiFeO_3$ remains (10 $\mu$m from the trench) and a trench area (b) where the $BiFeO_3$ had been milled away. In the images, the horizontal direction corresponds to $2\theta$ (increasing from left to right) and the vertical direction corresponds to $\chi$. The beating observed in the intensity pattern shown in (a) was due to thickness fringes from the 90 nm thick $SrRuO_3$ layer. In both images of the $BiFeO_3$ (002) Bragg condition, a narrow streak of intensity appears diagonally across the image. The intensity of this streak appeared to be superimposed on the expected "doughnut" of intensity from the film and remained fairly constant, although it was not fully removed by subtracting image (b) from image (a). Ideally the $BiFeO_3$ (002) diffraction image from the film should appear as a "doughnut" of intensity corresponding to either the angular acceptance width of the film or the $\sim 0.3^\circ$ divergence of the incident beam, whichever is smaller. No discernible pattern of intensity was expected at the $BiFeO_3$ (002) condition for the trench regions. Therefore, presence of the diagonal streak was unexpected both for the images on the film and in the trench. However, the observation of the streak persisting in the trench region suggested that it was not due to diffraction from the $BiFeO_3$ layer. The source of this extra intensity was undetermined, although it was found to remain fixed with respect to the doughnut pattern (i.e. moved with the doughnut) during scans of both sample $\theta$ and detector $2\theta$. It was not observed when aligned on the $SrTiO_3$ (002) substrate reflection, which is shown in Figure 5.6 (c), or the $SrRuO_3$ (002) reflection (not shown). The $SrTiO_3$ image in Figure 5.6 (c) resembles the pattern expected for a single crystal Bragg reflection as illustrated in Figure 3.3 (b). The narrow slice in $2\theta$ (minus the central region blocked

the $0^{th}$ order beam stop) appears broadened somewhat due to detector saturation. Since the diagonal streak appeared to move with the identified diffraction from the sample, the extra intensity appeared to be coming from the sample, although the source was not determined. Possible sources include diffraction from (001) oriented grains of Pt which could appear both outside and inside the trench regions (due to redeposition of milled material) or stray peak from the substrate due to multiple reflection.

The images shown in Figure 5.6 were acquired with with 5 second exposures with the BDA open such that the beam footprint in X was approximately 900 nm. This condition was used while investigating the origin of the diagonal intensity streak. For the data shown in Figures 5.4 and 5.5, the BDA was closed (25 nm) and the exposure time was increased to 60 seconds. Diffraction CCD images from the scan of the 15° nanostructure are shown in Figure 5.7. An image from the center of the nanostructure is shown both with and without background correction in (a) and (b), respectively. The same is shown in (c) and (d) for an image from the trench region. The raw images show the entire 1024 × 1024 CCD reading while the corrected images show a 512 × 512 ROI. Comparing the $BiFeO_3$ (002) diffraction spot in Figure 5.7 (a) to the spot from the unpatterned film shown in Figure 5.6 (a) and using the diagonal streak as a fixed reference, the diffraction spot from the nanostructure appears shifted toward smaller pixel number (smaller $2\theta$). This indicates that the annealed nanostructure has a larger out-of-plane lattice constant than the unpatterned film, which may be due to chemically induced strain resulting from oxygen vacancies or cation nonstoichiometry in the recrystallized nanostructure [103, 104]. In both sets of images, a low signal-to-background ratio was observed. For the image from the nanostructure, while the average pixel intensity in the diffraction spot

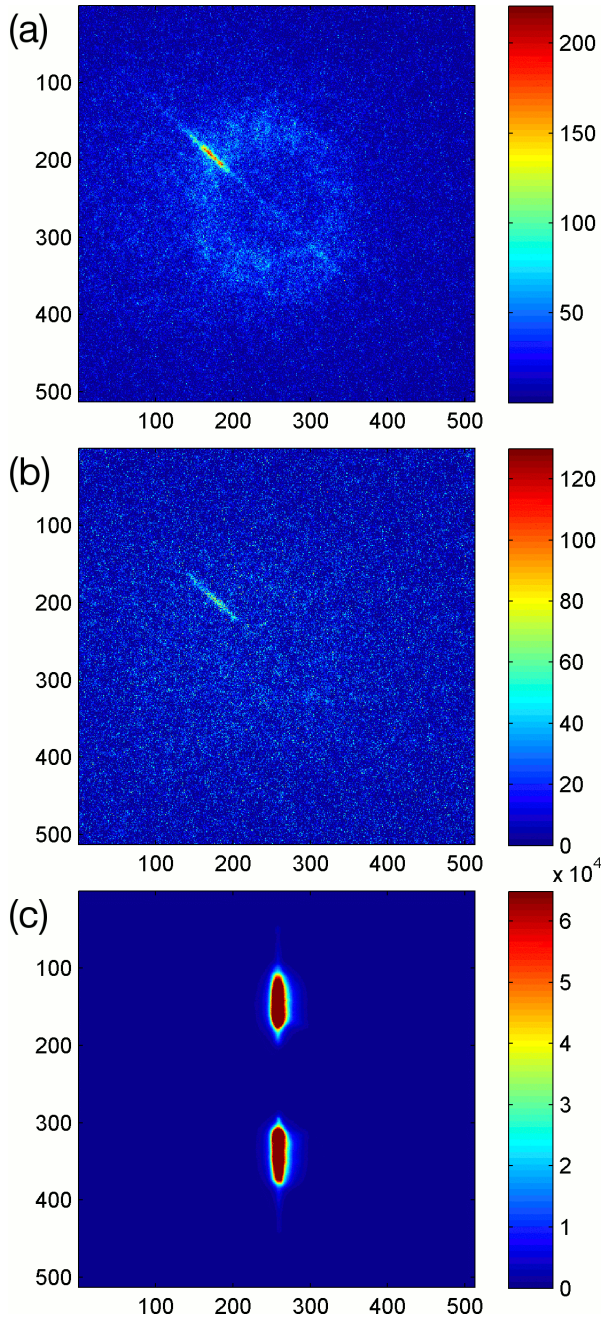


Figure 5.6. Diffraction CCD detector images from the Pt / $BiFeO_3$ sample. A diagonal streak of intensity was seen in $BiFeO_3$ (002) images of areas where $BiFeO_3$ remains (a), and where $BiFeO_3$ has been milled away (b). The streak was not observed when aligned on the $SrTiO_3$ (002) substrate reflection (c).

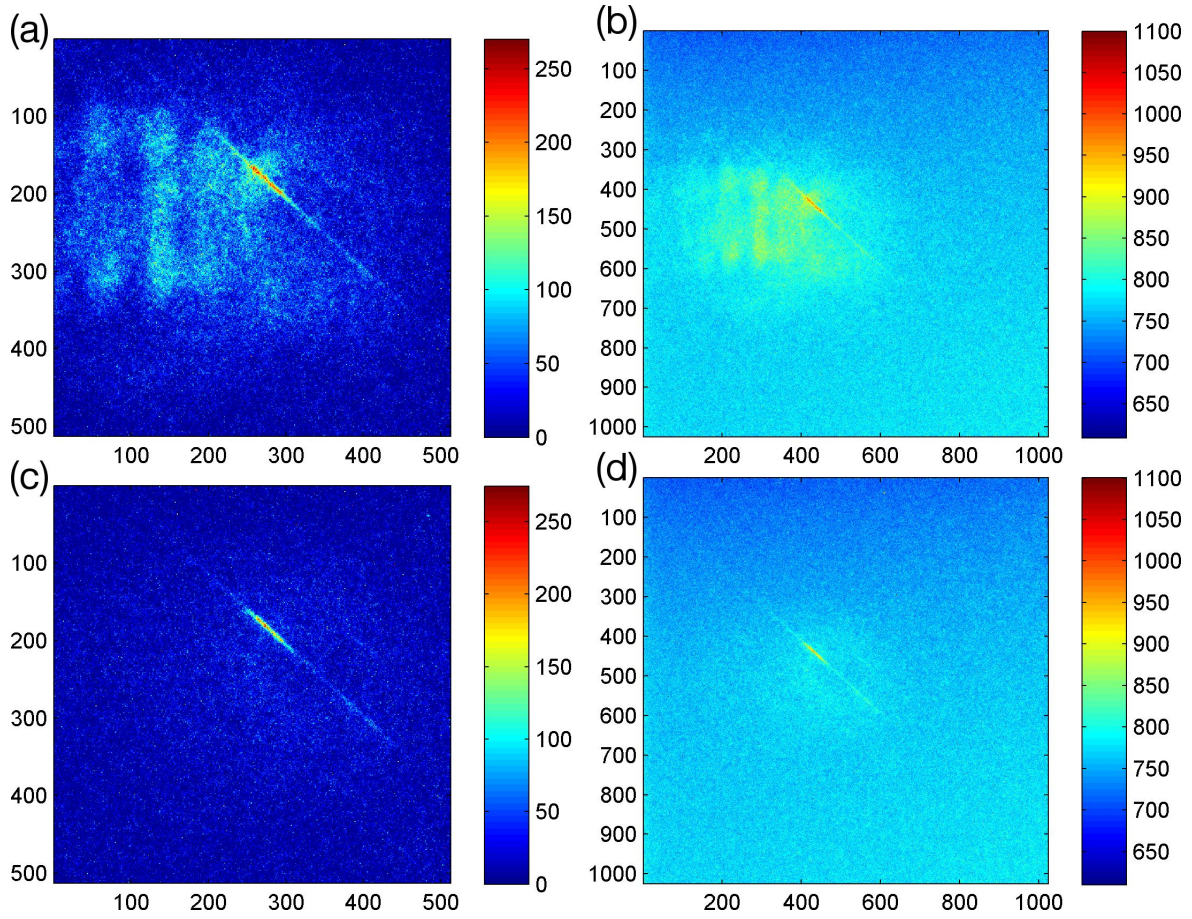


Figure 5.7. Background corrected [(a) and (c)] and raw [(b) and (d)] $BiFeO_3$ (002) diffraction CCD images from a 500 nm × 400 nm Pt / $BiFeO_3$ nanostructure [(a) and (b)] and the trench surrounding it [(c) and (d)].

is approximately 100 counts above background (observed in the background corrected image), the average pixel intensity of the background is on the order of 800 counts. The poor signal-to-background and the presence of the unexplained additional intensity streak complicated reliable analysis of the $2\theta$ and $\chi$ distributions of intensity in the CCD-collected diffraction data. Information about local strain or lattice rotation was therefore not extracted from the Pt-protected $BiFeO_3$ data. However, the nanodiffraction results

from the annealed nanostructures represented a clear improvement in crystallinity over those from the unannealed structures.

### 5.3. W-Protected $BiFeO_3$ Nanodiffraction Results and Discussion

Diffraction measurements of W-protected $BiFeO_3$ nanostructures were performed during a June 2009 beamtime at 26ID-C. The nanostructures, which are shown in Figure 4.22, were fabricated from the 37 nm $BiFeO_3$ described in Table 4.2 and Figures 4.15 and 4.16, using a protective patterned W mask as detailed in Section 4.3.3. The sample was characterized as-fabricated with no annealing. Measurements were made on both fully isolated and low ion-dose supported nanostructures as well as a comparably sized region of the unpatterned film. Nanodiffraction measurements were performed with He gas flowing in the Nanoprobe Instrument chamber which houses the FOM and SM.

The focused beam size was approximately 40 nm and the resulting footprint on the sample was 40 nm in Y and 130 nm in X. Data were collected with 2D scans of FOM Y (inner) and FOM X (outer) with 30 nm steps in FOM Y and 10 nm steps in FOM X. The resulting footprint corrected step size in X was 32 nm. An exposure time of 10 seconds was used at each point in the scans of the nanostructures, while 5 second exposures were used in the scan of the unpatterned film. A strong $BiFeO_3$ (002) signal was observed from all measured structures, and the diffraction maps were found to be reproducible in repeated back-to-back scans of the same object, indicating that there were no detectable x-ray induced changes in the local structure of the sample over the course of a typical data acquisition (4 to 8 hours). Nanodiffraction results for a series of W-protected $BiFeO_3$ nanostructures are shown in Figures 5.8–5.11. Results from a region of the unpatterned

film are shown in Figure 5.12. In each figure, the maps of integrated $BiFeO_3$ (002) intensity (a), $2\theta$ center of mass (b), and $\chi$ center of mass (c) were calculated from CCD images collected at each point in a 2D lateral scan.

Figure 5.8 shows the results for a 1 $\mu$m $\times$ 500 nm fully isolated structure where the long axis of the rectangular object was oriented along the [010], parallel to the higher resolution Y scanning direction. Some contrast was observed in the integrated $BiFeO_3$ (002) intensity map within the nanostructure, particularly around the edges. A decrease in intensity near the edges was expected due to both sidewall ion damage and beam size effects. The latter should have a larger observed effect in the X (vertical in the image) direction due to the larger beam footprint and the reduced effective film thickness near the edge (due to the incident angle $\theta$). These effects were expected to be symmetric for the top and bottom edges, as well as for the left and right edges. However, the intensity contrast was neither confined to the near-edge regions, nor was it top-bottom or left-right symmetric. Some of the observed contrast therefore results from variation in either the local structure factor or scattering volume across the nanostructure. This variation may be due to static disorder within the unpatterned film or damage incurred during FIB fabrication.

Considerable variation was observed in the $2\theta$ and $\chi$ COM maps even in regions of uniform integrated intensity. The total peak-to-peak changes were $\Delta(2\theta) = 0.065^\circ$ and $\Delta\chi = 0.051^\circ$ corresponding to changes of $> 50$ detector pixels (as each pixel has an angular size of $0.001^\circ \times 0.001^\circ$). The average $2\theta$ COM position was $\bar{2\theta} = 35.224^\circ$ indicating a mean out-of-plane lattice constant of 4.098 Å. This was determined from a weighted average of the $2\theta$ COM values where the corresponding integrated intensity values were

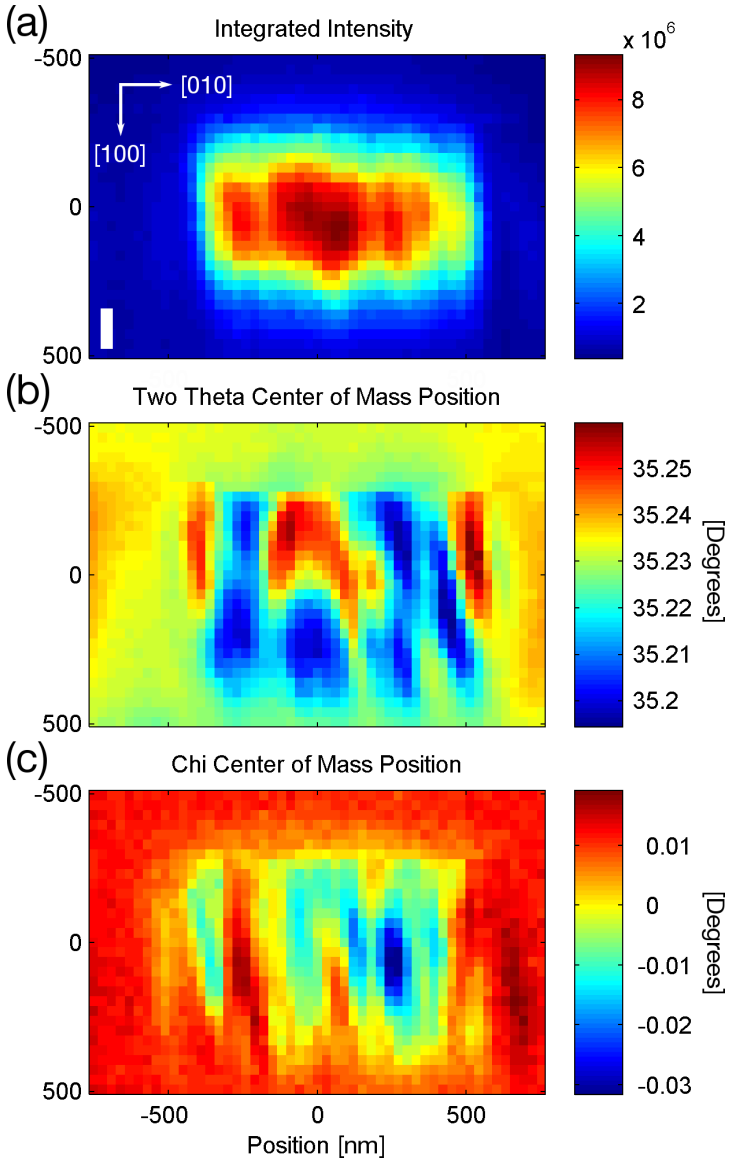


Figure 5.8. Nanodiffraction results from a 1 $\mu$m $\times$ 500 nm isolated $BiFeO_3$ nanostructure. Integrated $BiFeO_3$ (002) intensity (a), $2\theta$ center of mass (b), and $\chi$ center of mass (c) were calculated from CCD images collected at each point in a 2D lateral scan with 30 nm steps. The crystallographic orientation is indicated in the top left of (a). The white bar in (a) represents the x-ray footprint size.

used as weights. The variation in the out-of-plane lattice constant was calculated to be $\Delta d/d = 1.8 \times 10^{-3}$. The distribution of contrast in the $2\theta$ COM map indicated the presence of an inhomogeneous strain field characterized by domains with irregular size ($\sim$100-300 nm) and shape.

Similar diffraction results were obtained for an isolated 500 nm $\times$ 500 nm square structure with edges along the [100] and [010] directions and an isolated 1 $\mu$m $\times$ 500 nm rectangular object with the long axis parallel to the [100]. The diffraction maps for these two nanostructures are shown in Figures 5.9 and 5.10. For the square object, the peak-to-peak COM changes were $\Delta(2\theta) = 0.047^\circ$ and $\Delta\chi = 0.028^\circ$. For the [100] oriented rectangle, the peak-to-peak COM changes were $\Delta(2\theta) = 0.070^\circ$ and $\Delta\chi = 0.052^\circ$. While the total variation in the COM values are smaller for the square nanostructure compared to either of the isolated rectangular structures, they are of the same order of magnitude. Furthermore, the average $2\theta$ COM position for both the square and [100] oriented rectangular nanostructures was $\bar{2\theta} = 35.233^\circ$, and the corresponding mean out-of-plane lattice constant was 4.097 Å, which is in close agreement with that of the [010] oriented rectangle. The variation in the average out-of-plane lattice constant was $\Delta d/d = 1.3 \times 10^{-3}$ for the 500 nm square and $\Delta d/d = 1.9 \times 10^{-3}$ for the 1 $\mu$m $\times$ 500 nm rectangle, which are both similar to that from the [010] oriented isolated rectangle.

Figure 5.11 shows the results from a supported 1 $\mu$m $\times$ 500 nm rectangular object oriented with the long axis parallel to the [100] direction. The integrated intensity drop-off near the edges was observed over a smaller lateral depth compared to the isolated nanostructures, which indicates reduced sidewall damage in the supported structure. This was not surprising given the lower ion dose that was used to fabricate the supported

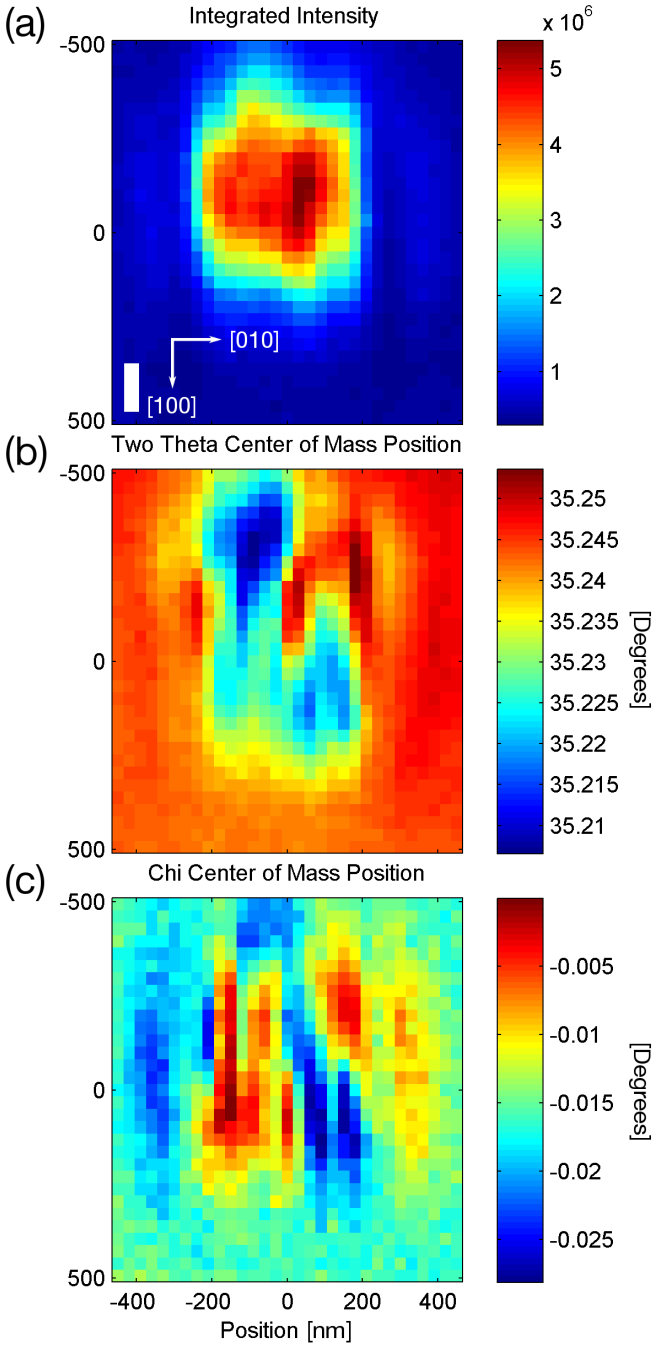


Figure 5.9. Nanodiffraction results from a 500 nm × 500 nm isolated nanostructure showing integrated $BiFeO_3$ (002) intensity (a), $2\theta$ center of mass (b), and $\chi$ center of mass (c). The crystallographic orientation and x-ray footprint are shown in the bottom left of (a).

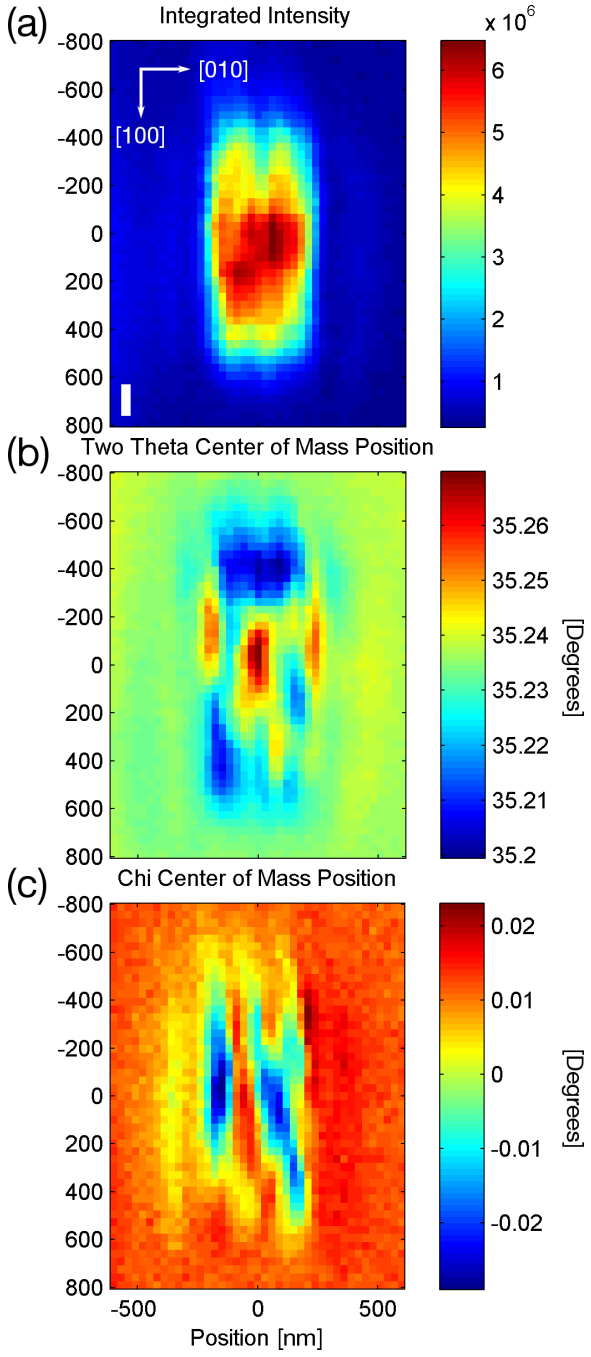


Figure 5.10. Nanodiffraction results from a 1 $\mu$m $\times$ 500 nm isolated nanostructure showing integrated $BiFeO_3$ (002) intensity (a), $2\theta$ center of mass (b), and $\chi$ center of mass (c). The crystallographic orientation and x-ray footprint are shown in the top and bottom left of (a).

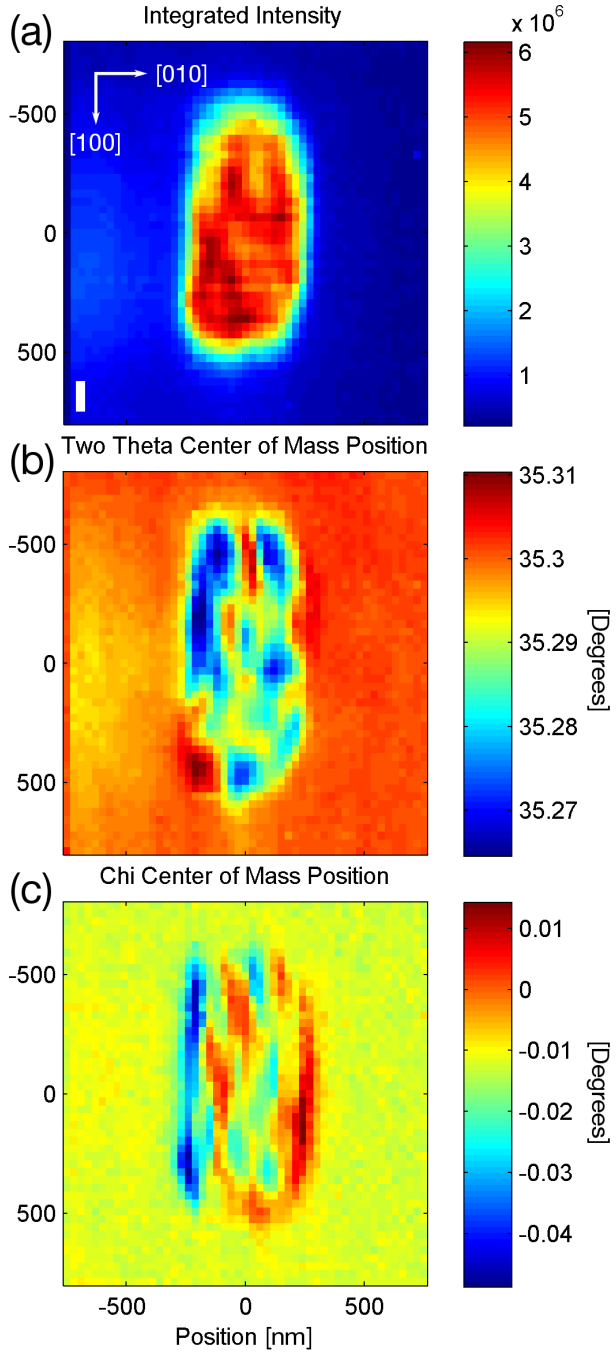


Figure 5.11. Nanodiffraction results from a 1 $\mu$m $\times$ 500 nm supported nanostructure showing integrated $BiFeO_3$ (002) intensity (a), $2\theta$ center of mass (b), and $\chi$ center of mass (c). The crystallographic orientation and x-ray footprint are shown in the top and bottom left of (a).

nanostructure. The $2\theta$ and $\chi$ COM maps were qualitatively similar to those obtained for the isolated structures, and the peak-to-peak COM changes were $\Delta(2\theta) = 0.046°$ and $\Delta\chi = 0.063°$. However, the average $2\theta$ COM position was $\bar{2\theta} = 35.291°$, and the corresponding mean out-of-plane lattice constant was 4.090 Å. This represents a difference on the order of 60 detector pixels between the average $2\theta$ COM positions of the supported and isolated nanostructures. The corresponding mean out-of-plane lattice constant of the supported structure was 0.2% smaller than that of the isolated nanostructures. The variation in out-of-plane lattice constant of the supported structure was $\Delta d/d = 1.3\times10^{-3}$.

Nanodiffraction results from a 1.6 $\mu$m $\times$ 1.5 $\mu$m region of the unpatterned film are shown in Figure 5.12. The data were taken from an area 14 $\mu$m from the pattern array. The peak-to-peak variation in the integrated intensity was approximately $\pm$20%, which was similar to that observed within the isolated and supported nanostructures (neglecting the near-edge drop-off). This suggests that the observed intensity contrast within the W-protected nanostructures may originate from variation in the local structure factor of the film, rather than damage incurred during FIB fabrication. The maps of $2\theta$ and $\chi$ COM were observed to be qualitatively similar to those obtained from the patterned structures. Both COM maps showed inhomogeneous contrast with regions of varied size and irregular shape. However, the peak-to-peak variation in the COM positions were $\Delta(2\theta) = 0.024°$ and $\Delta\chi = 0.015°$, which are smaller than the corresponding values for the nanostructures by a factor of 2-4. The variation in the out-of-plane lattice constant, $\Delta d/d = 6.5 \times 10^{-4}$ is also smaller than that of the nanostructures by at least a factor of 2.

The variation in $2\theta$ and $\chi$ observed in each of the W-protected $BiFeO_3$ nanostructures and the unpatterned film region is collected in Table 5.1. While the observed contrast in

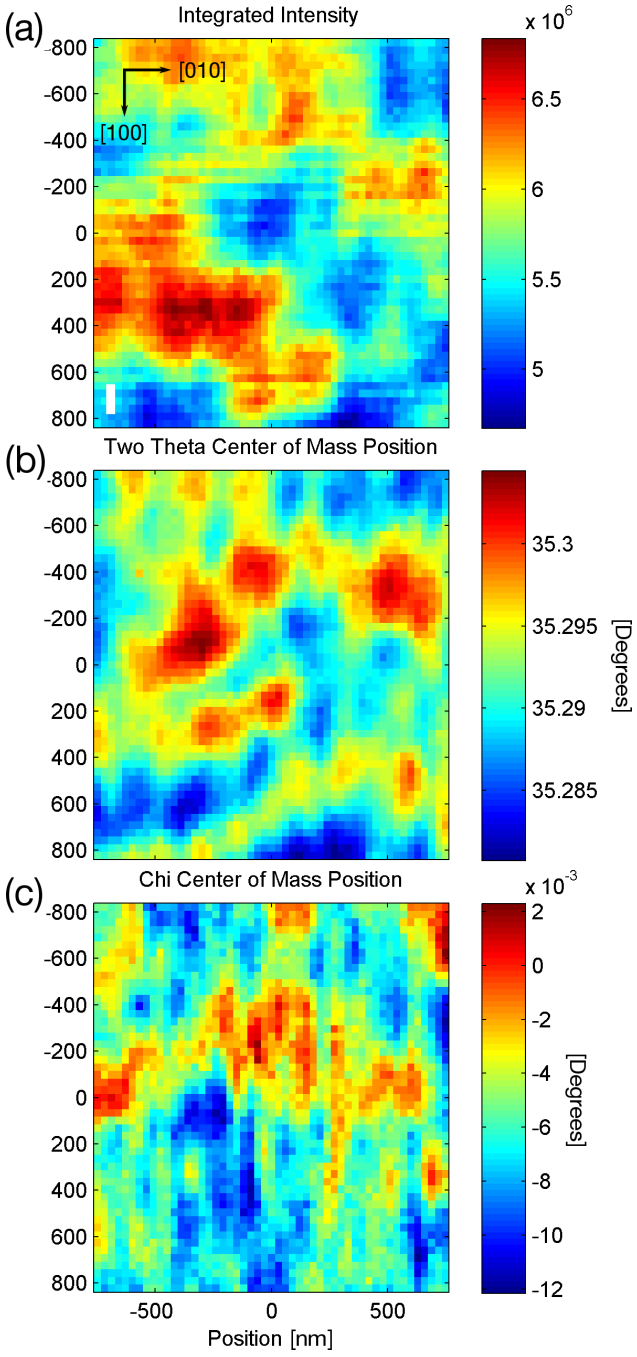


Figure 5.12. Nanodiffraction results from the unpatterned film showing integrated $BiFeO_3$ (002) intensity (a), $2\theta$ center of mass (b), and $\chi$ center of mass (c). The crystallographic orientation and x-ray footprint are shown in the top and bottom left of (a).

the integrated intensity images of the nanostructures and the unpatterned film was both qualitatively and quantitatively similar, and the COM contrasts were all qualitatively similar, Table 5.1 illustrates that there were clear similarities and differences between the various characterized sample regions. The average out-of-plane lattice constant of the three isolated structures was 0.2% larger than that of the supported structure and the unpatterned film, while the variation in the out-of-plane lattice constant was similar for the supported and isolated nanostructures and 2-3 times smaller for the unpatterned film.

Closer examination of the coherent CCD diffraction images can give further information to compliment the analysis of the average quantities discussed thus far. The intensity distribution in the CCD images is sensitive to disorder within the illuminated sample area due to interference between the x-rays diffracted from across the beam footprint. Representative diffraction CCD detector images from the center and edge of the [010] oriented isolated rectangular nanostructure, the center and edge of the [100] oriented supported nanostructure, and the unpatterned film are shown in Figure 5.13 (a)-(e) respectively. The ROI for the images of the isolated nanostructure is centered 65 pixels lower in the horizontal ($2\theta$) direction compared to that for the supported structure and the unpatterned film. The image in (e) from the unpatterned film region resembles the familiar

Table 5.1. Variation in $2\theta$ and $\chi$ centers of mass for W-protected $BiFeO_3$ nanostructures and unpatterned film. For comparison, unstrained $BiFeO_3$ has a pseudocubic lattice constant $a_c = 3.965$ Å.

| | $\Delta\chi$ | $\Delta(2\theta)$ | $\overline{2\theta}$ | $\bar{c}$ | $\Delta d/d$ |
|---|---|---|---|---|---|
| 500 nm × 1 $\mu$m, isolated | 0.051° | 0.065° | 35.224° | 4.098 Å | $1.8\times10^{-3}$ |
| 500 nm × 500 nm, isolated | 0.028° | 0.047° | 35.233° | 4.097 Å | $1.3\times10^{-3}$ |
| 1 $\mu$m × 500 nm, isolated | 0.052° | 0.070° | 35.233° | 4.097 Å | $1.9\times10^{-3}$ |
| 1 $\mu$m × 500 nm, supported | 0.063° | 0.046° | 35.291° | 4.090 Å | $1.3\times10^{-3}$ |
| 1.6 $\mu$m × 1.5 $\mu$m, unpatterned | 0.015° | 0.024° | 35.293° | 4.090 Å | $6.5\times10^{-4}$ |

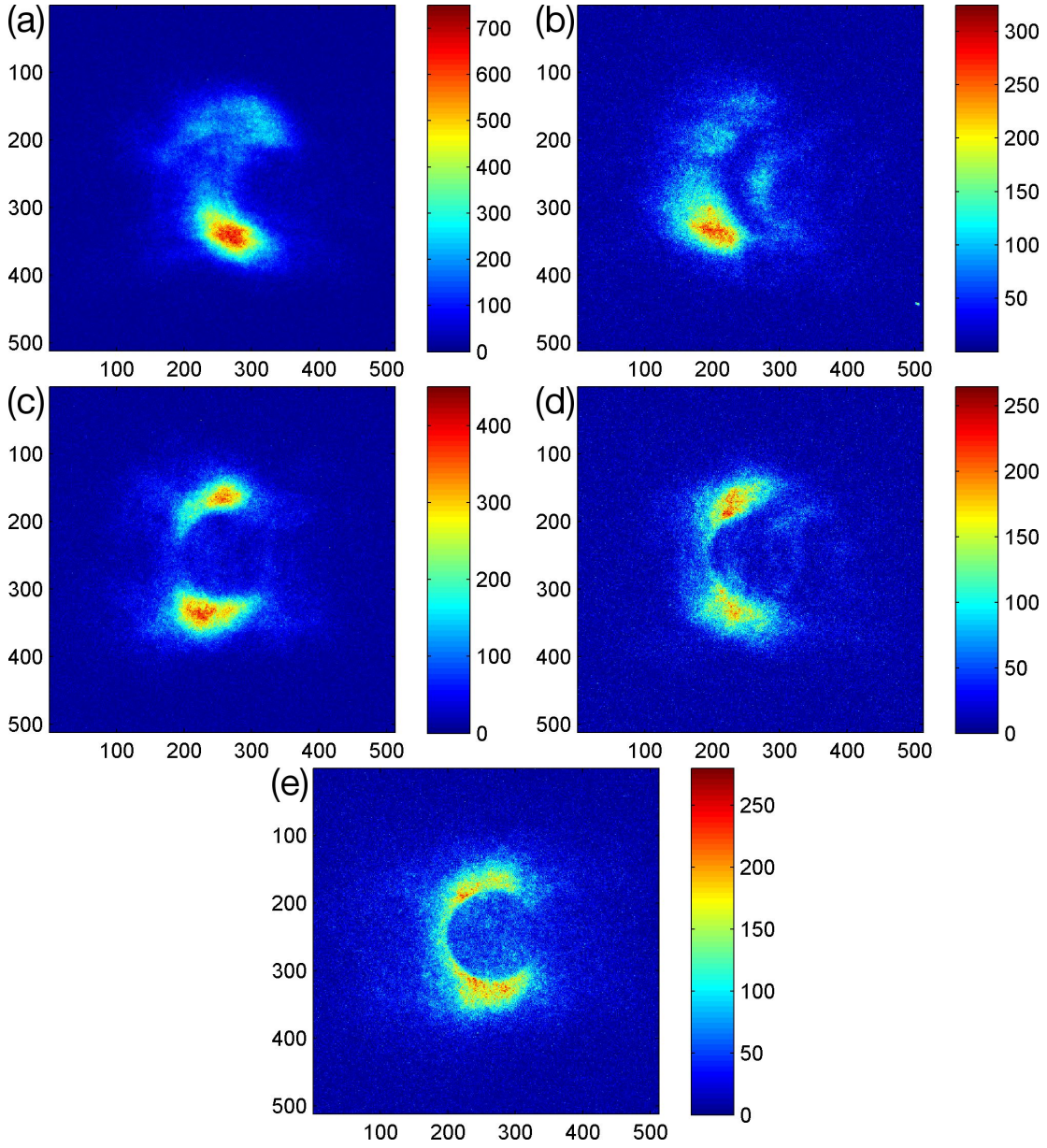


Figure 5.13. Representative diffraction CCD detector images from the center (a) and edge (b) of a fully isolated nanostructure, the center (c) and edge (d) of a supported low ion-dose nanostructure, and the unpatterned film (e). The ROI for images (a) and (b) is centered 65 pixels lower in the horizontal ($2\theta$) direction compared to that for (c)-(e). The coherent diffraction images reveal greater disorder at the edges of the nanostructures, and more disorder in the 500 nm $\times$ 1 $\mu$m isolated object compared to either the low dose object or the blanket film.

doughnut pattern of intensity and represents the area of the film with the least disorder. The image from the center of the supported nanostructure (c) is similar to that from the unpatterned region although some twisting of the intensity distribution can be observed. The bottom lobe of intensity appears to stretch to the left, while the top lobe appears to stretch to the right. The intensity pattern in the image from the center of the isolated structure (a) is highly asymmetric in both the vertical ($\chi$) and horizontal ($2\theta$) directions. In the images from the edge regions of both the supported (d) and isolated (b) nanostructures, the diffracted intensity distributions appear more distorted than those from the corresponding center regions. The coherent diffraction images therefore indicate the presence of greater disorder at the edges of both nanostructures, and more disorder in the 500 nm $\times$ 1 $\mu$m isolated object compared to either the low dose object or the blanket film.

These results suggest that lateral confinement by either removal or amorphization of the surrounding $BiFeO_3$ leads to enhanced variation in the local strain and lattice rotation fields. Both isolated and supported nanostructures were observed to contain distributions of $2\theta$ and $\chi$ domains with variations in size and shape consistent with the unpatterned film but with greater overall contrast in the $2\theta$ and $\chi$ COM positions. The static disorder present in the unpatterned $BiFeO_3$ film which gave rise to the intensity and $2\theta$ and $\chi$ COM contrasts observed in Figure 5.12 may lead to larger $\chi$ rotations and greater variation in the out-of-plane lattice constant in the absence of the constraint of a continuous film. The larger out-of-plane lattice constant and greater disorder observed in the diffraction CCD images of the isolated nanostructures are both consistent with a

larger concentration of cation or anion vacancies, which may result from the higher ion-dose used during fabrication. Regardless, the patterned 100 nm thick W mask was found to be significantly more effective in limiting FIB damage compared to the 50 nm thick Pt film.

## 5.4. $BiFeO_3$ Nanodiffraction Summary

Nanodiffraction measurements of epitaxial $BiFeO_3$ nanostructures were performed utilizing a sub-100 nm focused x-ray beam at the Hard X-ray Nanoprobe beam line at APS sector 26ID-C. These measurements of laterally confined, strained heteroepitaxial structures represent the first such use of a new hard x-ray diffraction instrument with unmatched and unprecedented spatial resolution.

Nanostructures fabricated using a 50 nm thick Pt film and a patterned 100 nm thick W mask as protective layer were both characterized. Measurements of an as-fabricated Pt-protected sample revealed significant ion damage as structures as large as 1 $\mu$m $\times$ 1 $\mu$m showed no diffraction signal. In contrast, measurements of an annealed Pt-protected sample found that objects as small as 200 nm had a detectable diffraction signal. Comparison of $BiFeO_3$ (002) integrated diffraction and Fe K$\alpha$ XRF intensity maps measured for two annealed 500 nm $\times$ 400 nm nanostructures found that the distributions of diffracted and XRF intensity were comparable within the 230 nm $\times$ 70 nm resolution of the measurement. This indicated that within the resolution of the measurement, there was not significant variation in the crystalline volume across the lateral span of either object. A low signal-to-background ratio ($\sim 1:8$) and the presence of an addition streak of intensity of unconfirmed origin complicated further reliable analysis of the data.

Diffraction measurements of an as-fabricated W-protected sample were carried out with a focused beam footprint of 130 nm × 40 nm. The patterned W mask was found to be a significantly more effective protective layer compared to the Pt film. Contrast observed in integrated $BiFeO_3$ intensity maps of both isolated and supported nanostructures was consistent with that collected from a region of the unpatterned film. Furthermore, the measured $2\theta$ and $\chi$ COM maps for the nanostructures were qualitatively similar to that of the unpatterned film, although differences in the contrast amplitude of both COM positions indicated enhanced variation in the local strain and lattice rotation fields in the nanostructures. The isolated structures were observed to have a 0.2% larger mean out-of-plane lattice constant compared to the supported structure or the unpatterned film, which may indicate a larger degree of chemical strain due to oxygen or cation vacancies resulting from a higher ion-dose during fabrication.

CHAPTER 6

# XSW Measurements of Commensurate $SrTiO_3$ / Si (001)

## 6.1. Introduction

The growth of a ferroelectric oxide directly on Si without the use of intermediate layers or the formation of an amorphous $SiO_2$ layer at the interface is a significant step in the integration of perovskite-based devices with current semiconductor technology. Such integration is complicated due to the thermodynamic instability of many metal oxides in contact with Si [105]. The high reactivity of Si can lead to the formation of a rough or amorphous interfacial layer which is detrimental to device performance. In the past 20 years, much work has been directed at the growth of epitaxial films of the insulating perovskite $SrTiO_3$ on Si [106]. $SrTiO_3$ has been of interest for application both as a candidate for high-K ($\kappa = 300$) gate dielectric layers for field effect transistors (FETs) and as a template or buffer layer for the integration of other functional materials with Si including piezoelectrics, ferroelectrics [107–109], and multiferroics [87]. This was due in part to evidence demonstrating the growth of epitaxial $SrTiO_3$ on Si with an atomically flat interface which was reported first by McKee *et al.* [110]. More recently, strain-induced room temperature ferroelectricity has been demonstrated in ultra-thin commensurate $SrTiO_3$ films on Si (001) [17].

In bulk, $SrTiO_3$ is not ferroelectric at any temperature. However, room temperature ferroelectricity was reported by Haeni *et al.* in coherently strained $SrTiO_3$ films grown

by molecular beam epitaxy (MBE) on $DyScO_3$ (110), thereby confirming predictions by Pertsev *et al.* based on Landau-Ginsburg-Devonshire theory [111]. Furthermore, a strain-induced ferroelectric phase was predicted [15, 112] for fully commensurate $SrTiO_3$ films on Si (001). A synchrotron x-ray diffraction study by Woicik *et al.* found an anomalous expansion of the out-of-plane lattice constant in commensurate $SrTiO_3$ on Si (001) [113]. For films grown below a critical thickness of ∼20 Å (5 unit cells), the in-plane $SrTiO_3$ lattice constant was indistinguishable from that of the Si (001) 1×1 surface (3.84 Å), and the tetragonal $c/a$ ratio was found to exceed that expected from elastic theory. The measured $c/a$ ratio was consistent with that predicted by mean field [111] and first principles calculations [112] for ferroelectric $SrTiO_3$ under a similar biaxial compressive strain. The report by Woicik and coworkers also showed by first principles calculations that a combination of oxygen vacancies near the interface and OH adsorbates on the surface could sufficiently screen the depolarizing electric field and stabilize ferroelectricity in such a thin $SrTiO_3$ film. In another study by Woicik *et al.*, evidence of a ferroelectric distortion in a 5 ML $SrTiO_3$ film on Si (001) was observed by x-ray absorption fine structure spectroscopy [114].

The experiments discussed in this chapter were part of a collaborative research effort combining PFM, TEM, synchrotron x-ray measurements, phase field modeling, and density functional theory (DFT) calculations to demonstrate ferroelectricity in ultra-thin commensurate films of $SrTiO_3$ grown directly on Si (001) [17]. Single crystal Bragg diffraction XSW and (00$l$) CTR measurements were made on a 5 ML $SrTiO_3$ film to determine the cation positions within the strained $SrTiO_3$ unit cell. These measurements

were performed in order to provide independent verification of a room temperature non-centrosymmetric phase in commensurate $SrTiO_3$ on Si.

## 6.2. $SrTiO_3$ / Si (001) Structure and Growth

Bulk $SrTiO_3$ has a simple cubic perovskite structure, with space group $Pm\bar{3}m$ and a room temperature lattice constant of $a = 3.905$ Å. Commensurate $SrTiO_3$ is grown on the face-centered diamond cubic Si ($Fd3m$, $a = 5.43095$ Å) with the epitaxial relationship (001) $SrTiO_3$ // (001) Si and $SrTiO_3$ [100] // Si [110], and is subject to a biaxial compressive strain of -1.66%. First principles DFT calculations [113, 114] by C. Stephen Hellberg (Navy Research Laboratory) predict a ferroelectric structure for a commensurate 5 ML thick $SrTiO_3$ film on Si (001). Hellberg's lowest energy polar and nonpolar calculated structures are depicted in Figure 6.1 and Figure 6.2, respectively. The structure shown in Figure 6.1 was calculated using a $\sqrt{8}$ by $\sqrt{8}$ supercell while that of the structure shown in Figure 6.2 was 2 by 2. Both calculations were performed at zero temperature using the glsgga [115] and projector-augmented wave functions as implemented in the Vienna *Ab-initio* Simulation Package (VASP) [116–118]. However, the nonpolar structure has a significantly higher energy than the polar structure at $T = 0$ K [119].

A fully commensurate 5 ML thick ultra-thin film of $SrTiO_3$ was grown on a 3 inch diameter, $n$-type phosphorous-doped ($1 - 4$ Ω·cm resistivity) Si (001) wafer by Maitri Warusawithana in the laboratory of Darrell Schlom at Pennsylvania State University. The film was grown by a MBE-based kinetically controlled sequential deposition (KCSD) process [120, 121], which is the same method used to grow the films studied by Woicik *et al.* in Refs. [113, 114]. The KCSD process, which was developed by Li and coworkers

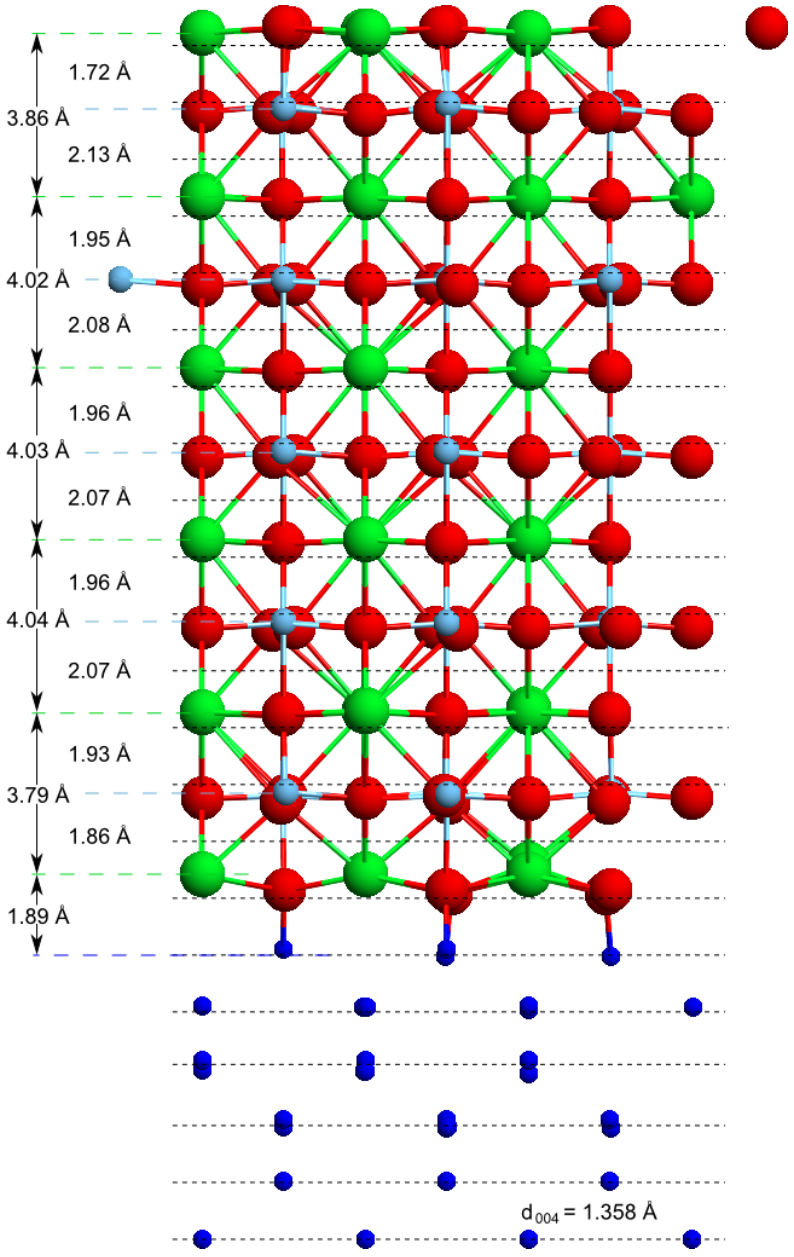


Figure 6.1. DFT predicted lowest-energy structure of a commensurate 5 unit cell $SrTiO_3$ film on Si (001). The calculated structure is polar. The dashed black lines represent the spacing of the Si (004) diffraction planes. The DFT calculation was performed by C. S. Hellberg.

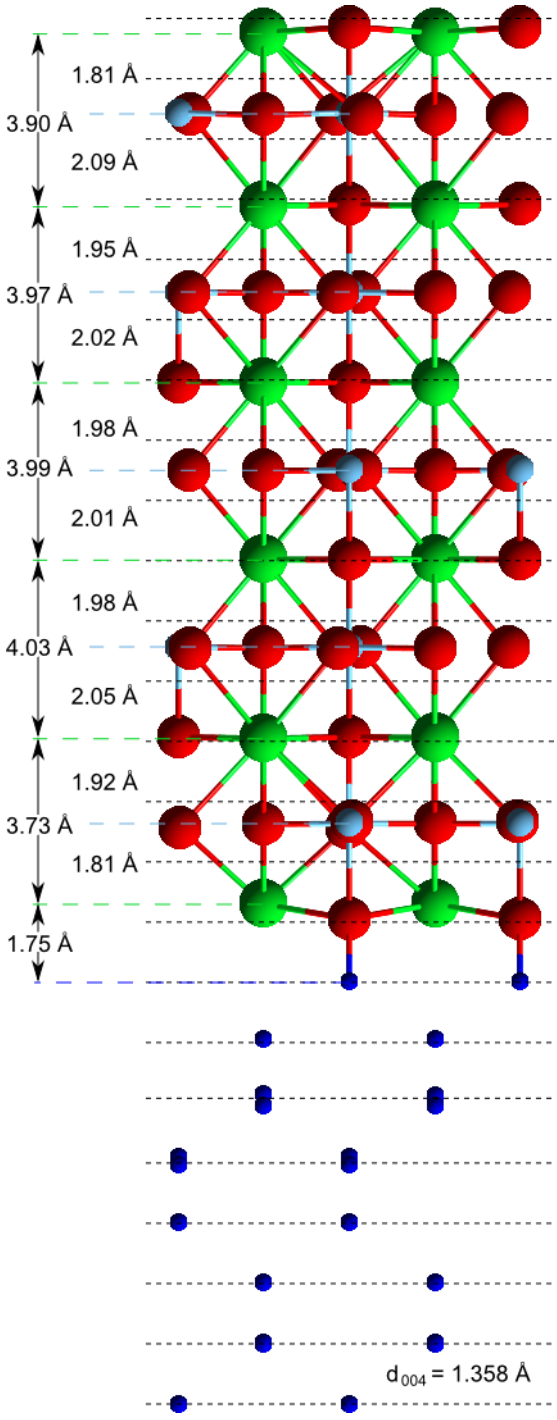


Figure 6.2. Structure of nonpolar 5 ML $SrTiO_3$ / Si from DFT calculation by C. S. Hellberg.

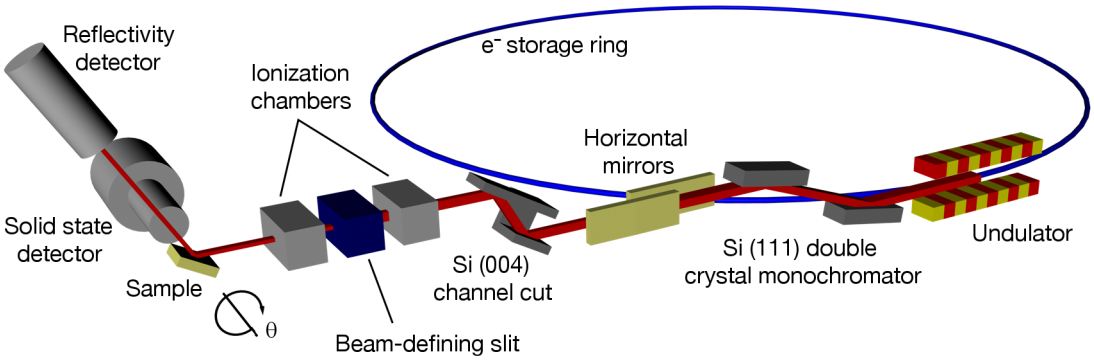


Figure 6.3. Schematic diagram of the experimental XSW setup at APS beam line 5ID-C. The setup for CTR measurements was similar, although the Si (004) channel cut post-monochromator and the solid state fluorescence detector were not used.

at Motorola Corporation, exploits the fact that oxidation requires both sufficiently high temperature and $O_2$ pressure. Oxidation of the Si surface was suppressed by using a sequence of alternating low temperature ($\sim 300°C$) / high pressure ($\sim 1.5 \times 10^{-7}$ Torr) deposition and high temperature ($\sim 580°C$) / low pressure ($< 2 \times 10^{-9}$ Torr) annealing steps. The detailed growth conditions of the sample discussed in this dissertation can be found in the supporting online material published with Ref. [17]. In contrast to the films grown by McKee and coworkers [110], the KCSD-grown films are epitaxial throughout the deposition process. The absence of a step involving the recrystallization of an amorphous layer is believed to enable the growth of commensurate $SrTiO_3$ on Si [17].

## 6.3. $SrTiO_3$ / Si (001) Experimental

Single crystal XSW and specular (00$l$) CTR measurements were carried out using the 5-circle kappa diffractometer located at APS beam line 5ID-C [122] which is operated by the DuPont-Northwestern-Dow Collaborative Access Team (DND-CAT). The experimental setup is shown in Figure 6.3. Photons were supplied by an APS "Undulator A"

insertion device which was operated in the third harmonic. The XSW and CTR measurements were performed with incident x-ray energies of 17 keV and 15 keV, respectively. The desired energy was selected from the white beam undulator radiation using a $LN_2$-cooled Si (111) double crystal HHL monochromator. A pair of horizontally deflecting Rh-coated glass mirrors were used to provide horizontal focusing and harmonic rejection. For XSW measurements, the angular divergence and wavelength spread were further reduced by the use of a channel cut Si (001) post-monochromator. The (004) reflection of the channel cut was used to match the d-spacing of the measured sample reflection. A set of horizontal and vertical beam defining slits were used to determine the x-ray spot size on the sample. The respective horizontal and vertical slit sizes used for XSW measurements were $\sim 0.2$ mm and $\sim 0.1$ mm, while those used for the CTR measurement were $\sim 0.5$ mm and $\sim 0.2$ mm. Ionization chambers were used to monitor the beam flux before and after the slits and post-monochromator (when in use).

The channel cut post-monochromator and the second crystal of the HHL monochromator were "detuned" in angle to 80% of the maximum intensity to aid in harmonic rejection as well as monochromator stability since locking in on the side on a rocking curve rather than the peak provides better feedback control of the angular position. Positioning and feedback control of the channel cut and monochromator were achieved using monochromator stabilizer (MOSTAB) [123] control units. Each MOSTAB unit maintains a user set ratio between two input signals, generally the output signals of the ion chambers immediately upstream and downstream of the crystal being controlled. An ion chamber reading and a signal proportional to the APS ring current are used to maintain the position of the second crystal of the HHL monochromator. The MOSTAB units drive

piezoelectric actuators to maintain the fine position of the monochromator angles with sub-microradian resolution.

A Linux PC running SPEC (Certified Scientific Software) in *fivec* geometry was used for data acquisition and motor control during both XSW and CTR measurements. The XSW measurements were made by scanning the Si (001) substrate through the (004) reflection. The diffracted beam intensity was recorded with an ion chamber mounted on the $2\theta$ (delta) detector arm of the kappa diffractometer, and the XRF spectra were collected with a single-element Rontec XFlash silicon drift diode (SDD) energy dispersive fluorescence detector. Digital pulse-height processing of the SDD preamp output was achieved using a DXP-2X unit (X-ray Instrumentation Analysis) installed in a CAMAC crate. The DXP system was controlled by a Labview program, MESA, and the processed spectra were subsequently read and recorded by SPEC. A measured fluorescence spectrum from the 5 ML $SrTiO_3$ / Si sample is shown in Figure 6.4. XSW scans were performed using custom SPEC macros which provide drift control and output the full fluorescence spectrum and all SPEC detector channels (ion chambers, scintillation detectors, etc.) recorded at each angular step.

The CTR measurement was made using a high-resolution (1:1 fiber optic ratio with 25 lp/mm) CCD area detector (Princeton Instruments PI-SCX:1300) in place of a ion chamber or scintillation point detector. This method allows for significantly reduced acquisition time, improved angular resolution, and more efficient background correction [124]. The PI-SCX:1300 detector has a 1300 $\times$ 1340 array of 20 $\mu$m $\times$ 20 $\mu$m pixels and features a $Gd_2O_2S$:Tb phosphor optimized for 17 keV photons. The CCD detector was controlled by a Windows PC with EPICS software developed at the APS. The EPICS

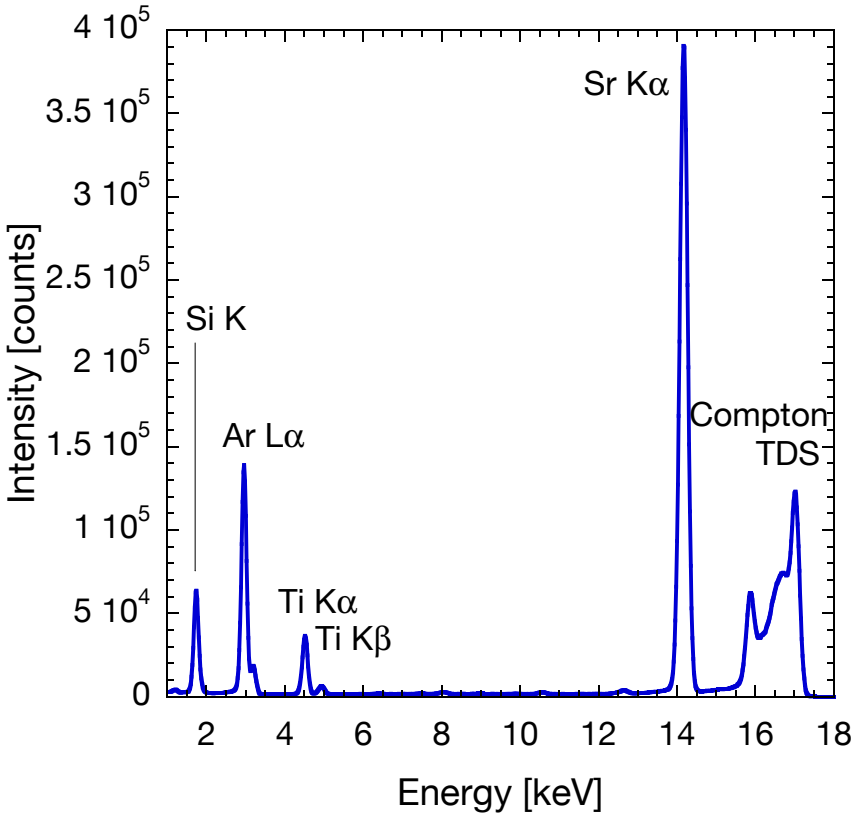


Figure 6.4. Fluorescence spectrum collected by the Rontec SDD detector for the 5 ML $SrTiO_3$ / Si (001) sample M145b5 with an incident x-ray energy of 17 keV.

PC acts as a server which can be used as a virtual detector by SPEC. SPEC triggers and reads back from the CCD detector via a network connection to the EPICS host. CCD images were collected at each step in a series of scans along the specular Si (00$l$) rod from $l = 0.45$ to $l = 6$ (Si r.l.u.). The background corrected integrated intensity was extracted from the CCD images using MATLAB routines developed by and received from Paul Fenter (Argonne). The image processing included dark count correction, efficiency correction (to adjust for variation in efficiency across the CCD chip), zinger correction,

and background subtraction. The background correction strategy was similar to that described in Section 5.1.

For the XSW measurements, two 10 mm × 10 mm pieces (M145b3 and M145b5) of a commensurate 5 ML $SrTiO_3$ film on Si (001) were characterized under ambient conditions, although the sample temperature was determined to be ∼ 35 °C due to heating from stepping motors on the sample goniometer. The sample was mounted to an aluminum chuck using double-sided Scotch tape. Other methods of mounting the sample (e.g. the use of a vacuum chuck or metal clips) introduced considerable strain which significantly broadened the Si (004) rocking curve. XSW measurements were made on one sample (M145b5) under vacuum at temperatures between -50 °C and 50 °C using a custom built temperature cell equipped with a x-ray transparent Be dome. Sample heating was achieved by the use of a pyrolytic boron nitride heater (Momentive Performance Materials Quartz, Strongsville, Ohio, part no HTR1001). Sample cooling was achieved by flowing cold nitrogen gas from a pressurize $LN_2$ dewar through cooling lines inside the base of the temperature cell. The cooling lines were originally designed to be used to prevent the cell from overheating during sample heating. However, the thermal isolation between the sample and the base was bypassed by wrapping the ceramic heater with Ag foil (without shorting the electrical contacts) and placing the heater in thermal contact with the floor of the cell with a custom-built Cu block. Inside the temperature cell, the sample was mechanically held to the Ag-coated ceramic heater by two Pt-Ir wire clips. The optimal balance between sample drift and strain was achieved with the sample held down by one clip and resting snugly against the other such that the second clip opposed the force of gravity on the sample when rotated to the Si (004) Bragg condition. The sample

temperature was measured with a type-K thermocouple held to the sample surface by the Pt-Ir clip. Rough vacuum was maintained with an oilless diaphragm pump. The pressure inside the cell was not monitored. To minimize angular drift, measurements were made without $N_2$ flow. After sufficiently cooling the sample, the flow was stopped and short ($\sim$ 16 seconds), repeated XSW scans were performed with constant monitoring of the sample temperature. Scans taken at sample temperatures within a range of 2-3 °C were then combined to achieve sufficient counting statistics.

The CTR measurement was performed on a single 10 mm $\times$ 10 mm sample (M145b5) under ambient conditions, although at a slightly lower temperature ($\sim$ 30 °C). The temperature difference between the ambient XSW and CTR measurements was due to the use of a glass slide between the sample and the aluminum sample holder in the CTR experiment. This effectively reduced a diffuse scattering background from the aluminum which was observed in the CTR without the glass present. The sample was mounted to the glass slide using double-sided tape.

The XSW experiments were performed during beamtimes in March and June 2007, and the CTR measurement was made in August 2007. During the March XSW measurements (sample M145b3), the APS operated in a standard 24 singlet Top-Up mode. A hybrid fill (singlet) Top-Up operation mode was used during the June XSW beamtime (sample M145b5). The APS operated in a 324 singlet non-Top-Up mode during the August CTR measurement (sample M145b5).

## 6.4. $SrTiO_3$ / Si (001) XSW Results and Discussion

A Si (004) XSW measurement was made of 5 ML $SrTiO_3$ / Si (001) sample M145b3 at room temperature in March 2007. The angular dependence of the (a) Si K$\alpha$, (b) Sr K$\alpha$, and (c) Si K$\alpha$ XRF yields, the (d) Si (004) rocking curve, and the corresponding best fits to the data are shown in Figure 6.5. The XRF yields were collected with a take-off angle $\alpha \sim 4^\circ$ as indicated by the fit to the Si K$\alpha$ data. The Si K$\alpha$ yield was analyzed to confirm the reliability of the measurement (i.e. that the SDD detector and digital processing were functioning properly). The Si XRF fit parameters are sensible, as $P_{004}$ is close to one and $f_{004}$ is large, although $f_{004} = 0.74$ indicates that the substrate is measurably strained. Analysis of the Sr K$\alpha$ and Ti K$\alpha$ yields found that the coherent fractions were nearly twice as high as those measured by the Bedzyk group for previously studied perovskite films on Si and Ge [125]. Since each $P_{004}$ measures the location of the atomic species relative to the Si (004) diffraction planes and

$$\frac{c_{\text{film}} - 3d_{004}}{3d_{004}} \sim 3.3\% \tag{6.1}$$

where $c_{\text{film}} = 3.94$ Å is the out-of-plane lattice constant of the film determined by high-resolution XRD, the coherent positions represent the average Sr and Ti locations in units of Si $d_{004}$. The difference of 0.417(7) between the Ti and Sr coherent positions represents a difference of 1.92(1) Å between the average cation locations in the film, indicating that the Ti atoms are shifted a mean value of 0.05(1) Å downward from the midpoint between Sr planes.

The results of the June 2007 room temperature Si (004) XSW measurement of sample M145b5 are shown in Figure 6.6. A closer dynamical diffraction fit to the Si (004) rocking

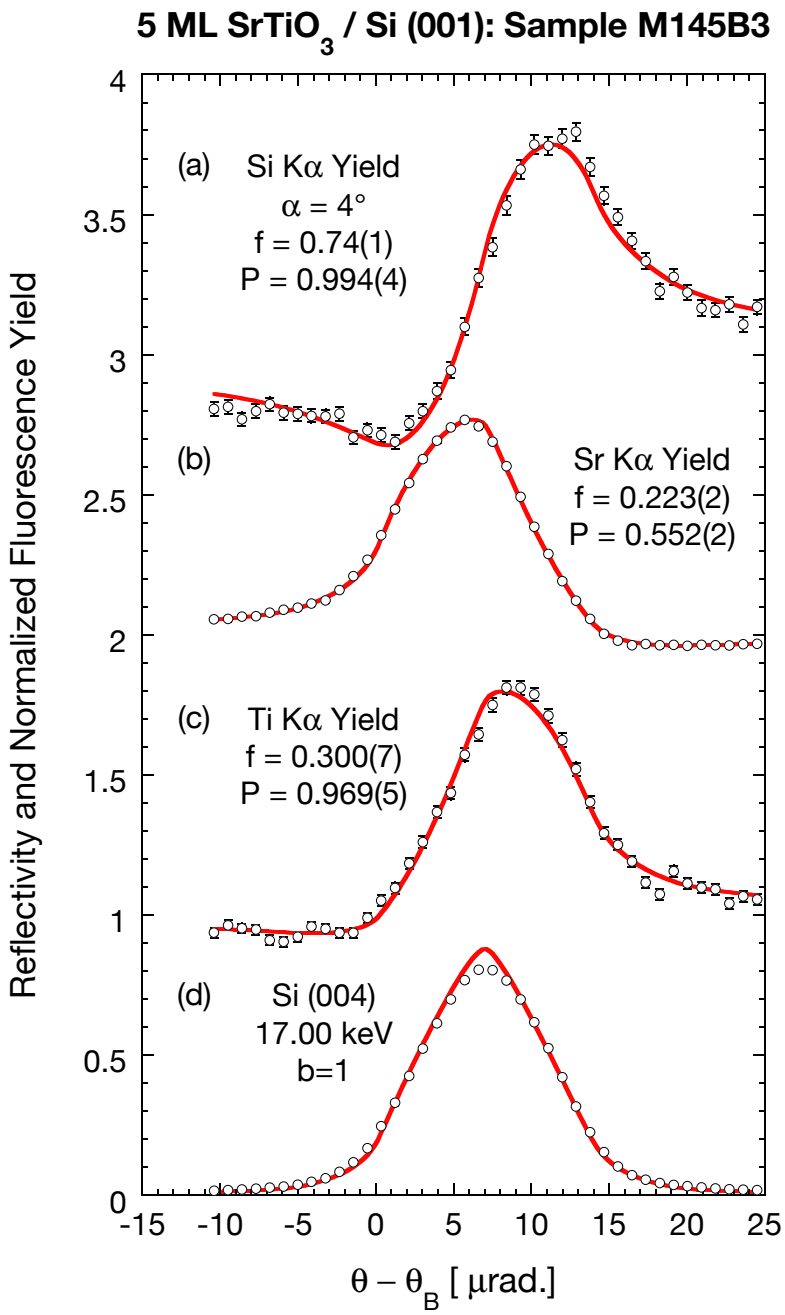


Figure 6.5. Room temperature XSW results for 5 ML $SrTiO_3$ / Si sample M145b3. The data were collected in air with a 5-circle kappa diffractometer and an incident photon energy of 17 keV. Measurements were made at beam line 5ID-C in March 2007. The Si (a) and Sr (b) yields are offset by an addition of 2 and 1, respectively.

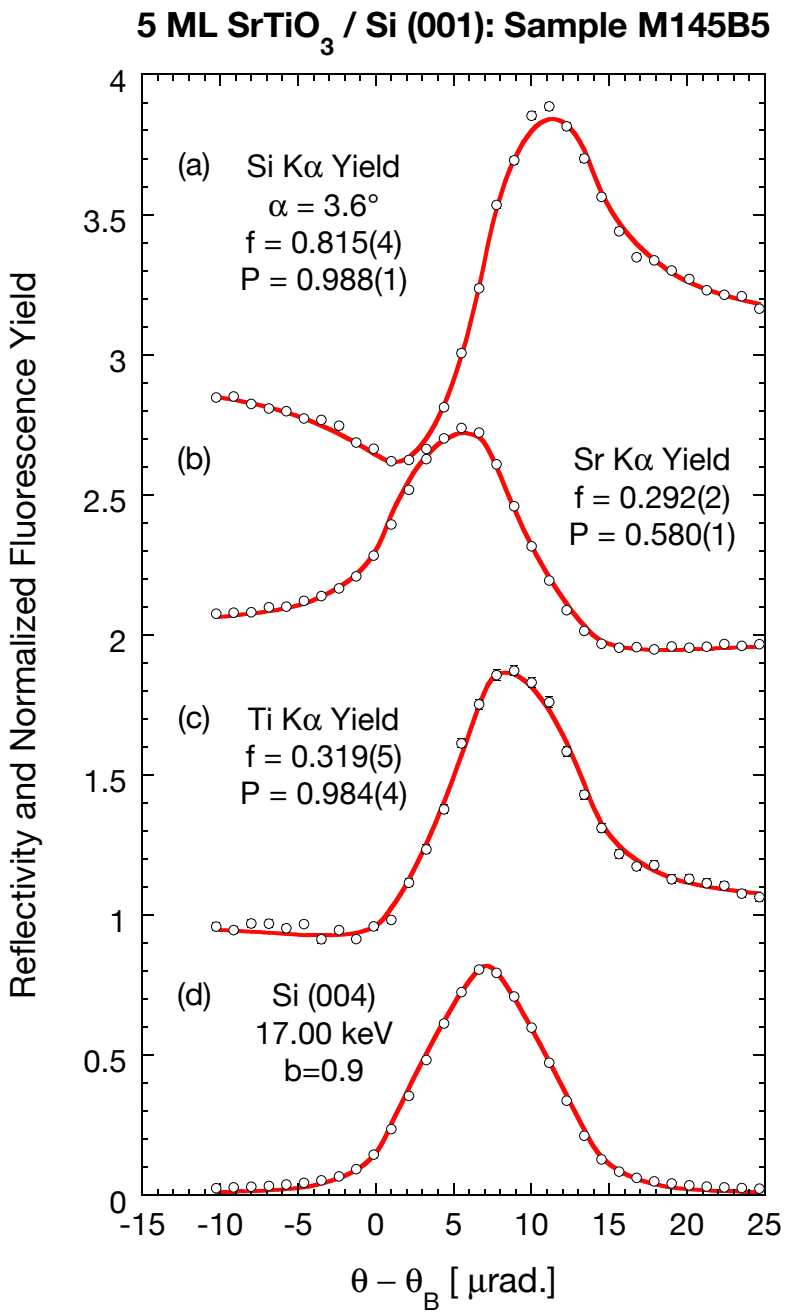


Figure 6.6. Room temperature XSW results for 5 ML $SrTiO_3$ / Si sample M145b5. The data were collected in air with a 5-circle kappa diffractometer and an incident photon energy of 17 keV. Measurements were made at beam line 5ID-C in June 2007. The Si (a) and Sr (b) yields are offset by an addition of 2 and 1, respectively.

curve was obtained for the M145b5 measurement compare to that of M145b3, and analysis of the K$\alpha$ XRF yields from Si, Sr, and Ti resulted in higher coherent fractions for each. The three coherent positions are similar to those from the M145b3 measurement, and an analysis following that described above found that the difference of 0.404(5) between the Ti and Sr coherent positions corresponds to a difference of 1.906(7) Å between the mean cation positions. The Ti sublattice is therefore shifted an average of 0.064(7) Å downward from the midpoint between Sr planes.

Of the June XSW measurements using the Be dome temperature cell, only the data acquired at 10 °C could be analyzed reliably. The rest of the measurements were subject to excessive sample drift and resulted in overly broadened Si (004) rocking curves. Fitting the XSW data required unrealistically large values (2.5 to 7.6) for the substrate asymmetry factor b, which is given by $b = \gamma_0/\gamma_H$, where $\gamma_0$ and $\gamma_H$ are the direction cosines of the incident and reflected x-ray beams. In the XSW analysis, setting $b = 1$ corresponds to the Si(004) emittance function from the postmonochromator crystal and the acceptance function from the sample crystal having ideal reflectivity curves as defined by dynamical diffraction theory for a symmetric reflection. Even though neither reflection is asymmetric in the experiment, a value $b > 1$ is used to simulate angular broadening effects due to non-ideal reflectivity. Consequently, only the 10 °C results shown in Figure 6.7 are discussed here. Over the 15 minute duration of the measurement, the sample temperature drifted from 9.5 °C to 12.5 °C. The Ti and Sr coherent fractions were both similar to those from the two ambient measurements. The coherent positions, however, were 0.987(9) for Ti and 0.611(2) for Sr, and the difference of 0.38(1) between them indicates that the mean

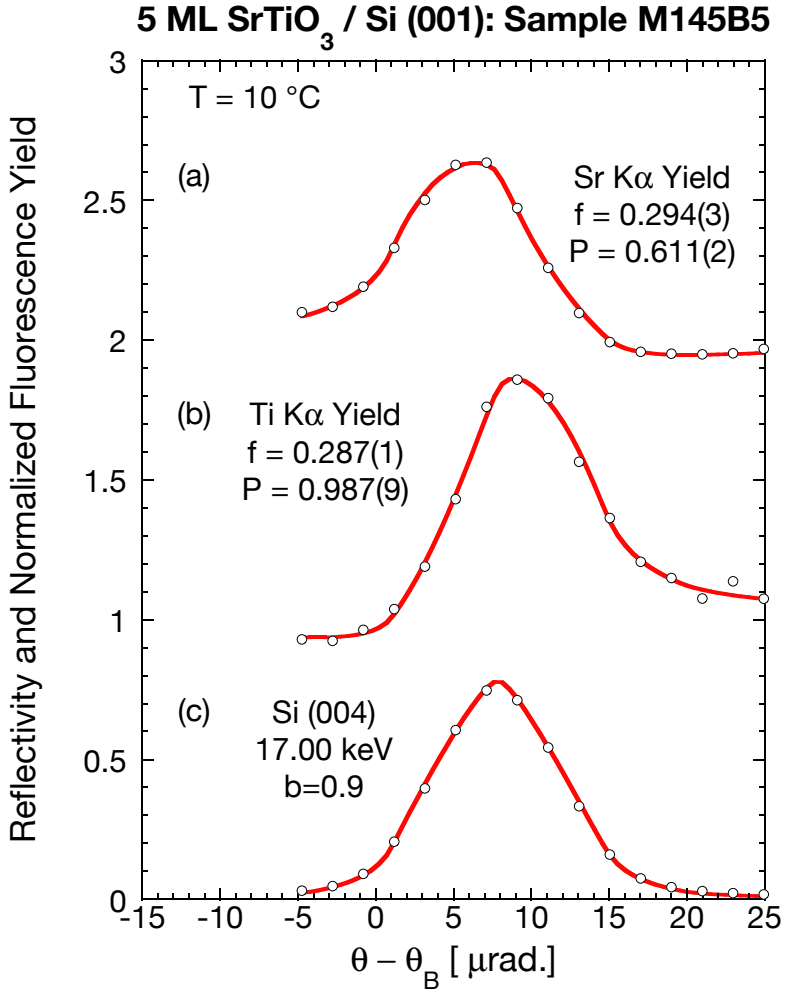


Figure 6.7. XSW results for 5 ML $SrTiO_3$ / Si sample M145b5 at 10 °C. The data were collected in vacuum ($\sim 10^{-3}$ Torr) with Be dome temperature cell mounted on a 5-circle kappa diffractometer. Measurements were made with an incident photon energy of 17 keV at 5ID-C in June 2007. The Sr yield (a) is offset by an addition of 1.

cation positions are different by 1.87(1) Å. The Ti atoms are shifted downward by an average of 0.10(1) Å, which is significantly larger than the Ti shift measured at 35 °C.

The results from the (004) XSW measurements of M145b3 and M145b5 are collected in Table 6.1. For comparison, the predicted coherent fractions and positions based on

Table 6.1. Results of the (004) XSW measurements and calculated XSW parameters for DFT predicted structures for 5 ML $SrTiO_3$ / Si (001). Rows marked with an asterisk (*) indicate that the Sr and Ti z-coordinates of the DFT model have been scaled so that the out-of-plane lattice spacing matches the measure value $c_{\text{film}} = 3.94$ Å.

| | Si | | Sr | | Ti | |
|---|---|---|---|---|---|---|
| | $f_{004}$ | $P_{004}$ | $f_{004}$ | $P_{004}$ | $f_{004}$ | $P_{004}$ |
| M145B3 35 °C | 0.74(1) | 0.994(4) | 0.223(2) | 0.552(2) | 0.300(7) | 0.969(5) |
| M145B5 35 °C | 0.815(4) | 0.988(1) | 0.292(2) | 0.580(1) | 0.319(5) | 0.984(4) |
| M145B5 10 °C | - | - | 0.294(3) | 0.611(2) | 0.287(1) | 0.987(9) |
| DFT polar | - | - | 0.76 | 0.09 | 0.97 | 0.65 |
| DFT nonpolar | - | - | 0.66 | 0.95 | 0.88 | 0.51 |
| DFT polar* | - | - | 0.38 | 0.89 | 0.70 | 0.46 |
| DFT nonpolar* | - | - | 0.40 | 0.82 | 0.65 | 0.39 |

Hellberg's polar and nonpolar DFT calculated structures are also presented. None of the measured coherent fractions or positions match those calculated from either the polar or nonpolar DFT structure. The coherent fractions for the DFT-calculated structures are significantly higher than the measured values, between 0.66 and 0.95. This is primarily due to the larger out-of-plane lattice constant of the DFT-predicted structures. For the polar model, the average spacing between the three middle Sr planes is 4.03 Å, which is only 1% different than $3d_{004}$ for Si. Likewise, the average Sr spacing for the three middle layers of the nonpolar model is 4.00, which is 1.9% different from $3d_{004}$. To determine the influence of the larger DFT lattice spacing, the z coordinates of the polar and nonpolar models were scaled by factors of 0.978 and 0.985, respectively. The calculated XSW parameters from the rescaled structures are listed in the rows marked with an asterisk (*). As expected, reduced Sr and Ti coherent fractions were calculated for the rescaled models, although they were still larger than the corresponding measured values. This was likely due to the fact that the model assumes mostly full occupation of the cation layers (both

models have full Ti occupation, while the Sr occupation fractions are (bottom-to-top) $\{5/8, 1, 1, 1, 1, 7/8\}$ and $\{1/2, 1, 1, 1, 1, 1\}$ for the polar and nonpolar models), when this may not be the case in the actual film. The calibrated off-Bragg fluorescence yield (OBY) from the ambient measurement of M145b5 corresponded to Sr and Ti coverages of 3.86(3) ML and 2.76(6) ML, respectively. The low measured coverages, which were $\sim 60-70\%$ of the expected values for the nominally 5 ML film, can be attributed to the morphology of the film. High resolution TEM images taken by D. A. Muller (Cornell) of another piece of the same sample revealed incomplete coverage due to islanding [17]. The absolute atomic coverages were determined by comparison to a identical measurement of the XRF yield from a Rutherford backscattering spectroscopy (RBS)-calibrated Sr-implanted standard. The apparent lateral inhomogeneity of the sample does complicate interpretation of the XSW result, as the discussion thus far has assumed equally occupied atomic layers. As this assumption may not be appropriate, the layer occupation fractions determined from a CTR measurement, which is discussed in Section 6.5, were incorporated into a model to determine the effect of the incomplete coverage on the XSW results.

However, before leaving the current discussion, it is useful to compare the calculated $f_{004}$ values from the DFT models with those experimentally obtained by determining the differences between the average Ti and Sr positions as before. For the polar model, the difference of 0.56 corresponds to a mean difference of 2.12 Å between the Ti and Sr planes. The Ti cations are therefore shifted an average of 0.13 Å upward from the midpoint between Sr layers (assuming a lattice constant equal to the mean interplanar distance 3.99 Å). Remarkably, this value is identical to the actual 0.13 Å average upward displacement of the Ti planes in the model. However, the nonpolar coherent positions indicate a similar,

larger mean upward Ti displacement of 0.14 Å, while the actual value is 0.07 Å. Similarly, the coherent positions calculated from the scaled DFT structures indicate mean upward Ti displacements of 0.18 Å for both the polar and nonpolar models, while the actual Ti shifts are 0.12 Å and 0.07 Å, respectively.

The failure to detect the difference between the average Ti shifts in the polar and nonpolar models casts doubt on the accuracy of extracting the relative cation displacements from the coherent positions without the use of a model to account for the difference between the out-of-plane $SrTiO_3$ layer spacing and the Si (004) d-spacing or the incomplete cation coverages. Therefore, to analyze the XSW results further, a simplified 1D model was used to account for the averaging of the coherent positions due to the incommensurate out-of-plane layer spacing. This model also allowed the inclusion of occupation fractions for each cation layer. The model assumed 3.94 Å periodic Sr layers with a variable 1st layer offset, $\delta_{\text{film}}$, relative to the Si bulk lattice and periodic Ti layers at the Sr layer midpoints with a variable Ti noncentrosymmetric displacement, $\delta_{\text{Ti}}$. A cartoon of the model is shown in Figure 6.8. For each set of coherent positions, $P_{004}^{\text{Sr}}$ and $P_{004}^{\text{Ti}}$, the parameters $\delta_{\text{film}}$ and $\delta_{\text{Ti}}$ were calculated from

$$\delta_{\text{film}} = d_{004}\left\{P_{004}^{\text{Sr}} - \frac{1}{2\pi}\text{Arg}\left[\frac{1}{N}\sum_{j=1}^{N}\exp\left(2\pi i z_j^{\text{Sr}}/d_{004}\right)\right]\right\} \tag{6.2a}$$

and

$$\delta_{\text{Ti}} = d_{004}\left\{P_{004}^{\text{Ti}} - \frac{1}{2\pi}\text{Arg}\left[\frac{1}{N}\sum_{j=1}^{N}\exp\left(2\pi i z_j^{\text{Ti}}/d_{004}\right)\right]\right\} - \delta_{\text{film}} \tag{6.2b}$$

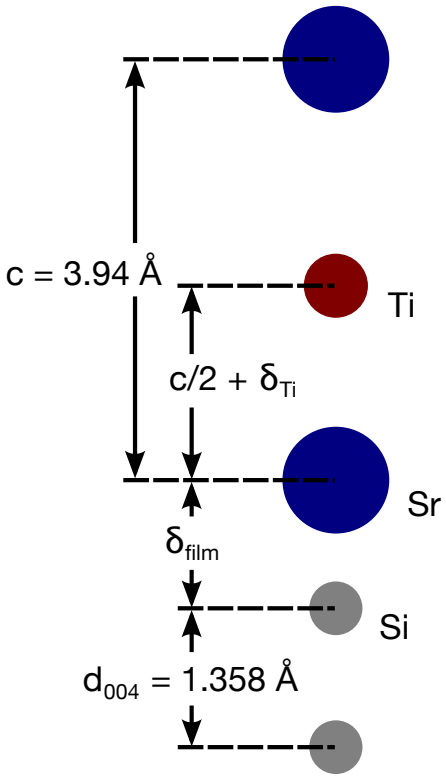


Figure 6.8. Cartoon of simplified 1D model for $SrTiO_3$ / Si (001). The model assumes 3.94 Å periodic Sr layers with a variable 1st layer offset, $\delta_{\text{film}}$ relative to the Si bulk lattice and periodic Ti layers at the Sr layer midpoints with a variable Ti noncentrosymmetric displacement, $\delta_{\text{Ti}}$.

where $z_j$ is the out-of-plane position of the $j^{\text{th}}$ atom assuming zero offset. The coherent fractions for this idealized structure are given by

$$f_{004}^{\text{x}} = \left| \frac{1}{N} \sum_{j=1}^{N} \exp\left(2\pi i z_j^{\text{x}} / d_{004}\right) \right| \tag{6.3}$$

where $\text{x} = \{\text{Sr}, \text{Ti}\}$.

The results of this analysis are listed in Table 6.2. The $\delta_{\text{film}}$ and $\delta_{\text{Ti}}$ values are all 1.358 Å mod-d, although generally only one value is physically realistic. For the results of the M145b3 XSW measurement, calculations were performed for two cases with different Sr

Table 6.2. Simplified model analysis of (004) XSW results. $\delta_{\text{film}}$ and $\delta_{\text{Ti}}$ are the Sr first layer offset (1.358 Å mod-d) and Ti noncentrosymmetric displacement, respectively. Values listed for each measurement were calculated from the respective experimental Sr and Ti coherent positions, which are collected in Table 6.1 with the corresponding experimental coherent fractions. Rows marked with an asterisk (*) were calculated with the layer occupancy fractions determined from the CTR measurement. An out-of-plane STO lattice constant of 3.94 Å was assumed except for the analysis of the polar (3.99 Å) and nonpolar (3.96 Å) DFT structures.

| | Number of Layers | | | | | |
|---|---|---|---|---|---|---|
| Measurement | Sr | Ti | $\delta_{\text{film}}$ (Å) | $\delta_{\text{Ti}}$ (Å) | Sr $f_{004}$ | Ti $f_{004}$ |
| M145b3 35 °C | 6 | 5 | 0.403 | -0.113 | 0.529 | 0.660 |
| M145b3 35 °C | 1/2 + 5 | 5 | 0.437 | -0.147 | 0.582 | 0.660 |
| M145b5 35 °C | 6 | 5 | 0.441 | -0.130 | 0.529 | 0.660 |
| M145b5 35 °C | 1/2 + 5 | 5 | 0.475 | -0.164 | 0.582 | 0.660 |
| M145b5 35 °C | 6* | 6* | 0.420 | -0.079 | 0.573 | 0.612 |
| M145b5 10 °C | 6 | 5 | 0.483 | -0.168 | 0.529 | 0.660 |
| M145b5 10 °C | 1/2 + 5 | 5 | 0.517 | -0.202 | 0.582 | 0.660 |
| M145b5 10 °C | 6* | 6* | 0.462 | -0.117 | 0.573 | 0.612 |
| DFT polar | 5/8 + 4 + 7/8 | 5 | 1.019 | 0.072 | 0.819 | 0.858 |
| DFT nonpolar | 0.5 + 5 | 5 | 0.921 | 0.054 | 0.685 | 0.747 |

layer occupancies: a fully occupied bottom layer and a half occupied bottom layer. For the M145b5 measurements, a third case was examined in addition to the two used for the M145b3 data. Values in the rows marked with an asterisk (*) were calculated with the layer occupancy fractions determined from the M145b5 CTR measurement. The calculated film and Ti offsets were observed to depend on the Sr occupancy, with uniformly larger values for the half-filled bottom layer model. Additionally, uniformly smaller offsets were determined for the calculations including the experimentally determine layer occupancies. In particular, the $\delta_{\text{Ti}}$ values were smaller by $30-50\%$ for the coverage corrected models. The largest offsets for each of the occupancy models corresponded to the 10 °C M145b5 measurement. For each of the three pairs of coherent positions, the calculated

$\delta_{\mathrm{Ti}}$ values indicated that the Ti was shifted downward from the midpoint between Sr planes regardless of the occupancy model. The largest value ($\delta_{\mathrm{Ti}} = -0.20$ Å) was calculated for the 10 °C measurement assuming a 1/2 + 5 Sr occupancy. The smallest value ($\delta_{\mathrm{Ti}} = -0.079$ Å) was obtained for the 35 °C data with the coverage corrected model. Interestingly, for the experimental occupancy corrected calculations, which are likely the most accurate, the 10 °C and 35 °C $\delta_{\mathrm{Ti}}$ values were close in magnitude to the mean Ti offset in the polar DFT model (0.13) and the nonpolar model (0.07), respectively, although they all represented Ti shifts in the opposite direction. This may indicate that the film was polar at 10 °C and nonpolar at 35 °C. This would not be unreasonable since the polar-nonpolar transition temperature was observed via PFM measurements to be $\sim$ 41 °C [17].

To check the consistency of the simplified model with a known structure, $\delta_{\mathrm{film}}$ and $\delta_{\mathrm{Ti}}$ were calculated for the polar and nonpolar DFT structures using the Sr and Ti coherent positions listed in Table 6.1. The Sr and Ti layer periodicities were assumed to be equal to the mean layer spacings of 3.99 Å and 3.96 Å for the polar and nonpolar structures, respectively. The results are listed in Table 6.2. In both cases, the film and Ti offsets were underestimated. This is likely due to the fact that the layer spacings were not constant as the simplified model assumed. However, the analysis found that Ti offset was larger in the polar structure compared to that of the nonpolar structure, which is qualitatively correct.

Without accurate knowledge of the individual layer occupancies and spacings, it is unlikely that a simple model will allow precise extraction of the cation positions from the XSW results. However, by incorporating experimentally determined layer occupancy

Table 6.3. Layer occupancies and positions from error-correction analysis of (00$l$) CTR data. Positions are relative to the topmost Si layer.

| Atom | Position (Å) | Occupancy |
|---|---|---|
| Sr | 1.41 | 0.52 |
| Ti | 3.55 | 0.48 |
| Sr | 5.50 | 0.61 |
| Ti | 7.54 | 0.57 |
| Sr | 9.49 | 0.56 |
| Ti | 11.53 | 0.58 |
| Sr | 13.47 | 0.59 |
| Ti | 15.49 | 0.53 |
| Sr | 17.56 | 0.56 |
| Ti | 19.41 | 0.56 |
| Sr | 21.44 | 0.37 |
| Ti | 23.29 | 0.20 |

fractions, an analysis of the calculated positions extracted with a simplified model suggests that at 10 °C the Ti cations are displaced from the centrosymmetric position by an amount consistent in magnitude with the DFT-predicted value for ferroelectric $SrTiO_3$ on Si (001). In contrast, the analysis finds that at 35 °C, the Ti displacements are similar to those predicted for a nonpolar $SrTiO_3$ / Si (001).

## 6.5. $SrTiO_3$ / Si (001) CTR Results and Discussion

Figure 6.9 (a) shows the results of the August 2007 specular (00$l$) CTR measurement of 5 ML $SrTiO_3$ / Si (001) sample M145b5. The data (black dots) are shown with a simulated curve (blue line) calculated based on layer spacings and densities determined by a model-independent analysis of the data performed by Argonne collaborator Paul Fenter. Fenter used a modified Fienup-based error-correction algorithm [126] to produce the 1D electron density map shown in Figure 6.9 (b). The out-of-plane Sr and Ti coordinates and occupation factors resulting from the error-correction analysis are listed in Table 6.3. The

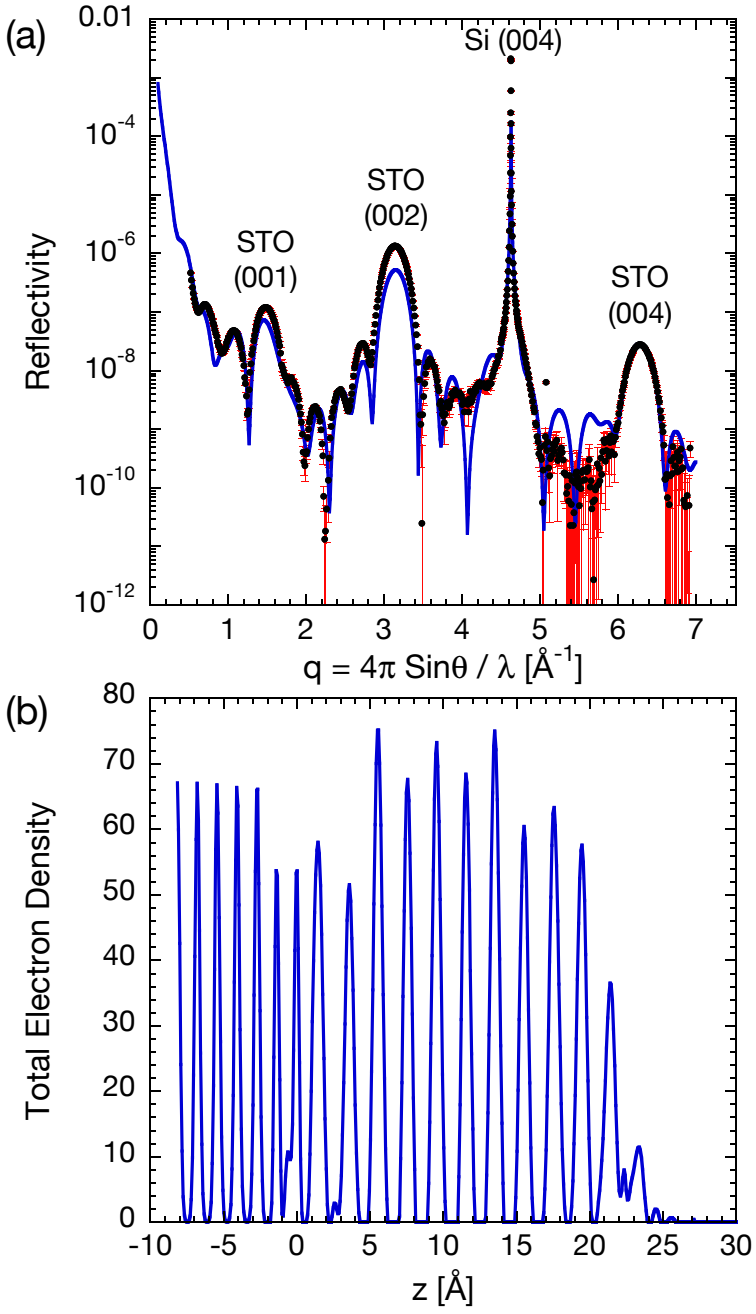


Figure 6.9. Room temperature (00$l$) CTR results for 5 ML $SrTiO_3$ / Si (001) sample M145b5. The data (black dots) are shown (a) with a simulated curve (blue line) calculated based on layer spacings and densities (b) determined by a model-independent Fienup-like error correction analysis performed by Argonne collaborator Paul Fenter.

simulated reflectivity curve plotted with the experimental data was calculated using a film structure factor based on these coordinates. The simulation also includes a multiplicative roughness factor

$$\frac{(1-\beta)^2}{1+\beta^2-2\beta\cos(c\mathrm{q})} \tag{6.4}$$

with $\beta = 0.3$. The occupation fractions listed in Table 6.3 were calculated from the integrated peaks in the electron density profile. The five leftmost peaks were assumed to represent fully occupied Si layers. The Sr and Ti layers are therefore $\sim 60\%$ occupied, which is consistent with the low measured coverages discussed in Section 6.4. The out-of-plane layer positions indicate that while the first three Ti cations were shifted up relative to the midpoint between Sr layers, the fourth and fifth were shifted down. The resulting mean displacement from the centrosymmetric position was $\sim 0.02$ Å, which is significantly smaller than that of the polar DFT model. This may indicate that the film was not polar or that the measurement was performed too close to the polar-nonpolar transition temperature, which PFM measurements observed to be $\sim 41$ °C [17]. It may also be the case that the measurement sampled an area with a mixed polarization state, either due to the presence of ferroelectric domains or due to lateral variation in the film thickness (the beam footprint on the sample varied between $\sim 2.92$ mm$^2$ and $\sim 0.22$ mm$^2$ during the measurement).

## 6.6. $SrTiO_3$ / Si (001) Summary

Commensurate films of $SrTiO_3$ epitaxially grown on Si by a MBE-based kinetically controlled sequential deposition process were characterized with single crystal XSW and

CTR measurements. Room temperature XSW measurements of two 5 ML $SrTiO_3$ / Si (001) samples, and a 10 °C measurement of one observed the highest coherent fractions measured by the Bedzyk group for a perovskite film on a semiconductor substrate. Extracting the mean cation shifts from the Sr and Ti coherent positions yielded inconsistent results without the use of a model to account for the smearing of the atomic positions due to the incommensurate out-of-plane layer spacing of the film relative to the Si (004) diffraction planes. Furthermore, the XRF measurement atomic coverages were $60 - 70\%$ of the expected values for the nominally 5 ML film. A simplified 1D model assuming 3.94 Å periodic Sr and Ti planes with a variable film and Ti displacement parameters and experimentally determined layer occupancies enabled a more consistent analysis. The layer occupation fractions were determined from analysis of a specular CTR measurement of the same sample. The average noncentrosymmetric displacement of the Ti cations at 10 °C was found to be opposite in direction but consistent in magnitude with that from a DFT-predicted polar structure. The Ti displacement at 35 °C was similar in magnitude to that predicted for a nonpolar structure. A room temperature $(00l)$ CTR measurement of a 5 ML sample was analyzed by collaborator Paul Fenter using a model-independent error-correction algorithm. The resulting 1D electron density profile of the film indicated that the Sr and Ti layer occupancies were $\sim 60\%$, which was consistent with the XRF coverage measurement of the same sample. This was likely a result of film thickness variation due to islanding which was observed by TEM. Additionally, the results of the CTR analysis indicated that the mean Ti displacement was in the same direction but significantly smaller than that of the polar DFT model.

The seeming inconsistency of the XSW and CTR measurements may be due to the presence of ferroelectric domains or effects of lateral variation in the film thickness as the beam footprint on the sample was significantly different for the two measurements. For the XSW measurements, the spot size was fixed at $\sim 0.07$ mm$^2$, while the footprint varied between $\sim 2.92$ mm$^2$ and $\sim 0.22$ mm$^2$ during the CTR measurement.

CHAPTER 7

# High Resolution X-ray Studies of $BaTiO_3$ / $DyScO_3$ (110)

Strain-enhanced ferroelectricity in $BaTiO_3$ thin films was investigated using high-resolution x-ray methods to understand the strain-induced atomic-scale structural modifications responsible for the increased ferroelectric polarization and transition temperature observed in such films. A coherently strained 50 nm thick $BaTiO_3$ film on $DyScO_3$ (110) was characterized with the thin film XSW technique to provide structural confirmation of enhanced polarity (i.e. larger cation displacements), as electrical characterization of this sample was hindered by high dielectric leakage. A specular CTR measurement near the $BaTiO_3$ (001) and $DyScO_3$ (110) peaks was made to characterize the film polarity and interface morphology.

## 7.1. $BaTiO_3$ Structure and Growth

$BaTiO_3$ and $DyScO_3$ are both distorted perovskites. At room temperature, bulk $BaTiO_3$ has a tetragonally distorted perovskite structure, with space group $P4mm$ and lattice constants $a = 3.992$ Å and $c = 4.036$ Å. The tetragonal unit cell with "down" polarity is shown in Figure 7.1. With the $Ba^{2+}$ cation at the origin, the $Ti^{4+}$ ion is displaced 0.073 Å down from the body-center position. The $O^{2-}$ anions are shifted 0.06 Å up from the face-center positions resulting in a ferroelectric polarization of $P_r = 26\ \mu C/cm^2$ along the [001] direction [1]. The tetragonal phase is stable in the temperature range 278 K $< T <$ 393 K. Above $T_C \sim 393$ K, bulk $BaTiO_3$ has a nonpolar, centrosymmetric cubic

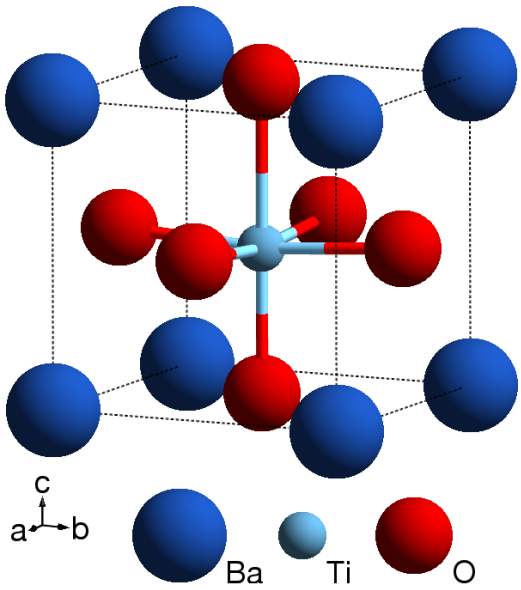


Figure 7.1. The crystal structure of tetragonal $BaTiO_3$ in the "down" orientation: $P4mm$, $a = 3.992$ Å, $c = 4.036$ Å. With the $Ba^{2+}$ cation at the origin, the $Ti^{4+}$ ion is displaced 0.073 Å down from the body-center position. The $O^{2-}$ anions are shifted 0.06 Å up from the face-center positions resulting in a ferroelectric polarization along the [001] direction [1].

structure ($Pm\bar{3}m$). At 278 K, $BaTiO_3$ remains ferroelectric but the structure changes from tetragonal to orthorhombic ($Amm2$). The small orthorhombic distortion results in a polarization along the pseudocubic [011] direction. A third phase transition occurs at 183 K, below which the structure is rhombohedral ($R3m$) with a ferroelectric distortion along the pseudocubic [111] direction [127].

$DyScO_3$ is an orthorhombically distorted perovskite with space group $Pbmn$ and room temperature lattice constants $a = 5.443(2)$ Å, $b = 5.717(2)$ Å, and $c = 7.901(2)$ Å [128]. The primitive unit cell is shown in Figure 7.2 (a). Within the orthorhombic unit cell, which is outlined in solid grey, there is a pseudocubic structure ($a_c = 3.946$ Å) outlined in dashed black. Figure 7.2 (b) shows the pseudocubic (001) surface viewed along the

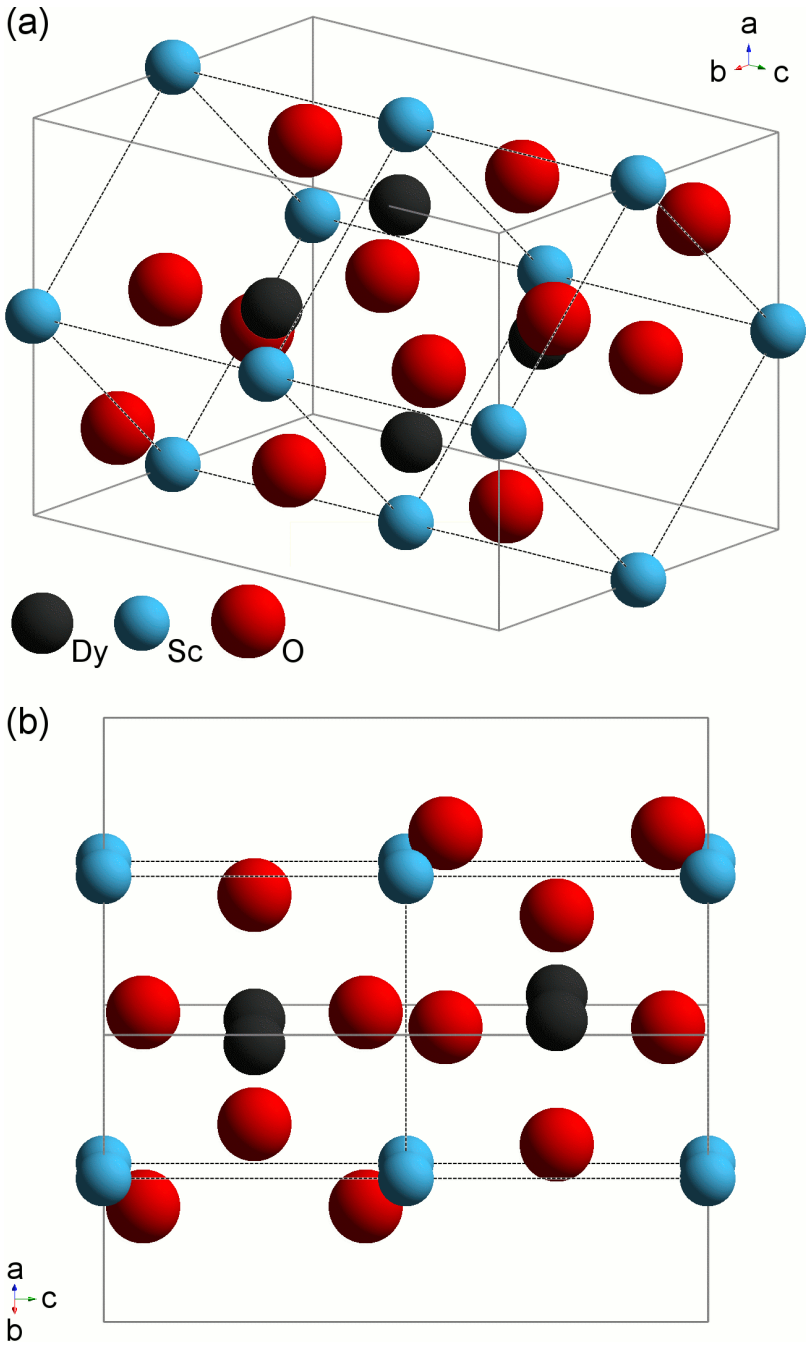


Figure 7.2. The crystal structure of orthorhombic $DyScO_3$: *Pbnm*, $a$ = 5.443(2) Å, $b$ = 5.717(2) Å, $c$ = 7.901(2) Å [128]. The dashed black lines (a) outline the pseudocubic unit cell: $a_c$ = 3.946 Å. The (001) pseudocubic surface (b) viewed along the orthorhombic [110] direction.

orthorhombic [110] direction. $DyScO_3$ is isostructural with other rare earth scandates (e.g. $GdScO_3$, $TbScO_3$) [129] as well as the conductive oxide $SrRuO_3$ [130]. The structure is also described by the standard space group $Pnma$, the axes $a'$, $b'$, $c'$ of which are related to those of $Pbnm$ by the transformation $a' = b$, $b' = c$, and $c' = a$. $DyScO_3$ is not ferroelectric down to 4 K [16], and has no reported structural phase transitions in the temperature range $298 - 1273$ K [131].

The $BaTiO_3$ sample discussed in this chapter was deposited via MBE on a (110)-oriented $DyScO_3$ single crystal substrate. The 50 nm thick film (sample MB127) was grown by Michael Biegalski in the laboratory of Darrell Schlom at Pennsylvania State University. The deposition conditions are described in the supporting online material published with Ref. [18] and the references therein. Individual layers of BaO and $TiO_2$ were deposited sequentially using Ba and Ti sources in a 9:1 gas mixture of $O_2$ and ozone at a pressure of $5\times10^{-6}$ Torr. The substrate temperature was 700 °C. From high resolution XRD, the film was found to be fully strained with lattice constants $a = 3.940(2)$ Å and 4.0953(5) Å [18]. This represents a biaxial in-plane compressive strain of $\epsilon_s = -1.7\%$.

As discussed in Section 2.2, an increased ferroelectric Curie temperature of $T_C \sim 813$ K was observed for a 50 nm film on $DyScO_3$, and a significantly enhanced polarization was expected based on hysteresis measurements of two thicker (200 nm) films with less strain. Although hysteresis measurements of the coherent 50 nm film on $DyScO_3$ were impaired by excessive leakage, remnant polarization values of $P_r \sim 50$ $\mu C/cm^2$ and $P_r \sim 70$ $\mu C/cm^2$ were observed for a coherent film grown on $GdScO_3$ (which has a slightly smaller lattice mismatch with $BaTiO_3$) with $\epsilon_s = -1.0\%$ and a partially relaxed film on $DyScO_3$ with $\epsilon_s = -1.3\%$, respectively [18].

## 7.2. $BaTiO_3$ / $DyScO_3$ (110) Thin Film XSW Measurement

A thin film XSW measurement of 50 nm $BaTiO_3$ / $DyScO_3$ (110) sample MB127 was made in July of 2005. The experiment was performed with an incident photon energy of 7.0 keV using the four circle diffractometer XSW setup located at APS undulator beam line 12ID-D, which is operated by the Basic Energy Sciences Synchrotron Radiation Center (BESSRC-CAT). The 12ID-D XSW setup has since been relocated to APS beam line 33ID-D. The experimental setup was similar to that at 5ID-C, which is shown in Figure 6.3, although 12ID-D was not equipped with horizontal focusing mirrors. Additionally, a channel cut post-monochromator was not used during the thin film XSW measurement as the HHL Si (111) monochromator was sufficient to resolve the rocking curves of the thin film sample. During the measurement, the APS operated in the standard 24 singlet Top-Up mode.

A x-ray energy of 7.0 keV was chosen in order to be above the Ti $K$ and Ba $L$ fluorescence edges but below the Fe $K$ and Dy $L_3$ edges. The incident beam slit size was 1 mm $\times$ 1 mm and the resulting beam footprint was 1 mm $\times$ 4.7 mm on the 10 mm $\times$ 10 mm sample. The reflected x-ray beam was measured with a NaI scintillation point detector (Cyberstar, Oxford-Danfysik), and the XRF spectra were collected with a single element Ultra LEGe solid state detector (SSD) (Canberra) placed at a distance of 35 mm from the sample. The fluorescence detector was equipped with a Pb collimator with a 4 mm x 1.7 mm rectangular aperture, the bottom of which was aligned with the sample surface. This limited the take-off angle of the measured fluorescence to $\sim 2.78^\circ$ resulting in an escape depth of $\mu_f^{-1}\,(\alpha = 2.78^\circ) \sim 300$ nm for Sc $K$ fluorescence from the substrate. This was significantly less than 1 mm substrate thickness and therefore resulted in a

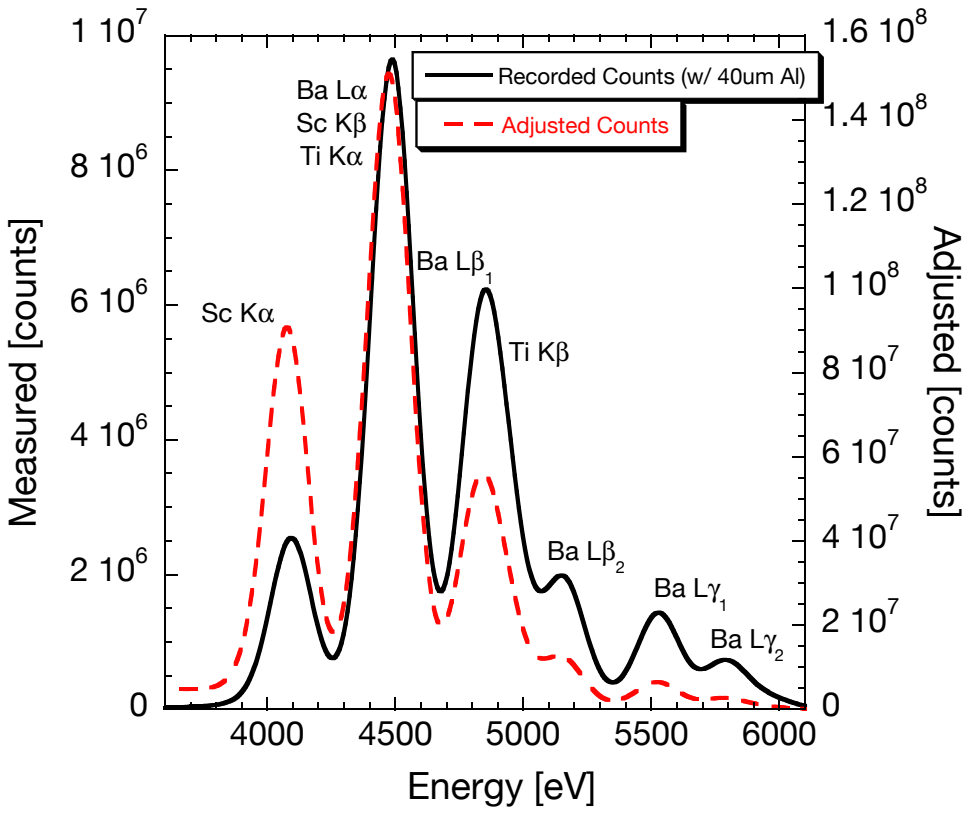


Figure 7.3. The experimentally measured XRF spectrum (solid black) obtained for a 50 nm $BaTiO_3$ / $DyScO_3$ (110) sample with an incident x-ray energy of 7.0 keV. The fluorescence was measured with a single element Ultra LEGe solid state detector (Canberra) with a 4 mm x 1.7 mm rectangular aperture at a distance of 35 mm from the sample. A 40 $\mu$m thick Al filter was used to reduce the relative intensity of the lower energy Sc $K$ peaks from the substrate. The attenuation corrected spectrum is shown as dashed red.

reduction of the measured substrate fluorescence signal. A 40 $\mu$m thick Al filter was used to further reduce the relative intensity of the lower energy Sc $K$ peaks from the substrate. An experimentally measured XRF spectrum from the 50 nm $BaTiO_3$ / $DyScO_3$ sample is shown in Figure 7.3. Both the actual recorded spectrum and an adjusted spectrum (corrected for the energy-dependent attenuation of the Al filter) are plotted.

Table 7.1. $BaTiO_3/DyScO_3$ x-ray fluorescence energies (in eV) of principal $K$ and $L$ lines. Values are taken from Ref. [132].

| Element | $K\alpha_1$ | $K\alpha_2$ | $K\beta_1$ | $L\alpha_1$ | $L\alpha_2$ | $L\beta_1$ | $L\beta_2$ | $L\gamma_1$ | $L\gamma_2$ |
|---|---|---|---|---|---|---|---|---|---|
| 21 Sc | 4090.6 | 4086.1 | 4460.5 | 395.4 | 395.4 | 399.6 | | | |
| 22 Ti | 4510.84 | 4504.86 | 4931.81 | 452.2 | 452.2 | 458.4 | | | |
| 56 Ba | 32193.6 | 31817.1 | 36378.2 | 4466.26 | 4450.9 | 4827.53 | 5156.5 | 5531.1 | 5796.9 |
| 66 Dy | 45998.4 | 45207.8 | 52119 | 6495.2 | 6457.7 | 7247.7 | 7635.7 | 8418.8 | 8714.0 |

Currently, the available energy resolution of our XRF measurements has allowed performing reliable measurement of only the Ba XSW signal for $BaTiO_3$ samples. The Ti $K$ fluorescence yield could not be measured due to the close proximity of the Ba $L\alpha$ and $L\beta$ lines as well as the Sc $K\alpha$ lines. The energies of the $K$ and principal $L$ fluorescence lines of Sc, Ti, Ba, and Dy are listed in Table 7.1. As observed in Figure 7.3, the Sc $K\beta$, Ba $L\alpha$, and Ti $K\alpha$ lines, which are separated by at most $\sim 40$ eV, are indistinguishable in the SSD-measured spectrum. Additionally, Ti $K\beta$ and Ba $L\beta_1$, which are separated by $\sim 100$ eV, appear as a single peak with a significant overlap with the Ba $L\beta_2$ line. Consequently, the only Ba $L\gamma_1$ XSW signal was extracted and analyzed.

XSW data from both the $BaTiO_3$ (001) and (002) Bragg reflections were collected. A significant slope in the measured off-Bragg XRF yield was observed in both sets of scans. This was the result of a geometrical effect due to the rectangular aperture on the fluorescence detector. The detector was mounted to the optical table on which the diffractometer sits, and consequently remained fixed while the sample rotated in $\theta$. To correct for the resulting angular dependence of the effective aperture size and shape, XRF spectra were collected for coarse long range $\theta$ scans of $\pm 7^\circ$ about each Bragg condition. The two coarse scans were fit with a polynomial function of $1/\sin(\theta)$ which was then used to flatten each respective XSW Ba $L\gamma_1$ yield. However, while the slope correction scan

for the (001) data set was performed immediately following the (001) XSW measurement, the XRF collimator was physically moved between the (002) XSW measurement and the corresponding coarse correction scan. Consequently, the slope correction measurement was found to be insufficient to flatten the (002) XSW data, and the (002) measurement was not fully analyzed. The (001) XSW fluorescence yield was flattened with the following geometrical correction:

$$\mathrm{Y} = \left(-6.398 + 6.812\mathrm{x} + 0.2065\mathrm{x}^2\right)/1000 \tag{7.1}$$

where $\mathrm{x} = 1/\sin(\theta)$. The experimentally measured (001) XSW data and best fits for sample MB127 are shown in Figure 7.4 with simulated curves for bulk-like films of each polarity (up and down). The sum of square deviation for the best fit to the XRF yield was 0.26, while for the up and down curves it was 0.90 and 1.13, respectively. The data were analyzed using MATLAB routines adapted from code written by David Marasco for the analysis of $PbTiO_3$ and PZT thin film XSW data [62].

The XRF modulation, given by Equation (3.13), depends on the reflectivity of the Bragg reflection responsible for generating the XSW field. In the thin film XSW case, the reflectivity depends on the cation positions determined from the analysis of the XRF modulation, since the structure generating the XSW is the same as that being probed. It is therefore necessary to iterate until the XSW analysis arrives at a self-consistent solution. For $BaTiO_3$, a single iteration would ideally include a reflectivity fit followed by a fit to both the Ba and Ti XRF yields. Each subsequent reflectivity fit would be calculated from a structure factor including the Ba and Ti positions determined from the previous iteration. However, without the measured Ti XRF yield, the Ti cation

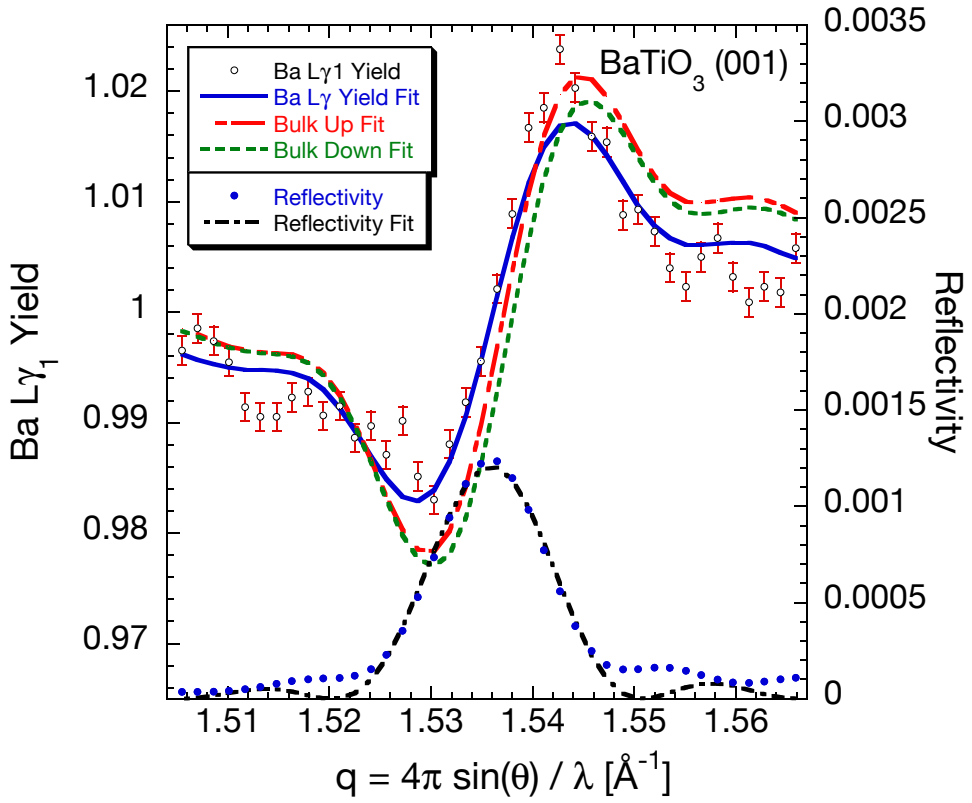


Figure 7.4. The experimental XSW data measured from a 500 Å thick $BaTiO_3$ film on (110) $DyScO_3$. The best fit to Ba $L\gamma_1$ fluorescence yield is shown as solid blue. Best fits for bulk up and down polarization are shown as dashed red and green, respectively. The fit suggests that the film is polarized up and that the polar displacement of the Ba cation is larger than in bulk.

position could not be determined experimentally at each iteration step. Therefore, to analyze the incomplete (001) XSW data set, an assumption had to be made about the Ti position for a given Ba position. The Ba $L\gamma_1$ XSW data were analyzed assuming a bulk-like ratio between the displacements of the Ti and Ba cations relative to their high temperature centrosymmetric positions ($\delta z_{\mathrm{Ti}}/\delta z_{\mathrm{Ba}} \sim 2$). This partial analysis of the XSW data suggested that the Ba displacement from the centrosymmetric position was larger than in bulk $BaTiO_3$. The best fit shown in Figure 7.4 found that the film was polarized

up, and the Ba coherent position was $P_{\mathrm{Ba}} = 0.1286$ (assuming $P_{\mathrm{Ti}} = 0.7572$) whereas for bulk up-polarized $BaTiO_3$, $P_{\mathrm{Ba}} = 0.013$ and $P_{\mathrm{Ti}} = 0.526$. The static Debye-Waller factor was determined to be 0.76, which is similar to although lower than most of the values from the previous $PbTiO_3$ XSW measurements. Typical values were greater than 0.8 for most $PbTiO_3$ samples [62]. Additionally, the Ti displacement seems unrealistically large, suggesting that the assumption of $\delta z_{\mathrm{Ti}}/\delta z_{\mathrm{Ba}} \sim 2$ may not be appropriate. It is possible that the large Ti displacement and the small Debye-Waller factor are related, as the (001) reflection is particularly sensitive to film polarity. Since for a centrosymmetric structure the BaO and $TiO_2$ planes would scatter 180° out of phase for the (001) reflection, an overly displaced Ti cation may result in a calculated reflectivity which is too large. If that were the case, the fitting routine would adjust the Debye-Waller factor to compensate in order to maintain a good fit. Nevertheless, the larger Ba displacement is qualitatively consistent with the increased remnant polarization reported in $BaTiO_3$ films on $DyScO_3$ (110). Without the experimentally measured Ti fluorescence yield, it is unlikely that a robust quantitative analysis of the thin film XSW data can be performed.

## 7.3. $BaTiO_3$ / $DyScO_3$ (110) CTR Measurement

A specular CTR measurement was made of the 50 nm $BaTiO_3$ sample MB127 in September of 2005. The data were collected in the J. B. Cohen X-ray Diffraction Facility at Northwestern with Cu $K\alpha_1$ from an 18 kW rotating anode source coupled to a multilayer mirror and a high resolution thin film diffractometer (Rigaku ATX-G) equipped with an asymmetric Ge (111) condenser channel cut monochromator. The incident x-ray intensity was $\sim 2.2 \times 10^7$ photons/sec.

Since a nonzero substrate miscut affects the orientation of the CTR in reciprocal space, the direction and magnitude of the $DyScO_3$ (110) substrate miscut were determined experimentally. The sample surface normal was optically aligned parallel to the $\phi$ rotation axis of the diffractometer. The substrate (110) rocking curve was then measured with an $\omega$ scan at eight sample $\phi$ positions each separated by 45°. Since the relative peak position in $\omega$ at each $\phi$ is directly related to the projection of the miscut vector in the $2\theta/\omega$ scattering plane, the magnitude and direction of the miscut were determined from a sinusoidal fit to the $\omega$ peak position as a function of $\phi$. For sample MB127, the substrate was found to be miscut 0.0619(6)° from the (110). The miscut was directed $\sim 25°$ from one of the substrate edges. The typical $DyScO_3$ (110) rocking curve full width-at-half maximum was 0.016°. For the CTR measurement, the sample was oriented with the $DyScO_3$ (110) substrate miscut vector lying in the plane perpendicular to the scattering plane. In this orientation the influence of the miscut was minimized since the beam divergence in $\chi$ was much larger than 0.062°.

The specular scattering profile of the 50 nm film was measured in the vicinity of the $BaTiO_3$ (001) and $DyScO_3$ (110) peaks over the range 1.4 $\text{Å}^{-1} \leq q \leq 1.7$ $\text{Å}^{-1}$. Figure 7.5 shows the measured data (black circles) and a best fit to Equation (3.30) which was calculated using MATLAB. Table 7.2 lists the fitting parameters that were used in the analysis. A bulk-like unit cell was assumed with the experimentally determined lattice parameters $a_{\text{film}} = 3.940$ Å and $c_{\text{film}} = 4.0953$ Å. The Up Fraction, which represents the

Table 7.2. Fitting parameters for analysis of the 50 nm $BaTiO_3$ / $DyScO_3$ CTR measurement. The analysis is outlined in Section 3.4.

| Up Fraction | $\sigma_{\text{sub}}$ (Å) | $\sigma_{\text{film}}$ (Å) | $N_{\text{avg}}$ | $\sigma_N$ | $\delta_{\text{film}}$ | Scale Factor |
|---|---|---|---|---|---|---|
| 1.0 | 10.83 | 7.639 | 122.0 | 5.232 | -0.0666 | 0.9735 |

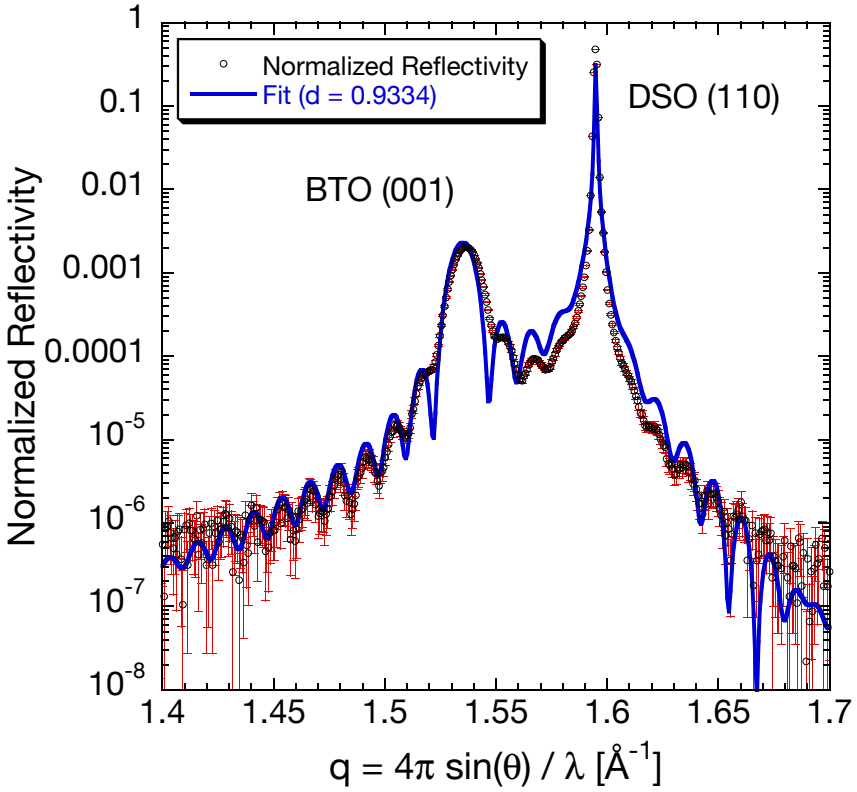


Figure 7.5. CTR data (black circles) and best fit to Equation (3.30) (solid blue) for the 50 nm $BaTiO_3$ / $DyScO_3$ (110) sample. The specular CTR was measured in the vicinity of the $BaTiO_3$ (001) (left) and $DyScO_3$ (110) (right) peaks. The best fit was obtained with an Up Fraction of 1. Data were collected with Cu $K\alpha_1$ from an 18 kW rotating anode source and a high resolution thin film diffractometer (Rigaku ATX-G) equipped with an asymmetric Ge (111) condenser channel cut monochromator.

fraction of the film with an "up" oriented structure factor, was a user-set parameter which was generally kept fixed during fitting. Variation in the film thickness across the sampled area was accounted for by performing a weighted average of Equation (3.29) calculated for a Gaussian distribution of film thickness defined by $\sigma_N$ about an average thickness $N_{avg}$. The parameters $N_{avg}$ and $\sigma_N$ are both measured in units of $c_{film}$, as is the interface layer spacing, $\delta_{film}$. The Scale Factor adjusts the overall amplitude of the scattered intensity to

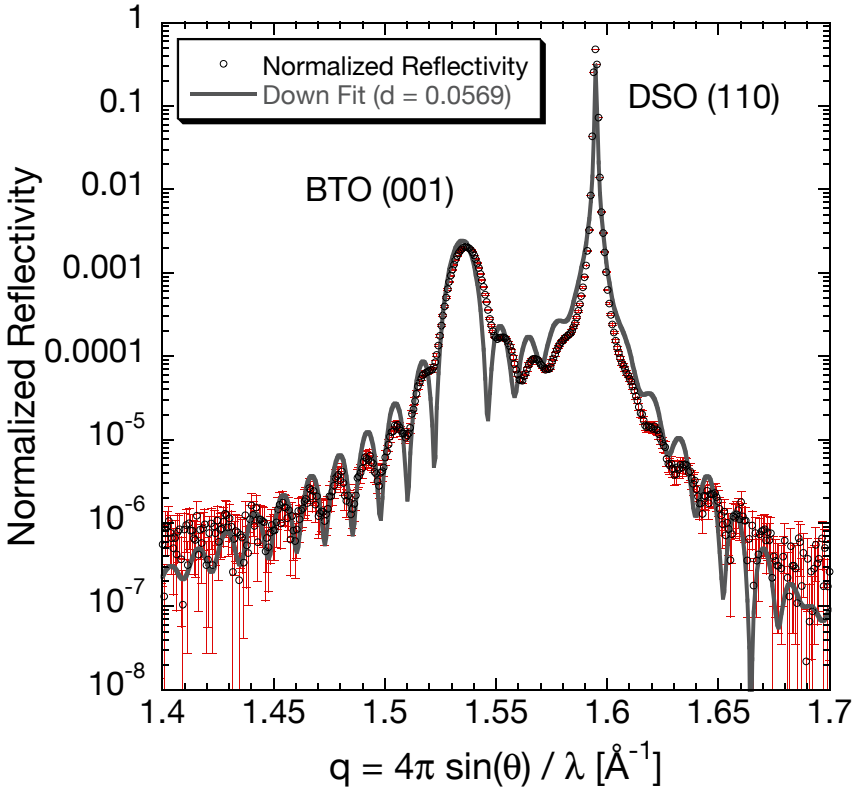


Figure 7.6. CTR data (black circles) and best "Down" polarity fit to Equation (3.30) (solid grey) for the 50 nm $BaTiO_3$ / $DyScO_3$ (110) sample. The calculated curve is noticeably worse than the "up" fit in Figure 7.5, particularly on the low q side of the $BaTiO_3$ (001) peak.

match theory. This enables analysis of data in the absence of an accurate measure of the incident beam intensity (i.e. when the absolute reflectivity is not experimentally known). For a properly normalized data set the Scale Factor should be close to unity.

Analysis of the CTR data suggests that the film was polarized up, which is consistent with the thin film XSW measurement. The best fit to Equation (3.30) with a "down" structure factor (Up Fraction = 0.0) is shown in Figure 7.6. The calculated curve is noticeably worse than the "up" fit in Figure 7.5, particularly on the low q side of the $BaTiO_3$ (001) peak. The film and interface roughness values were $\sigma_{film} \sim 7.6$ Å and

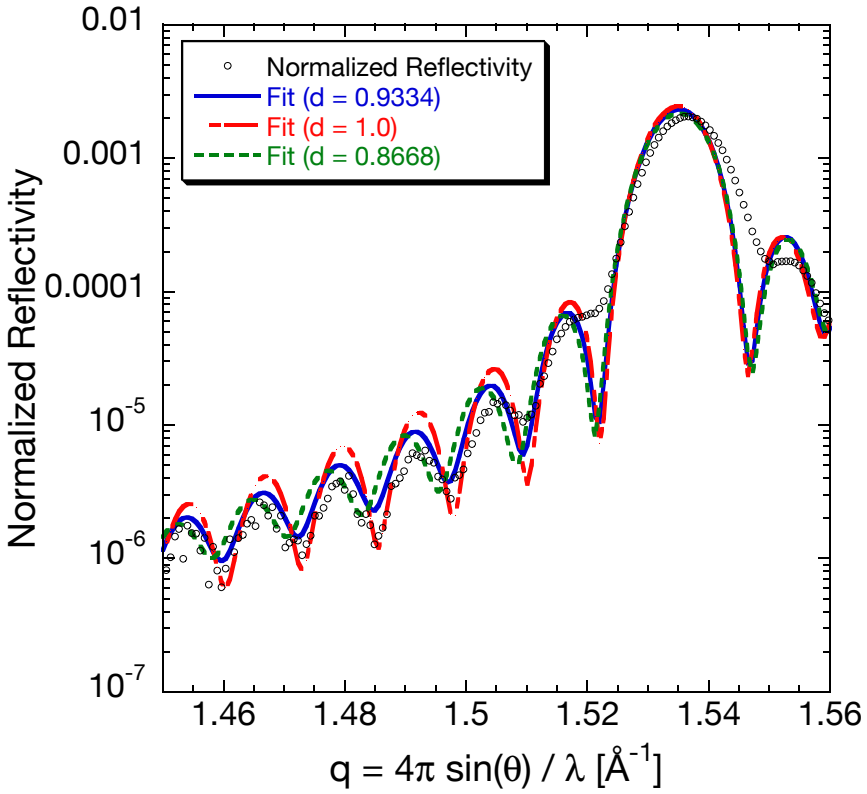


Figure 7.7. Fit dependence on interface spacing for the 50 nm $BaTiO_3$ / $DyScO_3$ (110) CTR measurement. The data and best fit ($\delta_{\text{film}} = 0.9334$) are shown as black circles and solid blue. Simulated curves with a larger offset ($\delta_{\text{film}} = 1.0$) and a smaller offset ($\delta_{\text{film}} = 0.8668$) are shown in dashed red and green, respectively. This demonstrates the sensitivity of the scattering profile to small changes in interface spacing, $\delta_{\text{film}}$.

$\sigma_{sub} \sim 10.8$ Å, respectively, and the $BaTiO_3$ film thickness was determined to be $N_{\text{avg}} = 122$ layers (500 Å) with a Gaussian spread of $\sigma_N \sim 5.2$ layers (21 Å). The interface spacing was found to be $\delta_{\text{film}} = -0.0666$ (0.9334). This suggests that at the $BaTiO_3$ / $DyScO_3$ interface, the O-O nearest neighbor spacing is $c_{\text{film}}\delta = 0.27$ Å smaller than the out-of-plane lattice constant of the film, $c_{\text{film}} = 4.0953$ Å. This is reasonable since in an up polarized film the oxygen anions are shifted down relative to the cations. Thus a closer O-O spacing at the interface is expected. Accordingly, although the "up" fit was a

better match overall, the "down" constrained fit to the data found a small positive value of $\delta_{\text{film}}$ consistent with a slightly larger interfacial O-O spacing. Figure 7.7 illustrates the sensitivity of the analysis to the interface spacing. The data (black circles) are shown with the best fit (solid blue) and simulated curves with a larger offset (dashed red) and a smaller offset (dashed green) over the range 1.45 $\text{Å}^{-1} \leq \text{q} \leq 1.56$ $\text{Å}^{-1}$. The deviation of the three curves increases further to the left (low q) of the $BaTiO_3$ (001) peak since the scattered intensity profile is most sensitive to the interface offset where the reflected amplitudes from the film and substrate are of similar magnitude.

## 7.4. $BaTiO_3$ / $DyScO_3$ (110) Summary

A MBE-grown, 50 nm thick coherently strained $BaTIO_3$ film on $DyScO_3$ (110) was characterized by the thin film XSW technique and a specular CTR measurement. The goal of XSW measurement was to observe any modification of the polar cation displacements due to the biaxial compressive strain of $\epsilon_{\text{s}} = -1.7\%$ imposed by the lattice mismatch between the film and substrate. In the XSW experiment, the resolution of the energy dispersive XRF measurement was insufficient to resolve either the Ti $K\alpha$ or Ti $K\beta$ signals due to the close proximity of of the Sc $K\beta$, Ba $L\alpha$, Ba $L\beta_1$ and Ba $L\beta_2$ fluorescence lines. Consequently, only the Ba $L\gamma_1$ signal was extracted and analyzed. A partial analysis of the $BaTiO_3$ (001) thin film XSW data was performed assuming a bulk-like ratio between the polar displacements of the $Ba^{2+}$ and $Ti^{4+}$ cations ($\delta z_{\text{Ti}}/\delta z_{\text{Ba}} \sim 2$). The best fit of the Ba $L\gamma_1$ XSW yield to Equation (3.13) suggests that the film was polarized "up", and that the polar displacement of the $Ba^{2+}$ cation was larger than in bulk. The specular CTR measurement was performed to confirm the XSW-determined film polarity, and to

characterize the interface morphology. The data were analyzed according to the treatment described in Section 3.4. The best fit of the data to Equation (3.30) found that the film was polarized "up" with smooth interfaces and a slightly smaller O-O spacing at the film-substrate interface. The smaller interfacial oxygen spacing was consistent with the upward displacements of the cations in the "up" oriented unit cell.

The results of the advanced x-ray characterization of sample MB127 are qualitatively consistent with increased polar displacements of the cations within the unit cell. A full set of thin film XSW data including both the Ba and Ti XRF yields would be required to quantify the enhancement in order to provide conclusive atomic-scale structural evidence of increased ferroelectric polarization in a 50 nm thick fully strained $BaTiO_3$ film on $DyScO_3$ (110).

CHAPTER 8

# Summary

In the work discussed in this dissertation, ferroelectric thin films and epitaxial thin film nanostructures were studied with advanced synchrotron x-ray measurements. Measurements included focused beam nanodiffraction, the x-ray standing wave (XSW) technique and its thin film extension, and crystal truncation rod (CTR) analysis. Thin films of the ferroelectric antiferromagnet $BiFeO_3$ were synthesized by off-axis radio frequency (RF) magnetron sputter deposition. The $BiFeO_3$ growth process was optimized using standard thin film characterization methods including x-ray diffraction, scanning electron microscopy, and atomic force microscopy. Single-phase, epitaxial (001)-oriented films with low surface roughness ($\sim$ 3Å) and small mosaic (glsfwhm $\sim 0.08^\circ$ for (001) rocking curve) were produced on single crystal $SrTiO_3$ (001) substrates. Optimal film growth was achieved with a substrate temperature of $T_{\text{sub}} = 650$ °C and a Ar:$O_2$ gas mixture of 7:3 at a total pressure $P_{\text{total}} = 9.0$ mTorr. A buffer layer of conductive $SrRuO_3$ was used as a bottom electrode for electrical measurements.

Epitaxial $BiFeO_3$ nanostructures with lateral dimensions from 1 $\mu$m down to 200 nm were fabricated from the sputter-grown films using focused ion-beam (FIB) processing. Two patterning strategies were explored to limit ion-induced damage to the $BiFeO_3$ layer. The first method used a 50 nm thick platinum film as a protective layer, and the second used electron-beam lithography to pattern a 100 nm thick protective tungsten mask. The use of a pattern metal layer provided more effective protection since in contrast to

a continuous metal film, it was not necessary to mill through the metal layer in order to pattern the oxide underneath. Consequently, the required ion dose was reduced and the thickness of the metal layer could be increase. Furthermore the use of W enabled optional removal of the metal layer using $H_2O_2$. For the W-protected sample, both fully isolated structures (where the surrounding $BiFeO_3$ was sputtered away) and supported islands (where the surrounding material was rendered amorphous, but not removed) were fabricated.

Nanopatterned $BiFeO_3$ samples fabricated by both strategies were subsequently characterized with sub-100 nm resolution, spatially resolved nanodiffraction measurements at the newly operational Hard X-ray Nanoprobe beam line at the Advanced Photon Source. These measurements represent the first use of this unparalleled hard x-ray instrument to examine local strain in laterally confined heteroepitaxial nanostructures. Significantly more damage was observed in Pt-protected nanostructures, which had a detectable diffraction signal only after annealing in oxygen at 650 °C for one hour. The $BiFeO_3$ (002) nanodiffraction data from the annealed Pt-protected structures suffered from a low signal-to-background ratio and the presence of an unexplained streak of intensity in the collected diffraction charge coupled device (CCD) images. The extra intensity was observed in the diffraction from the $BiFeO_3$ nanostructures, the trench regions, and the unpatterned film. Consequently, information about the local strain distribution could not be reliably extracted and only the integrated diffraction intensity was analyzed. However, examination of the CCD images indicated that the out-of-plane lattice constant of the annealed nanostructures was larger than that of the unpatterned film, which may have been due to oxygen vacancies or cation nonstoichiometry in the recrystallized nanostructures.

In contrast to the Pt-protected sample, the as-fabricated W-protected nanostructures exhibited a strong diffraction signal. The collected diffraction CCD images were analyzed to produce spatially resolved maps of integrated $BiFeO_3$ (002) intensity, and $2\theta$ and $\chi$ center of mass (COM) positions, with the latter two representing the lateral distributions of strain and lattice rotation, respectively. Comparison of the results from three isolated nanostructures (a 500 nm $\times$ 1 $\mu$m rectangle, a 500 nm $\times$ 500 nm square, and a 1 $\mu$m $\times$ 500 nm rectangle), a 1 $\mu$m $\times$ 500 nm rectangular supported structure, and a 1.6 $\mu$m $\times$ 1.5 $\mu$m area of the unpatterned film found qualitatively and quantitatively similar variations in the integrated intensity maps. The $2\theta$ and $\chi$ COM maps of the different sample regions were qualitatively similar, exhibiting inhomogeneous contrast with regions of varied size and irregular shape. However, the magnitude of the variation in the COM values was at least a factor of two smaller for the unpatterned film. This suggests that lateral confinement by either removal or amorphization of the surrounding $BiFeO_3$ leads to an enhanced variation in the local strain and lattice rotation fields in epitaxial nanostructures.

High resolution synchrotron x-ray techniques were also used to study the effects of epitaxial strain on ferroelectric cation displacements in perovskite films. XSW and CTR measurements were employed to study room temperature ferroelectricity in ultra-thin $SrTiO_3$ films resulting from epitaxial strain due to commensurate growth on Si (001). Single crystal XSW measurements using the Si (004) Bragg reflection were made for a 5 monolayer (ML) $SrTiO_3$ film. Two samples were characterized at a temperature of 35 °C and one was measured additionally at 10 °C. The XSW results were analyzed using a simplified 1D model to account for the slightly incommensurate out-of-plane lattice constant of the film relative to the Si (004) d-spacing as well as variations in the individual layer

occupancies. The analysis found that on average, the Ti cations were displaced down by $\sim 0.12$ Å from the midpoint between Sr planes at 10 °C, and by $\sim 0.08$ Å at 35 °C. These noncentrosymmetric displacements were opposite in direction but consistent in magnitude with those from a density functional theory (DFT)-predicted ferroelectric structure and DFT-predicted nonpolar structure, respectively. A specular $(00l)$ CTR measurement from $l = 0.45$ to $l = 6$ (Si r.l.u.) was performed on the same 5 ML film. The data were analyzed by collaborator P. Fenter using a model independent error-correction algorithm. The resulting 1D electron density profile indicated that each SrO and $TiO_2$ layer in the film was $\sim 60\%$ occupied, which was consistent with an x-ray fluorescence (XRF) atomic coverage measurement that found that the nominally 5 ML thick film had Sr and Ti coverages of 3.86(3) ML and 2.76(6) ML, respectively. The CTR analysis also found that while the first three Ti cations were shifted up relative to the midpoint between Sr layers, the fourth and fifth were shifted down, which resulted in a mean upward displacement of 0.02 Å from the centrosymmetric position. This shift was in the same direction, although significantly smaller than that of the polar DFT model. The inconsistency of the XSW and CTR measurements may be due to lateral inhomogeneity (either due to polarization domains or thickness variation) in the sample and the significantly larger beam footprint in the CTR measurement.

High resolution x-ray measurements were used to study enhanced ferroelectric polarization in strained $BaTiO_3$ films on $DyScO_3$ (110). A 50 nm thick coherently strained film, which was too thin for reliable electrical measurements, was characterized with the thin film XSW technique to verify the presence of increased polarization, i.e. larger cation displacements, relative to bulk $BaTiO_3$. The XSW measurement was limited to the Ba

$L\gamma_1$ as the energy differences between the Ba $L\alpha$, Ba $L\beta$, Ti $K\alpha$, Ti $K\beta$, and Sc $K\beta$ fluorescence lines were beyond the resolution of our energy dispersive XRF measurement. This complicated the analysis of the XSW data since in the thin film extension, the standing wave probe is generated by a film reflection and the probe, therefore, depends on the structure being examined. Therefore, since the Ti position could not be determined experimentally, an assumption about the Ti position was required to analyze the Ba XSW data. A bulk-like ratio between the Ba and Ti displacements was assumed, and the resulting analysis suggested that the film was polarized "up" with a Ba displacement larger than the bulk value. This was qualitatively consistent with a strain-enhanced polarization. A specular CTR measurement was made in the vicinity of the $BaTIO_3$ (001) and $DyScO_3$ (110) Bragg peaks. Analysis of the data found that the film was polarized "up," which was consistent with the XSW measurement, and that the O-O spacing at the interface was 0.27 Å smaller than the out-of-plane lattice constant of the film. A contracted interface spacing was expected for an "up" oriented film.

Currently, isolated $BiFeO_3$ nanostructures are electrically accessed with an atomic force microscopy (AFM)-based probe, which is impractical for in situ nanodiffraction studies of polarization dynamics. Future synchrotron studies should utilize electron-beam based nanolithography methods to produce electrode contacts which will allow direct electrical characterization and in situ nanodiffraction measurements of ferroelectric switching in isolated nanostructures. Additionally, if time resolved x-ray methods are utilized (a capability currently being implemented at the Advanced Photon Source (APS) Hard X-ray Nanoprobe) nanoscale structural studies of high speed domain dynamics (in addition to

quasistatic switching) will be possible. These measurements will provide critical information concerning size and shape effects as well as device performance in isolated epitaxial $BiFeO_3$ nanocapacitors.

Future XSW studies of strained ferroelectric films, particularly of the $SrTiO_3$ / Si (001) system should focus on successful measurements over a wider range in temperature. Since the XSW method is highly sensitive to small changes in atomic positions, it will likely be easier to identify a structural phase transition rather than to extract absolute cation positions from a measurement with a periodic probe that averages over layers with an incommensurate spacing. To improve the temperature dependent XSW measurements, a sample stage with heating and cooling must be designed to provide sufficient temperature control without sacrificing angular stability or resulting in excessive sample strain. A temperature range of $\pm 50$ °C should be sufficient for the 5 ML $SrTiO_3$ / Si system, and the angular stability of the sample must be $\sim 1$ $\mu$rad or better in order to measure the Si (004) rocking curve. The measured rocking curve full width-at-half maximum should be $\sim 0.5$ mdeg or better.

## References


[1] F. Jona and G. Shirane, *Ferroelectric Crystals* (Dover Publications, New York, 1993).

[2] O. Auciello, J. F. Scott, and R. Ramesh, *The physics of ferroelectric memories*, Physics Today **51**, 22 (1998).

[3] R. Ramesh, S. Aggarwal, and O. Auciello, *Science and technology of ferroelectric films and heterostructures for non-volatile ferroelectric memories*, Materials Science and Engineering: R: Reports **32**, 191 (2001).

[4] M. Dawber, K. M. Rabe, and J. F. Scott, *Physics of thin-film ferroelectric oxides*, Reviews of Modern Physics **77**, 1083 (2005).

[5] N. Setter, D. Damjanovic, L. Eng, G. Fox, S. Gevorgian, S. Hong, A. Kingon, H. Kohlstedt, N. Y. Park, G. B. Stephenson, et al., *Ferroelectric thin films: Review of materials, properties, and applications*, Journal of Applied Physics **100**, 051606 (2006).

[6] S. Srinivasan, J. Hiller, B. Kabius, and O. Auciello, *Piezoelectric / ultrananocrystalline diamond heterostructures for high-performance multifunctional micro / nanoelectromechanical systems*, Applied Physics Letters **90**, 134101 (2007).

[7] B. W. Wessels, *Ferroelectric epitaxial thin films for integrated optics*, Annual Review of Materials Research **37**, 659 (2007).

[8] N. A. Hill, *Why are there so few magnetic ferroelectrics?*, Journal of Physical Chemistry B **104**, 6694 (2000).

[9] W. Eerenstein, N. D. Mathur, and J. F. Scott, *Multiferroic and magnetoelectric materials*, Nature **442**, 759 (2006).

[10] R. Ramesh and N. A. Spaldin, *Multiferroics: progress and prospects in thin films*, Nature Materials **6**, 21 (2007).

[11] J. Wang, J. B. Neaton, H. Zheng, V. Nagarajan, S. B. Ogale, B. Liu, D. Viehland, V. Vaithyanathan, D. G. Schlom, U. V. Waghmare, et al., *Epitaxial $BiFeO_3$ multiferroic thin film heterostructures*, Science **299**, 1719 (2003).

[12] W. Eerenstein, F. D. Morrison, J. Dho, M. G. Blamire, J. F. Scott, and N. D. Mathur, *Comment on "Epitaxial $BiFeO_3$ multiferroic thin film heterostructures"*, Science **307**, 1203a (2005).

[13] J. Wang, A. Scholl, H. Zheng, S. B. Ogale, D. Viehland, D. G. Schlom, N. A. Spaldin, K. M. Rabe, M. Wuttig, L. Mohaddes, et al., *Response to comment on "Epitaxial $BiFeO_3$ multiferroic thin film heterostructures"*, Science **307**, 1203b (2005).

[14] Y. H. Chu, L. W. Martin, Q. Zhan, P. L. Yang, M. P. Cruz, K. Lee, M. Barry, S. Y. Yang, and R. Ramesh, *Epitaxial multiferroic $BiFeO_3$ thin films: Progress and future directions*, Ferroelectrics **354**, 167 (2007).

[15] D. G. Schlom, L. Q. Chen, C. B. Eom, K. M. Rabe, S. K. Streiffer, and J. M. Triscone, *Strain tuning of ferroelectric thin films*, Annual Review of Materials Research **37**, 589 (2007).

[16] J. H. Haeni, P. Irvin, W. Chang, R. Uecker, P. Reiche, Y. L. Li, S. Choudhury, W. Tian, M. E. Hawley, B. Craigo, et al., *Room-temperature ferroelectricity in strained $SrTiO_3$*, Nature **430**, 758 (2004).

[17] M. P. Warusawithana, C. Cen, C. R. Sleasman, J. C. Woicik, Y. L. Li, L. F. Kourkoutis, J. A. Klug, H. Li, P. Ryan, L. P. Wang, et al., *A Ferroelectric Oxide Made Directly on Silicon*, Science **324**, 367 (2009).

[18] K. J. Choi, M. Biegalski, Y. L. Li, A. Sharan, J. Schubert, R. Uecker, P. Reiche, Y. B. Chen, X. Q. Pan, V. Gopalan, et al., *Enhancement of ferroelectricity in strained $BaTiO_3$ thin films*, Science **306**, 1005 (2004).

[19] A. F. Devonshire, *Theory of barium titanate - Part II*, Philosophical Magazine Series 7 **42**, 1065 (1951).

[20] Y. L. Li and L. Q. Chen, *Temperature-strain phase diagram for $BaTiO_3$ thin films*, Applied Physics Letters **88**, 072905 (2006).

[21] J. X. Zhang, Y. L. Li, Y. Wang, Z. K. Liu, L. Q. Chen, Y. H. Chu, F. Zavaliche, and R. Ramesh, *Effect of substrate-induced strains on the spontaneous polarization of epitaxial $BiFeO_3$ thin films*, Journal of Applied Physics **101**, 114105 (2007).

[22] C. Ederer and N. A. Spaldin, *Influence of strain and oxygen vacancies on the magnetoelectric properties of multiferroic bismuth ferrite*, Physical Review B **71**, 224103 (2005).

[23] C. Ederer and N. A. Spaldin, *Effect of Epitaxial Strain on the Spontaneous Polarization of Thin Film Ferroelectrics*, Phys. Rev. Lett. **95**, 257601 (2005).

[24] H. W. Jang, S. H. Baek, D. Ortiz, C. M. Folkman, R. R. Das, Y. H. Chu, P. Shafer, J. X. Zhang, S. Choudhury, V. Vaithyanathan, et al., *Strain-Induced Polarization Rotation in Epitaxial (001) $BiFeO_3$ Thin Films*, Physical Review Letters **101**, 107602 (2008).

[25] C. Lichtensteiger, M. Dawber, and J.-M. Triscone, in *Physics of Ferroelectrics: A Modern Perspective*, edited by K. M. Rabe, C. H. Ahn, and J.-M. Triscone (Springer, Berlin, 2007), vol. 105 of *Topics in Applied Physics*, pp. 305–338.

[26] D. D. Fong, G. B. Stephenson, S. K. Streiffer, J. A. Eastman, O. Auciello, P. H. Fuoss, and C. Thompson, *Ferroelectricity in Ultrathin Perovskite Films*, Science **304**, 1650 (2004).

[27] A. Gruverman, O. Auciello, and H. Tokumoto, *Imaging and Control of Domain Structures in Ferroelectric Thin Films Via Scanning Force Microscopy*, Annual Review of Materials Science **28**, 101 (1998).

[28] H. Béa, S. Fusil, K. Bouzehouane, M. Bibes, M. Sirena, G. Herranz, E. Jacquet, J.-P. Contour, and A. Barthélémy, *Ferroelectricity Down to at Least 2 nm in Multiferroic $BiFeO_3$ Epitaxial Thin Films*, Japanese Journal of Applied Physics **45**, L187 (2006).

[29] V. Nagarajan, A. Roytburd, A. Stanishevsky, S. Prasertchoung, T. Zhao, L. Chen, J. Melngailis, O. Auciello, and R. Ramesh, *Dynamics of ferroelastic domains in ferroelectric thin films*, Nature Materials **2**, 43 (2003).

[30] Y.-H. Chu, M. P. Cruz, C.-H. Yang, L. W. Martin, P.-L. Yang, J.-X. Zhang, K. Lee, P. Yu, L.-Q. Chen, and R. Ramesh, *Domain control in mulfiferroic $BiFeO_3$ through substrate vicinality*, Advanced Materials **19**, 2662 (2007).

[31] H. W. Jang, S. H. Baek, D. Ortiz, C. M. Folkman, C. B. Eom, Y. H. Chu, P. Shafer, R. Ramesh, V. Vaithyanathan, and D. G. Schlom, *Epitaxial (001) $BiFeO_3$ membranes with substantially reduced fatigue and leakage*, Applied Physics Letters **92**, 062910 (2008).

[32] J. Seidel, L. W. Martin, Q. He, Q. Zhan, Y. Chu, A. Rother, M. E. Hawkridge, P. Maksymovych, P. Yu, M. Gajek, et al., *Conduction at domain walls in oxide*

*multiferroics*, Nature Materials **8**, 229 (2009).

[33] S. Hong, J. A. Klug, M. Park, A. Imre, M. J. Bedzyk, K. No, A. Petford-Long, and O. Auciello, *Nanoscale piezoresponse studies of ferroelectric domains in epitaxial $BiFeO_3$ nanostructures*, Journal of Applied Physics **105**, 061619 (2009).

[34] P. G. Evans and E. D. Isaacs, *Magnetic x-ray microdiffraction*, Journal of Physics D: Applied Physics **39**, R245 (2006).

[35] P. Kirkpatrick and A. V. Baez, *Formation of Optical Images by X-Rays*, Journal of the Optical Society of America **38**, 766 (1948).

[36] J. Kirz, *Phase zone plates for x rays and the extreme uv*, Journal of the Optical Society of America **64**, 301 (1974).

[37] B. Lai, W. B. Yun, D. Legnini, Y. Xiao, J. Chrzas, P. J. Viccaro, V. White, S. Bajikar, D. Denton, F. Cerrina, et al., *Hard x-ray phase zone plate fabricated by lithographic techniques*, Applied Physics Letters **61**, 1877 (1992).

[38] W. Yun, B. Lai, A. A. Krasnoperova, E. D. Fabrizio, Z. Cai, F. Cerrina, Z. Chen, M. Gentili, and E. Gluskin, *Development of zone plates with a blazed profile for hard x-ray applications*, Review of Scientific Instruments **70**, 3537 (1999).

[39] Z. Cai, B. Lai, Y. Xiao, and S. Xu, *An X-ray diffraction microscope at the Advanced Photon Source*, Journal de Physique IV **104**, 17 (2003).

[40] Y. Xiao, Z. Cai, Z. L. Wang, B. Lai, and Y. S. Chu, *An X-ray nanodiffraction technique for structural characterization of individual nanomaterials*, Journal of Synchrotron Radiation **12**, 124 (2005).

[41] Y. S. Chu, J. M. Yi, F. D. Carlo, Q. Shen, W.-K. Lee, H. J. Wu, C. L. Wang, J. Y. Wang, C. J. Liu, C. H. Wang, et al., *Hard-x-ray microscopy with Fresnel zone plates reaches 40 nm Rayleigh resolution*, Applied Physics Letters **92**, 103119 (2008).

[42] J. Als-Nielsen and D. McMorrow, *Elements of modern X-ray physics* (J. Wiley, New York, 2001).

[43] Y. Feng, M. Feser, A. Lyon, S. Rishton, X. Zeng, S. Chen, S. Sassolini, and W. Yun, *Nanofabrication of high aspect ratio 24 nm x-ray zone plates for x-ray imaging applications*, Journal of Vacuum Science and Technology B **25**, 2004 (2007).

[44] M. Holt, K. Hassani, and M. Sutton, *Microstructure of Ferroelectric Domains in $BaTiO_3$ Observed via X-Ray Microdiffraction*, Physical Review Letters **95**, 085504

(2005).

[45] M. J. Bedzyk and L. W. Cheng, *X-ray standing wave studies of minerals and mineral surfaces: Principles and applications*, Reviews in Mineralogy and Geochemistry **49**, 221 (2002).

[46] J. Zegenhagen and A. Kazimirov, *The x-ray standing wave technique: Recent trends and developments*, Synchrotron Radiation News **17**, 2 (2004).

[47] A. Kazimirov, J. Zegenhagen, M. Bedzyk, T.-L. Lee, E. Sozontov, and V. Kohn, *X-ray Standing Waves in Epitaxial Thin Films*, Synchrotron Radiation News **17**, 17 (2004).

[48] M. J. Bedzyk and G. Materlik, *Two-Beam Dynamical Diffraction Solution of the Phase Problem: a Determination With X-Ray Standing Waves*, Physical Review B **32**, 6456 (1985).

[49] B. W. Batterman and H. Cole, *Dynamical Diffraction of X Rays by Perfect Crystals*, Rev. Mod. Phys. **36**, 681 (1964).

[50] J. Zegenhagen, *Surface structure determination with X-ray standing waves*, Surface Science Reports **18**, 202 (1993).

[51] A. Kazimirov, T. Haage, L. Ortega, A. Stierle, F. Comin, and J. Zegenhagen, *Excitation of an X-ray standing wave in a $SmBa_2Cu_3O_{7-\delta}$ thin film*, Solid State Communications **104**, 347 (1997).

[52] M. J. Bedzyk, A. Kazimirov, D. L. Marasco, T. L. Lee, C. M. Foster, G. R. Bai, P. F. Lyman, and D. T. Keane, *Probing the polarity of ferroelectric thin films with x-ray standing waves*, Physical Review B **61**, R7873 (2000).

[53] D. L. Marasco, A. Kazimirov, M. J. Bedzyk, T. L. Lee, S. K. Streiffer, O. Auciello, and G. R. Bai, *Atomic-scale observation of polarization switching in epitaxial ferroelectric thin films*, Applied Physics Letters **79**, 515 (2001).

[54] A. Kazimirov, G. Scherb, J. Zegenhagen, T.-L. Lee, M. J. Bedzyk, M. K. Kelly, H. Angerer, and O. Ambacher, *Polarity determination of a GaN thin film on sapphire (0001) with x-ray standing waves*, Journal of Applied Physics **84**, 1703 (1998).

[55] A. Kazimirov, N. Faleev, H. Temkin, M. J. Bedzyk, V. Dmitriev, and Y. Melnik, *High-resolution x-ray study of thin GaN film on SiC*, Journal of Applied Physics **89**, 6092 (2001).

[56] S. Takagi, *A Dynamical Theory of Diffraction for a Distorted Crystal*, Journal of the Physical Society of Japan **26**, 1239 (1969).

[57] S. Takagi, *Dynamical theory of diffraction applicable to crystals with any kind of small distortion*, Acta Crystallographica **15**, 1311 (1962).

[58] D. Taupin, *Théorie dynamique de la diffraction des rayons X par les cristeaux déformés*, Bulletin de liaison de la Société Française de Minéralogie et Cristallographie **87**, 469 (1964).

[59] W. J. Bartels, J. Hornstra, and D. J. W. Lobeek, *X-ray diffraction of multilayers and superlattices*, Acta Crystallographica Section A **42**, 539 (1986).

[60] T.-L. Lee, D. L. Marasco, and M. J. Bedzyk, *X-ray dynamical diffraction calculation of total d-field intensity for single-crystal thin films using takagi-taupin approach* (1997), unpublished report.

[61] T.-L. Lee, *High-Resolution Analysis of Adsorbate-Induced GaAs(001) Surface Structures and Strain in Buried III-V Semiconductor Heterolayers by X-Ray Standing Waves*, Ph.d., Northwestern University, Evanston, Illinois (1999).

[62] D. Marasco, *X-ray Investigations of Ferroelectric Thin Films and Related Surface Structures*, Ph.d., Northwestern University, Evanston, Illinois (2002).

[63] I. K. Robinson and D. J. Tweet, *Surface X-ray diffraction*, Reports on Progress in Physics **55**, 599 (1992).

[64] C. Thompson, C. M. Foster, J. A. Eastman, and G. B. Stephenson, *Observation of the polarization of domains in ferroelectric thin films using x-ray interference*, Applied Physics Letters **71**, 3516 (1997).

[65] C. Thompson, A. Munkholm, S. K. Streiffer, G. B. Stephenson, K. Ghosh, J. A. Eastman, O. Auciello, G. R. Bai, M. K. Lee, and C. B. Eom, *X-ray scattering evidence for the structural nature of fatigue in epitaxial $Pb(Zr,Ti)O_3$ films*, Applied Physics Letters **78**, 3511 (2001).

[66] F. Kubel and H. Schmid, *Structure of a Ferroelectric and Ferroelastic Monodomain Crystal of the Perovskite $BifeO_3$*, Acta Crystallographica Section B-Structural Science **46**, 698 (1990).

[67] J. B. Neaton, C. Ederer, U. V. Waghmare, N. A. Spaldin, and K. M. Rabe, *First-principles study of spontaneous polarization in multiferroic $BiFeO_3$*, Physical Review B **71**, 014113 (2005).

[68] I. Sosnowska, T. Peterlinneumaier, and E. Steichele, *Spiral Magnetic-Ordering in Bismuth Ferrite*, Journal of Physics C-Solid State Physics **15**, 4835 (1982).

[69] C. Ederer and N. A. Spaldin, *Weak ferromagnetism and magnetoelectric coupling in bismuth ferrite*, Physical Review B **71**, 060401 (2005).

[70] B. Ruette, S. Zvyagin, A. P. Pyatakov, A. Bush, J. F. Li, V. I. Belotelov, A. K. Zvezdin, and D. Viehland, *Magnetic-field-induced phase transition in $BiFeO_3$ observed by high-field electron spin resonance: Cycloidal to homogeneous spin order*, Physical Review B **69**, 064114 (2004).

[71] H. Béa, M. Bibes, S. Petit, J. Kreisel, and A. Barthélémy, *Structural distortion and magnetism of $BiFeO_3$ epitaxial thin films: A Raman spectroscopy and neutron diffraction study*, Philosophical Magazine Letters **87**, 165 (2007).

[72] G. Xu, H. Hiraka, G. Shirane, J. Li, J. Wang, and D. Viehland, *Low symmetry phase in (001) $BiFeO_3$ epitaxial constrained thin films*, Applied Physics Letters **86**, 182905 (2005).

[73] X. Qi, M. Wei, Y. Lin, Q. Jia, D. Zhi, J. Dho, M. G. Blamire, and J. L. MacManus-Driscoll, *High-resolution x-ray diffraction and transmission electron microscopy of multiferroic $BiFeO_3$ films*, Applied Physics Letters **86**, 071913 (2005).

[74] K. Saito, A. Ulyanenkov, V. Grossmann, H. Ress, L. Bruegemann, H. Ohta, T. Kurosawa, S. Ueki, and H. Funkakubo, *Structural Characterization of $BiFeO_3$ Thin Films by Reciprocal Space Mapping*, Japanese Journal of Applied Physics **45**, 7311 (2006).

[75] H. Bea, B. Dupe, S. Fusil, R. Mattana, E. Jacquet, B. Warot-Fonrose, F. Wilhelm, A. Rogalev, S. Petit, V. Cros, et al., *Evidence for Room-Temperature Multiferroicity in a Compound with a Giant Axial Ratio*, Physical Review Letters **102**, 217603 (2009).

[76] R. J. Zeches, M. D. Rossell, J. X. Zhang, A. J. Hatt, Q. He, C.-H. Yang, A. Kumar, C. H. Wang, A. Melville, C. Adamo, et al., *A Strain-Driven Morphotropic Phase Boundary in BiFeO3*, Science **326**, 977 (2009).

[77] S. K. Streiffer, C. B. Parker, A. E. Romanov, M. J. Lefevre, L. Zhao, J. S. Speck, W. Pompe, C. M. Foster, and G. R. Bai, *Domain patterns in epitaxial rhombohedral ferroelectric films. I. Geometry and experiments*, Journal of Applied Physics **83**, 2742 (1998).

[78] A. E. Romanov, M. J. Lefevre, J. S. Speck, W. Pompe, S. K. Streiffer, and C. M. Foster, *Domain pattern formation in epitaxial rhombohedral ferroelectric films. II.*

*Interfacial defects and energetics*, Journal of Applied Physics **83**, 2754 (1998).

[79] H. W. Jang, D. Ortiz, S.-H. Baek, C. M. Folkman, R. R. Das, P. Shafer, Y. Chen, C. T. Nelson, X. Pan, R. Ramesh, et al., *Domain Engineering for Enhanced Ferroelectric Properties of Epitaxial (001) $BiFeO_3$ Thin Films*, Advanced Materials **21**, 817 (2009).

[80] C. B. Eom, J. Z. Sun, K. Yamamoto, A. F. Marshall, K. E. Luther, T. H. Geballe, and S. S. Laderman, *Insitu Grown $YBa_2Cu_3O_{7-\delta}$ Thin-Films from Single-Target Magnetron Sputtering*, Applied Physics Letters **55**, 595 (1989).

[81] C. B. Eom, A. F. Marshall, S. S. Laderman, R. D. Jacowitz, and T. H. Geballe, *Epitaxial and Smooth Films of a-Axis $YBa_2Cu_3O_7$*, Science **249**, 1549 (1990).

[82] W. H. Tang, T. L. Kam, and J. Gao, *Deposition of high quality CMR thin films by rf magnetron sputtering under pure argon gas*, Materials Research Bulletin **36**, 1463 (2001).

[83] O. Kuffer and O. Fischer, *Low temperature growth of pseudocubic perovskites by off-axis rf magnetron sputtering for the realization of epitaxial ferroelectric-based heterostructures*, Journal of Applied Physics **97**, 014103 (2005).

[84] R. R. Das, D. M. Kim, S. H. Baek, C. B. Eom, F. Zavaliche, S. Y. Yang, R. Ramesh, Y. B. Chen, X. Q. Pan, X. Ke, et al., *Synthesis and ferroelectric properties of epitaxial $BiFeO_3$ thin films grown by sputtering*, Applied Physics Letters **88**, 242904 (2006).

[85] H. Béa, M. Bibes, A. Barthélémy, K. Bouzehouane, E. Jacquet, A. Khodan, J. P. Contour, S. Fusil, F. Wyczisk, A. Forget, et al., *Influence of parasitic phases on the properties of $BiFeO_3$ epitaxial thin films*, Applied Physics Letters **87**, 072508 (2005).

[86] S. R. Basu, L. W. Martin, Y. H. Chu, M. Gajek, R. Ramesh, R. C. Rai, X. Xu, and J. L. Musfeldt, *Photoconductivity in $BiFeO_3$ thin films*, Applied Physics Letters **92**, 091905 (2008).

[87] S. Y. Yang, F. Zavaliche, L. Mohaddes-Ardabili, V. Vaithyanathan, D. G. Schlom, Y. J. Lee, Y. H. Chu, M. P. Cruz, Q. Zhan, T. Zhao, et al., *Metalorganic chemical vapor deposition of lead-free ferroelectric $BiFeO_3$ films for memory applications*, Applied Physics Letters **87**, 102903 (2005).

[88] H. Béa, M. Bibes, S. Fusil, K. Bouzehouane, E. Jacquet, K. Rode, P. Bencok, and A. Barthélémy, *Investigation on the origin of the magnetic moment of $BiFeO_3$ thin films by advanced X-ray characterizations*, Physical Review B **74**, 020101(R) (2006).

[89] A. T. Aldred and J. N. Pratt, *Vapor Pressure of Liquid Bismuth*, The Journal of Chemical Physics **38**, 1085 (1963).

[90] M. Seah, *An accurate semi-empirical equation for sputtering yields, II: for neon, argon and xenon ions*, Nuclear Instruments and Methods in Physics Research Section B: Beam Interactions with Materials and Atoms **229**, 348 (2005).

[91] P. Thompson, D. E. Cox, and J. B. Hastings, *Rietveld refinement of Debye–Scherrer synchrotron X-ray data from $Al_2O_3$*, Journal of Applied Crystallography **20**, 79 (1987).

[92] M. Kawasaki, K. Takahashi, T. Maeda, R. Tsuchiya, M. Shinohara, O. Ishiyama, T. Yonezawa, M. Yoshimoto, and H. Koinuma, *Atomic Control of the $SrTiO_3$ Crystal Surface*, Science **266**, 1540 (1994).

[93] G. Koster, G. Rijnders, D. H. A. Blank, and H. Rogalla, *Surface morphology determined by (001) single-crystal $SrTiO_3$ termination*, Physica C: Superconductivity **339**, 215 (2000).

[94] M. Hambe, S. Wicks, J. M. Gregg, and V. Nagarajan, *Creation of damage-free ferroelectric nanostructures via focused ion beam milling*, Nanotechnology **19**, 175302 (2008).

[95] M. M. Saad, R. M. Bowman, and J. M. Gregg, *Characteristics of single crystal "thin film" capacitor structures made using a focused ion beam microscope*, Applied Physics Letters **84**, 1159 (2004).

[96] A. Schilling, T. Adams, R. M. Bowman, and J. M. Gregg, *Strategies for gallium removal after focused ion beam patterning of ferroelectric oxide nanostructures*, Nanotechnology **18**, 035301 (2007).

[97] J. F. Ziegler, J. P. Biersack, and U. Littmark, *The Stopping and Range of Ions in Solids* (Pergamon Press, New York, 1985).

[98] A. Stanishevsky, B. Nagaraj, J. Melngailis, R. Ramesh, L. Khriachtchev, and E. McDaniel, *Radiation damage and its recovery in focused ion beam fabricated ferroelectric capacitors*, Journal of Applied Physics **92**, 3275 (2002).

[99] J. Maser, R. Winarski, M. Holt, D. Shu, C. Benson, B. Tieman, C. Preissner, A. Smolyanitskiy, B. Lai, S. Vogt, et al., in *Proceedings of the 8th International Conference on X-ray Microscopy*, edited by S. Aoki, Y. Kagoshima, and Y. Suzuki (2006), vol. 7 of *IPAP Conference Series*, pp. 26–29.

[100] J. L. Provis, V. Rose, S. A. Bernal, and J. S. J. van Deventer, *High-Resolution Nanoprobe X-ray Fluorescence Characterization of Heterogeneous Calcium and Heavy Metal Distributions in Alkali-Activated Fly Ash*, Langmuir **25**, 11897 (2009).

[101] D. Shu, J. Maser, B. Lai, S. Vogt, M. Holt, C. Preissner, A. Smolyanitskiy, B. Tieman, R. Winarski, and G. B. Stephenson, in *Proceedings of the 8th International Conference on X-ray Microscopy*, edited by S. Aoki, Y. Kagoshima, and Y. Suzuki (2006), vol. 7 of *IPAP Conference Series*, pp. 56–58.

[102] D. Shu, J. Maser, M. Holt, R. Winarski, C. Preissner, A. Smolyanitskiy, B. Lai, S. Vogt, and G. B. Stephenson, in *Synchrotron Radiation Instrumentation, Pts 1 and 2*, edited by J. Y. Choi and S. Rah (2007), vol. 879 of *AIP Conference Proceedings*, pp. 1321–1324.

[103] R. Krishnamurthy and B. W. Sheldon, *Stresses due to oxygen potential gradients in non-stoichiometric oxides*, Acta Materialia **52**, 1807 (2004).

[104] T. Kamo, K. Nishida, K. Akiyama, J. Sakai, T. Katoda, and H. Funakubo, *RF Magnetron Sputtering Growth of Epitaxial $SrRuO_3$ Films with High Conductivity*, Japanese Journal of Applied Physics **46**, 6987 (2007).

[105] K. Hubbard and D. Schlom, *Thermodynamic stability of binary oxides in contact with silicon*, Journal of Materials Research **11**, 2757 (1996).

[106] H. Mori and H. Ishiwara, *Epitaxial Growth of $SrTiO_3$ Films on Si(100) Substrates Using a Focused Electron Beam Evaporation Method*, Japanese Journal of Applied Physics **30**, L1415 (1991).

[107] A. Lin, X. Hong, V. Wood, A. A. Verevkin, C. H. Ahn, R. A. McKee, F. J. Walker, and E. D. Specht, *Epitaxial growth of $Pb(Zr_0.2Ti_0.8)O_3$ on Si and its nanoscale piezoelectric properties*, Applied Physics Letters **78**, 2034 (2001).

[108] Y. Wang, C. Ganpule, B. T. Liu, H. Li, K. Mori, B. Hill, M. Wuttig, R. Ramesh, J. Finder, Z. Yu, et al., *Epitaxial ferroelectric Pb(Zr, Ti)$O_3$ thin films on Si using $SrTiO_3$ template layers*, Applied Physics Letters **80**, 97 (2002).

[109] K. Eisenbeiser, R. Droopad, Z. Yu, C. Overgaard, J. Kulik, J. Finder, S. Smith, S. Voight, and D. Penunuri, *Crystalline Oxide-Based Devices on Silicon Substrates*, Journal of Electronic Materials **32**, 868 (2003).

[110] R. A. McKee, F. J. Walker, and M. F. Chisholm, *Crystalline Oxides on Silicon: The First Five Monolayers*, Phys. Rev. Lett. **81**, 3014 (1998).

[111] N. A. Pertsev, A. K. Tagantsev, and N. Setter, *Phase transitions and strain-induced ferroelectricity in SrTiO3 epitaxial thin films*, Physical Review B **61**, R825 (2000).

[112] A. Antons, J. Neaton, K. Rabe, and D. Vanderbilt, *Tunability of the dielectric response of epitaxially strained $SrTiO_3$ from first principles*, Physical Review B **71**, 024102 (2005).

[113] J. C. Woicik, H. Li, P. Zschack, E. Karapetrova, P. Ryan, C. R. Ashman, and C. S. Hellberg, *Anomalous lattice expansion of coherently strained $SrTiO_3$ thin films grown on Si(001) by kinetically controlled sequential deposition*, Physical Review B **73**, 024112 (2006).

[114] J. C. Woicik, E. L. Shirley, C. S. Hellberg, K. E. Andersen, S. Sambasivan, D. A. Fischer, B. D. Chapman, E. A. Stern, P. Ryan, D. L. Ederer, et al., *Ferroelectric distortion in $SrTiO_3$ thin films on Si(001) by x-ray absorption fine structure spectroscopy: Experiment and first-principles calculations*, Physical Review B **75**, 140103(R) (2007).

[115] J. P. Perdew, K. Burke, and M. Ernzerhof, *Generalized Gradient Approximation Made Simple*, Phys. Rev. Lett. **77**, 3865 (1996).

[116] G. Kresse and J. Furthmüller, *Efficient iterative schemes for ab initio total-energy calculations using a plane-wave basis set*, Physical Review B **54**, 11169 (1996).

[117] G. Kresse and D. Joubert, *From ultrasoft pseudopotentials to the projector augmented-wave method*, Physical Review B **59**, 1758 (1999).

[118] P. E. Blöchl, *Projector augmented-wave method*, Physical Review B **50**, 17953 (1994).

[119] C. S. Hellberg, private communication (2007).

[120] H. Li, X. Hu, Y. Wei, Z. Yu, X. Zhang, R. Droopad, A. A. Demkov, J. J. Edwards, K. Moore, W. Ooms, et al., *Two-dimensional growth of high-quality strontium titanate thin films on Si*, Journal of Applied Physics **93**, 4521 (2003).

[121] X. Hu, H. Li, Y. Liang, Y. Wei, Z. Yu, D. Marshall, J. J. Edwards, R. Droopad, X. Zhang, A. A. Demkov, et al., *The interface of epitaxial $SrTiO_3$ on silicon: in situ and ex situ studies*, Applied Physics Letters **82**, 203 (2003).

[122] D. A. Walko, O. Sakata, P. F. Lyman, T.-L. Lee, B. P. Tinkham, J. S. Okasinski, Z. Zhang, and M. J. Bedzyk, in *Synchrotron Radiation Instrumentation: Eighth International Conference on Synchrotron Radiation Instrumentation*, edited by

T. Warwick, J. Stöhr, H. A. Padmore, and J. Arthur (AIP, 2004), vol. 705 of *AIP Conference Proceedings*, pp. 1166–1169.

[123] A. Krolzig, G. Materlik, M. Swars, and J. Zegenhagen, *A Feedback-Control System for Synchrotron Radiation Double Crystal Instruments*, Nuclear Instruments & Methods in Physics Research Section A-Accelerators Spectrometers Detectors and Associated Equipment **219**, 430 (1984).

[124] P. Fenter, J. G. Catalano, C. Park, and Z. Zhang, *On the use of CCD area detectors for high-resolution specular X-ray reflectivity*, Journal of Synchrotron Radiation **13**, 293 (2006).

[125] D. M. Goodner, *Atomic-Scale Surface Studies of Alkaline-Earth Metals on Si(001)*, Ph.d., Northwestern University, Evanston, Illinois (2005).

[126] P. Fenter and Z. Zhang, *Model-independent one-dimensional imaging of interfacial structures at $< 1$ Å resolution*, Physical Review B **72**, 081401(R) (2005).

[127] G. H. Kwei, A. C. Lawson, S. J. L. Billinge, and S. W. Cheong, *Structures of the ferroelectric phases of barium titanate*, The Journal of Physical Chemistry **97**, 2368 (1993).

[128] B. Veličkov, V. Kahlenberg, R. Bertram, and M. Bernhagen, *Crystal chemistry of $GdScO_3$, $DyScO_3$, $SmScO_3$ and $NdScO_3$*, Zeitschrift für Kristallographie **222**, 466 (2007).

[129] J. Schubert, O. Trithaveesak, A. Petraru, C. L. Jia, R. Uecker, P. Reiche, and D. G. Schlom, *Structural and optical properties of epitaxial $BaTiO_3$ thin films grown on $GdScO_3$ (110)*, Applied Physics Letters **82**, 3460 (2003).

[130] C. W. Jones, P. D. Battle, P. Lightfoot, and W. T. A. Harrison, *The structure of $SrRuO_3$ by time-of-flight neutron powder diffraction*, Acta Crystallographica Section C **45**, 365 (1989).

[131] M. Biegalski, J. Haeni, S. Trolier-McKinstry, D. Schlom, C. Brandle, and A. Ven Graitis, *Thermal expansion of the new perovskite substrates $DyScO_3$ and $GdScO_3$*, Journal of Materials Research **20**, 952 (2005).

[132] J. A. Bearden, *X-Ray Wavelengths*, Reviews of Modern Physics **39**, 78 (1967).

[133] C. Y. Kim, J. A. Klug, P. C. Stair, and M. J. Bedzyk, *Hydration and Reduction of Molecular Beam Epitaxy Grown $VO_x/\alpha$-$Fe_2O_3(0001)$: Ambient Pressure Study*, Journal of Physical Chemistry C **113**, 1406 (2009).

[134] S. Puri, B. Chand, D. Mehta, M. L. Garg, N. Singh, and P. N. Trehan, *K and L Shell X-Ray Fluorescence Cross Sections*, Atomic Data and Nuclear Data Tables **61**, 289 (1995).

[135] J. H. Scofield, *Exchange corrections of K x-ray emission rates*, Physical Review A **9**, 1041 (1974).

[136] D. A. Close, R. C. Bearse, J. J. Malanify, and C. J. Umbarger, *Yield Ratios, $K\alpha K\beta$, $L\alpha L\beta$, $L\alpha L\gamma$, and $L\alpha Ll$, for X Rays Produced by Protons of 1.0 to 3.7 MeV*, Physical Review A **8**, 1873 (1973).

[137] S. Puri, D. Mehta, B. Chand, N. Singh, J. Hubbell, and P. Trehan, *Production of $L_i$ subshell and M shell vacancies following inner-shell vacancy production*, Nuclear Instruments and Methods in Physics Research Section B: Beam Interactions with Materials and Atoms **83**, 21 (1993).

[138] J. L. Campbell and J. X. Wang, *Interpolated Dirac-Fock values of L-subshell x-ray emission rates including overlap and exchange effects*, Atomic Data and Nuclear Data Tables **43**, 281 (1989).

[139] S. Puri, D. Mehta, B. Chand, N. Singh, and P. N. Trehan, *L shell fluorescence yields and coster - kronig transition probabilities for the elements with $25 \leq Z \leq 96$*, X-Ray Spectrometry **22**, 358 (1993).

[140] D. T. Cromer, *Calculation of anomalous scattering factors at arbitrary wavelengths*, Journal of Applied Crystallography **16**, 437 (1983).

[141] G. P. Williams, in *X-Ray Data Booklet*, edited by A. C. Thompson and D. Vaughan (Lawrence Berkeley National Laboratory, Berkeley, 2001), pp. 1–1–1–7.

[142] O. Auciello, C. M. Foster, and R. Ramesh, *Processing Technologies for Ferroelectric Thin Films and Heterostructures*, Annual Review of Materials Science **28**, 501 (1998).

[143] M. S. Kartavtseva, O. Y. Gorbenko, A. R. Kaul, T. V. Murzina, S. A. Savinov, and A. Barthélémy, *$BiFeO_3$ thin films prepared using metalorganic chemical vapor deposition*, Thin Solid Films **515**, 6416 (2007).

[144] R. Ueno, S. Okaura, H. Funakubo, and K. Saito, *Crystal Structure and Electrical Properties of Epitaxial $BiFeO_3$ Thin Films Grown by Metal Organic Chemical Vapor Deposition*, Japanese Journal of Applied Physics **44**, L1231 (2005).

[145] M. V. R. Murty, S. K. Streiffer, G. B. Stephenson, J. A. Eastman, G.-R. Bai, A. Munkholm, O. Auciello, and C. Thompson, *In situ x-ray scattering study of $PbTiO_3$ chemical-vapor deposition*, Applied Physics Letters **80**, 1809 (2002).

[146] J. Thery, C. Dubourdieu, T. Baron, C. Ternon, H. Roussel, and F. Pierre, *MOCVD of $BiFeO_3$ Thin Films on $SrTiO_3$*, Chemical Vapor Deposition **13**, 232 (2007).

[147] J. W. Elam and S. T. Christensen, private communication (2009).

# Acronyms

**AFM:** atomic force microscopy. 17, 31, 32, 68, 80, 81, 85, 86, 172, 202, 205, 206
**APS:** Advanced Photon Source. 19, 20, 37, 39, 97, 98, 123, 130–132, 135, 156, 172

**BDA:** beam-defining aperture. 97, 108
**BESSRC-CAT:** Basic Energy Sciences Synchrotron Radiation Center. 156
**BFO:** $BiFeO_3$. 17, 54
**BTO:** $BaTiO_3$. 17

**c-AFM:** conductive atomic force microscopy. 29
**CCD:** charge coupled device. 37–39, 100, 101, 106–110, 112, 113, 120–122, 132, 133, 169, 170
**CMOS:** complimentary metal-oxide-semiconductor. 199, 200
**CMR:** colossal magnetoresistance. 59
**CNM:** Center for Nanoscale Materials. 39, 98
**COM:** center of mass. 101, 112, 114, 118, 120, 122, 124, 170
**CTR:** crystal truncation rod. 18, 20, 21, 49, 51–53, 83, 126, 130–132, 135, 142, 145, 147, 148, 150–152, 161–166, 168, 170–172, 204

**DFT:** density functional theory. 4, 20, 30, 126–129, 141–143, 145–147, 149, 150, 171
**DIW:** deionized water. 88, 93, 94
**DND-CAT:** DuPont-Northwestern-Dow Collaborative Access Team. 130
**DSO:** $DyScO_3$. 20

**eBL:** electron-beam lithography. 92–95
**EMC:** Electron Microscopy Center. 90

**FeRAM:** ferroelectric random access memory. 17, 22, 29, 199
**FET:** field effect transistor. 125
**FIB:** focused ion-beam. 18, 32, 85–89, 92–96, 102, 106, 112, 118, 123, 168
**FOM:** focusing optics module. 99, 100, 104, 105, 111
**FWHM:** full width-at-half maximum. 78, 79, 82
**FZP:** Fresnel zone plate. 34, 99

**HHL:** high heat load. 97, 131, 156

**HTSC:** high temperature superconductor. 59
**HVPE:** hydride vapor phase epitaxy. 47
**HXN:** Hard X-ray Nanoprobe. 96, 99

**IPA:** isopropanol. 88, 93

**KB:** Kirkpatrick-Baez. 34
**KCSD:** kinetically controlled sequential deposition. 127, 130

**L-PFM:** lateral-PFM. 85, 86
**LDDM:** laser Doppler displacement meter. 99
**LPE:** liquid phase epitaxy. 56
**LSAT:** $(LaAlO_3)_{0.29} \times (SrAl_{0.5}Ta_{0.5}O_3)_{0.71}$. 26

**MBE:** molecular beam epitaxy. 19, 126, 127, 149, 155, 166
**MEMS:** microelectromechanical systems. 17, 22
**MIBK:** methyl isobutyl ketone. 93
**ML:** monolayer. 20, 47, 126, 127, 129, 132–134, 136–138, 140–142, 147, 148, 150, 170, 171, 173
**MMA(8.5)MAA:** copolymer mixture of PMMA and 8.5% methacrylic acid. 93
**MOCVD:** metalorganic chemical vapor deposition. 57, 199, 200, 202, 204, 206
**MOSTAB:** monochromator stabilizer. 131

**NA:** numerical aperture. 34
**NEMS:** nanoelectromechanical systems. 17, 22

**OBY:** off-Bragg fluorescence yield. 142
**OSA:** order-sorting aperture. 36, 97, 99

**PFM:** piezoresponse force microscopy. 28, 30–32, 85, 86, 126, 146, 149, 205, 206
**PIMBE:** plasma induced molecular beam epitaxy. 47
**PLD:** pulsed laser deposition. 56, 57, 68, 69, 75
**PMMA:** polymethyl methacrylate. 93
**PTO:** $PbTiO_3$. 47

**RBS:** Rutherford backscattering spectroscopy. 142
**RF:** radio frequency. 18, 30, 59–61, 67, 70, 71, 79, 80, 83, 88, 93, 168
**RMS:** root mean square. 60, 80, 81
**ROI:** region of interest. 101, 108, 120, 121
**RSM:** reciprocal space mapping. 56

**SCR:** silicon controlled rectifier. 62
**SDD:** silicon drift diode. 132, 133, 136
**SEM:** scanning electron microscopy. 68, 70–76, 81, 88, 89, 94, 95, 102, 103

**SM:** sample positioning module. 99, 111
**SRO:** $SrRuO_3$. 18
**SSD:** solid state detector. 156, 158
**STO:** $SrTiO_3$. 17

**TEM:** transmission electron microscopy. 27, 30, 90, 91, 102, 126, 142, 150
**TER:** total external reflection. 34

**V-PFM:** vertical-PFM. 85, 86
**VASP:** Vienna *Ab-initio* Simulation Package. 127

**XRD:** x-ray diffraction. 68–71, 75, 80, 81, 136, 155, 200
**XRF:** x-ray fluorescence. 40, 44, 101, 104–106, 123, 132, 136, 139, 142, 150, 156–159, 166, 167, 171, 172, 191
**XRR:** x-ray reflectivity. 81
**XSW:** x-ray standing wave. 4, 18, 20, 40, 43–45, 47, 48, 126, 130–132, 134–146, 149–152, 156, 158–161, 164, 166–168, 170–173, 191

APPENDIX A

# XRF_XSECT: A C Program to Calculate *K* and *L* Shell Atomic X-ray Fluorescence Cross Sections

## A.1. Introduction

In many x-ray standing wave (XSW) experiments, particularly measurements of surface adsorbates such as oxide supported catalysts [133] and ultra-thin films such as the $SrTiO_3$ / Si (001) system discussed in Chapter 6, it is important to quantify the atomic coverage of the of the atomic species being probed. The absolute coverage can be determined by comparing the x-ray fluorescence (XRF) yield measured from the sample of interest with the yield measured from a calibrated standard sample. Standard samples are typically calibrated by Rutherford backscattering spectroscopy (RBS). Since RBS is costly, it is impractical to produce a calibrated standard for an arbitrary atomic species of interest. However, it is possible to compare the fluorescence yields of two dissimilar atoms such that an unknown coverage, $\Theta_x$, can be determined using a known coverage, $\Theta_s$, even if the fluorescing atoms are different. This is calculated by the equation

$$\frac{\Theta_x}{\Theta_s} = \frac{Y_x}{Y_s}\left[\frac{\sigma_s\left(E_\gamma\right)}{\sigma_x\left(E_\gamma\right)}\right]\left[\frac{\eta\left(E_s\right)}{\eta\left(E_x\right)}\right]\left[\frac{T\left(E_s\right)}{T\left(E_x\right)}\right] \tag{A.1}$$

where $Y$ is the measured off-Bragg fluorescence yield, $\sigma\left(E_\gamma\right)$ is the x-ray fluorescence cross section at incident x-ray energy $E_\gamma$, and $\eta\left(E\right)$ and $T\left(E\right)$ are the detector efficiency and transmission through the path from sample to detector, respectively, for fluorescent x-rays

with energy $E$. The XRF cross sections are the most complicated of the necessary parameters, as they are dependent on the particular atomic species, the specific fluorescence line, and the incident energy.

Puri *et al.* calculated a large set of $K$- and $L$-shell XRF cross sections from a comprehensive set of physical parameters available in the literature [134]. For incident x-ray energies in the range $1 - 200$ keV, K-shell cross sections were calculated for $13 \leq \mathrm{Z} \leq 92$ and $L$-shell cross sections were calculated for $35 \leq \mathrm{Z} \leq 92$. Puri *et al.* published a table of the calculated values and developed a logarithmic interpolation to calculate the cross sections for a particular element at a given incident photon energy. However, the calculations by Puri do not include $L$-shell cross sections for incident energies in the range $E_{L_3} \leq \mathrm{h}\nu \leq E_{L_1}$. Furthermore, there is only one energy dependent physical parameter, the photoionization cross section, used to calculate the XRF cross sections. Therefore, the calculation can be performed over a broader energy range than that provided by the method of Puri *et al.* if the energy interpolation is performed on the photoionization cross sections rather than the XRF cross sections.

In this respect, a console application XRF_XSECT was written in the C programming language to calculate $K$- and $L$-shell atomic XRF cross sections at incident x-ray energies up to 80 keV. $K$-shell cross sections can be calculated for elements $13 \leq \mathrm{Z} \leq 98$, and $L$-subshell cross sections can be calculated for elements $25 \leq \mathrm{Z} \leq 94$. The XRF cross sections are calculated from the $K$-shell x-ray emission rates of Scofield [135], the $K$-shell fluorescence yields of Close *et al.* [136], the $K$ to $L$ vacancy transition probabilities of Puri, *et al.* [137], the $L$-subshell x-ray emission rates of Campbell and Wang [138], the $L$-subshell fluorescence yields of Puri *et al.* [139], and the photoionization cross section

data file provided by D. T. Cromer [140]. A polynomial interpolation based on that implemented in Cromer's FORTRAN program was used to calculate the photoionization cross sections at a given incident photon energy. However, the interpolation was achieved by the use of Neville's algorithm in place of the similar, but no longer widely used Aitken's algorithm employed by Cromer.

## A.2. Procedure

Following the procedure outlined by Puri *et al.* [134], the $K$-shell cross sections were calculated using

$$\sigma_{Ki} = \sigma_K^p(E)\omega_K F_{Ki}. \tag{A.2}$$

for $(i = \alpha, \beta)$ where $\sigma_K^p(E)$ is the photoelectric cross section of the $K$-shell of a given atom at an incident photon energy $E$, $\omega_K$ is the $K$-shell fluorescence yield, and

$$F_{Ki} = \sum_i \frac{\Gamma_{Ki}}{\Gamma_K} \tag{A.3}$$

is the fractional emission rate for the $K_i$ $(i = \alpha, \beta)$ group.

The $L$-subshell cross sections were calculated using

$$\sigma_{Ll} = \sigma'_{L_3}\omega_3 F_{3l} \tag{A.4a}$$

$$\sigma_{L\alpha} = \sigma'_{L_3}\omega_3 F_{3\alpha} \tag{A.4b}$$

$$\sigma_{L\beta} = \sigma'_{L_1}\omega_1 F_{1\beta} + \sigma'_{L_2}\omega_2 F_{2\beta} + \sigma'_{L_3}\omega_3 F_{3\beta} \tag{A.4c}$$

(A.4d) $$\sigma_{L\gamma} = \sigma'_{L_1}\omega_1 F_{1\gamma} + \sigma'_{L_2}\omega_2 F_{2\gamma}$$

where $\omega_i$ are the fluorescence yields for the $L_i$ $(i = 1-3)$ subshells, $F_{ik}$ are the fractional emission rates for the $Lk$ $(k = l, \alpha, \beta, \gamma)$ groups, and $\sigma'_{L_i}$ are modified photoionization cross sections which are corrected to account for nonradiative transitions, and are given by

(A.5a) $$\sigma'_{L_1} = \sigma_{L_1}$$

(A.5b) $$\sigma'_{L_2} = \sigma_{L_2} + \sigma_{L_1} f_{12}$$

(A.5c) $$\sigma'_{L_3} = \sigma_{L_3} + \sigma_{L_2} f_{23} + \sigma_{L_1}(f_{13} + f_{12} f_{23})$$

where $f_{ij}$ are the nonradiative Coster-Kronig transition probabilities. For incident energies above the $K$-shell edge, $\sigma_{L_i}$ are replaced by $(\sigma_{L_i} + \sigma_K^p \eta_{KL_i})$ where $\eta_{KL_i}$ are the $K$ to $L_i$ vacancy transition probabilities.

The C program was compiled and tested on the Microsoft Windows XP and Macintosh OS X (both Intel and Power PC based) platforms using the Microsoft Visual Studio and the GNU Compiler Collection (GCC), respectively. A screenshot of XRF_XSECT version 0.9.2 running on Windows XP is shown in Figure A.1. The program outputs the $K$- and $L$-shell cross sections for up to five specified elements at a given incident photon energy. The physical parameters used in the calculation are read from a group of ascii (.dat) files which are listed in Table A.1. As experimental measurements lead to refinement of theoretical data sets, the ascii files can be updated as new data is published. It should be

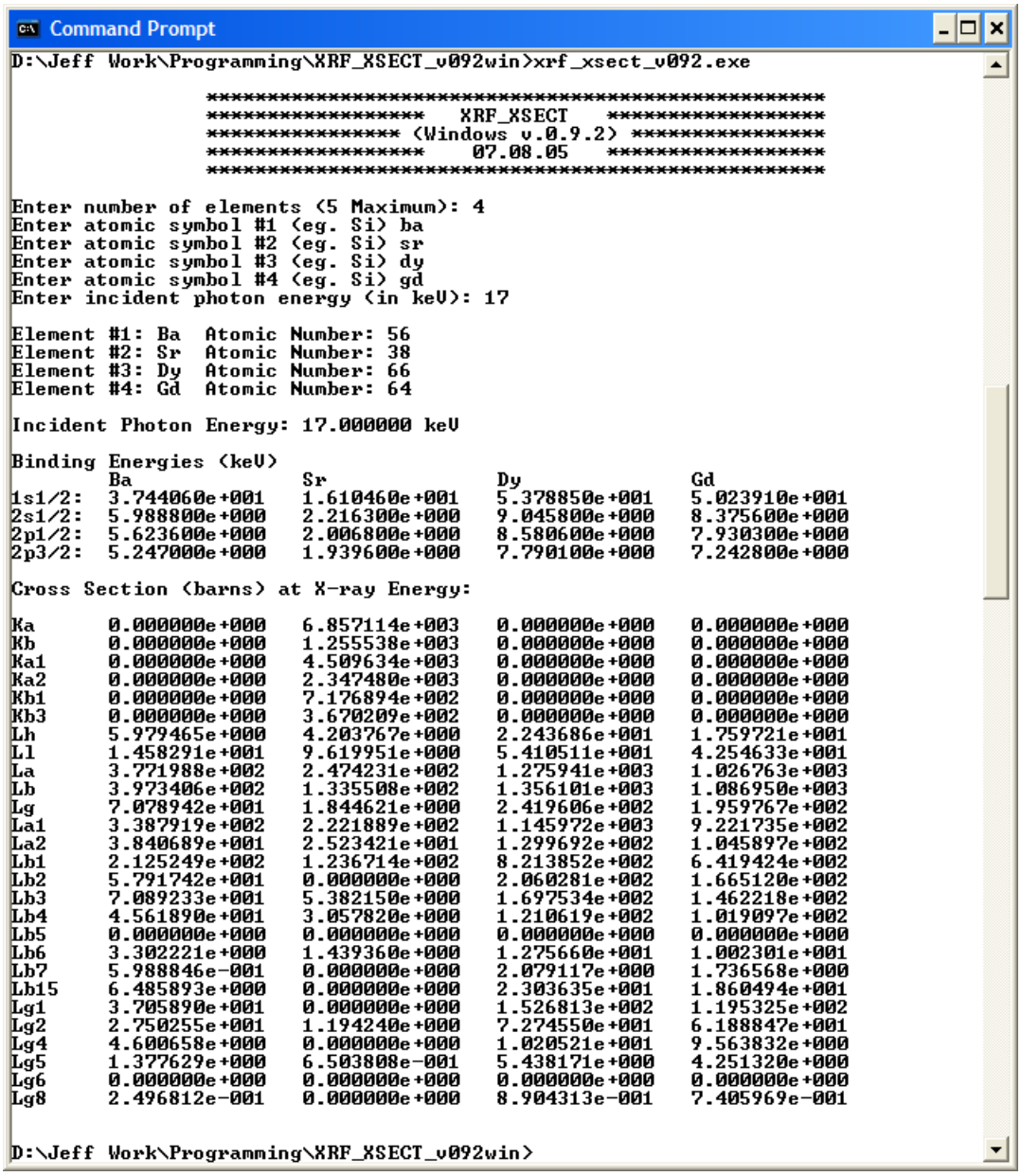

```
Command Prompt
D:\Jeff Work\Programming\XRF_XSECT_v092win>xrf_xsect_v092.exe

                ******************************************************
                ******************   XRF_XSECT   ******************
                ***************** (Windows v.0.9.2) *****************
                ******************    07.08.05   ******************
                ******************************************************

Enter number of elements (5 Maximum): 4
Enter atomic symbol #1 (eg. Si) ba
Enter atomic symbol #2 (eg. Si) sr
Enter atomic symbol #3 (eg. Si) dy
Enter atomic symbol #4 (eg. Si) gd
Enter incident photon energy (in keV): 17

Element #1: Ba  Atomic Number: 56
Element #2: Sr  Atomic Number: 38
Element #3: Dy  Atomic Number: 66
Element #4: Gd  Atomic Number: 64

Incident Photon Energy: 17.000000 keV

Binding Energies (keV)
        Ba              Sr              Dy              Gd
1s1/2:  3.744060e+001   1.610460e+001   5.378850e+001   5.023910e+001
2s1/2:  5.988800e+000   2.216300e+000   9.045800e+000   8.375600e+000
2p1/2:  5.623600e+000   2.006800e+000   8.580600e+000   7.930300e+000
2p3/2:  5.247000e+000   1.939600e+000   7.790100e+000   7.242800e+000

Cross Section (barns) at X-ray Energy:

Ka      0.000000e+000   6.857114e+003   0.000000e+000   0.000000e+000
Kb      0.000000e+000   1.255538e+003   0.000000e+000   0.000000e+000
Ka1     0.000000e+000   4.509634e+003   0.000000e+000   0.000000e+000
Ka2     0.000000e+000   2.347480e+003   0.000000e+000   0.000000e+000
Kb1     0.000000e+000   7.176894e+002   0.000000e+000   0.000000e+000
Kb3     0.000000e+000   3.670209e+002   0.000000e+000   0.000000e+000
Lh      5.979465e+000   4.203767e+000   2.243686e+001   1.759721e+001
Ll      1.458291e+001   9.619951e+000   5.410511e+001   4.254633e+001
La      3.771988e+002   2.474231e+002   1.275941e+003   1.026763e+003
Lb      3.973406e+002   1.335508e+002   1.356101e+003   1.086950e+003
Lg      7.078942e+001   1.844621e+000   2.419606e+002   1.959767e+002
La1     3.387919e+002   2.221889e+002   1.145972e+003   9.221735e+002
La2     3.840689e+001   2.523421e+001   1.299692e+002   1.045897e+002
Lb1     2.125249e+002   1.236714e+002   8.213852e+002   6.419424e+002
Lb2     5.791742e+001   0.000000e+000   2.060281e+002   1.665120e+002
Lb3     7.089233e+001   5.382150e+000   1.697534e+002   1.462218e+002
Lb4     4.561890e+001   3.057820e+000   1.210619e+002   1.019097e+002
Lb5     0.000000e+000   0.000000e+000   0.000000e+000   0.000000e+000
Lb6     3.302221e+000   1.439360e+000   1.275660e+001   1.002301e+001
Lb7     5.988846e-001   0.000000e+000   2.079117e+000   1.736568e+000
Lb15    6.485893e+000   0.000000e+000   2.303635e+001   1.860494e+001
Lg1     3.705890e+001   0.000000e+000   1.526813e+002   1.195325e+002
Lg2     2.750255e+001   1.194240e+000   7.274550e+001   6.188847e+001
Lg4     4.600658e+000   0.000000e+000   1.020521e+001   9.563832e+000
Lg5     1.377629e+000   6.503808e-001   5.438171e+000   4.251320e+000
Lg6     0.000000e+000   0.000000e+000   0.000000e+000   0.000000e+000
Lg8     2.496812e-001   0.000000e+000   8.904313e-001   7.405969e-001


D:\Jeff Work\Programming\XRF_XSECT_v092win>
```

Figure A.1. Screenshot of XRF_XSECT version 0.9.2 running on Windows XP. The program was compiled and tested on the Microsoft Windows XP and Macintosh OS X (both Intel and Power PC based) platforms.

noted that XRF_XSECT has limited accuracy near fluorescence line edges.

Table A.1. Data files included with XRF_XSECT.

| Filename | Description | Ref. |
|---|---|---|
| be.dat | 1s1/2, 2s1/2, 2p1/2, and 2p3/2 binding energies for $13 \leq Z \leq 98$ | [141] |
| elements.dat | atomic symbols for $1 \leq Z \leq 98$ | |
| elements1c.dat | atomic symbols for single character elements | |
| k_ems_rates.dat | $K$-shell emission rates for $13 \leq Z \leq 98$ | [135] |
| k_yields.dat | $K$-shell fluorescence yields for $11 \leq Z \leq 99$ | [136] |
| ktol.dat | $K$ to $L$ vacancy transition probabilities for $18 \leq Z \leq 96$ | [137] |
| l_emis_rates.dat | $L$-subshell emission rates for $18 \leq Z \leq 94$ | [138] |
| l_yields.dat | $L$-subshell fluorescence yields and Coster-Kronig transition probabilities for $25 \leq Z \leq 96$ | [139] |
| pxsect.dat | photoionization cross sections | [140] |

## A.3. Results

To verify the accuracy of the XRF_XSECT calculated cross sections, a series of calculated values were compared with those tabulated by Puri *et al.* [134]. Figure A.2 shows $K$-shell cross sections which were calculated at 17.4 keV for several atomic species with $14 \leq Z \leq 39$, and for Ti $K$ fluorescence at several incident energies in the range 4.97 keV $\leq h\nu \leq$ 80 keV. All of the $K$-shell cross sections calculated at 17.4 keV were within 7% of the Puri values, and all of the calculated Ti $K$-shell values were within 5% of those calculated ny Puri. Figure A.3 shows cross sections which were calculated at 8.048 keV for several atomic species with $35 \leq Z \leq 61$, and for Hg $L$ fluorescence at several incident energies in the range 14.94 keV $\leq h\nu \leq$ 80 keV. All of the $L$-subshell cross sections calculated at 8.048 keV were within 5% of the Puri values with the exception of Nb ($Z = 41$) $L\beta$ cross section which was different by 7.4%. All of the calculated Hg $L$-shell values were within 3% of those calculated by Puri.

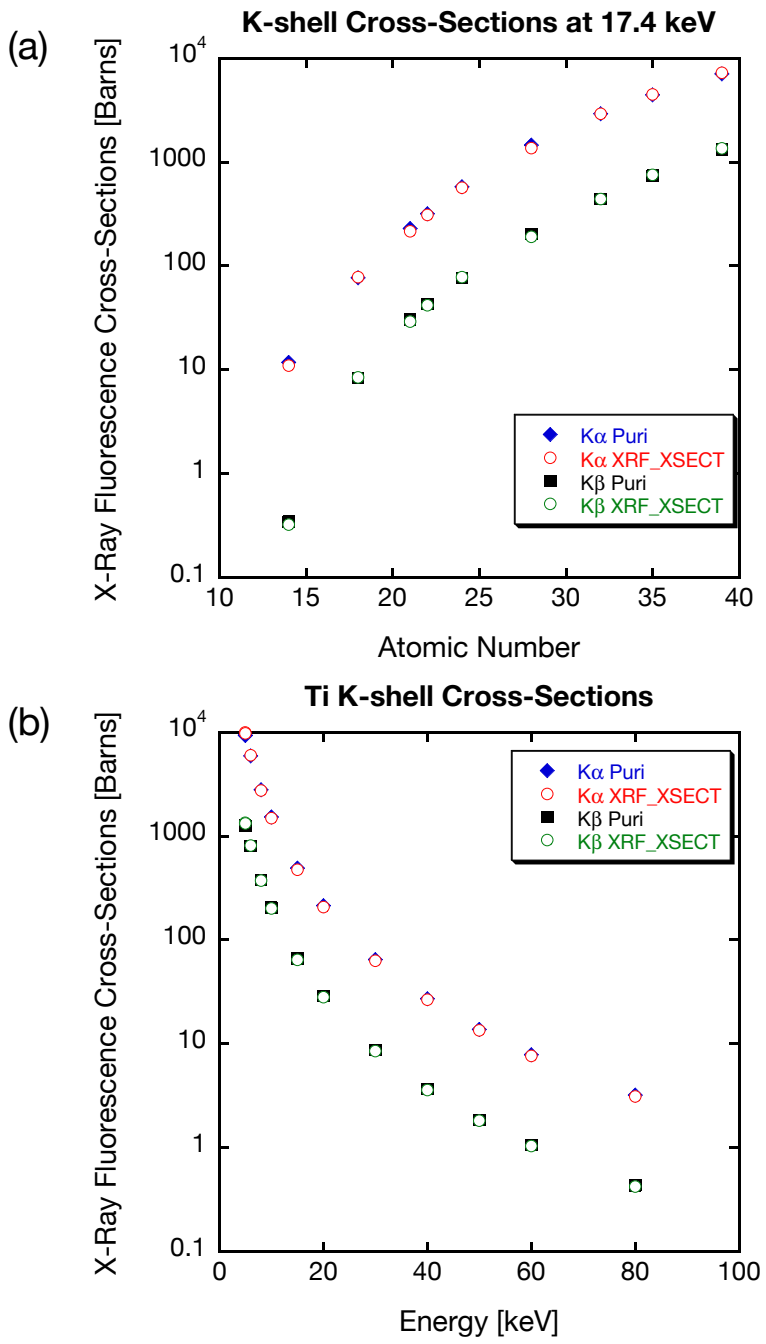


Figure A.2. Comparison of $K$-shell cross sections calculated by Puri and by XRF_XSECT. Cross sections were calculated (a) at 17.4 keV for several atomic species with $14 \leq Z \leq 39$, and (b) for Ti $K$ fluorescence at several incident energies in the range 4.97 keV $\leq h\nu \leq$ 80 keV.

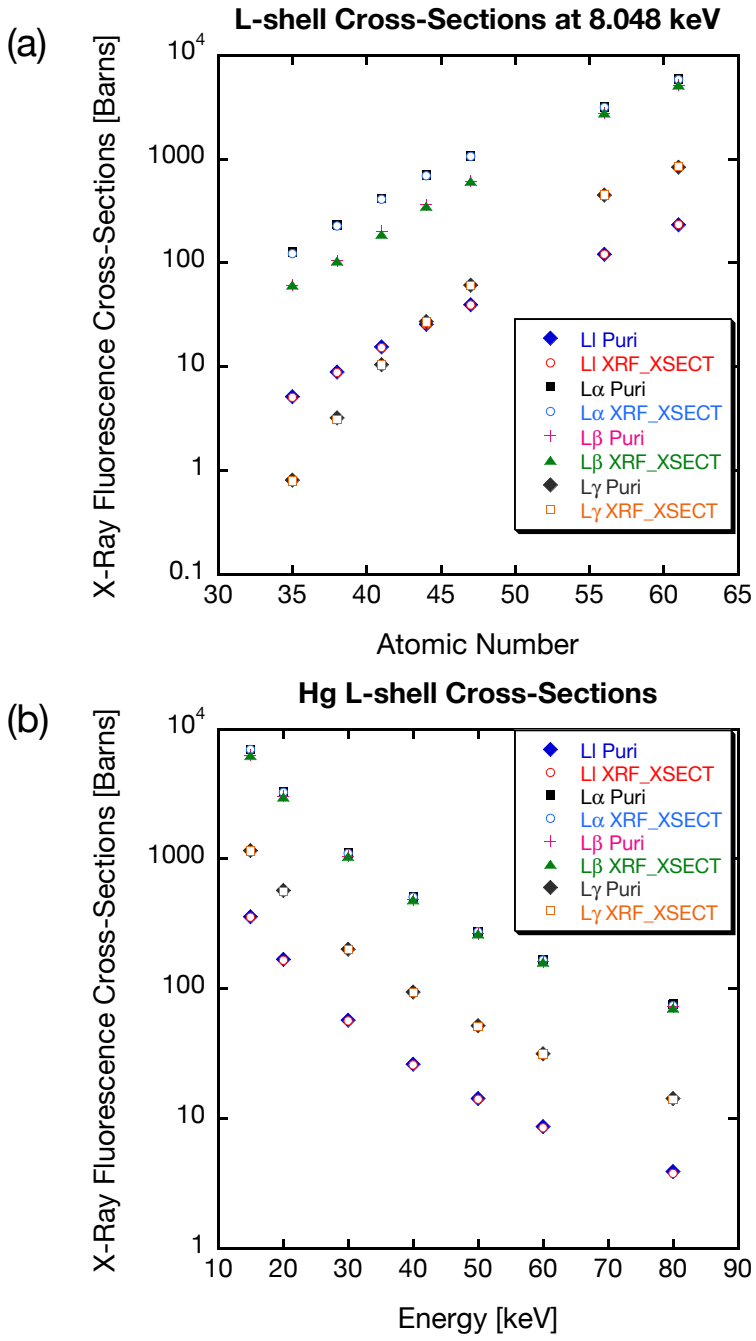


Figure A.3. Comparison of $L$-shell cross sections calculated by Puri and by XRF_XSECT. Cross sections were calculated (a) at 8.048 keV for several atomic species with $35 \leq Z \leq 61$, and (b) for Hg $L$ fluorescence at several incident energies in the range 14.94 keV $\leq h\nu \leq$ 80 keV.

APPENDIX B

# Low Temperature MOCVD Growth of $BiFeO_3$ Thin Films

## B.1. Introduction

The development of a growth process for low temperature metalorganic chemical vapor deposition (MOCVD) of $BiFeO_3$ thin films is important not only from a fundamental science point of view, but also for integration of $BiFeO_3$ film-based capacitors with current complimentary metal-oxide-semiconductor (CMOS) devices for ferroelectric random access memory (FeRAM) fabrication, since it has already been demonstrated that MOCVD is the technique currently used in the fabrication of $Pb(Zr_xTi_{1-x})O_3$ and $SrBi_2Ta_2O_7$-based FeRAMs in the market. MOCVD is the preferred growth method for manufacturing because it is an easily scalable technique, which produces films with extremely uniform thickness and composition not only on flat surfaces, but also on non-planar high aspect ratio features that might be needed for three dimensional structures required for high-density FeRAMs [142]. In addition, it has been shown that MOCVD has produced $Pb(Zr_xTi_{1-x})O_3$ and $SrBi_2Ta_2O_9$ films with the lowest growth temperatures among other deposition processes demonstrated today [142]. Single phase, highly (001) oriented $BiFeO_3$ films have recently been grown on $SrTiO_3$ (001) [143], $SrRuO_3$-coated $SrTiO_3$ (001) [74, 87, 144], and $SrRuO_3$-coated $SrTiO_3$/Si (001) [87] substrates by MOCVD at temperatures between 620 °C and 700 °C. However, a lower temperature process will be necessary, since growth

temperatures exceeding 450 °C would complicate integration of $BiFeO_3$ into CMOS devices. This appendix describes recent work at Argonne National Laboratory investigating low temperature glsmocvd growth of $BiFeO_3$. This work has produced phase-pure, epitaxial (001) oriented films on $SrTiO_3$ (001) substrates at temperatures as low as 500 °C.

## B.2. MOCVD Thin Film Growth

Initial work toward the development of a low temperature MOCVD growth process for $BiFeO_3$ was done with Guoren Bai and Orlando Auciello in the Interfacial Materials Group in the Materials Science Division at Argonne. Epitaxial (001)-oriented $BiFeO_3$ films were grown on (001) $SrTiO_3$ and $SrRuO_3$ coated (001) $SrTiO_3$ substrates using a vertical, gas delivery MOCVD system which is depicted schematically in Figure B.1. Phase-pure $BiFeO_3$ films were produced with volatile metalorganic precursors Triphenylbismuth [$Bi(C_6H_5)_3$] and Tris(2,2,6,6-tetramethyl-3,5-heptanedionate)iron (III) [$Fe(tmhd)_3$] at substrate temperatures between 500 °C and 600 °C. Nitrous oxide ($N_2O$) was used as the carrier gas and oxidant. The presence or absence of unwanted phases (e.g. $\alpha$-$Fe_2O_3$, $\beta$-$Bi_2O_3$) was determined by x-ray diffraction (XRD) immediately following growth. One sample was selected for further characterization. A 20 nm $BiFeO_3$ film was grown on an $SrRuO_3$ coated $SrTiO_3$ (001) substrate at a substrate temperature of 600 °C. The total $BiFeO_3$ deposition time was 1 hour. The MOCVD growth parameters are listed in Table B.1. The 160 nm $SrRuO_3$ layer was grown by off-axis radio frequency (RF) magnetron sputtering in the AJA Rapier Series system discussed in Section 4.2.2. Prior to deposition, the single crystal $SrTiO_3$ (001) substrate (CrysTec GmbH) was treated with a standard buffered-HF etch [92, 93] to produce a $TiO_2$ terminated surface.

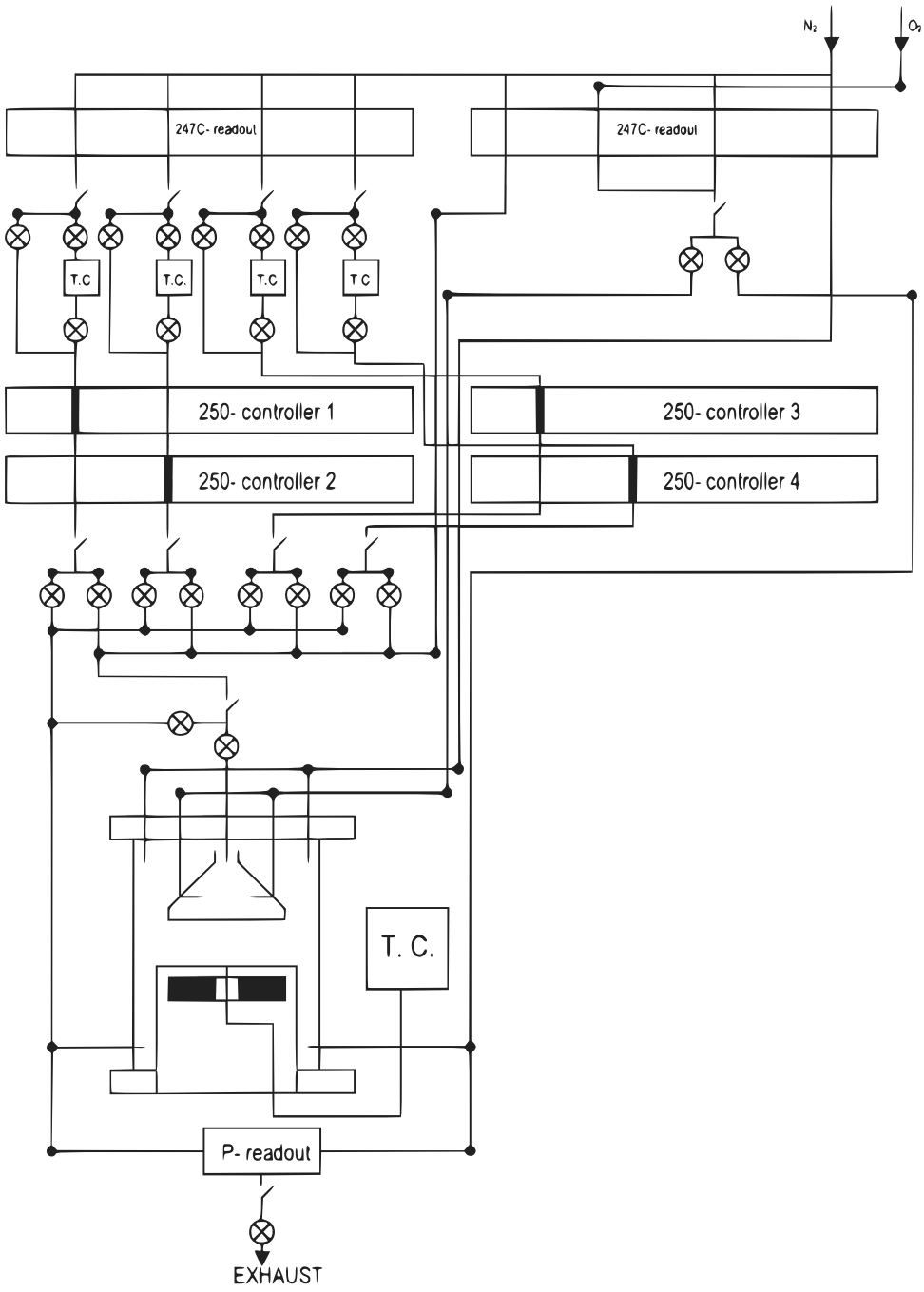


Figure B.1. Schematic diagram of the vertical MOCVD deposition system used for $BiFeO_3$ growth.

Table B.1. Deposition parameters for $BiFeO_3$ film growth by MOCVD.

| Parameter | Temperature | Pressure | $N_2O$ Flow |
|---|---|---|---|
| Substrate | 600 °C | 15 Torr | 1000 sccm |
| $Bi(C_6H_5)_3$ | 94 °C | 10 Torr | 120 sccm |
| $Fe(tmhd)_3$ | 120 °C | 37 Torr | 120 sccm |

## B.3. X-Ray Characterization

High resolution x-ray reflectivity and x-ray diffraction measurements were made in the J. B. Cohen X-Ray Diffraction Facility at Northwestern in order to determine film thickness and cyrstalline quality. Measurements were performed with Cu $K\alpha_1$ radiation from an 18 kW rotating anode source and a high resolution thin film diffractometer (Rigaku ATX-G) equipped with an asymmetric Ge (111) condenser channel cut monochromator.

The low angle reflectivity data, shown in Figure B.2, clearly show the presence of oscillations with two distinct periods. The larger period oscillations are related to the thickness of the (thinner) $BiFeO_3$ film and the smaller period oscillations correspond to the (thicker) $SrRuO_3$ film. From these fringes the thicknesses of 20 and 160 nm for the $BiFeO_3$ and $SrRuO_3$ layers were determined according to $t = 2\pi/\Delta q$. The 20 nm $BiFeO_3$ film thickness corresponds to a deposition rate almost an order of magnitude lower than that reported for MOCVD growth of $PbTiO_3$ [145], although it is consistent with published reports for $BiFeO_3$ [146]. The low growth rate is typical of processes which employ the $Fe(tmhd)_3$ precursor [147]. In addition to the low deposition rate, the reflectivity data also indicate that the surface of the $BiFeO_3$ film is rough as only two full thickness oscillations are visible before the interference is fully dampened. This is consistent with atomic force microscopy (AFM) measurements which are discussed in Section B.4.

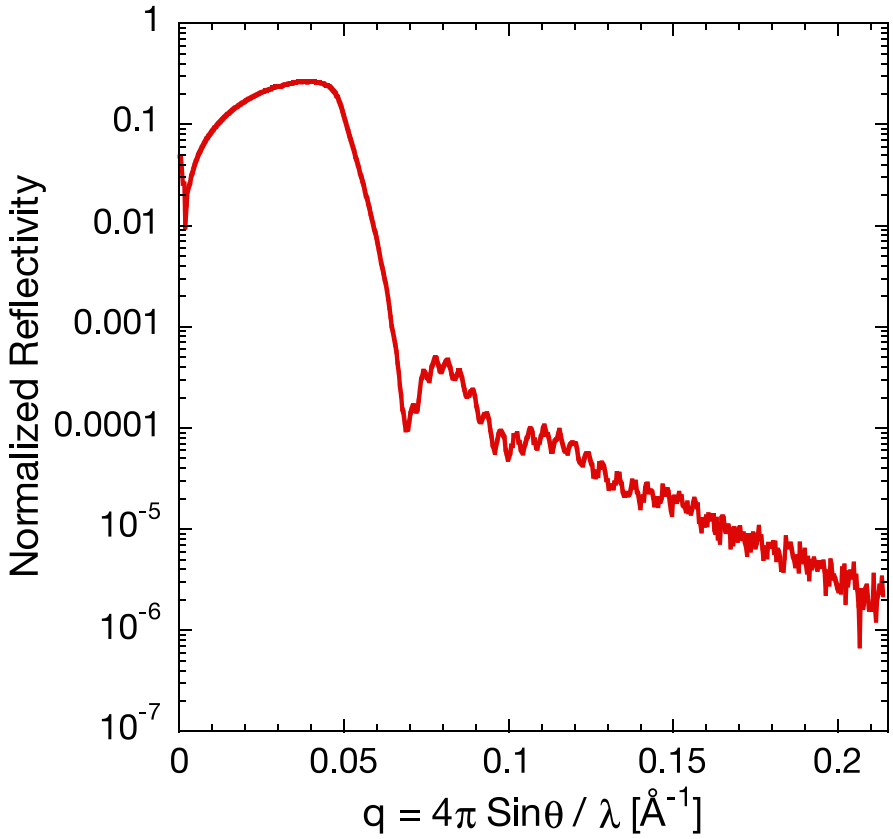


Figure B.2. Low angle x-ray reflectivity measurement of a 20 nm $BiFeO_3$/ 160 nm $SrRuO_3$ / (001) $SrTiO_3$ sample. The large and small period oscillations are related to the thickness of the $BiFeO_3$ and $SrRuO_3$ films, respectively.

The 1D reciprocal space map around the specular (001) peaks was also measured for the same sample. This data, shown in Figure B.3, demonstrate that both films are highly (001) oriented. Additionally, the well-defined thickness fringes from the $SrRuO_3$ layer indicate that the film is of high crystalline quality and uniform thickness. Thickness oscillations in the Bragg region are highly dependent on the crystalline order of a uniform layer, whereas the low angle fringes in Figure B.2 are due to the uniform thickness of a layer with a particular electron density. The fringes from the $BiFeO_3$ layer are much

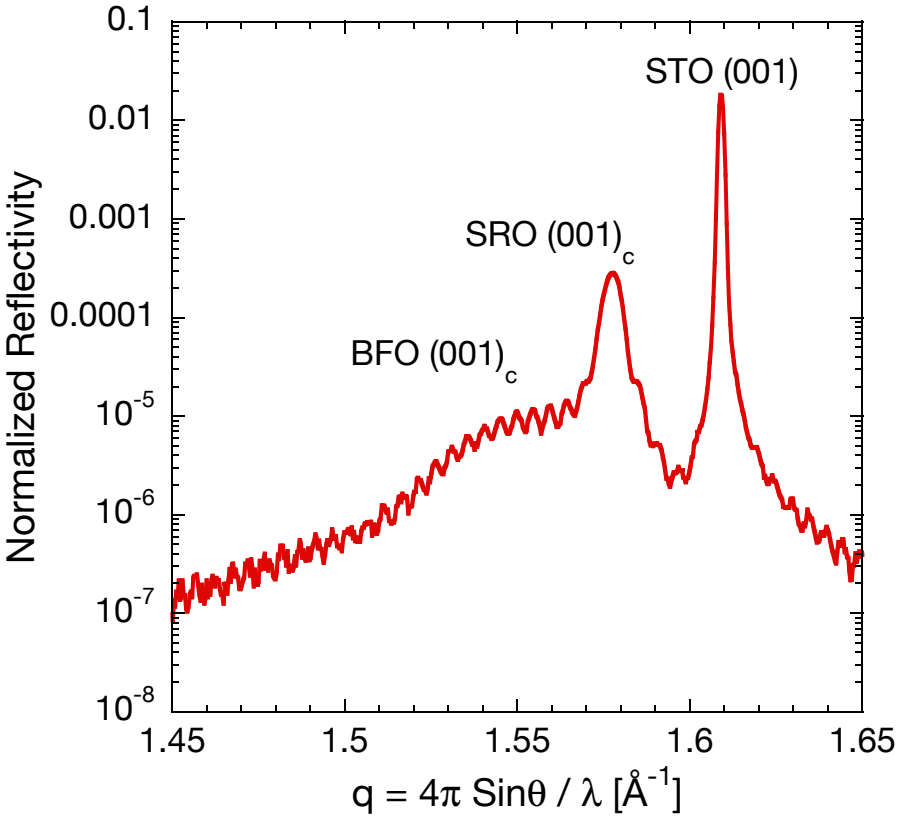


Figure B.3. Specular crystal truncation rod (CTR) measurement of a 20 nm $BiFeO_3$ / 160 nm $SrRuO_3$ / (001) $SrTiO_3$ sample. The $BiFeO_3$ and $SrRuO_3$ layers were grown by MOCVD and off-axis sputtering, respectively.

less pronounced due to the very low reflectivity of such a thin film. The (001) reciprocal space map together with the low angle reflectivity measurement indicated a uniform film thickness and high crystalline quality of both the sputter-grown $SrRuO_3$ and glsmocvd-grown $BiFeO_3$ layers.

## B.4. Ferroelectric Properties

Following X-ray characterization, the film was cut in half and $SrRuO_3$ top electrodes were deposited on one piece of the sample by off-axis sputtering through a mask. Electrical characterization revealed that the film was shorted, and as a result we were unable to make a hysteresis measurement. However, the second piece of the sample was sent to collaborator Alexi Gruverman (North Carolina State University), who performed preliminary piezoresponse force microscopy (PFM) measurements that demonstrated ferroelectricity in the $BiFeO_3$ layer. Results from Gruverman's measurements are shown in Figure B.4. The lateral-PFM (L-PFM) mode image of the as-deposited film reveals numerous grains with random in-plane polarization. The film was successfully poled at dc bias of -5 V applied to the central square. The vertical-PFM (V-PFM) mode image of the poled film shows a clear ferroelectric signature.

The AFM topography images in Figure B.4 (a) and (c) show a peak-to-peak height of approximately 9 nm within the sampled area of 3.5 $\mu$m $\times$ 3.5 $\mu$m. This is larger than the 2 nm value reported by Yang within a 3 $\mu$m $\times$ 3 $\mu$m area on a 250 nm-thick film.

## B.5. Summary

These preliminary X-ray and PFM results demonstrate the growth of epitaxial (001) oriented phase-pure $BiFeO_3$ films on $SrRuO_3$-coated $SrTiO_3$ (001) by gas delivery glsmocvd at a low growth temperature relative to reports in the literature. The films are uniform in thickness and of high crystalline quality, and they exhibit clear ferroelectric switching.

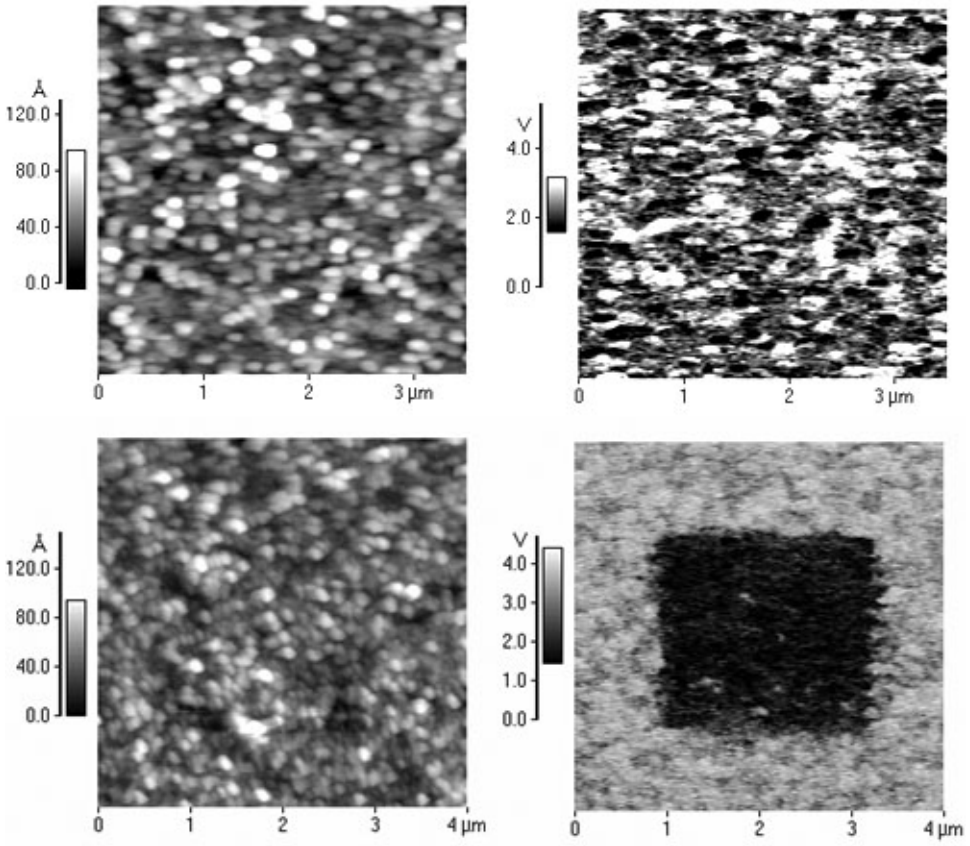


Figure B.4. Piezoresponse force microscopy images from Alexi Gruverman of a 20 nm MOCVD-grown $BiFeO_3$ film on 160 nm $SrRuO_3$ / (001) $SrTiO_3$. Shown are the AFM topography (a) and L-PFM (b) images of the as-grown film, and AFM topography (c) and V-PFM (d) images after poling (-5 V applied to the central square).